THÈSE

Pour obtenir le grade de

DOCTEUR DE L'UNIVERSITÉ DE GRENOBLE

Spécialité : **Mathématiques Appliquées**

Arrêté ministérial : 7 août 2006

Présentée par

Han WANG

Thèse dirigée par **Laurent DESBAT**

préparée au sein **CEA/LIST/DRT/DISC/LITT**
et de **Mathématiques, Sciences et Technologies de l'Information, Informatique**

Méthodes de Reconstruction d'Images à partir d'un Faible Nombre de Projections en Tomographie par Rayon X

Thèse soutenue publiquement le **24 octobre 2011**,
devant le jury composé de :

M. Jean-luc Starck
CEA, Président
M. Xiaochuan Pan
Univ. Chicago, Rapporteur
Mme. Françoise Peyrin
INSA de Lyon, Rapporteur
M. Laurent Desbat
Univ. Joseph Fourier, Directeur de thèse
M. Samuel Legoupil
CEA, Co-Directeur de thèse
M. Thierry Lemoine
THALES Electron Devices, Co-Directeur de thèse

UNIVERSITÉ DE GRENOBLE

Thèse

Pour obtenir le grade de

Docteur de l'Université de Grenoble

Spécialité Mathématiques Appliquées
Arrêté ministériel : 7 août 2006

Présentée et soutenue publiquement par

Han WANG

le 24 octobre 2011

Méthodes de Reconstruction d'Images à partir d'un Faible Nombre de Projections en Tomographie par Rayon X

Methods of X-ray CT Image Reconstruction from Few Projections

Thèse dirigée par Laurent DESBAT

JURY

Xiaochuan Pan	Univ. Chicago	Rapporteur
Françoise Peyrin	INSA de Lyon	Rapporteur
Laurent Desbat	Directeur, UJF	Examinateur
Samuel Legoupil	Encadrant, CEA	Examinateur
Thierry Lemoine	Encadrant, THALES	Examinateur
Jean-Luc Starck	CEA	Président

Thèse préparée au sein de CEA/LIST/DRT/DISC/LITT, dans l'École Doctorale Mathématiques, Sciences et Technologies de l'Information, Informatique.

Abstract

To improve the safety (low dose) and the productivity (fast acquisition) of a X-ray CT system, we want to reconstruct a high quality image from a small number of projections. The classical reconstruction algorithms generally fail since the reconstruction procedure is unstable and suffers from artifacts. A new approach based on the recently developed "Compressed Sensing" (CS) theory assumes that the unknown image is in some sense "sparse" or "compressible", and the reconstruction is formulated through a non linear optimization problem (TV/ℓ^1 minimization) by enhancing the sparsity. Using the pixel (or voxel in 3D) as basis, to apply the CS framework in CT one usually needs a "sparsifying" transform, and combines it with the "X-ray projector" which applies on the pixel image. In this thesis, we have adapted a "CT-friendly" radial basis of Gaussian family called "blob" to the CS-CT framework. The blob has better space-frequency localization properties than the pixel, and many operations, such as the X-ray transform, can be evaluated analytically and are highly parallelizable (on GPU platform). Compared to the classical Kaisser-Bessel blob, the new basis has a multiscale structure: an image is the sum of dilated and translated radial Mexican hat functions. The typical medical objects are compressible under this basis, so the sparse representation system used in the ordinary CS algorithms is no more needed. 2D simulations show that the existing TV and ℓ^1 algorithms are more efficient and the reconstructions have better visual quality than the equivalent approach based on the pixel or wavelet basis. The new approach has also been validated on 2D experimental data, where we have observed that in general the number of projections can be reduced to about 50%, without compromising the image quality.

Résumé

Afin d'améliorer la sûreté (faible dose) et la productivité (acquisition rapide) du système de la tomographie par rayons X (CT), on cherche à reconstruire une image de haute qualité avec un faible nombre de projections. Les algorithmes classiques ne sont pas adaptés à cette situation: la reconstruction est perturbée par artefacts donc instable. Une nouvelle approche basée sur la théorie récente du "Compressed Sensing" (CS) fait l'hypothèse que l'image inconnue est "parcimonieuse" ou "compressible", et formule la reconstruction en un problème d'optimisation (minimisation de la norme TV/ℓ^1) afin de promouvoir la parcimonie. Pour appliquer CS en CT avec le pixel (ou le voxel en 3D) comme la base de représentation, il nécessite une transformation de parcimonie, de plus il faut la combiner avec le "projecteur du rayon X" qui applique sur une image pixelisée. Dans cette thèse, on a adapté une base radiale de famille Gaussienne nommée "blob" à la reconstruction en CT par CS. Le blob a une meilleure localisation spatio-fréquentielle que le pixel, et des opérations comme la transformée en rayons X, peuvent être évaluée analytiquement et elles sont facilement parallélisables (sur le plate-forme GPU). Comparé au blob classique du Kaisser-Bessel, la nouvelle base a une structure multi-échelle: une image est la somme des translations et des dilatations d'un chapeau Mexicain radial. Les images médicales typiques sont compressibles sous cette base, ce qui entraîne que le système de la représentation parcimonieuse intervenu dans les algorithmes ordinaires de CS n'y est plus nécessaire. Des simulations numériques en 2D ont montré que, comparé à l'approche équivalente basée sur la base de pixel ou d'ondelette, les algorithmes du TV et du ℓ^1 existantes sont plus efficaces et les reconstructions ont de meilleures qualités visuelles. Cette nouvelle approche ont été également validée sur des données expérimentales bi-dimensionelles, où on a observé que le nombre de projection peut être réduit jusqu'à 50%, sans pour autant compromettre la qualité de l'image.

Contents

List of Figures

List of Tables

Acknowledgements

This thesis is co-funded by THALES Electron Devices, CEA (Commissariat d'Énergie Atomique) and France national CIFRE program (Conventions Industrielles de Formation par la REcherche), and it would not have been possible without the help of many people.

First, I wish to thank my advisors Laurent Desbat and Samuel Legoupil for their trust and guidance, and also for the abundant help that they offered during all these years. The numerical experiments of this thesis rely heavily on the implementation of the reconstruction algorithms, and I've learned a lot in computer and in programming from my collegues Juan Carlos Garcia, Vincent Picaud, and Olivier Lahaye. Special thanks also to Eric Barat for stimulating discussions, and to Marius Costin and Caifang Cai for having shared their works and data. Additionally, I want to thank Fanny Buyens, Dominique Chambellan, Djara Fall, Nathalie Jolivet, Michèle Quinto, Etienne Thevenot, Alexandre Vabre and many other collegues, for their kindness and for the interesting conversations during the innumerable lunches that we have taken together.

Finally, I wish to express my gratitude to my parents for their understanding and love, and also to my friends for their encouragement and constant support.

Dedicated to my parents

Part I

Regularizations and CS approaches in tomography

Chapter 1

Introduction

1.1 Motivations and Context

This thesis is a contribution to image reconstruction algorithms for the X-ray Computed Tomography (CT) system working at *full angle of view and few projections*. CT is a mature technology to represent visually the inside of a 2D or 3D physical object from exterior projection measurements. It has widespread applications in both industrial and medical domains. Some well known examples concerning our everyday life include dental and cardiac imaging systems in hospitals, or luggage controls in airports. A minimal CT system is composed of two elements :

- data acquisition: at different positions of a sampled trajectory around the object, the X-ray source generates photons which are attenuated by the object, and captured by the detector.
- image reconstruction : the spatial attenuation coefficient is reconstructed from the data collected on the detector (also called *sinogram*), and represented in a gray level image for visualization.

Let us denote $f : \mathbb{R}^d \to \mathbb{R}$ the attenuation function to be reconstructed. The mathematical expression for the data model is the X-ray transform:

$$\mathcal{P}f(\theta, y) = \mathcal{P}_\theta f(y) \triangleq \int_{\mathbb{R}} f(y + t\theta)dt, \ y \in \theta^\perp \tag{1.1}$$

with the direction $\theta \in \mathcal{S}^{d-1}$, the unit sphere of $\mathbb{R}^d$. In 2D, it is equivalent to the Radon transform, defined as:

$$\mathcal{R}f(\theta, s) = \mathcal{R}_\theta f(s) \triangleq \int_{y \in \theta^\perp} f(y + s\theta)dy, \ s \in \mathbb{R} \tag{1.2}$$

We are in a typical situation of ill-posed linear inverse problem, since the inversion of Radon transform $\mathcal{R}^{-1}$ is not bounded.

1.1.1 Sampling condition

In practice both the directions $\theta \in \{\theta_1 \dots \theta_P\}$ and the detector bins $y \in \{y_1 \dots y_D\}$ are finite in number. Typically, the P projections are equally positionned and the D detector bins have the same size. This defines a uniform sampling scheme on the domain $\mathcal{T} = \{(\theta, y), \theta \in \mathcal{S}^{d-1}, y \in \theta^{\perp}\}$. Suppose that the unknown f is essentially B-band-limited ([2], Chapter 3), then the Shannon sampling analysis states that at least $P \geq B/\pi$ projections and $D \geq B$ detector bins are needed in 2D standard sampling schemes to reconstruct f accurately [2]. In language of pixel, this implies that $P \gtrsim 512$ projections and $D \gtrsim 512$ would be necessary to reconstruct an image of dimension 512×512. This is the typical sampling condition required by the widespread analytical reconstruction algorithms such as the *Filtered Back Projection* (FBP).

1.1.2 Few projections problem

The *few projections problem* refers to the reconstruction using $P \ll B/\pi$ equally distributed projections, without compromising the image quality. By solving this problem we can improve both the safety (lower dose) and the productivity (faster acquisition) of a CT system. Unfortunately the classical analytical algorithms such as FBP generally fail in this situation: such a low angular sampling rate leads to heavy streak artifacts which can make the reconstruction impossible to be interpreted. Furthermore, the inversion procedure is unstable due to the presence of noise in data and the problem's ill-posedness (see Chapter 2, example 2.6.1).

Objective of this thesis In this thesis we aim to prove the feasibility of the CT reconstruction from few projections for *generic* objects (medical or industrial oriented), and provide some efficient and robust reconstruction algorithms validated on simulated and real data.

1.2 Previous works

A viable way to treat the few projections problem (and the *incomplete data problem* in general) is to use the *algebraic* or the *iterative* algorithm which allows to incorporate some prior information in the reconstruction procedure. Multiple solutions in this direction

have been proposed in the literature, which are based on different image models and oriented for different applications. In a Bayesian framework, the reconstruction can be done through the *Maximum A posteriori Probability* (MAP) estimation :

$$\hat{f} \triangleq \min_{f \in X} \; F(f, b) + R(f) \tag{MAP}$$

where X is a given functional space, $F(f, b)$ represents the data fidelity and encodes the physical data generation process from model f to sinogram b, and $R(\cdot)$ is the regularization term characterizing the prior information on f. A special case of $R(\cdot)$ is the *edge preserving prior*, which assumes that f is homogeneous by region with sharp edges, so contains little "information" outside the edges. Since a large class of CT object is well represented by this model, this method can effectively reconstruct such objects using a small number of projections.

In the same vein of the edge preserving prior, the popular *TV minimization* method models f in the *Bounded Variation* space and uses the TV semi-norm as $R(\cdot)$. The theoretical properties of this method, such as the edge preservation and the loss of low contrast regions and oscillating patterns, have been intensively investigated and relatively well understood in the literature. The surprising efficiency of TV minimization in treating the few projections problem have been reported in many publications [3–6].

Rather than reconstructing f directly as a visual object, another possibility is to regularize in the *Besov space*: one uses the Besov norm as $R(\cdot)$ via the wavelet transform, and reconstructs the wavelet coefficients [7, 8]. This approach is based on the fact that most natural image can be "compressed", *i.e.*, well represented by a multiresolution wavelet basis with a small number of coefficients. The compression ability and the multiresolution structure of the wavelet basis provides a flexible way to reduce the inherent dimension and compensate the ill-posedness of few projections problem.

The success of TV and wavelet methods can be roughly explained by "representing a function in a space where it is simple". For example, a piecewise homogeneous function of BV space is "simple" since there is practically no information outside edges. Similarly, a natural image represented by its wavelet coefficient has a small Besov norm since most of its information is concentrated on few most largest coefficients.

Sparsity The notion of *sparsity* then enters in our field of view. A vector is *sparse* if it contains few non zero entries, and *compressible* if it can be well approximated by retaining few largest entries. For a linear inverse problem where the number of available data is far fewer than the dimension of the unknown, finding the unknown in a space where it's supposed to be sparse can be much more advantageous than other

regularization techniques, since the sparsity reduces the inherent dimension of the linear system, and improves the trouble situation related to the ill-posedness, such as the non-uniqueness, the instability with respect to noise *etc.*.

From a signal sampling perspective, we are asking whether a unknown function f can be identified using only few samples of the sinogram by exploiting the sparsity, and what would be the sampling conditions and the reconstruction methods.

Compressed Sensing The emerging *Compressed Sensing* (CS) theory gives some rigorous answers to these questions. In a nutshell, if f is sufficiently sparse or compressible with respect to some representation system, then its information can be captured by some random linear measurements whose number is almost proportional to the sparsity level of f, and can be reconstructed through an optimization problem, *e.g.*, the ℓ^1 norm minimization. Furthermore, the reconstruction error is at the same order of the error of "compression". CS also proved that the random measurements together with the ℓ^1 minimization is an optimal combination since they reach some theoretical bound of performance. This theory provides us a general framework for the few projections problem. One needs to:

- represent/model f in a sparsity promoting space, for example, through a multiscale system like the wavelet/curvelet or an arbitrary dictionary which can synthesize a meaningful image with a small number of atoms.
- seek the sparse solution through specific nonlinear methods like the TV or ℓ^1 minimization.

Image representation in CT Remarkably, most of the reconstruction methods of the CS framework use the pixel (or voxel in 3D) as basis for image representation. Apart of the numerical simplicity, the pixel interfaces naturally with many fast transforms (FFT, DCT, DWT etc.). However vis-à-vis the iterative CT reconstruction algorithms, it is not an optimal way for representing a function for that:

- The space-frequency localization of pixel is mediocre. Large pixels are needed for controlling the bandwidth of the reconstruction and stabilizing the inversion procedure, while this can considerably reduce the image's visual quality.
- It requires the discretization or approximation of the X-ray projector, whose computational complexity depends only on the dimension of discretization but not on the sparsity of image under the representation system.

On the other side, a radial basis function called *Kaisser-Bessel blob*, which is better than pixel with these regards, has already been proposed several decades ago. However, it does not have a multiscale structure, and its representations of usual images are not sparse. Furthermore, most of the reconstruction methods proposed for the Kaisser-Bessel blob are not adequate for the few projections problem.

1.3 Contributions

Inspired by these elements and their limitations, we develop in this PhD thesis the "CT-friendly" radial bases of Gaussian family, baptized *blob*, for image representation and reconstruction. They have better space-frequency localization property than pixel, and many operations, such as the X-ray transform, the gradient or the interpolation, can be analytically evaluated, thus there is no need for discretization or approximation of the X-ray projector. An image represented by these bases has a compressible form, so the *ad hoc* sparse representation system used in the ordinary CS algorithms is not needed.

We will build a single scale and a multiscale image model based on blobs, which can be qualified as the mimics of pixel or multiresolution wavelet representation. Some approximation properties of these new image models will be studied. A function is represented in the shift invariant space generated by these blobs on an hexagonal lattice, and the reconstruction amounts to determining the blob coefficients, through the TV and the ℓ^1 minimization that we adapt for the blob image model. These two methods have different behavior depending on the object's content (*e.g.*piecewise constant or with low contrast regions), and on the number of projections. The computations with blob, *e.g.*the X-ray projection, the interpolation, are highly parallelizable on the GPU platform. A GPU based *blob-driven* X-ray projector for blob image, is developed. To demonstrate the efficiency of the new image models and the CS reconstruction algorithms, we will compare them with the equivalent approaches based on pixel/wavelet basis through numerical experiments of image reconstruction.

Organization of thesis In chapter 2, we introduce a widely accepted linear data model for CT, and prepare a general Bayesian framework in which the prior information can be easily introduced. Then the reconstruction is put in form of an optimization problem, which is fundamental to all our further development.

The choice of the prior in the Bayesian framework is essential to solve the reconstruction problem with few projections, and it needs to reflect our *a priori* knowledge on the unknown function f, primarily in term of its *smoothness*. In chapter 3, we give a

review on some state-of-the-arts regularization techniques and iterative reconstruction algorithms proposed in the CT literature, particularly those relevant to the few projections problem. We emphasize on the Total Variation minimization and the Besov norm minimization via wavelet because of their relations with CS theory. Some non Bayesian methods of regularization, in which the prior information is not expressed as a probability distribution, is also discussed.

In chapter 4, we resume some important results of Compressed Sensing theory and analyze its usefulness in CT reconstruction. Particularly we will explain why the random measurements are relevant to capture the information of a sparse signal, and in which sense the ℓ^1 minimization is the optimal method for the reconstruction.

In the second part of this thesis we present our main contributions. The radial blob functions is introduced in chapter 5, where two image representation models based on Gaussian family blobs are developed. First we span the shift invariant space with the Gaussian blob on an hexagonal lattice and prove that the translations of Gaussian blob constitute a Riesz basis. It is found that unlike the case of pixel basis, by simply dilating the Gaussian blob and the lattice, one cannot approximate $L^2(\mathbb{R}^d)$ with the shift invariant space. Then we give a general way to construct the tight frame of $L^2(\mathbb{R}^d)$ using the multiscale blob system, which can give compressible representations of natural images. Some practical criteria on the choice of blob parameters are also discussed, and finally we show that there exits a multiscale system named *vaguelette blob* in the sinogram domain associated the multiscale blob system of space domain, by using the Wavelet-Vaguelette Decomposition.

The CS reconstruction methods, namely the TV and the ℓ^1 minimizations, can be applied on the new image representation models, by solving some technical challenges such as the evaluation of the Total Variation semi-norm on a blob image. In chapter 6 we propose some reconstruction methods for blob image by adapting and improving the existing algorithms.

2D reconstruction results using simulated data using the blob image models and the CS reconstruction methods are presented in chapter 7. In order to demonstrate their effectiveness in reducing the number of projections, we confront the methods based on blob with the equivalent approaches based on pixel. We also make comparison between different methods in order to understand their pros and cons in function of the application context, *e.g.*, medical (low contrast objects) or industrial (piecewise homogeneous objects) oriented. In chapter 8 we present some preliminary results of reconstructions using real data collected from different industrial/medical applications.

Some perspectives are given in the last part. First, 3D numerical experiments are not presented in this thesis, while the whole theory and the reconstruction methods that we have developed include the 3D as a special case. Nevertheless, more efforts seem to be necessary for the efficient parallelization of algorithms in 3D case, due to the large dimension of the problem. Second, our blob image model lacks the geometric sensitivity due to the blob's radial symmetry, and their representation coefficients have a decaying rate similar to that of the wavelet basis. Particularly, one needs a large number of blobs for representing a contour. A possible improvement would be a curvelet-like multiscale blob system, in which the radial symmetry of blob is dropped in favor of the angular orientation, while it still keeps the "CT-friendly" characters of the radial blob. Lastly, all the reconstruction techniques studied previously search a solution in the object space. While another way is to restore the entire sinogram, then proceed by the standard algorithm like FBP. Under the new context of few projections problem, we need to restore a highly incomplete sinogram. This is possible by exploiting the sparsity of sinogram under the *vaguelette blobs* using an analysis prior. We give some preliminary investigations by presenting an algorithm on the efficient implementation of this prior.

Chapter 2

Linear data model and Bayesian framework

The reconstruction of a spatial object from few projections is an ill-posed inverse problem on which the analytical methods cannot be applied [2]. The *iterative methods* (also called *algebraic methods*) on the contrary, can stabilize the inversion and provide visually acceptable solutions by taking advantage of the prior information about the object. In this chapter, we introduce a widely accepted linear data model for CT, which states the linear relation between the observation and the unknown object, and is fundamental to all our further development. Then we prepare a general Bayesian framework in which the prior information can be easily introduced, and we put the reconstruction in form of an optimization problem.

2.1 Physical model

The X-ray used in most CT systems has a continuous energy spectrum. Let's denote by $m_S(E)$ the photon number of energy E emitted by source S, and $f(x;E)$ the linear attenuation coefficient at position x (for a given material with a known mass attenuation value, $f(x;E)$ depends only on the density of material). The photon flux is attenuated when travel between the source and the detector, and only $y_i(E)$ photons arrive finally on the i-th detector bin D_i. For reason of simplicity, here we have supposed that the detector is perfect, *i.e.*, it captures each arriving photon with probability 1, and ignored the undesired factors such as the spatial variation of source intensity, the photon scattering and the background radiation. The photon number $y_i(E)$ are commonly accepted as

independent Poisson random variables of mean $m_i(E)$:

$$y_i(E) \sim \textbf{Poisson}(m_i(E)), \quad \text{for } i \in \mathbb{Z} \tag{2.1}$$

and the mean $m_i(E)$ is given by the well-known Beer-Lambert law:

$$m_i(E) = m_S(E) \exp\left(-\int_{L_i} f(x;E)dx\right) \tag{2.2}$$

where the integration is on the line segment L_i from S to D_i. We note y_i the total intensity for the whole energy spectrum on the i-th detector bin, and y_i is the sum of $y_i(E)$ on the whole spectral range $[E_0, E_1]$: $y_i = \int_{E_0}^{E_1} y_i(E)dE$. By the summability of independent Poisson variables $y_i(E)$, y_i follows also a Poisson distribution with the mean m_i given by:

$$\int_{E_0}^{E_1} m_i(E)dE = \int_{E_0}^{E_1} m_S(E) \exp\left(-\int_{L_i} f(x;E)dx\right) dE \tag{2.3}$$

The reconstruction amounts to determining the parameter $f(x;E)$ for every position x and energy E from the samples of random variables $y_i(E)$. Nevertheless, due to the limited energy resolution of X-ray detector, in practice $y_i(E)$ are not observed for all E, which makes the estimation of $f(x;E)$ rarely feasible.

Monochromatic source We make the important assumption that the source is monochromatic, and drop the dependence on E in previous notations. Finally, the reconstruction problem becomes estimating the attenuation coefficient $f(x)$ from the the observations y_i, which are independent Poisson variables:

$$y_i \sim \textbf{Poisson}(m_i) \tag{2.4}$$

and the mean m_i:

$$m_i = m_S \exp\left(-\int_{L_i} f(x)dx\right) \tag{2.5}$$

This allows to derive a simple linear model in the sequel. However, it is worth to point out that the X-ray source is always polychromatic in reality, and this assumption is at the origin of the so called *beam-hardening* artefacts in reconstruction [2, 9].

2.2 Bayesian framework and linear data model

In the following we identify the physical object with its attenuation value f. X denotes the "solution space", a separable Hilbert space which contains all possible f. We note $\mathbf{y} \triangleq [y_1, y_2 \ldots]^\top$ the observation in photon intensity, and $\mathbf{m}(f) = [m_1, m_2 \ldots]^\top$ the vector of mean photon intensity at source. y_i, m_i follow the definition in Eq. (2.4) and Eq. (2.5).

The *Poisson likelihood function* (PLF) $\mathbb{P}(\mathbf{y}|\mathbf{m}(f))$ is the probability to observe the data $\mathbf{y}$ given the parameters $\mathbf{m}(f)$. Recall the Poisson density function of mean λ: $\mathbb{P}(n|\lambda) \triangleq \exp(-\lambda)\lambda^n/n!$. Then under the hypothesis that y_i are mutually independent, we have:

$$\mathbb{P}(\mathbf{y}|\mathbf{m}(f)) = \prod_i \mathbb{P}(y_i|m_i) = \prod_i \frac{m_i^{y_i}}{y_i!} \exp(-m_i) \tag{PLF}$$

The Bayesian framework provides a general approach to the statistical estimation of f based on (PLF). Taking the maximum of (PLF) as an estimator of f leads to the *maximum likelihood* (ML) estimation:

$$\hat{f}_{ML} \triangleq \arg\max_{f \in X} \ \mathbb{P}(\mathbf{y}|\mathbf{m}(f)) \tag{2.6}$$

If we have a prior probability density $\pi(f)$ on the parameter space X, then in place of ML the *maximum a posterior probability* (MAP) estimator can be used:

$$\begin{aligned} \hat{f}_{MAP} &= \arg\max_{f \in X} \mathbb{P}(f|\mathbf{y}) \\ &= \arg\max_{f \in X} \mathbb{P}(\mathbf{y}|\mathbf{m}(f))\pi(f) \end{aligned} \tag{2.7}$$

Remark 2.2.1. MAP estimator picks up only the maximizer of $\mathbb{P}(\cdot|\mathbf{y})$. From a general point of view, other statistical inferences can replace MAP if one can generate the samples from the distribution $\mathbb{P}(\cdot|\mathbf{y})$. In Positron Emission Tomography (PET) for example, the prior spatial distribution π governs the unknown emission concentration $\lambda(x)$. By sampling the posterior distribution $\mathbb{P}(\lambda|\mathbf{y})$ one generates infinite number of realizations of $\lambda(x)$ on which the statistical inferences, as the estimation of conditional mean and variance, can be done (See the work of E.Barat [10]). In CT the situation is similar but having a totally different interpretation. Even though the parameter space X is equipped with a prior distribution π, one must keep in mind that the unknown f is a fixed function but not a random spatial distribution as the $\lambda(x)$ in PET.

2.2.1 Logarithm Poisson likelihood function

Taking the logarithm of (PLF) $\log \mathbb{P}(\mathbf{y}|\mathbf{m}(f))$ does not change the maxima of (2.6). After removing the irrelevant constants, the *log-Poisson likelihood function* (LPLF) reads:

$$L(f;\mathbf{y}) \triangleq -\sum_i y_i (Af)_i - m_S \sum_i \exp\left(-Af\right)_i \tag{LPLF}$$

where $A : X \to \ell^2(\mathbb{Z})$ the linear operator yielding the discrete sinogram and $(Af)_i$ denotes the linear integration:

$$(Af)_i = \int_{L_i} f(x)dx \tag{2.8}$$

In regularization theory of inverse problem, (LPLF) corresponds to the data fitting term, whose level set consists of objects yielding the data $\mathbf{y}$ with equal probability. We will replace it by a quadratic form as done in usual linear inverse problem formulations, and this can greatly simplify the numerical treatment of the reconstruction problem. The following arguments can be found in [11, 12].

2.2.1.1 Approximation of LPLF by quadratic form

Let's rewrite $L(f;\mathbf{y}) = \sum_i h((Af)_i, y_i)$, with $h(u, y_i) = -m_S e^{-u} - uy_i$, and note $b_i = -\log(y_i/m_S)$ the logarithm transformed data. Remark that $h(\cdot, y_i)$ is maximized at b_i. Then by a local development of $h(\cdot, y_i)$ around b_i we find:

$$h((Af)_i, y_i) \simeq -\frac{1}{2} y_i ((Af)_i - b_i)^2 + h(b_i, y_i) \tag{2.9}$$

thus LPLF is approximated around b_i by the sum of a weighted quadratic form and an irrelevant constant:

$$\begin{aligned} L(f;\mathbf{y}) &\simeq -\frac{1}{2} \sum_i y_i ((Af)_i - b_i)^2 + \text{cst} \\ &= -\frac{1}{2} \|Af - \mathbf{b}\|_Y^2 + \text{cst} \end{aligned} \tag{2.10}$$

with $\mathbf{b} = [b_1, b_2 \ldots]^\top$, and $\|\centerdot\|_Y$ the ℓ^2 norm weighted by the diagonal matrix $Y = \text{diag}(\mathbf{y})$. This approves the usage of the quadratic form as data fitting term in place of LPLF. Specifically, we admit the *linear data model*:

$$\mathbf{b} = Af + \mathbf{n}, \;\; n_i \sim \mathcal{N}(0, 1/m_i) \tag{2.11}$$

Remark 2.2.2. The above approximation is true only when we have $b_i \simeq (Af)_i$, for all i. To see when this condition is met, we remark that:

$$(Af)_i - b_i = \log\left(1 + \frac{y_i - m_i}{m_i}\right) \simeq \frac{y_i - m_i}{m_i}$$

where m_i is defined as in (2.5). Since y_i follows the Poisson law: $\mathbb{E}(y_i) = \mathrm{Var}(y_i) = m_i$, therefore:

$$\mathbb{E}\left[\left(\frac{y_i - m_i}{m_i}\right)^2\right] = \mathrm{Var}(y_i)/m_i^2 = 1/m_i$$

This means that $b_i \simeq (Af)_i$ when m_i is large. In other words, the previous approximation is true when the mean number of arriving photons is large, *i.e.*when the data is not very noisy. We shall still use (2.10) even on noisy data (low photon dosage case), and the bias introduced by this approximation is considered as compensated by the regularization term discussed in next chapter.

2.2.2 Variational formulations of the reconstruction problem

Taking the logarithm on (2.7) and using LPLF approximation (2.10), we put the MAP estimator in the following form:

$$\hat{f}_{MAP} = \arg\min_{f \in X} \ \frac{1}{2}\|Af - \mathbf{b}\|_Y^2 - \log \pi(f) \tag{2.12}$$

which can be further simplified if all the observed intensity y_i are of the same magnitude σ^{-1}: $Y \simeq \sigma^{-1}\,\mathrm{Id}$:

$$\min_{f \in X} \ \frac{1}{2}\|Af - \mathbf{b}\|^2 + \sigma R(f) \tag{2.13}$$

where $R(f) = -\log \pi(f)$ is the *regularization* term which represents the *a priori* knowledge on f. The constant σ determines the strength of the regularization. It is well known (see for example [13], Chapter 3) that as σ tends to 0, (2.13) is equivalent to the constraint optimization form:

$$\min_{f \in X} R(f) \ \text{ s.t. } \ Af = \mathbf{b} \tag{2.14}$$

The constraint here requires the noise-free data which is never the case in reality. To take into account the noise, we solve:

$$\min_{f \in X} R(f) \ \text{ s.t. } \ \|Af - \mathbf{b}\|^2 \leq \varepsilon \tag{2.15}$$

where ε should be set according to the noise level. Other variations to (2.13) are possible. For example, we can drop the regularization term and consider uniquely the *minimum squared error* (MSE) problem:

$$\min_{f \in \operatorname{Ker} A^{\perp}} \|Af - \mathbf{b}\|^2 \tag{MSE}$$

or even the simplest algebraic equation, in case that $\mathbf{b} \in \operatorname{Im} A$:

$$Af = \mathbf{b} \tag{2.16}$$

Remark that all these formulations can be incorporated with some explicit constraint on f, such as the positivity $f(x) \geq 0, \forall x$.

2.3 Discretization of the solution space X

For the numerical treatments of the optimization problems above, we need to develop the solution space X in more details. Let Ω be the unit ball of $\mathbb{R}^d (d = 2, 3)$, and $L^2(\Omega)$ be the space of squared integrable functions supported on Ω. We take X a closed subspace of $L^2(\Omega)$ representing the physical objects. A very first step in iterative reconstruction methods is to discretize X. Generally, the idea relies on using a countable family of *basis function* $\{\phi_k \in L^2(\Omega)\}_{k \in \mathbf{Z}}$. For example,

- either $\{\phi_k\}$ is a Riesz basis, then we take X as the span of $\{\phi_k\}$,
- or we choose first $X \subseteq L^2(\Omega)$, then prove that $\{\phi_k\}$ is a frame of X.

Then any $f \in X$ can be expressed using a coefficient sequence $\{f_k\} \in \ell^2(\mathbb{Z})$ in the following manner:

$$f(x) = \sum_{k \in \mathbf{Z}} f_k \phi_k(x) \tag{2.17}$$

and the reconstruction amounts to determining the coefficients $\{f_k\}$. In this early stage, we take into consideration the numerical efficiency of $\{\phi_k\}$, and prefer the spatially localized basis functions, *e.g.* those with small compact support. Formally speaking, the application of a general linear operator A on f can be done element-wisely in a parallel manner: $Af = \sum_{k \in \mathbf{Z}} f_k A\phi_k$. If the operator A is also "localized" in space, such as the X-ray transform, then the localization of ϕ_k can help to moderate the computational charge. See Chapter 5 and Annexe A for more detailed discussions.

Shift invariant space A more useful model than (2.17) is based on the *shift invariant space*, which is generated by the translations of a single function $\phi(x)$ (or by a family $\{\phi^j(x)\}$, see the discussion in Chapter 5). An immediate example is the pixel (or voxel in 3D) basis. Let $k = (k_1, k_2) \in \mathbb{Z}^2$, $x = (x_1, x_2) \in \mathbb{R}^2$, and $h > 0$ the sampling step of Cartesian lattice, the pixel basis is defined by:

$$\phi(x) = h^{-1} \mathbb{1}_{[0,1]}(x_1/h) \mathbb{1}_{[0,1]}(x_2/h), \tag{2.18}$$

Then the shift invariant space X is spanned by the translations $\{\phi_k(x) \triangleq \phi(x - hk)\}$, which is an orthogonal system of X. Coupled with the fixed regular Cartesian lattice, the pixel basis is *de facto* the standard way to represent image in today's most state-of-art reconstruction algorithms.

Wavelet basis [Chapter 7, [14]] Let ϕ be a monodimensional scaling function and ψ the related mother wavelet which defines an orthogonal basis of $L^2(\mathbb{R})$. We note $\psi^0 = \phi$ and $\psi^1 = \psi$, $0 \leq l \leq 2^d - 1$ and integer and $(l) = l_1 l_2 \dots l_d$ the binary form of l. In $\mathbb{R}^d$ the mother wavelet is usually defined as a tensorial product:

$$\psi^{(l)}(x) \triangleq \psi^{l_1}(x_1)\psi^{l_2}(x_2) \cdots \psi^{l_d}(x_d), x \in \mathbb{R}^d$$

The orthogonal wavelet basis in $\mathbb{R}^d$ is then obtained by dilating and translating $\psi^{(l)}(x)$:

$$\psi^{(l)}_{j,k} \triangleq 2^{-jd/2} \psi^{(l)}(2^{-j}x - k), \quad \text{for } j \in \mathbb{Z}, k \in \mathbb{Z}^d \tag{2.19}$$

To simplify the notation, sometimes we shall also use ψ_λ to note $\psi^{(l)}_{j,k}$ with the multi-index $\lambda = (l, j, k)$. Then any $L^2(\mathbb{R}^d)$ function f can be written as:

$$f = \sum_\lambda \langle f, \psi_\lambda \rangle \psi_\lambda \tag{2.20}$$

Thus f is uniquely represented by the coefficients $\{\langle f, \psi_\lambda \rangle\} \in \ell^2(\mathbb{Z})$, and we can think of f as "discretized" by the wavelet basis on the multiscale Cartesian lattice $\{2^j k, j \in \mathbb{Z}, k \in \mathbb{Z}^d\}$.

2.4 X-ray projector

The operator A in the variational problems of section 2.2.2 and its adjoint A^* (or $A^\top$ if understood as matrix), are of particular importance for the iterative reconstruction algorithms. They are also called the X-ray *projector* and *backprojector* in the CT jargon.

Numerically, the projector A is applied on a discrete image of type (2.17), and approximates the linear integral (2.8). Its development is an independent line of research in the tomography literature, with some objectives like: 1) numerical efficiency; 2) being faithful to the X-ray transform; 3) reducing the high frequency errors (due to the sampling of image and detector) in the reconstructed image. Most of existing methods for X-ray projector are based on the pixel/voxel discretization of image, for example, the Siddon ray-driven method [15], the Joseph pixel-driven method [16], the Distance-driven method [17] etc. See also [18–22].

The boundness of an operator in an infinite dimension setting is an important issue. We shall establish this point for the projector A under some simple but realistic assumptions. Let $\mathcal{P}_\theta$ be the X-ray transform taken at position θ:

$$\mathcal{P}_\theta f(y) \triangleq \int_{\mathbb{R}} f(y + t\theta)dt, \quad \text{with } \theta \in \mathcal{S}^{d-1}, y \in \theta^\perp \tag{2.21}$$

Let $w_B \in L^1(\mathbb{R}^{d-1})$ be a band-limited function: $\operatorname{supp} \hat{w}_B \subset [-B, B]^{d-1}$, which characterizes the response of the detector. The sampling operator on the detector is defined as $S_h = \sum_{k \in \mathbf{Z}^{d-1}} \delta(x - hk)$, with δ the Dirac and $h > 0$ the sampling step. We assume that the projector at θ acts as:

$$A^\theta f = S_h \circ (w_B * \mathcal{P}_\theta f) \tag{2.22}$$

which means that the projection is first band limited then followed by a sampling process.

Lemma 2.4.1 (Boundness of A^θ)**.** *Let Ω be the unit ball of $\mathbb{R}^d$. If the sampling step $h \leq (2B)^{-1}$, then the operator $A^\theta : L^2(\Omega) \to \ell^2(\mathbb{Z})$ is bounded, the bound is uniform for all $\theta \in \mathcal{S}^{d-1}$.*

Proof. We note $g(y) = w_B * \mathcal{P}_\theta f(y), y \in \theta^\perp$, and $\{g(hk)\}, k \in \mathbb{Z}^{d-1}$ the samples given by S_h. Clearly $g(y)$ is band-limited. For $h \leq 1/(2B)$, $g(y)$ can be reconstructed using the sampling kernel

$$\operatorname{sinc}_B(x) \triangleq \prod_{j=1}^{d} \frac{\sin(\pi B x_j)}{\pi B x_j} \tag{2.23}$$

as $g(y) = \sum_k g(hk) \operatorname{sinc}_{1/h}(x - kh)$, and $h^d \sum_k |g(hk)|^2 = \|\hat{g}\|^2$. Since $w_B \in L^1(\mathbb{R}^{d-1})$, $\hat{w}_B$ is bounded. Therefore:

$$\|\hat{g}\|^2 = 2\pi \int_{\omega \in \theta^\perp} |\hat{w}_B(\omega) \widehat{\mathcal{P}_\theta f}(\omega)|^2 d\omega \leq C \int_{\omega \in \theta^\perp} |\widehat{\mathcal{P}_\theta f}(\omega)|^2 d\omega$$

By the Theorem 2.3 from [2], $\mathcal{P}_\theta$ is a continuous mapping from $L^2(\mathbb{R}^d)$ to the weighted space $L^2(\theta^\perp, 1/\sqrt{1-|x|^2})$. Recall that f is supported on the unit ball Ω, then:

$$\int_{\theta^\perp} |\mathcal{P}_\theta f(y)|^2 dy \leq \int_{\theta^\perp} |\mathcal{P}_\theta f(y)|^2 \frac{1}{\sqrt{1-|y|^2}} dy \leq C \int_{\mathbb{R}^d} |f(x)|^2 dx$$

with the constant C independent of θ. This implies that

$$\sum_k |g(hk)|^2 \leq C \int_{\mathbb{R}^d} |f(x)|^2 dx$$

and the operator A^θ is continuous. □

The direction θ is defined on the periodic domain $\mathcal{S}^{d-1}$, so a fixed angular sampling step on $\mathcal{S}^{d-1}$ can yield only a finite number of different directions $\theta_1, \dots \theta_J$. We formalize the operator A appeared in the variational problems of section 2.2.2 in the following definition.

Definition 2.4.1 (Projector)**.** We note A^j the operator $S_h \circ (w_B * \mathcal{P}_{\theta_j})$, which is the projection at angular position θ_j, and define the projector A as the row concatenation of $A^1, \dots A^J$.

Then the next proposition follows directly from Lemma 2.4.1:

Proposition 2.4.2. *The projector $A : L^2(\Omega) \to \ell^2(\mathbb{Z})$ is a bounded operator.*

Remark 2.4.1. The continuity of A is a pleasant property. On the one hand, it is conform with the physical intuition: a small change in the object f produces a small change in the sinogram. On the other hand, the adjoint operator $A^* : \ell^2(\mathbb{Z}) \to L^2(\Omega)$ is well defined, which is important to the study of the variational problems.

Remark 2.4.2. The lemma 2.4.1 and the proposition 2.4.2 would fail if the detector response w_B is replace by the Dirac δ. In this case, some extra assumptions on the smoothness of the functions $f \in X$ would be necessary to establish the boundness of A^θ, and the arguments would become more involved. On the other hand, they are established only for parallel-beam geometry and don't handle the fan beam case. These problems will be solved if f is expressed as (2.17) using the a finite number N of localized basis function, *e.g.* the pixel basis or the blob introduced in Chapter 5. In fact:

$$(Af)_j = \sum_{k=1}^{N} f_k (A\phi_k)_j \tag{2.24}$$

So A can be represented in a matrix form, and the coefficient in j-th row and k-th column is $(A\phi_k)_j$. The boundness of A is then no more an issue. We will adopt this point of view in all the following chapters.

2.5 Existence of the solution

The optimization problem (2.13) will be the base of future discussions and it is important to establish the existence of its solution. This clearly depends on the regularization term R, on which we require the following conditions:

1. convex: $R(\lambda f + (1-\lambda)g) \leq \lambda R(f) + (1-\lambda)R(g)$
2. proper: $\{f | R(f) = \infty\} \neq X$
3. lower semi-continuous (l.s.c.): $\liminf_n R(f_n) \geq R(f)$, for $f_n \to f$
4. homogeneous: $R(\lambda f) = |\lambda| R(f)$
5. $R(f) > 0$ for any $f \in \operatorname{Ker} A, f \neq 0$

Lemma 2.5.1. *Suppose that the solution space X has finite dimension, then:*

$$\inf\{\|Af\|,\ f \in C\} > 0,\ C \triangleq \operatorname{Ker} A^{\perp} \cap \{\|f\| = 1\} \tag{2.25}$$

$$\inf\{R(f),\ f \in C'\} > 0,\ C' \triangleq \operatorname{Ker} A \cap \{\|f\| = 1\} \tag{2.26}$$

Proof. Since X has finite dimension, the projector A is automatically continuous and the closed subspace $\operatorname{Ker} A, \operatorname{Ker} A^{\perp}$ also have finite dimension. Let f_n be a minimizing sequence to (2.25). For all n, f_n is in the compact set C and $\|Af_n\| > 0$. There exists a converging subsequence noted again by f_n, $f_n \to f^* \in C$. Therefore, the value of (2.25) equals to $\|Af^*\| > 0$. The proof for (2.26) is similar. □

Proposition 2.5.2. *Suppose that X has finite dimension and under the assumptions 1-5 on R, there exists a global minimizer to the optimization problem (2.13).*

Proof. We note $J(f) = 1/2\|Af - \mathbf{b}\|^2 + \sigma R(f)$. $J(f)$ is convex on f since it is the sum of two convex functions. Therefore if a minimizer to (2.13) exists, it is a global one. We can uniquely decompose any $f \in X$ into:

$$f = g + (f - g), \quad \text{with } g \in \operatorname{Ker} A^{\perp}, \text{ and } (f-g) \in \operatorname{Ker} A.$$

f is unbounded only if either g or $f - g$ is so. Suppose that g is unbounded, then $J(f) \geq \|Ag - \mathbf{b}\|^2/2$ and by (2.25), $J(f)$ is unbounded. Suppose on the contrary that $f - g$ is unbounded, we rewrite it as $\lambda g'$ with $\lambda > 0$ and $g' \in \operatorname{Ker} A, \|g'\| = 1$. Then $J(f) \geq \sigma R(g + \lambda g') = \sigma\lambda R(g/\lambda + g')$, which is also unbounded since by l.s.c. of R and (2.26):

$$\liminf_{\lambda \to \infty} R(g/\lambda + g') \geq R(g') > 0, \text{ for any } g' \in \operatorname{Ker} A$$

Consequently, a minimizing sequence of (2.13) must be bounded, which implies that there exists a converging subsequent $\{f_n\}$, w.r.t. the Euclidean norm of X:

$$\lim_n f_n = f^*, \quad \text{and} \quad \lim_n J(f_n) = \min_{f \in X} J(f)$$

$J(f)$ being l.s.c., thus $J(f^*) \leq \liminf_n J(f_n)$, and f^* is a global minimizer to (2.13). □

For the constraint optimization problem, the existence of solution can be established by very similar technique as above. We prove the existence of solution for the variational problem (2.14) and (2.15):

Proposition 2.5.3. *Under the same condition as in Proposition 2.5.2, there exist a global minimizer to the following problem:*

$$\min_{f \in X} R(f), \quad s.t. \ f \in \{\|Af - \mathbf{b}\|^2 \leq \epsilon\} \tag{2.27}$$

for $\epsilon \geq 0$.

Remark 2.5.1. It is worth to point out that all the popular regularization term R in the literature do not meet all the conditions above as we shall see in next chapter. While the TV semi-norm and the ℓ^1 norm, which are two most important regularization techniques studied in this thesis, fulfill all the conditions. Taking TV semi-norm (3.23) on a pixel image as example, it fulfills the first 4 conditions trivially. A non-zero image has zero total variation if and only if it is constant, while the X-ray projection of a constant image cannot be zero. So the last condition holds too.

2.6 Ill-posedness of the few projections problem

The Radon transform $\mathcal{R}$ admits the singular value decomposition(SVD) (see [2], Chapter 4 for more details). In 2D this decomposition shows that the n-th singular value decays as $1/n$. The noise contained in the data makes the inversion of the Radon transform numerically unstable, since the n-th singular component will amplify the noise level by a factor n. When finite directions $\Theta_K = \{\theta_1, \dots \theta_K\}$ are used, the reconstruction suffers also from the non-uniqueness: there exists an infinite number of solutions which differ from the true object f but give exactly the same projection at the directions Θ_K (Theorem 3.7, Chapter 2, [2]).

As a discretization of the X-ray transform, the operator A defined in section 2.4 inherits these characters. In the matrix language, A has a non trivial kernel space, and is ill-conditioned. Let's consider the MSE problem:

$$\min_{f \in X} \|Af - \mathbf{b}\|^2 \tag{2.28}$$

which is the MAP problem without the regularization term. Its solution(s) is(are) given by the normal equation:

$$A^\top Af = A^\top \mathbf{b} \tag{2.29}$$

and can be solved numerically (without forming the matrix $A^\top A$) via the Conjugated Gradient (CG) method from many other possibilities [23]. The next example illustrates the instability of this solution.

Example 2.6.1 (Regularization-free reconstruction)**.** We use a modified shepp-logan phantom of 512×512 pixels, as test image, and a linear detector of 512 pixels. The parallel-beam projections equally distributed on $[0, \pi]$ are generated according to the model (2.11): we apply first a Siddon ray-tracing projector on the phantom, then add a white noise in such a way to obtain the desired SNR on the final sinogram $\mathbf{b}$. In this manner, four groups of data of 384 and 64 projections, and of the SNR at 50 and 25 dB are generated. We solve the normal equation (2.29) on the four groups of data using CG method initialized with 0. The reconstructed images are shown in Fig. 2.2. It can be seen that the reconstruction is highly unstable, and suffers greatly from the *streak artifacts*, the line patterns appearing around the object. These artifacts are typical signs of the insufficient angular sampling rate.

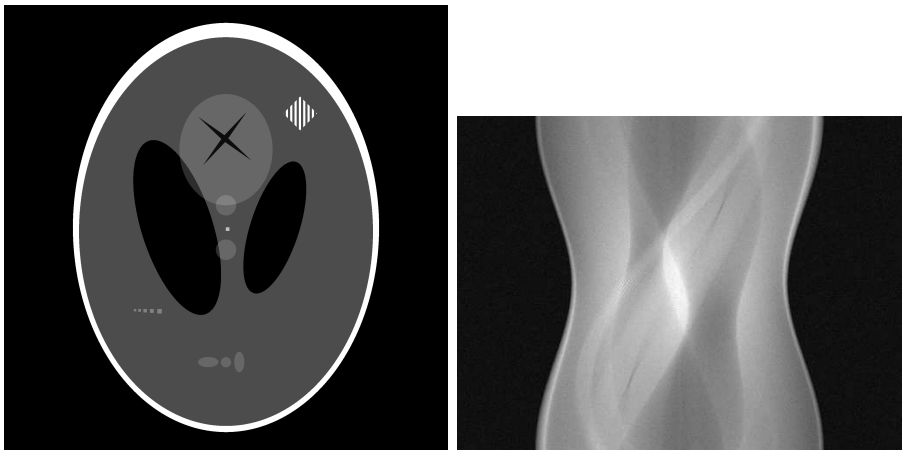

(a) Phantom (b) Sinogram

FIGURE 2.1: Modified shepp-logan phantom of 512×512 pixels and parallel-beam sinogram of SNR 25dB by 384 projections on a detector of 512 pixels.

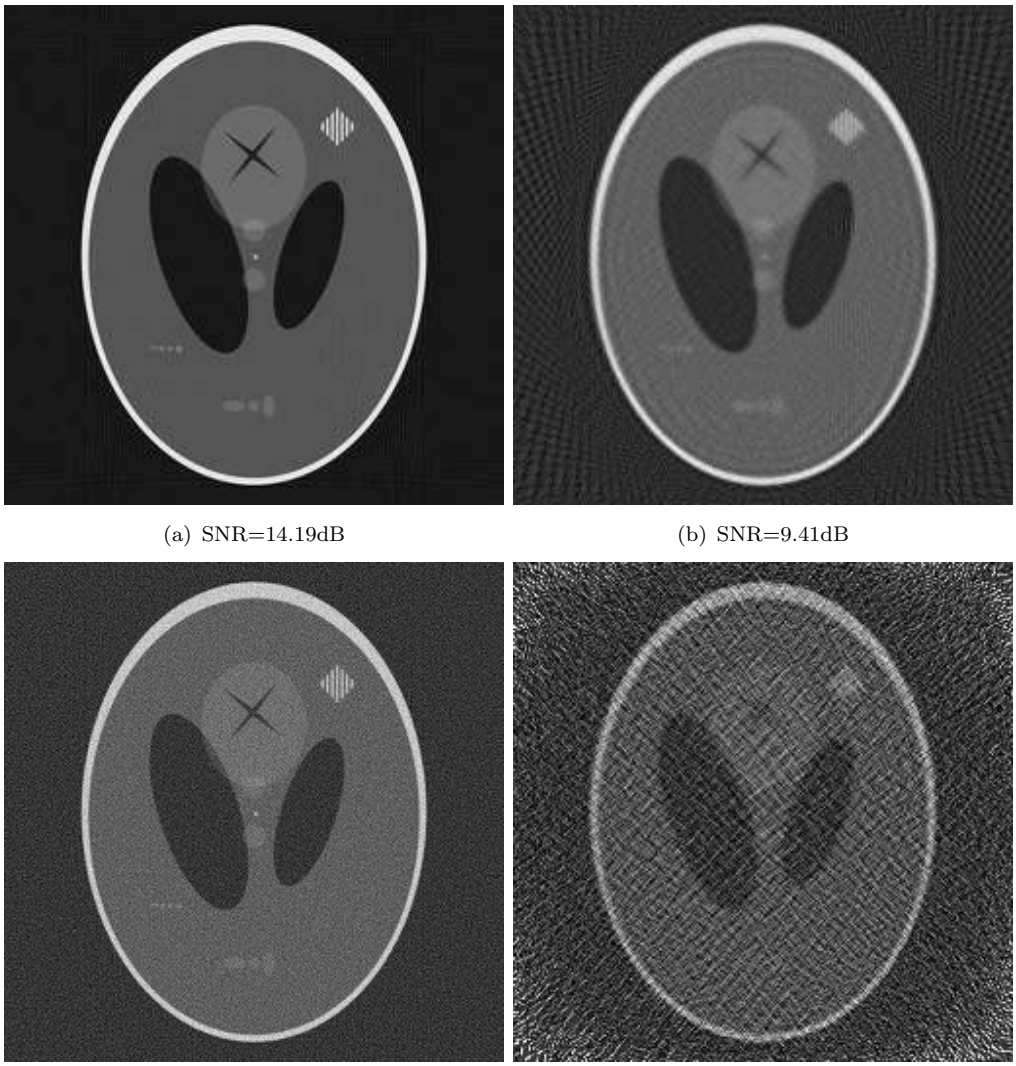

(a) SNR=14.19dB (b) SNR=9.41dB

(c) SNR=7.18dB (d) SNR=-9.86dB

FIGURE 2.2: Solution of (2.29) by CG using 250 iterations. The reconstructed images have dimension 256×256. The first and the second rows correspond to the sinogram data of SNR 50 and 25 dB respectively, while the first and the second columns correspond to the data of 384 and 64 projections respectively. The linear window $[-0.5, 2]$ is applied on all images.

As a conclusion, the reconstruction with MSE (2.28) is not appropriate for the few projections case, and some regularization term $R(f)$ should be introduced.

2.7 Concluding remarks

In this chapter, we have seen that the reconstruction of the attenuation coefficient can be handled under the Bayesian framework using ML or MAP estimators. These estimators are expressed through an optimization problem, where the objective function is composed of a quadratic data fitting term (likelihood) and a regularization term (prior).

The discretization of the function f is necessary for further numerical solution, and will be re-discussed in Chapter 5. The choice of regularization term R is essential to solve the reconstruction problem with few projections, and will be at the heart of our study. In the next chapter, we review some popular regularization techniques proposed in the tomography literature, which are relevant to the few projections problem.

Chapter 3

Review on regularization and iterative methods

The use of prior information can greatly improve the reconstruction quality, especially when the observed data are incomplete or corrupted by noise. Under the Bayesian framework, the regularization functional R needs to reflect our *a priori* knowledge on the unknown function f, primarily in term of its *smoothness*. A discrete pixel image is treated as a Markov random field, and the smoothness is expressed through a potential function (prior) acting on cliques. The *Bounded Variation* space and the *Besov* space are important smoothness spaces very useful for tomographic reconstruction. There exists also non Bayesian methods for the regularization of inverse problems, where the prior information is not expressed as a probability distribution. In this chapter we give a review on some important regularization techniques and iterative reconstruction methods proposed in the tomography literature, and we will detail particularly those relevant to the few projections problem.

Unless specified, throughout this chapter the function $f \in X$ is approximated using a finite number N of pixel basis on a Cartesian lattice, and we note $\mathbf{f} = [f_1 \dots f_N]^\top \in \mathbb{R}^N$ the vector of the pixel values. When applied on f, the X-ray projector A is understood as an operator, and accordingly understood as a matrix when applied on $\mathbf{f}$.

3.1 Prior and regularization

In the Bayesian framework and particularly the MAP estimation, a lot of priors π have been proposed for CT reconstruction. The most important among them are the local priors which characterize the local properties of f, such as the discontinuities and the

smoothness. These are often the most distinguish characters of f and are easily described as the interdependence between the neighborhood pixels.

3.1.1 Markov random fields

A convenient way to define local prior is via Markov random fields (MRF). In this context the pixel image $\mathbf{f} \in \mathbb{R}^N$ is considered as a random vector defined on a suitable probability space equipped with a density function $\pi(\mathbf{f})$. Then $\mathbf{f}$ is a MRF if each pixel depends only on its neighbors. Let $S = \{1 \dots N\}$ be the index set of pixels. Each index s has a set of neighbors noted by ∂s, which is a collection of indexes satisfying: 1) $s \notin \partial s$; 2) $r \in \partial s \Leftrightarrow s \in \partial r$. A *clique* c is a subset of indexes such that for any pixel pair $s, r \in c$, s and r are mutually neighbors. For example, on a 2D Cartesian lattice with the standard 4-neighbors system, a clique c contains only two horizontal or vertical adjacent pixels. The collection of all cliques is noted by $\mathcal{C}$. In a MRF the pixel f_r depends only on its neighbors ∂f_r, that is:

$$\mathbb{P}(f_r | f_s, s \neq r) = \mathbb{P}(f_r | f_s, s \in \partial r) \tag{3.1}$$

By the Hammerslay-Clifford theorem, (3.1) holds if and only if the MRF $\mathbf{f}$ has the Gibbs density:

$$\pi(\mathbf{f}) = \frac{1}{Z} \exp\left(-\beta U(\mathbf{f})\right), \text{ with } U(\mathbf{f}) = \sum_{c \in \mathcal{C}} V_c(\mathbf{f}) \tag{3.2}$$

where Z is a normalization constant, and $\beta > 0$ determines the strength of the prior. $V_c(\mathbf{f}) \geq 0$ is an energy function acting on the clique c. The MAP estimation problem on a MRF now takes the form:

$$\min_{\mathbf{f}} \frac{1}{2} \|A\mathbf{f} - \mathbf{b}\|^2 + \beta \sum_{c \in \mathcal{C}} V_c(\mathbf{f}), \quad \text{for } \mathbf{f} \in \mathbb{R}^N \tag{3.3}$$

As we will see in the following, different choices of potential function V_c can produce very different regularization effects.

3.1.1.1 Gaussian MRF and Tikhonov regularization

As an example, we consider the Gaussian Markov random field (GMRF) [24]:

$$\pi(\mathbf{f}) \propto \exp(-\mathbf{f}^\top B \mathbf{f}), \; U(\mathbf{f}) = \mathbf{f}^\top B \mathbf{f} \tag{3.4}$$

where the symmetric matrix B is definite positive, with the off-diagonal coefficient $B_{sr} = 0$ if $s \notin \partial r$, $B_{sr} \leq 0$ otherwise; and $B_{ss} > -\sum_{r \in \partial s} B_{sr}$ on the main diagonal. Then it

follows easily [24]:

$$\mathbf{f}^\top B\mathbf{f} = \sum_{s=1}^{N} a_s f_s^2 + \sum_{(s,r)\in\mathcal{C}} b_{sr}(f_s - f_r)^2, \tag{3.5}$$

with the positive constants $a_s = \sum_{r\in\partial s\cup s} B_{sr}$, and $b_{sr} = -B_{sr}$. On a Cartesian lattice, the term $f_s - f_r$ for the clique (s, r) is simply the difference between two adjacent pixels s and r, and b_{sr} is the directional weighting coefficient. Due to the quadratic term $(f_s - f_r)^2$, minimizing (3.3) with GMRF prior will strongly penalize the large difference between adjacent pixels, which corresponds generally to discontinuities and sharp transitions in image. Consequently, one should not be surprised by the over-smoothness of the corresponding reconstruction, see the images in example 3.1.1.

Relation with Tikhonov regularization The Tikhonov regularization (3.6) in a continuous form reads:

$$\min_{f\in X} \; J(f) = \frac{1}{2}\|Af - \mathbf{b}\|^2 + \delta_1\|f\|^2 + \delta_2\|\nabla f\|^2, \;\; \delta_1, \delta_2 \geq 0 \tag{3.6}$$

An admissible f such that $J(f) < \infty$ is clearly in the Sobolev space $H^1(\mathbb{R}^d)$, which consists of the square integrable functions with square integrable first order derivate:

$$\|f\|_{H^1}^2 = \int_{\mathbb{R}^d} |f(x)|^2 dx + \int_{\mathbb{R}^d} |\nabla f(x)|^2 dx < \infty, \tag{3.7}$$

Let $\triangle$ be the laplacian operator, then the Tikhonov regularization (3.6) has the unique solution f^* given by:

$$f^* = (A^*A + \delta_1 I + \delta_2\triangle)^{-1}A^*\mathbf{b} \tag{3.8}$$

One can take $\delta_2 = 0$, in which case the Tikhonov regularization acts as a "filter" on the singular system of A: the contribution of tiny singular components are weakened and the inversion becomes stable, due to the presence of $\delta_1 > 0$. In GMRF prior the weighting coefficients a_s and b_{sr} can be set to constants, then comparing with (3.7), we find that (3.5) is a weighted norm on a discrete analog of $H^1(\mathbb{R}^2)$. In this case the MAP solution is given by (3.8), with appropriately discretized operators A and $\triangle$.

Example 3.1.1 (GMRF reconstruction)**.** In light of the inversion formula (3.8), the MAP problem (3.3) with GMRF prior can be solved using CG. We reconstruct again the data of 64 projections at SNR of 25dB as in Example 2.6.1. From Figure 3.1.(a) we see that the inversion procedure with regularization becomes stable. To reduce the streak artifacts and the noise in reconstruction, one needs to increase the penalization constant δ_2, while this over-smoothes the whole image and suppress particularly the low contrast edges and the small details, as shown in Figure 3.1.(b).

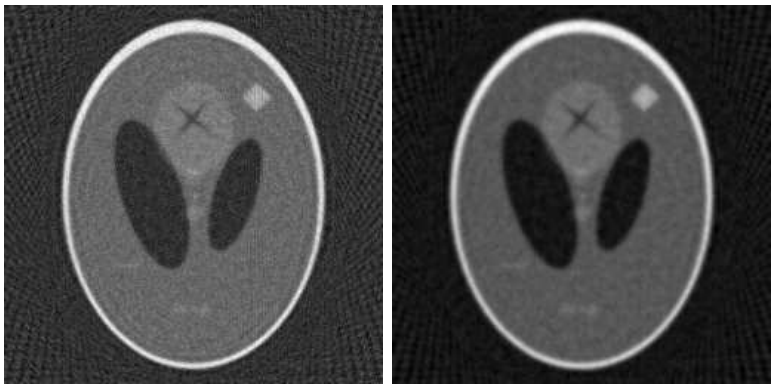

(a) $\delta_1 = 5, \delta_2 = 5$, SNR=9.88dB (b) $\delta_1 = 5, \delta_2 = 100$, SNR=10.25dB

FIGURE 3.1: GMRF reconstructions by solving (3.8) using CG with 250 iterations. The sinogram data contain 64 projections, and the SNR is 25dB. The linear window $[-0.5, 2]$ is applied on both images.

The edge one of the most prominent character of an image. In fact, many physical objects in CT applications consist of homogeneous regions separated by sharp edges. A such object contains very few information outside the edges. In this regard, GMRF is not appropriate for the few projections problem since it fails to preserve the edges. The edge-preserving priors discussed in the next is a remedy to overcome the over-smoothing effect of the GMRF prior, especially on the piecewise homogeneous object.

3.1.2 Edge-preserving prior

The *edge-preserving* regularization is a very popular technique to restore piecewise homogeneous image by preserving the edges. It has been widely employed in numerous imaging techniques [25, 26], it is useful particularly for CT reconstruction [24, 27–29] with limited-angle data [30] or low dose photon data [11].

An *edge-preserving prior*(EPP) has its potential function V_c depending only on the finite difference between pixels on the clique c, and differs from the non EPP in the way how the discontinuity is penalized. On a 2D pixel image $\mathbf{f}$ we define $D^1, D^2 : \mathbb{R}^N \to \mathbb{R}^N$ the discrete partial derivatives in horizontal and vertical directions:

$$(D^1\mathbf{f})_{i,j} = f_{i,j} - f_{i,j+1}, \text{ and } (D^2\mathbf{f})_{i,j} = f_{i,j} - f_{i+1,j} \tag{3.9}$$

where $f_{i,j}$ denotes the value of pixel (i,j) with periodic boundary conditions on $\mathbf{f}$ assumed. We define also the overall operator (discrete gradient) $D : \mathbb{R}^N \to \mathbb{R}^{2N}$:

$$D\mathbf{f} = \begin{pmatrix} D^1\mathbf{f} \\ D^2\mathbf{f} \end{pmatrix} = \begin{pmatrix} D_1\mathbf{f} \\ \vdots \\ D_{2N}\mathbf{f} \end{pmatrix}, \; D_n\mathbf{f} = (D\mathbf{f})_n \tag{3.10}$$

Edge-preserving prior We introduce the edge-preserving prior $\varphi(t) : \mathbb{R}_+ \to \mathbb{R}_+$, and rewrite the MAP problem (3.3) as:

$$\min J(\mathbf{f}) = \frac{1}{2}\|A\mathbf{f} - \mathbf{b}\|^2 + \beta \sum_{k=1,2} \sum_{i,j} \varphi((D^k\mathbf{f})_{i,j}) \tag{3.11}$$

Or in a more compact form that one may find in most of the edge-preserving regularization literature:

$$J(\mathbf{f}) = \frac{1}{2}\|A\mathbf{f} - \mathbf{b}\|^2 + \beta \sum_{n=1}^{2N} \varphi(D_n\mathbf{f}) \tag{3.12}$$

Some basic properties of $\varphi(t)$ includes:

1. $\lim_{t\to+\infty} \varphi(t)/t^2 = 0$
2. φ is increasing on $\mathbb{R}_+$, and $\varphi(0) = 0$
3. $\varphi \in C^1([0,+\infty))$, $\varphi'(0) = 0$, and $\varphi''(0^+) > 0$
4. $\varphi(\sqrt{t})$ is concave on $\mathbb{R}_+$

Some popular choices of φ are given in Tab. 3.1, and more examples can be found in [24, 27, 31, 32]. These priors can be divided into the convex and non convex families. The convex priors are preferred over the non convex ones for the global optimality and the stability of the solution, see [24] for more discussions.

Convex	Name	Ref.
$t^\alpha, \alpha \in (1,2)$	-	[24]
$\sqrt{\alpha + t^2}$	Abs	[6]
$\log(\cosh(\alpha t))$	Green	[33]
Non convex	**Name**	**Ref.**
$1 - \exp(-\alpha t^2)$	-	[34]
$t^2/(\alpha + t^2)$	Geman-McClure	[35]
$\min\{\alpha t^2, 1\}$	Huber	[36]

TABLE 3.1: Convex and non convex edge-preserving priors φ

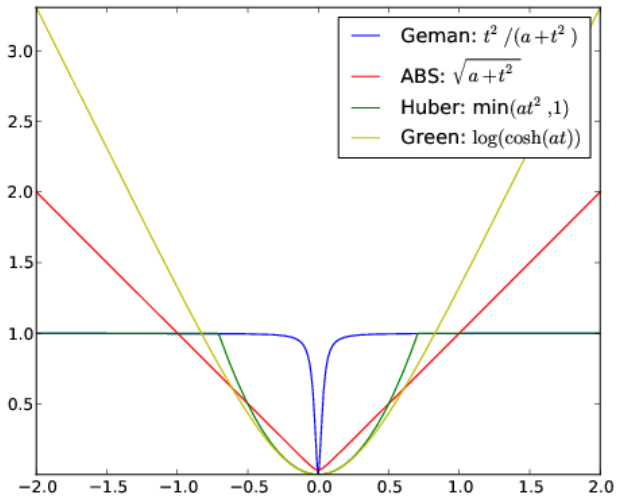

FIGURE 3.2: Graphs of some popular edge-preserving priors. $\alpha = 10^{-3}$ for Geman and Abs priors, and $\alpha = 2$ for Huber and Green prior.

Among the properties of φ listed above, the first point is essential to the preservation of edges. In fact, the φ increasing slower than quadratic function can tolerate much more large "jumps" between homogeneous regions, therefore avoid overly penalizing the edge discontinuities. The other conditions (2-4) are necessary for the establishment of a special numerical algorithm called *Half-Quadratic* minimization [27, 31, 37] that we briefly resume in 3.1.2.1.

3.1.2.1 Half-quadratic minimization

With the properties 1-4 of φ, it can be proven that $J(\mathbf{f})$ equals to the minimizer of a functional: $J(\mathbf{f}) = \inf_{\mathbf{t}} \mathcal{J}(\mathbf{f}; \mathbf{t})$, with $\mathcal{J}(\mathbf{f}; \mathbf{t})$ given by:

$$\mathcal{J}(\mathbf{f}; \mathbf{t}) = \frac{1}{2}\|A\mathbf{f} - \mathbf{b}\|^2 + \beta \sum_n \left(\frac{t_n}{2} \|D_n \mathbf{f}\|^2 + \psi(t_n) \right) \tag{3.13}$$

where $\psi(t) = \sup_{s \geq 0} -ts^2/2 + \varphi(s)$. Then we have the following two-steps alternating minimization algorithm, referred also as *Half-quadratic*:

Algorithm 1 Half quadratic minimization (HQ)

Initialization: $k = 0$
while not converged **do**
  $\mathbf{t}^{k+1} = \arg\min_{\mathbf{t}} \mathcal{J}(\mathbf{f}^k; \mathbf{t})$
  $\mathbf{f}^{k+1} = \arg\min_{\mathbf{f}} \mathcal{J}(\mathbf{f}; \mathbf{t}^{k+1})$
  $k \leftarrow k + 1$
end while

The first minimization in Algorithm 1 is component separable so it can be solved for each n:

$$t_n^{k+1} = \begin{cases} \varphi'(|D_n\mathbf{f}^k|)/|D_n\mathbf{f}^k| & \text{if } |D_n\mathbf{f}^k| > 0 \\ \varphi''(0^+) & \text{if } D_n\mathbf{f}^k = 0 \end{cases} \tag{3.14}$$

While the second minimization with respect to $\mathbf{f}$ is a quadratic problem and the solution is given by the linear system:

$$\left(A^\top A + \beta/2 \sum_n t_n^{k+1} D_n^\top D_n\right) \mathbf{f} = A^\top \mathbf{b} \tag{3.15}$$

It is commonly supposed that $\operatorname{Ker} A^\top A \cap \operatorname{Ker} D^\top D = \{0\}$, so that the system above is invertible [27, 31]. The variable $\mathbf{t}$ plays the roles of line process [35]: it renews iteratively the information about the discontinuities in image that will be taken into account in next iteration. The convergence of this algorithm is discussed in [27]. In [31], it has been pointed out that the HQ algorithm is indeed a basic *linearized gradient* method.

GGMRF prior In [24, 38, 39] the *generalized Gaussian Markov random field* (GGMRF) is introduced as an extension to the GMRF (3.5). It has the similar edge preserving effect as the EPP discussed above. The potential function of GGMRF is defined as:

$$U(\mathbf{f}) \triangleq \sum_{s=1}^{N} a_s |f_s|^p + \sum_{(s,r)\in\mathcal{C}} b_{sr} |f_s - f_r|^p, \tag{3.16}$$

where $1 < p \leq 2$ is a free parameter controlling the degree of edge preservation in reconstruction. To define a consistent potential function, one should choose the strictly positive weight coefficients a_s, b_{sr}. While in practice a_s can be 0 without affecting the uniqueness of the MAP solution [24].

q-GGMRF prior In [40] the GGMRF is again extended to the q-GGMRF prior, with the convex potential function defined as:

$$U(\mathbf{f}) \triangleq \sum_{(s,r)\in\mathcal{C}} b_{s,r} \frac{|f_s - f_r|^p}{1 + |(f_s - f_r)/c|^{p-q}} \tag{3.17}$$

where $2 \geq p \geq q \geq 1$, and $c > 0$. The combination of free parameters p, q and c can give a fine control on the penalization of discontinuity and homogeneous regions, and include many regularization priors in the literatures as special cases [4]. For example:

- $p = q = 2$: Gaussian prior

- $p = 2, q = 1$: Approximate Huber prior
- $1 < q = p \leq 2$: GGMRF with $a_s = 0$

Numerical experiments with real data [4, 40] have shown that q-GGMRF prior is effective for few projections problem and the reconstructions have better spatial resolution compared with analytical algorithm like FDK.

Example 3.1.2 (Edge-preserving reconstruction)**.** We reconstruct the same data of Example 2.6.1 by Abs prior $\sqrt{\alpha + t^2}, \alpha = 10^{-3}$ and Geman prior $t^2/(a + t^2), \alpha = 10^{-3}$ with HQ algorithm 1. Figure 3.3 shows the results with 64 projections data of SNR at 50dB (first row) and 25dB (second row). The results of Abs prior are always better than those of Geman prior in terms of SNR. Nevertheless, it can be seen from Figure 3.3.(d) that Geman prior preserves much better the constant region, even at the price of suppressing the low contrast small objects and the inaccurate contour shape. The different behavior of priors is related to their convexity and the choice of parameter α [32].

3.1.2.2 Discussions on EPP

The edge-preserving prior is a simple and efficient method in reconstructing piece-wise homogeneous image with edges. Nevertheless, we remark the following two drawbacks of this approach:

- All the priors discussed above depend on some free parameters (α for those in Table 3.1, and p, q, c for GGMRF, q-GGMRF priors). They control the penalization of the discontinuities and homogeneous regions. How to choose their value in practice is not very clear.
- None of the priors (except some special cases in GGMRF and q-GGMRF) define a norm or a semi-norm, for the simple reason that the homogeneous property of a norm:

$$\varphi(\lambda t) = |\lambda| \varphi(t) \tag{3.18}$$

  is not satisfied (for those defined in Table 3.1, remark that (3.18) is in conflict with the property $\varphi'(0) = 0$). If generalized to infinite dimension (by tending the pixel size to 0), it is not clear in which functional space the object is reconstructed or approximated. Except some important contributions [31, 32], the theoretical analysis on the effect of these priors seems to be limited in the literature.

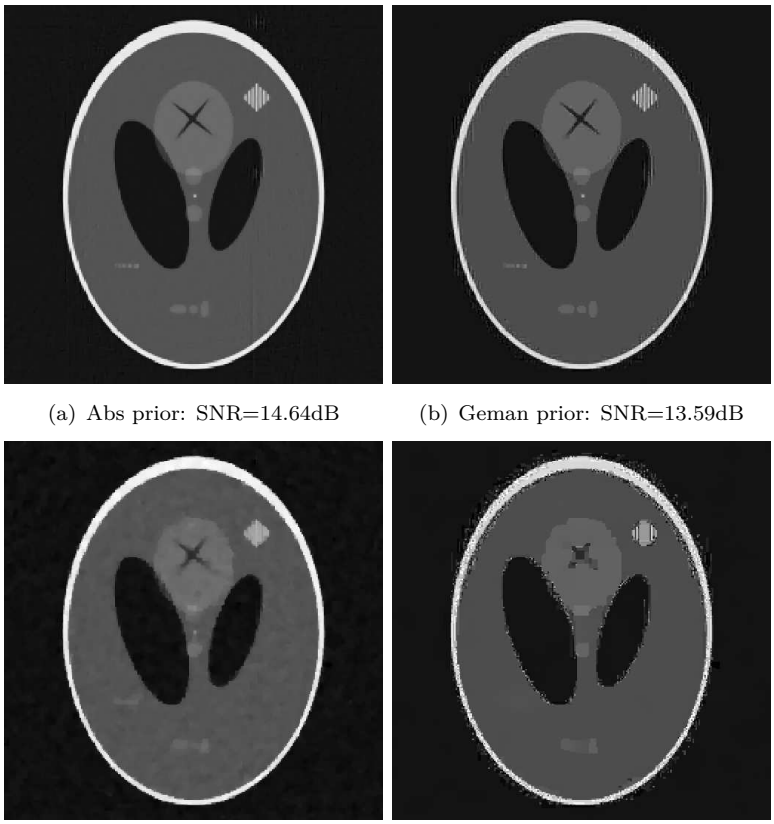

(a) Abs prior: SNR=14.64dB (b) Geman prior: SNR=13.59dB

(c) Abs prior: SNR=13.55dB (d) Geman prior: SNR=10.59dB

FIGURE 3.3: Edge-preserving reconstructions from 64 projections with the Abs prior $\varphi(t) = \sqrt{\alpha + t^2}$ and the Geman prior $\varphi(t) = t^2/(\alpha + t^2)$ both using $\alpha = 10^{-3}$. The parameter β in (3.11) is chosen manually. The first and the second row are obtained from sinogram data of SNR 50dB and 25dB respectively. The linear window $[-0.1, 1.2]$ is applied on all images.

3.1.3 BV space and Total Variation

The Bound Variation (BV) space is a pertinent model for representing images composed by relative homogeneous regions and sharp transitions between them. The BV space is a Banach space equipped by the norm:

$$\|f\|_{BV} \triangleq \int_{\mathbb{R}^d} |f(x)|dx + TV(f) \tag{3.19}$$

with $TV(f)$ the *Total Variation* (TV) semi-norm.

Definition 3.1.1 (Total Variation)**.** The total variation of a real-valued integrable function f supported on unit square region $\Omega = [0, 1]^d$ is defined as :

$$TV(f) \triangleq \sup \left\{ \int_\Omega f \mathrm{div}\varphi : \varphi \in C_c^1(\Omega, \mathbb{R}^d),\ \|\varphi\|_\infty \leq 1 \right\}, \tag{3.20}$$

where $C_c^1(\Omega, \mathbb{R}^d)$ is the set of continuously differentiable vector functions of compact support contained in Ω (in particular $\varphi|_{\partial\Omega} = 0$). For f differentiable, it can be shown

that (3.20) equals to :

$$TV(f) = \int_{\Omega} |\nabla f(x)|\, dx \tag{3.21}$$

Considered in $L^1(\Omega)$, the TV semi norm $TV : BV(\Omega) \to \mathbb{R}^+$ is known to be a strictly convex lower semi-continuous functional [41]. By the co-area theorem [14, 41], $TV(f)$ equals to the total length of level sets contour of f. Let $B_f(\alpha) \triangleq \{x|f(x) \leq \alpha\}$ be the level set and $\partial B_f(\alpha)$ its contour such that the length is finite for almost all α, then:

$$TV(f) = \int_{\mathbb{R}} |\partial B_f(\alpha)| d\alpha \tag{3.22}$$

3.1.3.1 Discrete TV norm

BV space does not admit any countable generating system. This means that one has to pass by some approximation schemes for discrete representation and numerical treatment of BV function. The usual way is to represent f by its samples $\mathbf{f}$ (pixel values) taken on a regular Cartesian lattice, and define a discrete analog of (3.21). Let's consider the 2D case here. We divide the unit square $\Omega = [0,1]^2 \subset \mathbb{R}^2$ is into $N = n \times n$ pixels, and note $f_{i,j} = f(i/n, j/n)$ for $i, j = 0, \ldots n-1$. Using the operators D^1, D^2 as in (3.9), the discrete TV semi-norm on the pixel image $\mathbf{f}$ is defined as:

$$\begin{aligned} \|\mathbf{f}\|_{TV} &\triangleq \sum_{i,j} \sqrt{(f_{i,j} - f_{i+1,j})^2 + (f_{i,j} - f_{i,j+1})^2} \\ &= \sum_{i,j} \sqrt{(D^1\mathbf{f})_{i,j}^2 + (D^2\mathbf{f})_{i,j}^2} \end{aligned} \tag{3.23}$$

Then by the trapezoidal rule, for n sufficiently large:

$$\begin{aligned} \int_{\Omega} |\nabla f(x)| dx &\simeq \frac{1}{n^2} \sum_{i,j} \sqrt{(\partial_1 f(i/n, j/n))^2 + (\partial_2 f(i/n, j/n))^2} \\ &= \frac{1}{n} \sum_{i,j} \sqrt{(f_{i,j} - f_{i+1,j})^2 + (f_{i,j} - f_{i,j+1})^2 + o(n^{-2})} \end{aligned}$$

comparing with (3.23), we obtain:

$$\int_{\Omega} |\nabla f(x)| dx \simeq \frac{1}{n} \|\mathbf{f}\|_{TV} \tag{3.24}$$

3.1.3.2 TV regularization

Let A be a linear operator from $L^2(\Omega)$ to another Hilbert space Y, and $b \in Y$. In the continuous form, the TV regularization problem announces:

$$\min_{f \in X} \frac{1}{2}\|Af - b\|^2 + \beta TV(f) \tag{3.25}$$

In practice f is replaced by its pixel version $\mathbf{f}$, and we solve the discrete optimization problem:

$$\min_{\mathbf{f} \in \mathbb{R}^N} \frac{1}{2}\|A\mathbf{f} - \mathbf{b}\|^2 + \beta \|\mathbf{f}\|_{TV} \tag{3.26}$$

or in a constrained form to take into account the noise in data:

$$\min_{\mathbf{f} \in \mathbb{R}^N} \|\mathbf{f}\|_{TV} \text{ s.t. } \|A\mathbf{f} - \mathbf{b}\|^2 \leq \varepsilon \tag{3.27}$$

Remark 3.1.1. The operator A in the CT reconstruction requires the discretization dimension N to be specified by user, and it does have impacts on the solution of (3.26). Let's consider a simple case here. Suppose that $f(x) = \mathbb{1}_K(x)$ is the indicator function of a set K with the smooth boundary ∂K which has finite length. The reconstruction of f then amounts to determine the position of ∂K, or the active pixels of $\mathbf{f}$, *e.g.*, those intersect with ∂K. It follows from (3.22), (3.24) and (3.23) that for $N = n^2 \to \infty$:

$$\frac{1}{n^2}\|\mathbf{f}\|_{TV} \simeq \frac{1}{n} TV(f) \to 0, \tag{3.28}$$

while $\|\mathbf{f}\|_{TV}/n^2$ can be interpreted as the percentage (up to a constant factor) of active pixels. Then eq. (3.28) suggests that it would be more interesting to reconstruct f by its approximation $\mathbf{f}$ in high dimension (n large) than in low dimension, for that in the high dimension the approximation quality is better, while the relative number of active unknowns is smaller than in low dimension. The numerical experiments in Example 3.1.3 confirm this intuition.

Rudin-Osher-Fatemi(ROF) model The TV regularization technique origins from the following ROF model [42], well known for image denoising applications:

$$\min_{f \in BV(\Omega)} \frac{1}{2}\int_\Omega |f - g|^2 + \beta \int_\Omega |\nabla f| \tag{3.29}$$

Here g is a noisy observation and the solution f is the denoised version of g. The ROF model has been well studied from both numerical and theoretical point of view. For example, we know that (3.29) can preserve the edges and the constant regions of the original image g, therefore produces piece-wise constant "cartoon" image, while quite

often small details and low contrast regions are smoothed out in the solution. Recently, it has been pointed out by Meyer [43], Haddad and Meyer [44] that (3.29) can be seen as a "texture separation" algorithm, in the sense that by solving (3.29), g is uniquely decomposed into:

$$g = f + v \tag{3.30}$$

with the BV part $f \in BV(\Omega)$ as the solution of (3.29), and $v \in G$. G is a Banach space characterizing the textures and oscillating patterns, such that these components are expected to have small $\|\cdot\|_G$ norm, defined as:

$$\|v\|_G \triangleq \inf_g \{\|g\|_\infty, \text{ s.t. } \operatorname{div}(g) = v, g \in (L^\infty(\Omega))^2\} \tag{3.31}$$

where $\|g\|_\infty = \|g_1^2 + g_2^2\|_\infty$. The unit ball of G is denoted by B_G. Then Chambolle [45] has proven that the solution to a discrete version of (3.29) is fully described by a convex projection operation:

$$f = g - \Pi_{\beta B_G}(g) \tag{3.32}$$

with $\Pi_{\beta B_G}(\cdot)$ the convex projector onto the closed convex set βB_G. Now it follows easily that if $\|g\|_G \leq \beta$, the solution f of (3.29) is 0; otherwise $\Pi_{\beta B_G}(g) \neq 0$ and the solution f never equals to g, even if g is "texture free" (*e.g.*, piece-wise constant function).

Drawbacks of TV regularization In case of the CT reconstruction, we consider:

$$\min_{f \in BV(\Omega)} \frac{1}{2}\|Af - Ag\|^2 + \beta \int_\Omega |\nabla f(x)| dx \tag{3.33}$$

As the projection number increases, A can even become over-determinant and invertible, then $\|f - g\| \asymp \|Af - Ag\|$ and one can expect the solution of (3.33) to be close to that of (3.29), therefore inherits the same drawbacks of the ROF model:

- If $\|g\|_G$ is smaller than β, which could happen when g is some oscillating patterns like textures, small objects or low contrast regions, then we will lose it in the solution.
- The solution never equals to the original image so one cannot reduce the reconstruction error $\|f - g\|$ to zero, especially when the original image contains textures, and when the data are noisy.

While in most cases the TV minimization results visually pleasant reconstructions, by preserving well the discontinuities and reducing the noise and streak artifacts, the "texture killer" behavior could make it harmful in medical applications. In Chapter 7 we give more numerical evidences for these theoretical findings.

3.1.3.3 Numerical algorithm for TV regularization

The numerical solution of (3.26) is a challenging problem in practice. Firstly, the discrete TV norm $\|\mathbf{f}\|_{TV}$ is non differentiable at 0 and the gradient-like methods cannot be applied. Secondly, due to the operator A, the TV regularization problem (3.26) is much more difficult than the TV denoising problem (3.29). Particularly, some efficient methods for (3.29), *e.g.*, Chambolle's projection algorithm [45], cannot be applied directly on (3.26). Recently, new algorithms dedicated to (3.26) and (3.27) have been proposed in [46–50]. These methods are developed for general image processing tasks, and apply as well on the CT reconstruction problem of large dimension. In this chapter and later, we will use the *TVAL3* algorithm proposed by Li et al. [48] to solve (3.26). TVAL3 is a special variant of the *Alternating Direction Method (ADM)* [49, 50], it operates on general system operator A and can incorporate positive constraints. This is a low complexity algorithm: in each iteration it involves only one forward and one backward operation of the X-Ray projector A and the gradient operator D. We resumed this algorithm in Annexe B.3.1.1, and refer readers to original report [48] and the reference therein for all technical details.

Example 3.1.3 (TV reconstruction)**.** Figure 3.4 shows the solution of (3.26) with 64 projections on the same data as in Example 3.1.2. It can be seen that the TV reconstructions outperform those of EPP presented in Example 3.1.2. As pointed out in Remark 3.1.1, the reconstruction in high dimension (512×512 pixels, Figure 3.4.(b) and (d)) are better than that in low dimension (256×256 pixels, Figure 3.4(a) and (c)). On the piecewise constant images like the Shepp-Logan phantom, our numerical findings show that one can reduce the number of projections down to 16, while the reconstruction image quality is still interpretable, as shown in figure 3.5. In order to achieve such a result, an iterative reweighted TV regularization with positivity constraint is solved instead of (3.26). More details can be found in Section 6.3. Comparing with the Figure 3.4, we can see that in very few projections case, TV regularization still recovers correctly the constant regions, while fails on low contrast objects, high frequency oscillation, and geometrical singularities.

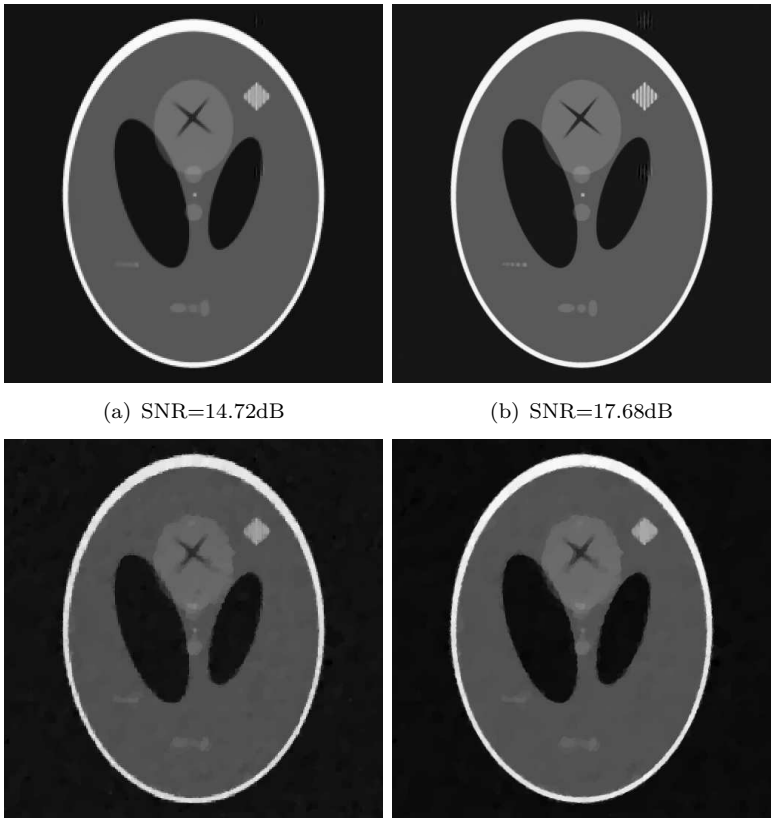

(a) SNR=14.72dB (b) SNR=17.68dB

(c) SNR=13.83dB (d) SNR=15.26dB

FIGURE 3.4: TV reconstructions from 64 projections. The parameter β in (3.26) is chosen manually based on visual result. The first and the second row correspond to the sinogram data at SNR of 50dB and 25dB respectively. The first and the second column are the reconstructions of dimension 256×256 and 512×512 respectively. The same linear window $[-0.1, 1.2]$ is used for the visualization of all images.

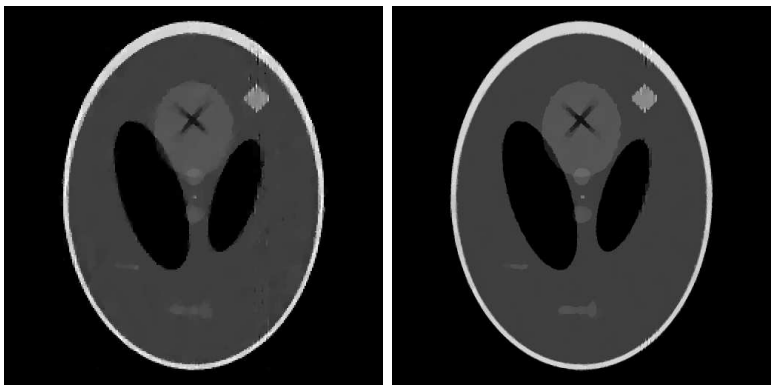

(a) SNR=13.19dB, SI=0.0150 (b) SNR=15.97dB, SI=0.0098

FIGURE 3.5: TV reconstructions from 16 projections. The SNR of the sinogram data is 50dB, and the reconstructions have the dimension 256×256 in (a) and 512×512 in (b).

3.1.4 Besov prior

The Besov space $B^{\alpha}_{p,q} = B^{\alpha}_{q}(L^p(\mathbb{R}^d))$ for $0 < \alpha < \infty, 1 \leq p, q \leq \infty$ is a family of Banach spaces covering a wide range of functional smoothness. Here α determines the order of smoothness, $L^p(\mathbb{R}^d)$ is the space in which it is measured, and q is a less important fine tuning parameter. For example $p = q = 2$ yields the Sobolev space $W^{\alpha,2}(\mathbb{R}^d)$. The smoothness of function $f \in B^{\alpha}_{q}(L^p(\mathbb{R}^d))$ can be characterized by its wavelet coefficients, thanks to the following norm equivalence:

$$\|f\|_{B^{\alpha}_{p,q}} \asymp \left(\sum_{k \in \mathbf{Z}^d} \left| \langle f, \psi^{(0)}_{j_0,k} \rangle \right|^p \right)^{1/p} + \left(\sum_{j \geq j_0} \left(\sum_{k \in \mathbf{Z}^d} \sum_{l=1}^{2^d-1} 2^{jps} \left| \langle f, \psi^{(l)}_{j,k} \rangle \right|^p \right)^{q/p} \right)^{1/q} \tag{3.34}$$

with $s = \alpha + d(1/2 - 1/p)$. Here the wavelets $\Psi = \{\psi^{(l)}, l = 1 \dots 2^d - 1\}$ follow the definition in Chapter 2, and have $n > \lceil \alpha \rceil$ vanishing moments. For reason of simplicity, we take $p = q$, and set the constant α such that $s \geq 0$, then $B^{\alpha}_{p,q}$ is embedded in $L^2(\mathbb{R}^d)$[51]. In practice the sequence norm (3.34) can be replaced by a computational effective definition:

$$\|f\|^p_{B^{\alpha}_{p,p}} \sim \sum_{k \in \mathbf{Z}^d} \left| \langle f, \psi^{(0)}_{j_0,k} \rangle \right|^p + \sum_{j \geq j_0} \sum_{k \in \mathbf{Z}^d} \sum_{l=1}^{2^d-1} 2^{jps} \left| \langle f, \psi^{(l)}_{j,k} \rangle \right|^p \tag{3.35}$$

We note the coefficient sequence $\mathbf{c} = \{c^{(l)}_{j,k}\}_{j,k,l}$, with $c^{(l)}_{j,k} = \langle f, \psi^{(l)}_{j,k} \rangle$, and define the sequence norm:

$$\|\mathbf{c}\|^p_{p,\alpha} = \sum_{k \in \mathbf{Z}^d} \left| c^{(0)}_{j_0,k} \right|^p + \sum_{j \geq j_0} \sum_{k \in \mathbf{Z}^d} \sum_{l=1}^{2^d-1} 2^{jps} \left| c^{(l)}_{j,k} \right|^p \tag{3.36}$$

Then the smoothness of f can be characterized by the membership of its wavelet coefficients in the weighted sequential space $\ell^p(\mathbb{Z})$, which implies that the n-th largest wavelet coefficient $|c_{(n)}|$ decays as $O(n^{-1/p})$, and the coefficient across scale decays as $2^{-j\alpha}$. For most of the natural images the wavelet coefficients enjoy a fast decay, *e.g.*, $p < 2$ [52], and the essential information can be coded in the first K biggest terms for K small. The idea of regularization by Besov norm is to search the solution in a Besov space $B^{\alpha}_{p}(L^p(\mathbb{R}^d))$ for $p < 2$, in which the inherent dimension K of the unknown is reduced, and in this way balance the ill-posedness of the reconstruction problem with few projections. This approach has been successfully applied to dental CT reconstruction with limited angle or few projections data [7, 8, 53–56].

Regularization by Besov norm The function f can be re-synthesized from $\mathbf{c}$ by $f = \Psi\mathbf{c}$, with the equality holds in L^2 sense, and Ψ the synthesis operator:

$$\Psi\mathbf{c}(x) = \sum_{k\in\mathbf{Z}^d} c^{(0)}_{j_0,k}\psi^{(0)}_{j_0,k}(x) + \sum_{j\geq j_0}\sum_{k\in\mathbf{Z}^d}\sum_{l=1}^{2^d-1} c^{(l)}_{j,k}\psi^{(l)}_{j,k}(x) \tag{3.37}$$

Then the regularization problem by Besov prior announces:

$$\min_{\mathbf{c}} \frac{1}{2}\|A\Psi\mathbf{c} - \mathbf{b}\|^2 + \beta\|\mathbf{c}\|^p_{p,\alpha}, \text{ for } \mathbf{c} \in \ell^2(\mathbf{Z}) \tag{3.38}$$

The wavelet basis here provides a natural multiresolution/multigrid discretization of $f \in X$ which can be exploited by the reconstruction algorithm. For example, in ROI reconstruction from truncated data [7] the computation grid can be easily adapted to the data acquisition for improving locally the resolution, reducing the number of unknowns, and accelerating the computation. Nevertheless, (3.38) is rarely feasible in practice, since the numerical implementation of the operator $A\Psi : \ell^2(\mathbf{Z}) \to \mathbb{R}^M$ would require to compute and store the X-ray transform of the wavelet: $A\psi^{(l)}_{j,k}$, which is numerically challenging in high dimension.

In order to solve (3.38) f is replaced by its samples $\mathbf{f}$ on a regular Cartesian lattice. Let W be the orthogonal discrete wavelet transform (a synthesis operator): $\mathbf{f} = W\mathbf{c}$, and $A : \mathbb{R}^N \to \mathbb{R}^M$ applies on the pixel image $\mathbf{f}$. The regularization problem (3.38) then becomes:

$$\mathbf{c}^* = \arg\min_{\mathbf{c}\in\mathbb{R}^N} \frac{1}{2}\|AW\mathbf{c} - \mathbf{b}\|^2 + \beta\|\mathbf{c}\|^p_{p,\alpha} \tag{3.39}$$

and the reconstructed pixel image is re-synthesized from the coefficients by: $\mathbf{f}^* = W\mathbf{c}^*$. Remark that the objective function in (3.39) is strictly convex, and differentiable for $p > 1$. The numerical solution (3.39) can be done by the nonlinear Conjugate Gradient method.

Example 3.1.4 (Besov norm reconstruction)**.** The reconstruction by (3.38) is affected mainly by the choice of wavelet basis W and the parameter p. To illustrate this point, we solve (3.38) on the phantom "Brain" of dimension 512×512 (Fig. 3.6 (a)) and the phantom "Lung" of dimension 334×512 (Fig. 3.6 (b)). The Haar and the Daubechies wavelets of 6 vanishing moments are used as wavelet basis W. We have simulated 128, 96 and 64 projections equally distributed between 0 and π on the pixel phantom images, and add a small white noise to the sinogram such that the SNR of data is around 50dB. The reconstruction dimension N is the same as that of each phantom image. We choose the parameter $p = 1.1$ in the Besov norm and $\alpha \simeq 0.81$ such that $s = \alpha + d(1/2 - 1/p) = 0$,

and set the value of β in (3.39) manually by maximizing reconstruction's visual quality. The same linear window $[0, 1]$ is applied on all images for screen display.

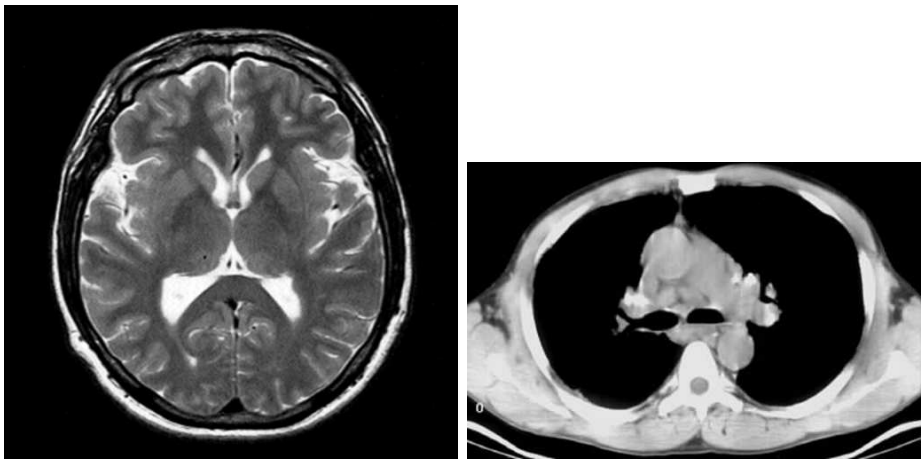

(a) Brain (b) Lung

FIGURE 3.6: Test phantom images.

The reconstructions using the Haar wavelet are shown in Fig. 3.7. The visual quality of the reconstructed image is affected severely by the annoying "pixelization" artifacts, which is a signature of the Haar wavelet. In practical applications the Haar wavelet is rarely used and the Daubechies wavelet of higher vanishing moments is preferred.

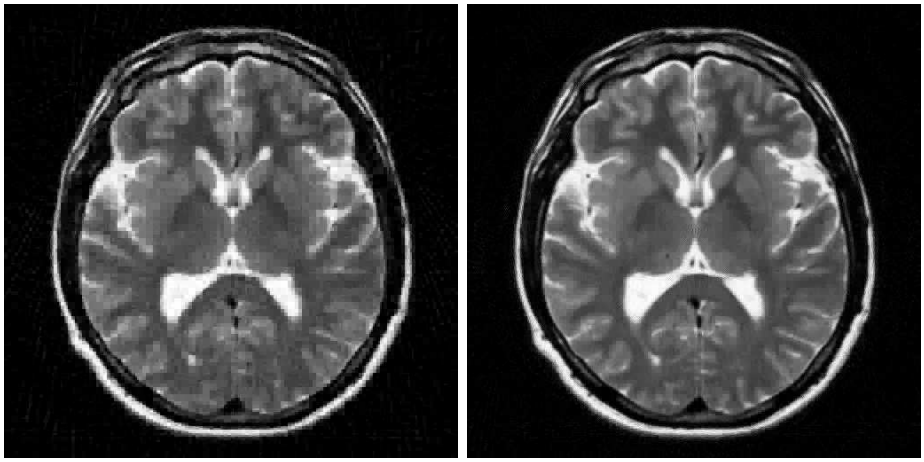

(a) SNR=12.77dB (b) SNR=15.22dB

FIGURE 3.7: Reconstructions using the Haar wavelet from 64 projections (a) and 128 projections (b). The pixelization artifacts are amplified when the number of projections is small.

The reconstructions on the same data but with the Daubechies wavelet of 6 vanishing moments are shown in Fig. 3.8. Compared to the reconstructions by the Haar wavelet, the visual quality is improved. Nevertheless, some isolated high frequency oscillation patterns, called *pseudo Gibbs phenomena*, are very visible when the projection number

is limited. This is a typical symptom when thresholding the coefficients of an orthogonal wavelet basis. In the application where small details are crucial, these artifacts can affect the interpretability of image.

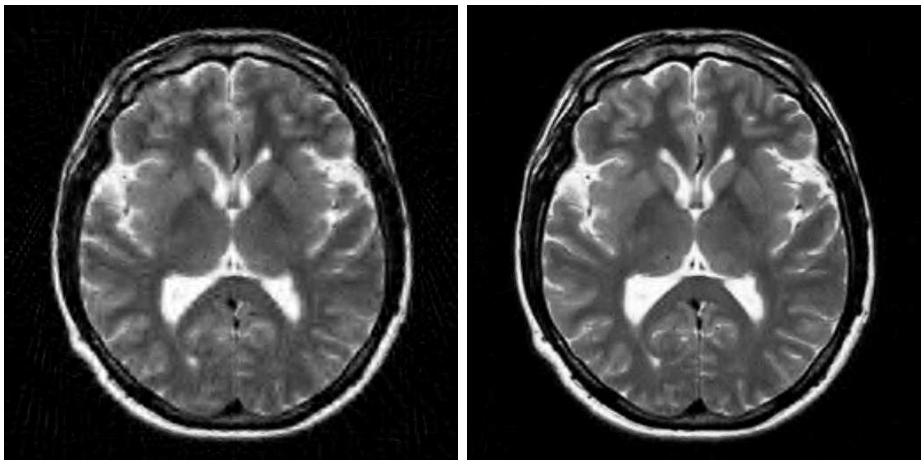

(a) SNR=14.21dB (b) SNR=17.79dB

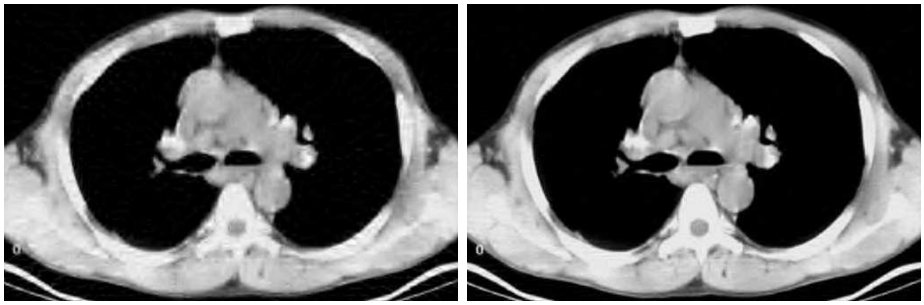

(c) SNR=17.75dB (d) SNR=19.08dB

FIGURE 3.8: Reconstructions using db6 wavelet from 64 (a,c) and 128 projections (b,d). The pseudo Gibbs artifacts are amplified when the number of projections is small.

More complete reconstruction results are presented in Table 3.2. Remark that on the Shepp-Logan phantom, the best performance in Table 3.2 is reached with 128 projections using Daubechies 6 wavelet (SNR 17.03 dB), which is still inferior to the TV reconstruction with only 64 projections, see Figure 3.4 (b). Generally speaking, the wavelet method is less efficient than the TV minimization in preserving the constant regions and the edges, and in removing the streak artifacts. It would need more projections but on the contrary doesn't suffer from the stair wise artifacts as the TV minimization does.

Phantom	a	b	c	d	e	f
Shepp	14.32	15.89	16.36	14.40	16.25	17.03
Brain	12.77	14.59	15.22	14.21	16.62	17.79
Lung	16.32	17.50	17.95	17.85	18.70	19.07

TABLE 3.2: SNR (dB) of the reconstructed images SNR using Haar wavelet (columns a, b, c) and Daubechies 6 wavelet (columns d, e, f) with high SNR (50dB) projection data generated from three test phantoms. Columns a,d: 64 projections, columns b,e: 96 projections, columns c,f: 128 projections.

3.2 Entropy methods

There exist non Bayesian methods in regularizing an ill-posed inverse problem. Here the prior information is not expressed through a prior probability describing the smoothness of the unknown object as in the Bayesian framework, but based on some information theory principles. The regularization by entropy discussed below is an important technique in tomography.

3.2.1 Maximum Entropy Principle

Entropy measures the "information" contained in a probability density function (pdf) in terms of the shortest average coding length. It is the only consistent information measure which satisfies some axiomatic formalism [57, 58]. The entropy of a probability density function (and also for general positive functions) f is denoted by $-H(f)$, with:

$$H(f) \triangleq \int_{\mathbb{R}^d} f(x) \log f(x) dx \tag{3.40}$$

On a positive coefficient vector $\mathbf{f} \in \mathbb{R}^N$, it's defined as $-H(\mathbf{f})$ with:

$$H(\mathbf{f}) \triangleq \sum_n f_n \log f_n \tag{3.41}$$

Among all discrete probability distribution ($\mathbf{f}$ positive and $\|\mathbf{f}\|_1 = 1$), $H(\mathbf{f})$ is maximized for uniform distribution $f_n = 1/N$ and minimized for Dirac $f_n = \delta_{n=k}$. The *Maximum Entropy* (ME) principle states that a "good" solution to inverse problem is the most informative one, *e.g.*, the one that maximizes the entropy. This is a popular technique in solving linear inverse problems, particularly for the situation that no prior information is available on the unknown function, except that it is positive. The tomography problem can be interpreted as reconstructing a d-dimensional pdf from its $d-1$-dimensional marginals, and by the ME principle the best solution is the one containing the most information. In the literature the ME reconstruction is generally formulated as a constraint optimization problem:

$$\min_f H(f) \quad \text{s.t. } Af = \mathbf{b} \tag{ME}$$

A such formulation admits a unique solution, which is automatically positive [59]. It has been reported in [60, 61] that the maximum entropy reconstruction outperforms the quadratic regularization techniques such as GMRF with limited or incomplete data. In [62] it has been proved that the ME reconstruction works well especially on sparse objects since it favorites the sparse solution, but it is not the *optimal* regularization technique on this kind of object.

3.2.1.1 MART

The ME problem (ME) can be solved by the *multiplicative algebraic reconstruction technique* (MART), a important row-action algorithm proposed in the tomography literature [63–65], that we summarize briefly here.

We suppose that the i-th projection data can be written as $(Af)_i = \langle a_i, f\rangle$, with $a_i(x)$ is the indicator function of a strip region B_i, covered by the i-th X-ray beam. At iteration $k+1$, MART uses only one constraint $(Af)_i = b_i$ and solves:

$$\min D(f, f^{(k)}) \quad \text{s.t. } (Af)_i = b_i \tag{3.42}$$

Here $f^{(k)}$ is the solution of k-th iteration. $D(f, f^{(k)})$ is the linearization of $H(f)$ around $f^{(k)}$, namely:

$$D(f, f^{(k)}) \triangleq H(f) - H(f^{(k)}) - \langle \nabla H(f^{(k)}), f - f^{(k)}\rangle \tag{3.43}$$

and the derivative $\nabla H(f) : X \to \mathbb{R}$ is a linear application:

$$\langle \nabla H(f), g\rangle = \int_\Omega (1 + \log f(x)) g(x) dx, \text{ for } g \in X \tag{3.44}$$

The solution of (3.42) is a saddle point of the Lagrangian:

$$L(f, \lambda) = D(f, f^{(k)}) - \lambda((Af)_i - b_i), \lambda \in \mathbb{R}$$

hence $\nabla_f L(f, \lambda) = 0 \Rightarrow \log f(x) = \log f^{(k)}(x) - \lambda a_i(x)$, and the solution of $k+1$-th iteration is:

$$f^{(k+1)}(x) = f^{(k)}(x) \exp(-\lambda a_i(x)) \tag{3.45}$$

Putting (3.45) back into the constraint $(Af)_i = \langle a_i, f\rangle = b_i$, we find:

$$\int_\Omega a_i(x) f^{(k)}(x) \exp(-\lambda a_i(x)) dx = e^{-\lambda} \int_{B_i} f^{(k)}(x) dx = b_i, \tag{3.46}$$

so $e^{-\lambda} = b_i / (Af^{(k)})_i$, and finally:

$$f^{(k+1)}(x) = \begin{cases} f^{(k)}(x) b_i / (Af^{(k)})_i & \text{if } x \in B_i \\ f^{(k)}(x) & \text{if not} \end{cases} \tag{3.47}$$

If initialized by a constant, the final solution of MART will clearly be piecewise constant on a irregular grid deduced from the partition of all beam regions B_i, which is called

optimal grid in [63]. On a pixel image $\mathbf{f}$, (3.47) is replaced by:

$$f_n^{(k+1)} = \begin{cases} f_n^{(k)} b_i / (A\mathbf{f}^{(k)})_i & \text{if pixel } n \text{ contributes to detector } i \\ f_n^{(k)} & \text{if not} \end{cases} \tag{3.48}$$

The MART algorithm on a pixel image is given in Algorithm 2.

Algorithm 2 MART

Initialization: $k = 0, \mathbf{f}^{(0)} = [1 \dots 1]^\top$
while not converged **do**
  Calculate the projection $A\mathbf{f}^{(k)}$
  for all detectors $i = 1 \dots M$ **do**
    for all pixels $n = 1 \dots N$ **do**
      Update the value of pixel n with detector i by (3.48)
    end for
  end for
  $k \leftarrow k + 1$
end while

3.2.2 Minimum Cross Entropy Principle

The minimum *cross-entropy* (MCE) principle is another entropy based regularization technique. The cross-entropy $H(p, q)$ is a non-symmetric measure of the difference between two probability density functions p, q:

$$H(p, q) \triangleq -\int_\Omega p(x) \log \frac{p(x)}{q(x)} dx \tag{3.49}$$

$H(p, q)$ measures the expected number of extra bits required to code samples from p when using a code based on q, rather than using a code based on p. It's also referred to as the *Kullback–Leibler* (KL) divergence. Typically p represents the distribution of data or observations, and q represents a model or a reference. In the medical imaging context for example, q could refer to the anatomical knowledge, and the cross-entropy express the prior information that the unknown object resembles to the anatomical image.

Let $\hat{f}$ be a prior estimation of the unknown density function f. Given some new information C (in form of constraint), the MCE principle says that one should choose f, from all possible solutions satisfying C, such that the extra information measured by $H(f, \hat{f})$ is minimized. For example, if C is given as the data fitting constraint, then:

$$\min_f H(f, \hat{f}) \quad \text{s.t. } Af = \mathbf{b} \tag{MCE}$$

The application of cross-entropy minimization in tomography can be found in [66, 67].

3.3 Regularization by Convex Constraints

Very often in a reconstruction problem our prior knowledges on the unknown object f are available in form of "hard" constraints, for example:

- Positivity : $C_+ = \{f(x) \geq 0, a.e.\}$
- Spatial localization : $C_\Omega = \{f(x) = 0, x \notin \Omega, a.e.\}$
- Prior values : $C_V = \{a \leq f(x) \leq b, a.e.\}$
- Bounded energy : $C_E = \{\|f\|_2 \leq E\}$

All these constraints listed above are closed and convex sets of $X \subset L^2(\mathbb{R}^d)$, so are their intersections. The incorporation of these constraints into the optimization problem can efficiently reduce the size of solution space and considerably improve reconstruction qualities.

Example 3.3.1 (Landwebber iteration with positive constraint)**.** Let's consider the MSE problem with a positive constraint, namely:

$$\min_{f \in X} \|Af - \mathbf{b}\|^2 \quad \text{s.t. } f \in C_+ \tag{3.50}$$

This problem can be solved using the simple gradient projection algorithm. At the n-th iteration:

$$\begin{cases} g^{(n)} & = A^\top (Af^{(n)} - \mathbf{b}) \\ f^{(n+1/2)} & = f^{(n)} - \alpha g^{(n)}, \quad \text{for } \alpha > 0 \\ f^{(n+1)} & = (1-\lambda) f^{(n)} + \lambda \Pi_{C^+}(f^{(n+1/2)}), \quad \text{for } \lambda > 0 \end{cases} \tag{3.51}$$

Π_{C_+} here is the convex projection onto C_+. It is well known that the positivity constraint can effectively reduce the streak artifacts and accelerate the convergence of the initial MSE problem, especially when the number of projection is limited.

3.3.1 Projection onto convex set

By incorporating a closed convex constraint set $C \subset X$, the MAP problem formulated in Section 2.2.2 now reads:

$$\min_f \frac{1}{2}\|Af - \mathbf{b}\|^2 + \beta R(f), \quad \text{s.t. } f \in C \tag{3.52}$$

and the constraint optimization form:

$$\min_f R(f), \quad \text{s.t. } \|Af - \mathbf{b}\|^2 \leq \epsilon^2, \text{ and } f \in C \tag{3.53}$$

The existence of solution has been studied in Proposition 4.2 and 4.3 of Chapter 2. However, solving numerically (3.52) and (3.53) could be much more difficult compared with their original form, due to the presence of constraint C. In a Hilbert space X, a basic tool for this purpose is the well-known theorem of projection onto convex set (POCS). It says that for convex closed C, there exists a unique solution to the problem:

$$\Pi_C(f) = \arg\min_{g \in C} \|f - g\|_X \tag{3.54}$$

The point $\Pi_C(f)$ is called the convex projection of f onto C. For many basic constraint sets, *e.g.*those listed above, $\Pi_C(\cdot)$ has simple analytical expression. Now suppose that C is the non empty intersection of $C_1, C_2, ..C_K$, which are all convex closed sets, and the projector Π_{C_k} is known for each C_k. One can then define the cyclic projection:

$$\Pi(f) \triangleq \Pi_{C_K} \circ ..\Pi_{C_2} \circ \Pi_{C_1}(f) \tag{3.55}$$

and note:

$$\Pi^n \triangleq \underbrace{\Pi \circ \ldots \circ \Pi}_{\text{n times}} \tag{3.56}$$

Then it can be shown that when $n \to \infty$, $\Pi^n(f)$ converges to a point in the intersection set C. Furthermore, if all sets $C_1 \ldots C_K$ are affine spaces, the converged point is indeed the convex projection of f onto $C = C_1 \cap C_2 \cap ..C_N$ [68]. This method called *cyclic projection* is particularly useful in numerical solution of optimization problems with several convex constraints.

Example 3.3.2 (Algebraic Reconstruction Technique(ART))**.** The well known ART in CT literature is a special case of the cyclic projection method. Rewrite the equality constraint $Af = \mathbf{b}$ as:

$$Af = \begin{pmatrix} \langle a_1, f \rangle \\ \vdots \\ \langle a_M, f \rangle \end{pmatrix} = \begin{pmatrix} b_1 \\ \vdots \\ b_M \end{pmatrix} = \mathbf{b} \tag{3.57}$$

The convex projection onto each of affine space $H_m = \{\langle a_m, f \rangle = b_m\}$ is given by:

$$\Pi_m(f) = f + \frac{b - \langle f, a_M \rangle}{\|a_M\|^2} a_M, \quad \text{for } 1 \leq m \leq M \tag{3.58}$$

If f is initialized by 0, then ART converges to the same solution as MSE problem[2].

3.3.1.1 Projection onto ℓ^1 ball

Consider the ℓ^1 ball in $\mathbb{R}^N$: $B_\alpha^1 \triangleq \{\|\mathbf{f}\|_1 \leq \alpha\}$, and define Π_{ℓ^1} the convex projector onto B_α^1. This projector is important in sparsity related algorithms, and it can be calculated using a thresholding operator $\text{SoftThresh}_\lambda(\mathbf{f})$ as defined in (B.2) with $O(N \log N)$ time (more efficient methods exist, see *e.g.*[69]):

$$\Pi_{\ell^1}(\mathbf{f}) = \text{SoftThresh}_\lambda(\mathbf{f}) \tag{3.59}$$

The constant λ is found through a linear search on the sorted coefficients of $\{|f_1|, |f_2|, \ldots\}$.

Example 3.3.3 (Reconstruction by TV minimization and ℓ^1 sparsity constraint)**.** In previous sections, we've seen that the regularization by TV and Besov norm minimizations are efficient techniques in treating the few projections problem. A natural extension would be the combination of these two methods. We replace the Besov norm by the equivalent ℓ^1 norm, and consider the following problem:

$$\min_{\mathbf{c}} \|W\mathbf{c}\|_{TV} \text{ s.t. } AW\mathbf{c} = \mathbf{b}, \text{ and } \|\mathbf{c}\|_1 \leq \alpha \tag{3.60}$$

where W is the discrete wavelet synthesis operator as in section 3.1.4. The constraint $\|\mathbf{c}\|_1 \leq \alpha$ is a prior knowledge on the solution: it restricts the possible solution to those whose wavelet coefficient vector $\mathbf{c}$ is inside the ℓ^1 ball of radius α.

Using the relaxation technique $|x| \simeq \sqrt{x^2 + \epsilon}$, we replace the objective function in (3.60) by a smooth term, therefore the problem can be approximately solved using descent method with gradient projection: at each iteration the gradient of objective function is projected onto the non empty convex constraint

$$C \triangleq \{AW\mathbf{c} = \mathbf{b}\} \cap \{\|\mathbf{c}\|_1 \leq \alpha\}$$

Let Π_M, and Π_{ℓ^1} be respectively the convex projectors onto the affine space $\{AW\mathbf{c} = \mathbf{b}\}$ and the ℓ^1 ball $\{\|\mathbf{c}\|_1 \leq \alpha\}$. Then a point in C can be obtained by applying successively the alternating projection $\Pi_M \circ \Pi_{\ell^1}$. Numerical results in [70] confirm that the formulation can effectively reduce the pseudo Gibbs artifacts appeared in the regularization by Besov norm due to the errors in the wavelet coefficients.

3.4 Concluding remarks

In this chapter we have reviewed some important regularization techniques and most of them are very popular in the tomography literature. The ill-posedness of few projections

problem is balanced by the regularization, which stabilizes the inversion procedure and improve the reconstruction quality.

The development of regularization techniques in tomography has started with the row-action algorithms (ART, MART, POCS *etc.*) in the 1970s [64] and evolved lately to the Bayesian framework, which allows to characterize the smoothness of the unknown function through regularization through a prior distribution (in case that the prior constitutes a (semi-)norm, *e.g.* the TV or Besov norm, the regularization is precisely done in a functional space of smoothness defined by this norm). In this direction, many different priors and related algorithms have been proposed since 1990s, with increasing interests on the Edge-preserving prior which allows to recover the piecewise homogeneous function from incomplete data.

We have reproduced some important algorithms of the literature to demonstrate the effect of these regularization techniques. It has been observed that the minimization of the TV norm and the Besov norm of the wavelet coefficients are generally efficient in treating the few projections problem: the former works very well on piecewise homogeneous phantom image by preserving the edges and constant regions, while the later reconstruct well the natural medical images which are "compressible" under wavelet transform. The reason can be roughly explained by "representing a function in a space where it's simple". For example, a piecewise homogeneous functions of the BV space is "simple" since near all its information is concentrated on the edges. Similarly, a natural image represented by its wavelet coefficient in Besov space for $p < 2$ is simple since near all its information is concentrated on few most largest coefficients.

The notion of *sparsity* then enters in our field of view. For a linear inverse problem where the number of data is far few than the dimension of the unknown, finding the unknown in a space where it is supposed to be sparse can be much more advantageous than other regularization techniques, since the sparsity reduces the inherent dimension of the linear system, consequently improve the trouble situation related to the ill-posedness, such as the non-uniqueness, the instability with respect to noise *etc.*. From a signal sampling point of view, the question of the few projections problem can be formulated in a more general way: is it possible to reconstruct a function from a limited samples in the Radon domain by exploiting the sparsity? This is precisely the theme of the recent developed Compressed Sensing theory, which brings new insights to the CT reconstruction problem. We shall dedicate the next chapter to this subject.

Chapter 4

Compressed Sensing and CT

Compressed Sensing (CS) is an emerging theory about signal acquisition and reconstruction, with the objective of capturing the whole information of a signal using a small number of measurements and then recovering the signal stably with small distortions. The acquisition process used by CS is specific and often randomized, which allows to "compress" the information in a small number of observations, while the reconstruction process in CS is nonlinear and one has quantitative estimations about the distortion in function of the signal's information complexity and the number of measurements. This framework is particularly useful in situations where a thorough acquisition of signal is expensive or impossible, such as MRI or the sampling of extra wide-band signal: by redesigning the acquisition protocol to conform to the CS principle, one can use a sampling rate much lower than the classical Shannon-Nyquist rate. In the situation where one can not modify the acquisition process but only reduce the number of measurements, one can still use the nonlinear reconstruction process employed in CS to get a stable reconstruction with small distortion.

Since the foundation work by Candes and Tao in [71] and Donoho in [72], this theory has been considerably extended. The main body of CS theory has been established on a discrete and finite dimensional setting, although there are efforts to generalize this theory to infinite dimension [73]. In this chapter we resume some key ingredients of CS and point out its usefulness for the CT reconstruction. Our expositions are mainly based on the papers [71, 74, 75]. To explain the motivation let us start by an example.

4.1 Motivations

Sampling of frequency sparse signal Let $x \in \mathbb{R}^N$ and and $\hat{x} = \mathcal{F}x$ with the Fourier matrix $\mathcal{F}[n,m] = \exp(-2\pi inm/N)/\sqrt{N}$. We note $\delta[n] = \mathbb{1}_{n=0}$ and $S_\tau[n] =$

$\sum_{k=0}^{w-1} \delta[n-k\tau]$ the sampling vector, with $\tau \in \mathbb{N}$ the sampling period such that $N = w\tau$ for $w \in \mathbb{N}$. We want to recover x from its samples x_d, defined as $x_d[n] = x[n]S_\tau[n]$. Recall a discrete version of Shannon-Nyquist sampling theory:

Proposition 4.1.1 (Shannon-Nyquist)**.** *Let x_d be samples of x with sampling period τ. If $|\operatorname{supp} \hat{x}| < w = N/\tau$, then x can be recovered from its samples x_d by: $x = \mathcal{F}_d^{-1}(\hat{x}_d \cdot \mathbb{1}_{0 \leq n < w})$.*

Suppose that x is sparse in frequency: $\hat{x}[n] = \delta[n] + \delta[n - \lfloor N/2 \rfloor]$. Since $|\operatorname{supp} \hat{x}| > N/2$ so by Proposition 4.1.1, the maximal sampling period $\tau = 1$, *i.e.*, all samples of x are needed. Given the sparsity $\hat{x}$, this seems to be overly pessimistic. On the contrary, let $T \subset \{0, \ldots, N-1\}$ and x_T the samples of x on T: $x_T[n] = x[n]\mathbb{1}_{n \in T}$. Then a result from [71] says the following:

Proposition 4.1.2 ([71], Theorem 1.1)**.** *Let N be prime, and Σ_K the set of all x such that $|\operatorname{supp} \hat{x}| \leq K/2$. Then limited on Σ_K and for any T of size $|T| \geq K$, the map $x \mapsto x_T$ is injective.*

Therefore, for N prime it would be possible to recover our previous signal x from only 4 arbitrary samples. The reconstruction process needs to find a signal which is sparse in frequency and conform with the samples x_T. This can be realized by solving the ℓ^1 minimization problem:

$$\min_{y \in \mathbb{R}^N} \|\hat{y}\|_1 \text{ s.t. } y_T = x_T \tag{4.1}$$

with $\|x\|_1 \triangleq \sum_n |x_n|$. Note that (4.1) is convex and easily solvable, *e.g.*by converting to a linear programming. Now using the ℓ^1 minimization as reconstruction process, a more precise and powerful result can be established, which confirms the sampling condition suggested by Proposition 4.1.2:

Proposition 4.1.3 ([71], Theorem 1.3)**.** *Let $x \in \mathbb{R}^N$ be a signal such that $\hat{x}$ is supported on Ω, and choose $T \subset \{0, \ldots, N-1\}$ uniformly at random. If*

$$|T| \geq C_\gamma |\Omega| \log N \tag{4.2}$$

with $C_\gamma \asymp \gamma$ a constant, then with probability at least $1 - O(N^{-\gamma})$, the solution to the ℓ^1 minimization problem (4.1) is unique and is equal to x.

Note that the probability $1 - O(N^{-\gamma})$ here is not uniform for all x but per x. So Proposition 4.1.3 says essentially that one can sample x arbitrarily, provided that the number of samples is at the same order of the sparsity of $\hat{x}$, then x can be reconstructed

through (4.1) with high probability. This is very different to the classical Shannon-Nyquist sampling theory.

4.2 Ingredients of CS

The above result is only an example of what CS can promise. In CS the concept of sampling is generalized to the *sensing matrix* $A : \mathbb{R}^N \to \mathbb{R}^M, M \ll N$ with each row a vector $a_m \in \mathbb{R}^N$. Applied on a vector x, it yields the observation Ax with $(Ax)_m = \langle a_m, x \rangle$. Given Ax, the *decoder* $\Delta : \mathbb{R}^M \to \mathbb{R}^N$ yields $\Delta(Ax)$, an estimated version of x, and the difference

$$E(x, \Delta, A) \triangleq \|\Delta(Ax) - x\|_2 \tag{4.3}$$

is called *distortion*. The central question of CS is to know what are good measurement matrices and decoding devices (Δ, A) such that the distortion on a class of signals is small. CS theory answers this question by relating the distortion to the information complexity of x.

4.2.1 Sparsity class

We note $\{x_n\}$ a sequence, and $\{x_{(n)}\}$ the sorted sequence in a decreasing order: $|x_{(0)}| \geq |x_{(1)}| \geq \ldots$. There exist various ways to measure the information complexity of $\{x_n\}$. We say that x is in weak ℓ^p $(p > 0)$ ball if there's a constant $R > 0$ such that

$$|x_{(n)}| \leq R n^{-1/p}, \quad \text{for } n \geq 1 \tag{4.4}$$

The weak ℓ^p norm $\|x\|_{w\ell^p}$ is defined as the smallest constant R such that (4.4) holds. We recall the definition of ℓ^p (quasi)-norm:

$$\|x\|_p \triangleq \begin{cases} (\sum_n |x_n|^p)^{1/p}, & \text{for } 0 < p < \infty \\ \max_n |x_n|, & \text{for } p = \infty \end{cases} \tag{4.5}$$

The special case $p = 0$ gives the ℓ^0 norm $\|x\|_0$, defined as the number of nonzero entries in x. For $0 < p < 1$, (4.5) fails to be a norm but we have a triangle inequality:

$$\|x + y\|_p^p \leq \|x\|_p^p + \|y\|_p^p \tag{4.6}$$

It can be shown easily that $\|x\|_p < \infty$ implies $\|x\|_{w\ell^p} < \infty$, so the n-th biggest terms of x decreases as in (4.4).

If x is non sparse, we can approximate it by preserving the first s-th biggest terms, and then obtain the *s-term approximation error*:

$$\sigma_s(x) \triangleq \inf_{y \in \Sigma_s} \|x - y\|_2 \tag{4.7}$$

where Σ_s denotes the set of all s sparse vector: $x \in \Sigma_s \Leftrightarrow \|x\|_0 \leq s$. The decaying rate of $\sigma_s(x)$ as a function of s reveals also the information complexity of x. It can be shown [75, 76] that $\sigma_s(x)$ decays as s^{-r} for a constant $r > 0$, if and only if x belongs to a weak ℓ^p ball for $1/p = r + 1/2$. Therefore, the decaying rate of the coefficient and that of the approximation error are completely equivalent. Particularly, we have:

$$\sigma_s(x) \leq \|x\|_p s^{1/2-1/p}, \quad \text{for } s \geq 1 \tag{4.8}$$

For p small, *e.g.*, $p < 2$, $\sigma_s(x)$ decays when s increases and we say that x is compressible. Similarly, it can be shown that if the approximation error in (4.7) is measured in ℓ^1 norm, *i.e.*, $\sigma_s(x) = \inf_{y \in \Sigma_s} \|x - y\|_1$, then:

$$\sigma_s(x) \leq \|x\|_p s^{1-1/p}, \quad \text{for } s \geq 1 \tag{4.9}$$

4.2.1.1 Theoretical limit of CS system performance

Under the hypothesis that the unknown signal x belongs to some sparsity class, there exists some theoretical bounds on the best possible performance of any (Δ, A) pair [72, 74, 75]. Let's note B_1 the unit ℓ^1 ball of $\mathbb{R}^N$, and define the symbol $E(B_1, \Delta, A)$ as the distortion of a given (Δ, A) pair on B_1:

$$E(B_1, \Delta, A) \triangleq \sup_{x \in B_1} E(x, \Delta, A) \tag{4.10}$$

The best performance for any (Δ, A) pair on B_1 is obtained by:

$$E(B_1) \triangleq \inf_{(\Delta, A)} E(B_1, \Delta, A) \tag{4.11}$$

where the infimum is taken on all possible measurement matrix and decoder for $M < N$ fixed. Then one can establish the upper and lower bounds on B_1 (similar result holds for other ℓ^p ball B_p):

Proposition 4.2.1 ([75], Lemma 2.1)**.** *There exists a constant $C_0 > 0$ such that for all $0 < M < N$ we have*

$$C_0 \sqrt{\frac{\log(N/M) + 1}{M}} \leq E(B_1) \leq 2C_0 \sqrt{\frac{\log(N/M) + 1}{M}} \tag{4.12}$$

4.2.2 Decoder

Given that the unknown signal x is sparse, the natural choice for decoder Δ is to solve the ℓ^0 minimization problem:

$$\min_{y \in \mathbb{R}^N} \|y\|_0 \text{ s.t. } Ay = Ax \tag{P_0}$$

Then a necessary and sufficient condition [75] for (P_0) to recover all s-sparse signal x is: $\ker A \cap \Sigma_{2s} = \{0\}$, *i.e.*, the kernel space of A does not contain any nonzero vector of sparsity of $2s$. Unfortunately, (P_0) is a NP-hard problem, and in practice it is often relaxed to some numerically tractable algorithms. To mention some of them: Matching Pursuit (MP) and Orthogonal MP [77], Iterative Hard Thresholding [78], CoSaMP [79] etc. Most of these methods are based on greedy strategy and benefit from equivalence to (P_0) under specific conditions. Another relaxation technique is by the ℓ^p minimization, for $0 < p \leq 1$:

$$\min_{y \in \mathbb{R}^N} \|y\|_p \text{ s.t. } Ay = Ax \tag{P_p}$$

This is mainly based on the fact that $\|x\|_p \to \|x\|_0$ point wisely as $p \to 0$.

Proposition 4.2.2 (Null Space Property (NSP))**.** *For any $x \in \Sigma_s$, the solution of (P_p) equals to x if and only if the following holds: for any set S of size $|S| < s$ and any non zero vector $v \in \ker A$*

$$\|v_S\|_p^p < \frac{1}{2}\|v\|_p^p, (\textit{or equivalently, } \|v_S\|_p^p < \|v_{\bar{S}}\|_p^p) \tag{4.13}$$

where v_S and $v_{\bar{S}}$ are the restriction of v on S and on its complement $\bar{S}$, respectively.

Proof. Suppose that (4.13) holds and $x \in \Sigma_s$. We need to prove that x is the unique solution of (P_p), which is equal to say that for any nonzero vector $v \in \ker A$, $\|x+v\|_p^p > \|x\|_p^p$. We write $v = v_S + v_{\bar{S}}$ with S the support of x, $\bar{S}$ its complement. Using (4.6):

$$\begin{aligned} \|x + v_S + v_{\bar{S}}\|_p^p &= \|x + v_S\|_p^p + \|v_{\bar{S}}\|_p^p \\ &> \|x + v_S\|_p^p + \|v_S\|_p^p \geq \|x\|_p^p \end{aligned}$$

On the contrary, suppose that for any $x \in \Sigma_s$, then x is also unique solution of (P_p). For kernel vector $v = v_S + v_{\bar{S}}$, we have $Av_S = A(-v_{\bar{S}})$. Since $v_S \in \Sigma_s$, so it is the unique solution of eq. (P_p), therefore $\|v_S\|_p^p < \|v_{\bar{S}}\|_p^p$. □

Proposition 4.2.2 actually gives a condition on what is a good measurement matrix: none of its kernel vector can concentrate more than half of its energy on a support of size s.

A special case is the (P_1) decoder ($p = 1$, ℓ^1 minimization) which is convex, therefore numerically much simpler than the decoder (P_p) for $p < 1$. Candès and Tao revealed the power of the (P_1) decoder by studying a condition called Restricted Isometry Property (RIP) [80].

4.2.2.1 Restricted Isometry Property (RIP)

The RIP constant $\delta_s \in [0, 1)$ is the smallest value such that the following holds:

$$(1 - \delta_s)\|x\|^2 \leq \|Ax\|^2 \leq (1 + \delta_s)\|x\|^2, \ \forall x \in \Sigma_s \tag{RIP}$$

We say that A has RIP of order s with δ_s if such constant exists. RIP is uniform to all sub-matrix A_S composed by the columns of A in a index set S of size $|S| \leq s$, and it indicates how close is A_S to an isometry. This is a powerful tool in the CS theory, because it links the ℓ^1 decoder with the good sensing matrix in a much simpler way than other tools like NSP.

Proposition 4.2.3 ([81], Theorem 1.1)**.** *Assume that the matrix A satisfies the RIP of order $2s$ with the RIP constant $\delta_{2s} < \sqrt{2} - 1$. Then the solution x^* of (P_1) obeys*

$$\|x^* - x\|_1 \leq C_0\|x - x_s\|_1, \ \text{and} \ \|x^* - x\|_2 \leq C_0\frac{\|x - x_s\|_1}{\sqrt{s}} \tag{4.14}$$

with x_s the s-terms approximation of x, and C_0 a small constant.

So if the true signal x is s-sparse, $x^* = x$; otherwise using (4.8) and (4.9) we see that the distortion is not much worse than the s-term approximation error $\|x - x_s\|_2$.

4.2.2.2 Robustness

Suppose that the vector Ax is corrupted by some additive noise z and gives the observation $b = Ax + z$. Then in place of (P_1), the robust ℓ^1 decoder solves:

$$\min_y \|y\|_1 \ \text{ s.t. } \|Ay - b\|_2 \leq \epsilon \tag{P_1^ϵ}$$

with $\epsilon = \|z\|_2$ the noise level. Then it has been proved that (P_1^ϵ) does not amplify the noise and the solution is stable.

Proposition 4.2.4 ([81], Theorem 1.2)**.** *Assume that the matrix A satisfies the RIP of order $2s$ with the RIP constant $\delta_{2s} < \sqrt{2} - 1$. Then the solution x^* of (P_1^ϵ) obeys*

$$\|x^* - x\|_2 \leq C_0\frac{\|x - x_s\|_1}{\sqrt{s}} + C_1\epsilon \tag{4.15}$$

with C_0, C_1 some small constants.

4.2.2.3 Optimality of ℓ^1 minimization

Under the condition of Proposition 4.2.3, we consider the distortion (4.14) introduced by the decoder $\Delta = (P_1)$:

$$\|x - \Delta(Ax)\|_2 \leq C_0 \frac{\|x - x_s\|_1}{\sqrt{s}} \leq C_0 \frac{\|x\|_1}{\sqrt{s}}$$

Taking superium for $x \in B_1$ the unit ℓ^1 ball, we obtain:

$$E(B_1) \leq E(B_1, \Delta, A) \leq C_0 \frac{1}{\sqrt{s}} \tag{4.16}$$

with $E(B_1)$ and $E(B_1, \Delta, A)$ the class distortions as defined in (4.11) and (4.10) respectively. Now use the theoretical lower bound in (4.12), we find:

$$s \leq C \frac{M}{\log(N/M)}$$

for some constant $C > 0$. This is the widest range on the sparsity level that a good sensing matrix A can have with the (P_1) decoder. On the other hand, if $1/\sqrt{s}$ is bounded by the upper bound in (4.12), or if for some constant C'

$$s \geq C' \frac{M}{\log(N/M)}$$

then by (4.16), the class distortion on B_1 introduced by (Δ, A) will be within the same range as the best performance $E(B_1)$. Therefore if we can find any sensing matrix A satisfying RIP of order $2s$ with

$$s \asymp M/\log(N/M) \tag{4.17}$$

such that the RIP constant $\delta_{2s} < \sqrt{2} - 1$, then (Δ, A) attains the best possible performance on B_1 and in this sense no other *sensing matrix-decoder* pair can do better a job.

4.2.3 Good sensing matrix A

Verifying RIP condition for a sensing matrix A is as hard as solving directly the ℓ^0 minimization problem, and for this reason most known good sensing matrices are random in nature, in the sense that: *with probability exceeding* $1 - O(e^{-\gamma N})$ *for constant* $\gamma > 0$,

the random matrix A satisfies the condition of Proposition 4.2.3 with the sparsity level[1] *for some constant $C_\gamma > 0$.* of $s \leq C_\gamma M / \log(N/M)$,

Well-known examples which can be associated to some probability distributions include the Gaussian and the Binary random matrices. The entries of these matrices are independent realizations of a same centered Gaussian or Bernoulli distribution, see [82]. There are also sensing matrices which can be implemented in a "matrix-free" manner:

- *Fourier measurements*[71, 82, 83]. Here A is obtained by selecting M rows of a discrete Fourier matrix uniformly at random, followed by a column-wise re-normalization. It has been shown [83] that the condition of Proposition 4.2.3 holds with overwhelming probability if

$$s \leq C_\gamma M / (\log N)^4 \tag{4.18}$$

- *Arbitrary orthonormal measurements*[82, 84]. Similar statement holds also for an arbitrary orthonormal system U. Here A is obtained by selecting M rows of U uniformly at random, followed by a column-wise re-normalization. Then the condition of Proposition 4.2.3 holds with overwhelming probability if

$$s \leq C_\gamma M \frac{1}{\mu^2(U)} \frac{1}{(\log N)^4} \tag{4.19}$$

  where $\mu(U) \triangleq \sqrt{N} \max_{m,n} |U_{m,n}|$ is called the *incoherence* of the matrix U. This result is of considerable importance since most of the real world signals are sparse or compressible only after an *orthonormal sparsifying transform*. Well known examples include the discrete cosines transform (DCT) and the wavelet system used respectively in the JPEG and the JPEG2 $\times 10^3$ image compression format. We note $W^\top$ a such transform and use the following ℓ^1 minimization problem as decoder:

$$\min_c \ \|c\|_1 \ \text{ s.t. } \ AWc = AWc_0 \tag{$P_{1,S}$}$$

  with $c_0 = W^\top x$ the coefficients of x. Then the same error estimation (4.14) holds now for the reconstructed coefficient vector.

[1] or with the number of measurements $M \geq C_\gamma^{-1} s \log(N/s)$.

4.3 Implications in CT reconstruction

Parallel beam CT The Fourier transform of each parallel beam projection acquired by detector is in fact a slice passing by the origin in the frequency domain (for the fan beam source, this relation holds approximately if one can transform the fan beam data to parallel beam data through a rebinning procedure[85]), as illustrated in Figure 4.1 (a). According to CS results about the Fourier measurement, one can expect to reconstruct any sparse object with large probability, as long as the number of projection lines is at the same order of the sparsity of the object, while the angular position of sources can be arbitrary. Numerical experiments in Figure 4.1 confirm this theoretical prediction. Here we use the standard Shepp-Logan phantom of 256×256 pixels as test image x, which contains only 3.3% of nonzero coefficients after the discrete gradient transform, and solve the TV minimization problem:

$$\min_y \|y\|_{TV}, \quad \text{s.t. } Ay = Ax \tag{4.20}$$

where A is the partial discrete Fourier transform with nonzero values only on radial lines[2]. The mask in Figure 4.1.(b) is obtained by uniformly sampling the angular position between $[0, \pi)$ at random. Although very irregular compared to Figure 4.1.(a), the projections using the mask of Figure 4.1.(b) produces high quality reconstruction. While the limited-angle projections Figure 4.1.(c) which can not be obtained from a uniform random sampling on $[0, \pi)$, fail to capture the whole information of the phantom despite its larger number of measurements. Actually, the image quality will not improve even if we increase further the number of projections in Figure 4.1.(c).

X-ray projector's encoding capacity The example above illustrates an ideal case where we make great simplifications on CT system model in order to conform to the CS framework. The practical situation is quite different. Particularly, it would not be possible to simplify the X-ray projector to a partial Fourier transform, due to the special source trajectory and X-ray beam employed in data acquisition system. Although there is no available result of type (4.18) for the general X-ray projector, one may hope that the CS principle still applies to a realistic CT system, which means that the X-ray projector can effectively capture the information of sparse objects with a small number of projections. Here we study this point through a Monte-Carlo test, see Figure 4.2. The fan beam X-ray projector A in use is a matrix of dimension $M \times N$ made from the Siddon ray-driven method, with $M = P \times 128$ and $N = 64 \times 64$. The $P \in \{32, \ldots, 64\}$ projections are equally distributed on $[0, 2\pi)$.

[2] see the document of Matlab package ℓ^1-magic for more information.

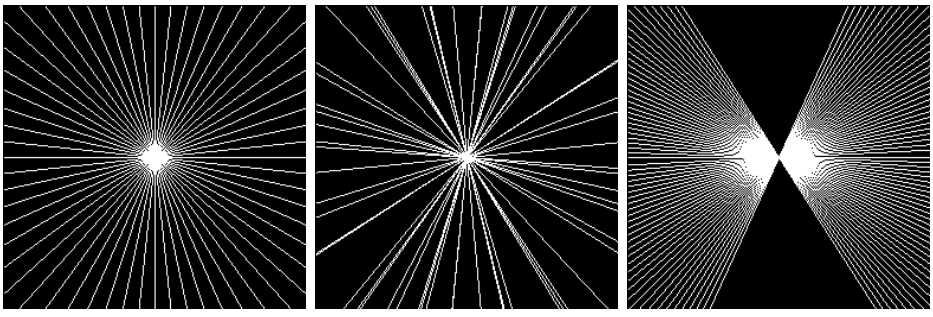

(a) 30 projections (b) 30 projections (c) 64 projections

(d) SNR=39.85db (e) SNR=29.10dB (f) SNR=6.27dB

FIGURE 4.1: Reconstructions by solving TV minimization problem with Matlab package ℓ^1-magic. Phantom dimension 256×256 pixels. X-ray projector is implemented through partial Fourier transform. First row: mask of observation. Figure (a): 30 equally distributed projections between $[0, \pi)$, (b): 30 projections between $[0, \pi)$ uniformly sampled at random, (c): 64 equally distributed projections between $[0, 1) \cup [2, \pi)$. Figure (d), (e) and (f): solutions of TV minimization with the data corresponded to (a), (b) and (c) respectively.

- Figure 4.2.(a): The test phantom x is generated as follows: we choose first uniformly S from N pixel positions at random, then for each position the pixel value is obtained by sampling the same Gaussian distribution $\mathcal{N}(0, 1)$. By varying the sparsity level $1 - S/N \in [0, 0.5]$ and the number of projections P, we obtain different x and corresponding sinogram Ax. Then we use the decoder $\Delta = (P_1)$ and plot the relative error $\|\Delta(Ax) - x\|_2 / \|x\|_2$ in Figure 4.2.(a), where one can clearly distinguish a sharp transition indicating the number of projections necessary for reconstructing an image of a given sparsity level.

- Figure 4.2.(b): The test phantom x is generated in the same way as Figure 4.2.(a). We add a small white noise e of energy $\|e\| = 10^{-3}$ to the sinogram Ax and use the decoder $\Delta = (P_1^{\epsilon})$, with $\epsilon = \|e\|$. The relative error $\|\Delta(Ax + e) - x\|_2 / \|x\|_2$ in plotted in Figure 4.2.(b), where the sharp transition still exists but considerably degraded if compared to Figure 4.2.(a).

- Figure 4.2.(c): We use the Haar wavelet basis W and generate the coefficient c in the same way as in (a), and use the decoder $\Delta = (P_{1,S})$. The relative error $\|\Delta(AWc) - c\|_2 / \|c\|_2$ in plotted in Figure 4.2.(c).

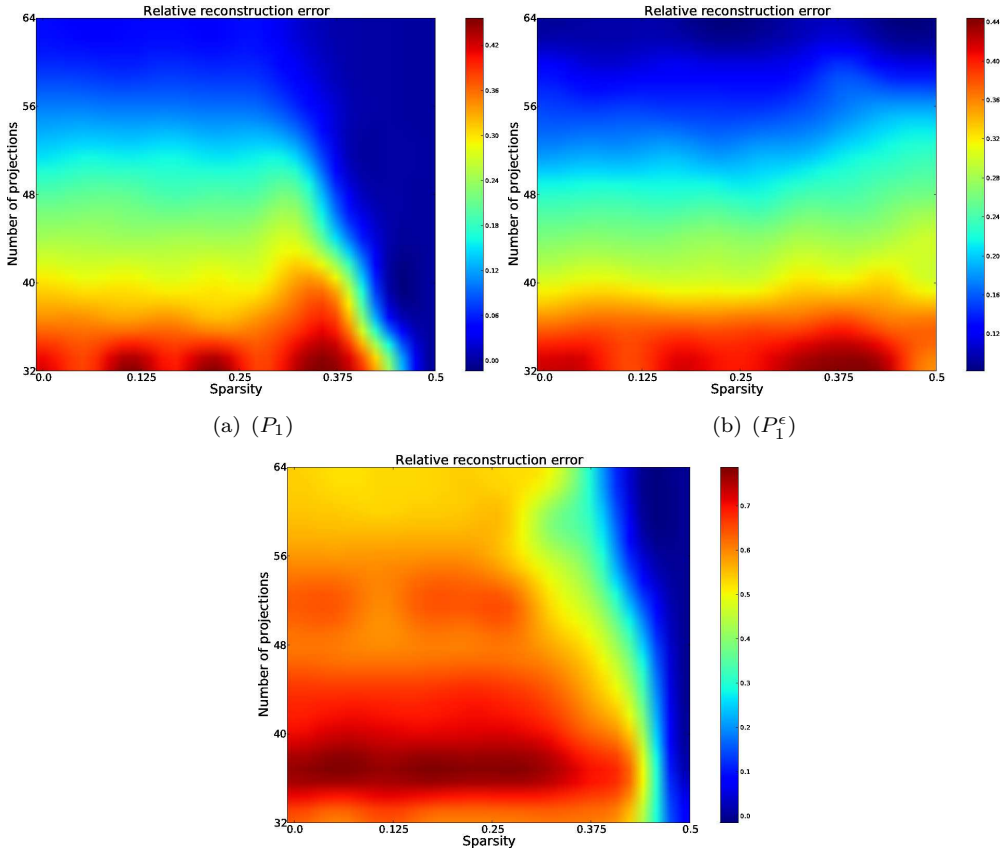

(a) (P_1) (b) (P_1^ϵ)

(c) $(P_{1,S})$

FIGURE 4.2: Monte-Carlo test of the X-ray projector's encoding capacity. See section 4.3 for descriptions on the experiments.

Acquisition geometry and sinogram inpainting CS theory helps to explain the surprising *inpainting* phenomena. Image inpainting usually refers to the restoration of a pixel image from a partial observation where a large portion of pixels, in random or regular positions, are lost. A simple solution to inpainting problem is as follows. Let W be a sparsifying transform (*e.g.* the discrete wavelet transform, see Section 3.1.4), which applies on an image x_0 and yields a sparse or compressible coefficient vector $c_0 = W^\top x_0$, and synthesizes the image by $x_0 = Wc_0$. One solves the ℓ^1 minimization problem:

$$\min_c \|c\|_1 \quad \text{s.t. } \mathcal{M}_T W c = y \tag{4.21}$$

where $\mathcal{M}_T$ is the "observation mask", *i.e.*, the restriction onto an index set T where pixels are observed, and y is the observed pixel values. For an orthonormal system W, $\mathcal{M}_T W$ is a sub-matrix of W by selecting the rows of indexes in T. Then according to the CS result about arbitrary orthonormal measurement (section 4.2.3), the original coefficient vector c_0 can be recovered with overwhelming probability, as long as the observed pixels number $|T|$ and the sparsity of c_0 meet the condition (4.19), while the observation site T only need to be chosen uniformly at random. In [86, 87], the authors

use redundant representation systems as W and report that the original image can be recovered with nice quality for a percentage of lost pixels up to 80%.

The CT image reconstruction can also be treated as an inpainting problem: in place of reconstructing an image from the incomplete sinogram data, we restore first the entire sinogram using the inpainting technique and then apply classical inversion formula, *e.g.*FBP, on the restored sinogram. For this, we work in $\mathbb{R}^{P\times M}$ which denotes the space of "complete" discrete sinogram of P projections and M detector pixels. The X-ray projection is a sampling process in $\mathbb{R}^{P\times M}$, and different acquisition geometries T correspond to different operator $\mathcal{M}_T$, as illustrated in Figure 4.3. Then CS theory suggests that if a sinogram g can be put into a sufficiently sparse or compressible form with the aid of some (redundant) representation system, then one can restore g from $\mathcal{M}_T g$ for $|T|$ small with overwhelming probability, and T can be taken by sampling in both angular and detector positions at uniformly random. This is in contrast with some carefully designed T which work generally at high sampling density, such as the well-known interlaced scheme [2, 88–90].

Remark 4.3.1. Positioning the X-ray source randomly with high precision is mechanically speaking very challenging. A compromise would be increasing the sampling density of an equally distributed source, at the same time decreasing proportionally the detector visibility by applying a random mask between the X-ray source and the patient. In this way one keeps the total number of samples unchanged, while the sampling mask is more close to a uniformly random one, see Figure 4.3. A such acquisition protocol, if the related physical and mechanical challenges can be solved, would be useful particularly for the dose reduction.

Efficient image representation system We say that a system $\{\psi_\lambda\}$ is efficient in representing a function $f = \sum_\lambda f_\lambda \psi_\lambda$ if the coefficient $\{f_\lambda\}$ belongs to some sparsity class, *e.g.*, the weak ℓ^p ball for $p < 2$. According to the relation (4.8), fast decay of $\{f_\lambda\}$ implies smaller approximation error $\sigma_s(f)$, therefore smaller reconstruction error, using CS result (4.15). Remark that if $\{\psi_\lambda\}$ is total in $L^2(\mathbb{R}^d)$, then $\{A\psi_\lambda\}$ is also a representation system in the sinogram domain. In this case, a sinogram $g = Af$ is sparse or compressible with respect to $\{A\psi_\lambda\}$ if it is the case for f with respect to $\{\psi_\lambda\}$.

Finding an efficient $\{\psi_\lambda\}$ is therefore a central issue to the performance of a CS system. Although the main CS theory at its current state is valid only for orthogonal representation systems, there are many numerical evidences showing that the same principle can work with over-complete systems such as wavelet packet[91], curvelet[92], or redundant *dictionary*[93–95]. By incorporating a redundant system D, we use the ℓ^1 minimization

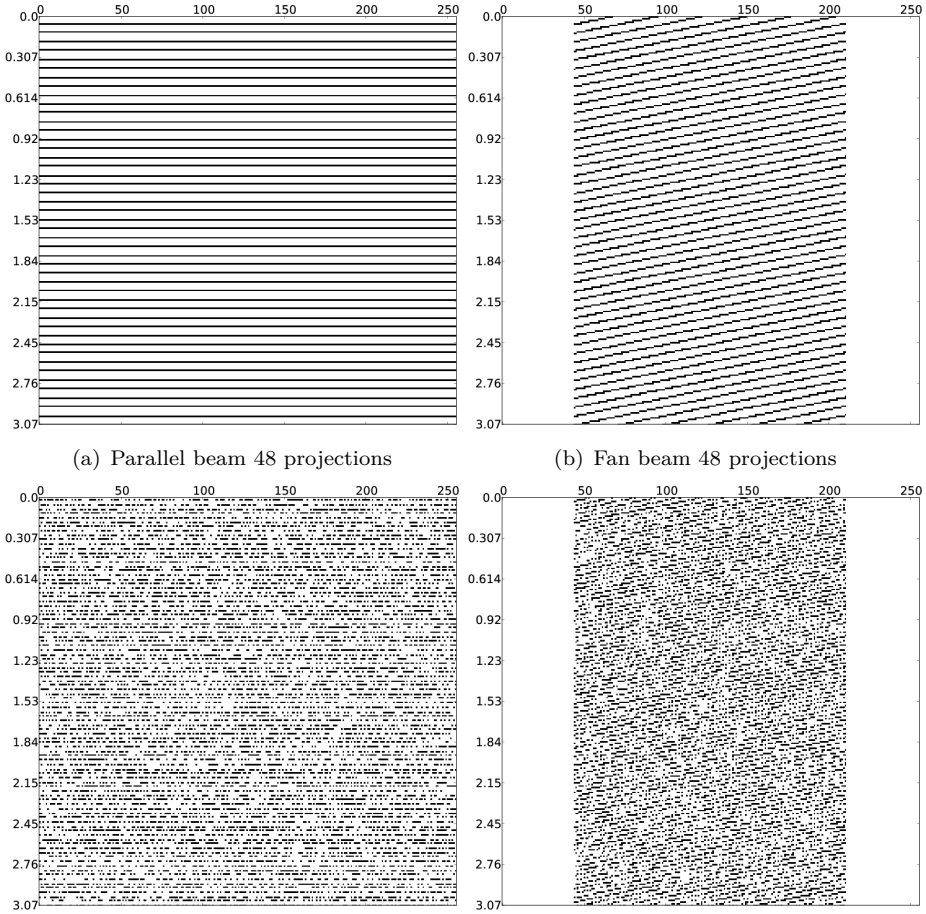

(a) Parallel beam 48 projections

(b) Fan beam 48 projections

(c) Parallel beam 96 projections

(d) Fan beam 96 projections

FIGURE 4.3: Visual representation of the mask $\mathcal{M}_T$ corresponding to different acquisition geometry, with $K = 256, M = 256$. Figure (a): Parallel beam equally distributed on $[0, \pi)$, 48 projections. (b): Fan beam equally distributed on $[0, 2\pi)$, 48 projections. (c): Parallel beam equally distributed on $[0, \pi)$, 96 projections with randomly sampled detector of 50% visibility. (d): Fan beam equally distributed on $[0, 2\pi)$, 96 projections with randomly sampled detector of 50% visibility. The vertical axis of each figure represents the source angular position, and the horizontal axis represents the detector pixel's index. The number of observation sites in (a) and (c) (or in (b) and (d)) are the same.

as CT reconstruction algorithm:

$$\min_c \|c\|_1 \quad \text{s.t.} \quad \|ADc - y\|_2 \leq \epsilon \tag{4.22}$$

or in an equivalent form:

$$\min_c \frac{1}{2}\|ADc - y\|_2 + \mu\|c\|_1 \tag{4.23}$$

with A the X-ray projector applying on the pixel image Dc, y the noisy sinogram, and μ a regularization parameter depending on ϵ.

4.4 Concluding remarks

The discussions above seem to provide a thorough framework for the few projections problem:

- Representing/modeling the image in a sparsity promoting space.
- Seeking the sparse solution through some specific nonlinear optimization problem (like TV or ℓ^1 minimization).

Then the main results of CS theory can be used to characterize quantitatively the reconstruction error. The regularization techniques based on the Besov and TV prior studied in Chapter 3 are concrete examples of this framework. Remarkably, all of them use pixel (on a regular Cartesian lattice) as the representation basis, for the reason that it enjoys great numerical simplicity and interfaces very naturally with an abundant fast transforms (FFT, DCT, DWT etc.) defined only for pixel image. For vision based image processing tasks, the pixel is with no doubt a natural choice of basis, however vis-à-vis the iterative CT reconstruction algorithms, it's not an optimal way for representing a function for that:

- The space-frequency localization of pixel is mediocre. Large pixels are needed for the control the bandwidth of the reconstruction, while this can considerably reduce the visual quality of an image.
- It requires the discretization or approximation of the X-Ray projector A, whose computational complexity depends only on the dimension of discretization but not on the sparsity of image under the representation system D. Furthermore, the application of D is separated from A which may also increase the computational charge.

The major contribution of this thesis is the development of the "CT-friendly" representation bases of Gaussian family, baptized *blob*, which have better space-frequency localization property, and on which there's no need to discretize or approximate the X-ray projector and no need for the representation system D as in (4.22) and (4.23). Using the TV and ℓ^1 related algorithms, the CT reconstructions from few projections with blobs are generally superior than with pixel/wavelet bases, in the sense that one can achieve better image quality with less computational resources. In the next part of this thesis we will 1)introduce the blob bases of Gaussian family and discuss their theoretical properties, 2) make adaptations and propose sparsity based reconstruction methods working with blobs, and 3) demonstrate their efficiency in solving few projections problem through numerical experiments.

Part II

Blobs basis and CS : analysis, methods, algorithms and experiments in tomography

Chapter 5

Radial blob for image representation

A "CT-friendly" radial basis function [96] called *(Kaisser-Bessel) blob* and the related reconstruction techniques [97] [98], have already been proposed several decades ago. Limited by the extra computation charge, it appears that the full potential behind this line of research stays unexploited by the community, and the efforts haven't been realized to adapt it to the few projections problem, where the notion of sparsity and the specific nonlinear reconstruction algorithms seem to be mandatory.

The purpose of this chapter is to introduce the radial blob functions of Gaussian family, and to develop two image representation models based on it: a single scale and a multiscale one. They can be qualified as the mimics of pixel or multiresolution wavelet representation, while they have better property in numerical computation for CT application that we will demonstrate in Chapter 7 through numerical experiments.

The chapter is organized as follows. In section 5.1, we start by introducing the definition of radial blob and particularly the Gaussian blob, and discuss some general properties of the blob image model in section 5.2. In section 5.3, we span the shift invariant space on an hexagonal lattice and we prove that the translations of Gaussian blob constitute a Riesz basis. Unlike the case of pixel basis, by simply dilating the Gaussian blob and the lattice, one cannot approximate the whole $L^2(\mathbb{R}^d)$ space with the shift invariant space. In section 5.4 we give a general way to construct the tight frame of $L^2(\mathbb{R}^d)$ using multiscale blob system, which can give compressible representation of natural images. Some practical criteria on the choice of blob parameters are discussed in section 5.5, and finally we show that there exits a multiscale system in the sinogram domain corresponding to the multiscale blob system, by using the Wavelet-Vaguelette Decomposition.

5.1 Blob basis function

Definition 5.1.1 (Radial blob)**.** We call *radial blob* a real radial symmetric function $\phi : \mathbb{R}^d \to \mathbb{R}$ satisfying the following conditions:

- ϕ is C^1 smooth (Fréchet derivative exists and is continuous) and belongs to $L^1(\mathbb{R}^d) \cap L^2(\mathbb{R}^d)$.
- it is well localized(*e.g.*, polynomial decay) in both frequency and space domain.

We note $b_\phi : \mathbb{R}^+ \to \mathbb{R}$ the monodimensional profile function associated to ϕ:

$$\phi(x) = b_\phi(\|x\|),\ x \in \mathbb{R}^d \tag{5.1}$$

Since ϕ is radial symmetric and C^1 smooth, therefore $\nabla\phi(0) = 0$, which implies $b_\phi \in C^1(\mathbb{R}_+)$, and $b'(0) = 0$. Clearly, the Fourier transform of ϕ is well defined and also radial symmetric:

$$\hat{\phi}(\omega) = b_{\hat{\phi}}(\|\omega\|),\ \omega \in \mathbb{R}^d \tag{5.2}$$

Remark 5.1.1. In order to simplify the theoretical analysis, the compact support is not required in our definition of blob, which differs from the examples of blob considered in the literature. Unless specified, the word "blob" refers to "radial blob", while the later is used to distinguish from the non-radial contour blob that will be introduced in Chapter 6.

Remark 5.1.2. Due to its radial symmetry, blob can be seen as a special case of the well known Radial Basis Function (RBF)[99], which is a powerful tool in interpolation with scattered data. Nevertheless, in our approach blob is used uniquely as the building blocks of a shift-invariant space generated on a regular lattice, therefore there's no further relations with the RBF theory except the radial symmetry.

5.1.1 Examples of blob

Kaisser-Bessel blob The Kaisser-Bessel (KB) blob proposed in [96–98] seems to be the first example of blob in the CT literature. One of its advantage is the easy control of the shape, the smoothness and the frequency localization by free parameters. Its profile function reads:

$$b_\phi(r) = \begin{cases} (1-(r/a)^2)^{m/2} I_m(\alpha(1-(r/a)^2)^{1/2})/I_m(\alpha) & 0 \le r \le a \\ 0 & r > a \end{cases} \tag{5.3}$$

where I_m is the modified Bessel function of first kind and m is its order. a is the radius and α is the shape parameter. Eq. (5.3) is a high dimensional generalization of the Kaisser-Bessel (or I_0-sinh) window function, which is an approximation to the optimal prolate spheroidal function [96].

KB blob is compactly supported, C^m smooth and $b_{\hat{\phi}}(R)$ decays in frequency domain as $O(R^{-(d+1)/2-m})$. Both the Fourier transform and the X-ray transform of KB blob can be evaluated analytically [96]. It has been pointed out in [100] that (5.3) is not positive-definite [99], which prevents it to represent perfectly constant region. However one can minimize the representation error by carefully choosing the parameters controlling its shape [100, 101].

B-Spline blob The cardinal B-Spline (CBS) is defined by the auto-convolution $B_n(r) = B_{n-1} * B_1(r)$ of rectangular function: $B_1(r) = \mathbb{1}_{-1/2 \leq r \leq 1/2}$. B_n is supported on $[-n/2, n/2]$, piecewise $n-1$ order polynomial on each interval $[k - n/2, k + 1 - n/2]$, and C^{n-2} smooth. Its Fourier transform $\hat{B}_n(s)$ decays as $O(s^{-n})$ in frequency domain, and its Abel transform can be calculated analytically on each interval $[k - n/2, k + 1 - n/2]$. These properties suggest that one can use the B-Spline $B_n(r)$ as the profile function of blob.

Gaussian blob This blob is defined as a simple Gaussian function:

$$\phi(x) = \exp(-\alpha \|x\|^2), \alpha > 0 \tag{5.4}$$

The Gaussian blob is optimal in the sense that it attains the best spatial-frequency concentration among all $L^2(\mathbb{R}^d)$ functions. Other blobs that belong to the Gaussian family will be deduced later in section 5.4.

We will not pursue the examples of Kaisser-Bessel and B-Spline blobs any further in this thesis. In fact, the parallelization of elementary calculations related to blob requires that the blob function has a simple expression. For the Kaisser-Bessel blob which contains the modified Bessel function of the first kind in its expression [96], there is no *computationally efficient* implementation on current parallel architecture[1], consequently many numerical evaluations become too time-consuming to be incorporated in iterative reconstruction algorithms. While for the B-Spline blob which can be implemented with moderate effort, there's no visible advantages over the blobs of Gaussian family, from

[1] Precisely, the NVIDIA GPU card GTX580/Tesla C2070

both the numerical and theoretical point of view. The blobs of Gaussian family are perfectly fitted in our framework for its mathematical properties and numerical simplicity, and will be considered exclusively in the following.

5.1.2 Abel transform of blob

The Abel transform of a 1D function $b(\cdot)$ is defined by:

$$\mathcal{A}b(s) \triangleq 2\int_s^{+\infty} b(r)\frac{r}{\sqrt{r^2-s^2}}dr \tag{5.5}$$

This transform arises very naturally when treating with the line integral of radial functions. On the blob ϕ the X-ray transform becomes the Abel transform of the profile function b_ϕ, noted by $\mathcal{A}b_\phi$, which is independent of the X-ray's angular direction $\theta \in \mathcal{S}^{d-1}$:

$$\mathcal{P}_\theta\phi(y) = 2\int_{\|y\|}^{+\infty} b_\phi(r)\frac{r}{\sqrt{r^2-\|y\|^2}}dr = \mathcal{A}b_\phi(\|y\|) \tag{5.6}$$

Furthermore, by using Abel transform one can get the expression of a blob by knowing it in the frequency domain, and *vice versa*.

Proposition 5.1.1. *The profile function $b_\phi(r)$ of blob $\phi(x)$ is related to that $b_{\hat{\phi}}(s)$ of the Fourier transform $\hat{\phi}(\omega)$ as follows:*

$$\underbrace{\mathcal{A}\circ\cdots\circ\mathcal{A}}_{d-1} b_{\hat{\phi}}(s) = \widehat{b_\phi}(s),\ \ s\in\mathbb{R} \tag{5.7}$$

where the left side means applying the Abel transform on $b_{\hat{\phi}}$ for $d-1$ times, and the right side is the 1D Fourier transform of b_ϕ.

Proof. The proof consists in applying recursively the Projection Slice Theorem. We note $\mathcal{F}_d$ the Fourier transform in a linear space (context dependent) of dimension d. By (5.6) $\mathcal{P}_{\theta_1}\phi(\cdot)$ is a radial function defined in the $d-1$ dimensional space $\theta_1^\perp$. The Projection Slice Theorem now says that for any $\omega \in \theta_1^\perp$:

$$\mathcal{F}_{d-1}(\mathcal{P}_{\theta_1}\phi)(\omega) = \mathcal{F}_d(\phi)(\omega) \tag{5.8}$$

We apply again the X-ray transform at angular direction $\theta_2 \in \theta_1^\perp$, to get another radial function $\mathcal{P}_{\theta_2}\mathcal{P}_{\theta_1}\phi(\cdot)$ which is defined in $\theta_1^\perp \cap \theta_2^\perp$, and use (5.8):

$$\mathcal{F}_{d-2}(\mathcal{P}_{\theta_2}\mathcal{P}_{\theta_1}\phi)(\omega) = \mathcal{F}_{d-1}(\mathcal{P}_{\theta_1}\phi)(\omega) = \mathcal{F}_d(\phi)(\omega) \tag{5.9}$$

which holds for $\omega \in \theta_1^{\perp} \cap \theta_2^{\perp}$. Iterating this procedure for $d-1$ times, finally one gets:

$$\mathcal{F}_1(\mathcal{P}_{\theta_{d-1}} \cdots \mathcal{P}_{\theta_1}\phi)(\omega) = \mathcal{F}_d(\phi)(\omega),\ \forall \omega \in \theta_1^{\perp} \cap \ldots \cap \theta_{d-1}^{\perp} \tag{5.10}$$

where the independent vectors $\theta_i \in \theta_1^{\perp} \cap \ldots \cap \theta_{i-1}^{\perp}$ for $i > 1$, and the mono dimensional space $\theta_1^{\perp} \cap \ldots \cap \theta_{d-1}^{\perp}$ can take any orientation in $\mathbb{R}^d$ by changing the directions $\theta_1, \ldots, \theta_{d-1}$. By the radial symmetry of ϕ, the 1D function $\mathcal{P}_{\theta_{d-1}} \cdots \mathcal{P}_{\theta_1}\phi$ equals $\underbrace{\mathcal{A} \circ \cdots \circ \mathcal{A}}_{d-1} b_\phi$, and (5.7) now follows by taking the Fourier transform and inverting the roles of ϕ and $\hat{\phi}$. □

5.2 Image representation by blob

A blob is used as the building block to construct the shift invariant space X, in which a function (*e.g.*, a d-dimensional image) is identified or approximated. For this purpose, two ingredients must be specified: 1) a blob ϕ or a family of blobs $\{\psi_j\}_{j \in \mathbf{Z}}$; 2) the lattice(s) on which the blobs are translated. In all cases, we will note X the closure in $L^2(\mathbb{R}^d)$ of the resulted shift invariant space. Two models are studied in the next.

Shift invariant space by a single blob In this model X is generated by translating a blob $\phi(x)$ on a d-dimensional hexagonal lattice $\mathcal{L}$, then any $f \in X$ can be written as:

$$f(x) = \sum_{k \in \mathbf{Z}^d} f_k \phi(x - x_k) \tag{5.11}$$

with x_k the k-th node of the lattice.

Tight frame by a multiscale blobs system In this model X is spanned by the shift invariant spaces X_j generated individually by a blob ψ_j on a d-dimensional hexagonal lattice $\mathcal{L}_j$. A function $f \in X$ can be written as:

$$f(x) = \sum_{j \in \mathbf{Z}} \sum_{k \in \mathbf{Z}^d} f_{j,k} \psi_j(x - x_k^j) \tag{5.12}$$

with x_k^j the k-th node of the lattice $\mathcal{L}_j$. We will show that (5.12) can be a tight frame under conditions on the family $\{\psi_j\}_{j \in \mathbf{Z}}$.

There are some important questions concerning the representation (5.11) and (5.12): 1) the approximation property of the space X *vis-à-vis* the choice(s) of blob(s); 2) the equivalent characterization of $f \in X$ by the coefficient sequences $\{f_k\}$, or $\{f_{j,k}\}$.

Before answering these questions in section 5.3 and section 5.4, we justify the use of the hexagonal lattice for generating the shift invariant spaces, and outline some remarkable properties of the blob image models.

5.2.1 Hexagonal lattice for blob image

Let $G = [g_1, \dots g_d]$ the invertible matrix formed by the independent vectors $g_1, \dots g_d \in \mathbb{R}^d$. We define the *lattice* $\mathcal{L}$ as a collection of nodes:

$$\mathcal{L} \triangleq \{x_k = Gk, k \in \mathbb{Z}^d\} \tag{5.13}$$

Let $G^{-\top}$ denotes the transpose of G^{-1}, and we define the *dual lattice* of $\mathcal{L}$:

$$\mathcal{L}^* \triangleq \{\omega_k = G^{-\top}k, k \in \mathbb{Z}^d\} \tag{5.14}$$

Definition 5.2.1 (Fundamental domain)**.** A *fundamental domain* associated to a lattice $\mathcal{L}$ is a region of $\mathbb{R}^d$, whose translations on nodes of the lattice produce a partition of $\mathbb{R}^d$.

Definition 5.2.2 ($\mathcal{L}$-periodicity)**.** A $L^1_{loc}(\mathbb{R}^d)$ function $f(x)$ is said $\mathcal{L}$-periodic if $f(x + x_k) = f(x), \forall x_k \in \mathcal{L}$. Then the integral of f on any fundamental domain is the same.

We will use the hexagonal lattice to place the blobs and span the shift invariant space. This lattice is generated by vectors of the same length, which form $\pi/3$ angle between each pair of them[2]. Compared to the widely used Cartesian lattice for pixel image, the hexagonal lattice has many interesting properties[102, 103]. It is the optimal lattice in packing spherical objects in both 2D and 3D [104] for that it achieves the highest packing density. Particularly, for recovering a 2D band-limited function, the hexagonal lattice requires a lower sampling density than the Cartesian one, that we give a brief explanation here.

Sampling efficiency of hexagonal lattice Consider a 2D band-limited function f whose frequency is supported inside a disk Ω of diameter 1. In order to reconstruct f from its samples on an arbitrary lattice $\mathcal{L}$, a sufficient condition is to include Ω in one of the fundamental domain of $\mathcal{L}^*$. For a 2D Cartesian lattice generated by $G = hI$, with I the identity matrix and h the *sampling step*, this implies that $h \leq 1$. While for an hexagonal lattice generated by the matrix $G = h[g_1, g_2]$, with the unitary vectors $g_1 = [1, 0]^\top, g_2 = [1/2, \sqrt{3}/2]^\top$, we can take the minimal hexagon including Ω as the

[2] In 3D it is also called the *Face Centered Cubic structure*, or the *Cubic Close Parking structure* in the crystallography literature.

fundamental domain of $\mathcal{L}^*$, therefore it's sufficient to take the sampling step $h \leq 2/\sqrt{3}$. Defining the lattice density as $|\det G|^{-1}$, we see that the hexagonal lattice density is about 86.6% of the Cartesian one.

5.2.2 Properties of blob representation

The reconstruction problem now amounts to identify a function (or finding a good approximation) in X. Due to the smoothness of blob and the use of hexagonal lattice, the shift invariant space X spanned by blob generally provides better image visual quality, compared with the piecewise constant space spanned by pixel. We list here some important theoretical advantages and refer the reader to the numerical experiments in Chapter 8 for more intuitive comparisons between blob and pixel reconstructions.

5.2.2.1 Efficient evaluation of linear operator

Formally speaking, any linear operator A on a function of form 5.11 (and also (5.12)) is reduced to the operations on individual blobs, namely:

$$Af = \sum_k f_k(A\phi_k) \tag{5.15}$$

where $\phi_k(x) = \phi(x - x_k)$. As already pointed out in Chapter 2.3, applying a "spatially localized" linear operator A on the localized blob is computationally efficient. In case that A enjoys some form of translation invariance, as those implicated in our reconstruction algorithm, then the expression (5.15) clearly suggests a parallel implementation.

Blob-driven X-ray projector Remark that on the k-th blob the X-ray transform can be expressed as:

$$\mathcal{P}_\theta \phi_k(y) = \mathcal{P}_\theta \phi(y - \Pi_{\theta^\perp} x_k) = \mathcal{A}b_\phi(\|y - \Pi_{\theta^\perp} x_k\|) \tag{5.16}$$

where $\Pi_{\theta^\perp} x \triangleq x - \langle x, \theta \rangle \theta$ is the orthogonal projection of x onto $\theta^\perp$. On a blob function (5.16) can be evaluated using the analytical expression of $\mathcal{A}b_\phi$, which is a cheap operation for the Gaussian family blobs[3]. This nice property is used to implement an efficient X-ray projector, see Annexe A for details.

[3]The computation can still be expensive on the Diff-Gaussian blob which has an asymptotic expression, see section 5.4.2

Blob-driven interpolator The interpolation operator consists in evaluating the value related to the function f of (5.11) or (5.12) on a discrete set of positions. Examples include the re-sampling of f on a Cartesian lattice for screen display, or the discrete gradient implicated in the edge-preserving reconstruction (c.f. Chapter 3). Let $\mathcal{L}'$ be the "interpolation lattice" which has a finite number of nodes. As the definition given in Chapter 3.2, the discrete gradient interpolator $D : X \to \mathbb{R}^{d\times|\mathcal{L}'|}$ is the row concatenation of the operator D^i:

$$Df \triangleq \begin{pmatrix} D^1 f \\ \vdots \\ D^d f \end{pmatrix} \in \mathbb{R}^{d\times|\mathcal{L}'|}$$

where $D^i : X \to \mathbb{R}^{|\mathcal{L}'|}$ yields the i-th directional derivative of f taken on the lattice $\mathcal{L}'$:

$$(D^i f)_n \triangleq \partial_i f(x'_n) = \sum_k f_k \partial_i \phi(x'_n - x_k) \tag{5.17}$$

with x'_n the n-th node of $\mathcal{L}'$. As the case of X-ray projector, (5.17) can be evaluated by using the analytical expression of $\partial_i \phi$. For example, on a Gaussian blob image with the blob given by eq. (5.4), we have the expression:

$$(D^i f)_n = -2\alpha \sum_k f_k \exp(-\alpha\|x'_n - x_k\|^2)(x'_{n,i} - x_{k,i})$$

The parallelization of this operator on GPU is trivial.

5.2.2.2 Control of bandwidth and suppression of ghosts

Taking the Fourier transform on 5.11:

$$\hat{f}(\omega) = \hat{\phi}(\omega) \sum_{k\in\mathbf{Z}^d} f_k \exp(-2\pi i\langle x_k, \omega\rangle), \tag{5.18}$$

we see that $\hat{\phi}(\omega)$ acts as a filter selecting the essential bandwidth of final reconstruction f, which is bounded by the bandwidth of the projection data, due to the Projections Slice Theorem. By limiting the bandwidth of the solution space X, one truncates the singular value system of X-ray transform [2] by keeping only the low frequency components, and improve in this way the conditioning of system. On the contrary, working with a bandwidth higher than necessary, one brings into the solution the kernel space of X-ray transform, which consists of high frequency functions called *ghosts* [105]. Roughly speaking, these functions contribute little to the visual quality of image, while "deteriorate" the conditioning of the linear system.

For the efficiency of the iterative reconstruction algorithm, it's important to choose a representation basis which can control the reconstruction bandwidth therefore suppress the ghost, while without damaging the image quality. The pixel basis (2.18) is less favorable than blob in this regard. In fact, its slow decay in the frequency domain requires an enlarged sampling step h of the Cartesian lattice to limit the essential bandwidth and suppress the ghosts. Meanwhile, this will considerably affect the reconstruction quality. A result of this flavor is given in the following lemma.

Lemma 5.2.1 (Approximation in H^1 by pixel basis)**.** *Let $f \in H^1([0,1]^d)$ be differentiable, and f_h be the orthogonal projection of f in the shift invariant space X_h spanned by the pixel basis $\phi(x) \triangleq h^{-d/2}\mathbb{1}_{[0,1]^d}(x/h)$. Then the L^2 approximation error $\|f - f_h\|$ decays as $O(h)$.*

Proof. Omitted. □

Although there is no theoretical evidence in our knowledge showing that the Gaussian blob provides better approximation than pixel for the $L^2(\Omega)$ functions, we have observed that as the sampling step h increases, the degradation in the reconstruction quality using blob is much less visible compared with pixel. See the numerical experiments presented in Chapter 7.

5.3 Shift invariant space generated by a single Gaussian blob

This section is dedicated to the shift invariant space X of type (5.11), spanned by a single Gaussian blob translated on an hexagonal lattice. In particular, we want to know the stability of this representation, as well as the approximation property of X in $L^2(\mathbb{R}^d)$. Our approach consists in establishing first the results which holds for general choice of basis function, then fit them to the Gaussian blob.

5.3.1 Stability of blob representation

In order to have a stable representation system, we require $\{\phi(x - x_k)\}$ to be a Riesz basis of X, which means that there exist constants $0 < A \leq B < \infty$ such that:

$$A\sum_k |f_k|^2 \leq \|f\|^2 \leq B\sum_k |f_k|^2, \text{ for any } f \in X \tag{5.19}$$

Proposition 5.3.1. *$\{\phi(x - x_k)\}$ is a Riesz basis of X for bounds $0 < A \leq B < \infty$ if and only if for a fundamental domain Γ of $\mathcal{L}^*$:*

$$|\det G|A \leq \sum_{k\in\mathbf{Z}^d} |\hat{\phi}(\omega + G^{-\top}k)|^2 \leq |\det G|B, \ \omega \in \Gamma \ a.e. \tag{5.20}$$

Proof. Let $\{f_k\}_k \in \ell^{2^2}(\mathbb{Z}^d)$, $f_d(x) = \sum_k f_k\delta(x - x_k)$, and $f(x) = f_d * \phi(x) = \sum_k f_k\phi(x - x_k)$. Since $\hat{f}_d(\omega) = \sum_k f_k \exp(-2\pi i\langle x_k, \omega\rangle)$ is $\mathcal{L}^*$-periodic, we can write:

$$\|\hat{f}\|^2 \ = \int_{\mathbb{R}^d} |\hat{\phi}(\omega)|^2|\hat{f}_d(\omega)|^2 d\omega = \int_\Gamma \sum_k |\hat{\phi}(\omega + G^{-\top}k)|^2|\hat{f}_d(\omega)|^2 d\omega \tag{5.21}$$

Remark that $\{|\det G|^{1/2} \exp(-2\pi i\langle x_k, \cdot\rangle)\}_k$ is an orthonormal system on $L^2(\Gamma)$, therefore $\sum_k |f_k|^2 = |\det G|\|\hat{f}_d\|^2_{L^2(\Gamma)}$. Then the Riesz basis condition (5.19) follows from (5.20); (5.19) implies also (5.20) since $\hat{f}_d(\omega)$ can be arbitrary. □

Using Proposition 5.3.1 we establish the following result for the Gaussian blob:

Proposition 5.3.2. *The translation of Gaussian blob $\{\phi(x - x_k)\}$ on an hexagonal lattice is a Riesz basis of the spanned shift invariant space.*

Proof. The Gaussian blob $\phi(x)$ is defined as in (5.4). We can take $\alpha = \pi^2$ without loss of generality. Then using the Proposition 5.3.1, we need to bound

$$F(\omega) \triangleq \sum_{k\in\mathbf{Z}^d} \exp(-\|\omega + G^{-\top}k\|^2)$$

by two constants $0 < A \leq B < \infty$ on the lozenge region $\{G^{-\top}x | x \in [0, 1)^d\}$. Let $\omega = G^{-\top}\omega_0$, with $\omega_0 \in [0, 1)^d$. Since G is invertible, there exists constants $0 < c_1 \leq c_2 < \infty$ such that

$$c_1\|\omega_0 + k\|^2 \leq \|G^{-\top}(\omega_0 + k)\|^2 \leq c_2\|\omega_0 + k\|^2$$

Therefore

$$\sum_{k\in\mathbf{Z}^d} \exp(-c_2\|\omega_0 + k\|^2) \leq F(\omega) \leq \sum_{k\in\mathbf{Z}^d} \exp(-c_1\|\omega_0 + k\|^2)$$

The conclusion now follows by using a simple property of Gaussian function. For any $\alpha > 0$, there exists constants $0 < C_1 < C_2$ such that for any $t \in [0, 1)^d$:

$$C_1 \int_{\mathbb{R}^d} e^{-\alpha\|x\|^2} dx \leq \sum_{k\in\mathbf{Z}^d} e^{-\alpha\|k+t\|^2} \leq C_2 \int_{\mathbb{R}^d} e^{-\alpha\|x\|^2} dx \tag{5.22}$$

□

5.3.2 Density of X in $L^2(\mathbb{R}^d)$

We will need the function $\sum_{k\in\mathbf{Z}^d}|\hat{\phi}(\omega+G^{-\top}k)|^2$ to be continuous on ω. For this purpose, let's make two assumptions on $\hat{\phi}$. Firstly,

$$\int_{\|\omega\|_\infty>R}|\hat{\phi}(\omega)|^2d\omega = O(R^{-p}),\ \text{for some } p>0 \tag{5.23}$$

which holds if $\hat{\phi}(\omega)$ decays like $O(\|\omega\|^{-q})$ for some $q > d/2$. Secondly, there exists a constant $p' > d$ and $C > 0$ such that for $\|x\|$ large,

$$|\hat{\phi}(x+y)-\hat{\phi}(x)| \le C\|x\|^{-p'}\|y\|,\ \forall y\in\mathbb{R}^d \tag{5.24}$$

Particularly, this condition will hold if $\|\nabla\hat{\phi}(\omega)\|$ decays as $O(\|\omega\|^{-p'})$.

Lemma 5.3.3. *Let $\{\phi(x-x_k)\}$ be a Riesz basis of X. Under the condition (5.23) and (5.24), the function $\sum_{k\in\mathbf{Z}^d}|\hat{\phi}(\omega+G^{-\top}k)|^2$ is continuous on ω.*

Proof. We only have to prove the continuity on the fundamental domain $\Gamma = \{G^{-\top}x|x\in[0,1]^d\}$. Let's define $h_N(\omega) \triangleq \sum_{\|k\|_\infty\le N}|\hat{\phi}(\omega+G^{-\top}k)|^2$, which is clearly continuous. Since $\{\phi(x-x_k)\}$ is a Riesz basis and by (5.20), $h_N(\omega)$ converges almost everywhere. For any $\omega\in\Gamma$, we note $\omega_0 = G^\top\omega\in[0,1]^d$. On the one hand, since $\hat{\phi}$ is a bounded function, we have

$$\begin{aligned}&\sum_{\|k\|_\infty\ge N+1}|\hat{\phi}(G^{-\top}(\omega_0+k))|^2 - \int_{\|x\|_\infty\ge N+1}|\hat{\phi}(G^{-\top}(\omega_0+x))|^2dx\\ &\le C_0\sum_{\|k\|_\infty\ge N+1}\int_{x\in[0,1]^d}|\hat{\phi}(G^{-\top}(k+\omega_0+x))-\hat{\phi}(G^{-\top}(k+\omega_0))|dx\end{aligned}$$

Using the condition (5.24), this is bounded by

$$C_1\sum_{\|k\|_\infty\ge N+1}\frac{1}{\|k+\omega_0\|_\infty^{p'}} \le C_1\sum_{\|k\|_\infty\ge N}\frac{1}{\|k\|_\infty^{p'}} \le C_2\sum_{n\ge N}n^{d-1-p'}$$

which tends to 0 with N. And on the other hand, by the condition (5.23),

$$\int_{\|x\|_\infty\ge N+1}|\hat{\phi}(G^{-\top}(\omega_0+x))|^2dx \le C_3\int_{\|x\|_\infty\ge C_4N}|\hat{\phi}(x)|^2dx = O(N^{-p})$$

All the constants $C_0,\dots,C_4$ appeared in above expressions depend only on G and d. By putting these two parts together, finally we've proved that for N large, the series $\sum_{\|k\|_\infty\ge N+1}|\hat{\phi}(G^{-\top}(\omega_0+k))|^2$ can be uniformly bounded by any small value, therefore $h_N(\omega)$ converges uniformly and the limit is continuous. □

Admissible basis function When representing a function f in the form of (5.11), we make the the following restrictions on the basis function ϕ:

$$\begin{cases} \hat{\phi}(0) \neq 0 \\ \{\phi(x - x_k)\}_k \text{ is a Riesz basis of } X. \\ (5.23) \text{ and } (5.24) \text{ hold.} \end{cases} \tag{5.25}$$

Clearly, if we take ϕ as the Gaussian blob and X as the shift invariant space generated on an hexagonal lattice, then the conditions in (5.25) are fulfilled.

Sampling step h One can improve the resolution of the representation system by modifying the lattice sampling step h and dilating proportionally the basis function. We note $h > 0$ the sampling step, $\phi_h(x) = h^{-d/2}\phi(x/h)$ the dilated basis function, $\mathcal{L}_h$ the lattice generated by matrix hG and Γ_h a fundamental domain of $\mathcal{L}_h^*$. The corresponding shift invariant space now reads:

$$X_h = \text{Span}\{\phi_h(x - y_k), k \in \mathbb{Z}^d\}, \text{ with } y_k = hGk \tag{5.26}$$

Then a natural question arises about whether X_h is dense in $L^2(\mathbb{R}^d)$ as h goes to 0. We remark that the general problem about the density and the approximation order of a shift invariant space is studied under the Strang-Fix theory [106] [107]. In the following we give an answer to this question using some basic techniques.

Proposition 5.3.4. *As $h \to 0$, the shift invariant space X_h generated by an admissible basis function of type (5.25) is dense in $L^2(\mathbb{R}^d)$ if and only if:*

$$|\hat{\phi}(G^{-\top}k)| = 0, \ \forall k \in \mathbb{Z}^d, k \neq 0 \tag{5.27}$$

That is, $\hat{\phi}(\omega)$ vanishes on all non zero nodes of the dual lattice.

Proof. Without loss of generality, we suppose $\hat{\phi}(0) = 1$. Let's first prove that(5.27) is a sufficient condition. Given $f \in L^2(\mathbb{R}^d)$, we will show that by taking the function

$$g(x) \triangleq h^{-d/2} \sum_k g_k \phi_h(x - y_k),$$

the error $\|\hat{f} - \hat{g}\|_{L^2(\mathbb{R}^d)}$ can be arbitrarily reduced as h tends to 0. For this, let's define $g_d \triangleq \sum_k g_k \delta(x - y_k)$. Then $g(x) = h^{-d/2} g_d * \phi_h(x)$, and its Fourier transform $\hat{g}(\omega) = \hat{\phi}(h\omega)\hat{g}_d(\omega)$. Remark that $\hat{g}_d(\omega)$ is $\mathcal{L}_h^*$-periodic, and we can always choose

coefficients $\{g_k\}$ such that $\hat{g}_d(\omega) = \hat{f}(\omega)$ a.e. on the fundamental domain

$$\Gamma_h = \{h^{-1}G^{-\top}\omega, \omega \in [0,1]^d\}.$$

By introducing $h' > h > 0$, we pose $\|\hat{f} - \hat{g}\|^2 = I_1 + I_2 + I_3$, with:

$$\begin{aligned}
I_1 &= \int_{\Gamma_{h'}} |\hat{f}(\omega) - \hat{\phi}(h\omega)\hat{g}_d(\omega)|^2 d\omega = \int_{\Gamma_{h'}} |\hat{f}(\omega)(1 - \hat{\phi}(h\omega))|^2 d\omega \\
I_2 &= \int_{\Gamma_h \setminus \Gamma_{h'}} |\hat{f}(\omega) - \hat{\phi}(h\omega)\hat{g}_d(\omega)|^2 d\omega = \int_{\Gamma_h \setminus \Gamma_{h'}} |\hat{f}(\omega)(1 - \hat{\phi}(h\omega))|^2 d\omega \\
I_3 &= \int_{\complement\Gamma_h} |\hat{f}(\omega) - \hat{\phi}(h\omega)\hat{g}_d(\omega)|^2 d\omega
\end{aligned}$$

Now we will bound I_1, I_2, I_3 by arbitrary small values.
For I_2: remark that $\hat{\phi}(\omega)$ is a bounded function, thus

$$\sup_{\omega \in \mathbb{R}^d} |1 - \hat{\phi}(h\omega)|^2 \leq C_0$$

for some constant C_0, and $I_2 \leq C_0 \int_{\complement\Gamma_{h'}} |\hat{f}(\omega)|^2 d\omega$ can be arbitrarily small by taking h' small.
For I_1: since $\hat{\phi}(\omega)$ is continuous, for a fixed h' we can choose $0 < h < h'$ small enough, such that $\sup_{\omega \in \Gamma_{h'}} |1 - \hat{\phi}(h\omega)|^2 < \epsilon$ for any $\epsilon > 0$, and have $I_1 \leq \epsilon \|\hat{f}\|^2$.
For I_3: Using the triangle inequality:

$$I_3 \leq 2 \int_{\complement\Gamma_h} |\hat{f}(\omega)|^2 d\omega + 2 \int_{\complement\Gamma_h} |\hat{\phi}(h\omega)\hat{g}_d(\omega)|^2 d\omega,$$

and the first term clearly tends to 0 with h, while for the second term we use the periodicity of $\hat{g}_d$ and rewrite it as:

$$\begin{aligned}
\int_{\complement\Gamma_h} |\hat{\phi}(h\omega)\hat{g}_d(\omega)|^2 d\omega &= \int_{\Gamma_h} \sum_{k \neq 0} |\hat{\phi}(h\omega + G^{-\top}k)|^2 |\hat{g}_d(\omega)|^2 d\omega \\
&= \int_{\mathbb{R}^d} F_h(\omega) |\hat{f}(\omega)|^2 d\omega
\end{aligned}$$

with $F_h(\omega) \triangleq \mathbb{1}_{\Gamma_h}(\omega) \sum_{k \neq 0} |\hat{\phi}(h\omega + G^{-\top}k)|^2$. Using the fact that $\{\phi(x - x_k)\}$ is a Riesz basis and by Proposition 2.1, $F_h(\omega)$ is bounded almost everywhere. It's also continuous at zero by Lemma 5.3.3. So using the condition (5.27), for any $\omega \in \mathbb{R}^d$, $F_h(\omega) \to 0$ as $h \to 0$. Finally we apply the dominated convergence theorem and achieve the proof for the sufficient condition.

For the other sense, note that by triangle inequality:

$$\sqrt{I_3} \geq \left(\int_{\mathbb{R}^d} F_h(\omega)|\hat{f}(\omega)|^2 d\omega\right)^{1/2} - \left(\int_{\mathbb{C}\Gamma_h} |\hat{f}(\omega)| d\omega\right)^{1/2}$$

so the first term must goes to 0 with h. Since $F_h(\omega)|\hat{f}(\omega)|^2$ is positive and $f \in L^2(\mathbb{R}^d)$ is arbitrary, we can extract a subsequence $h_j \to 0$ such that $\lim_j F_{h_j}(\omega) \to 0$ almost everywhere. This implies $\hat{\phi}(G^{-\top}k) = 0$ for any $k \neq 0$. In fact, if there is a $k_0 \neq 0$ for which $\hat{\phi}(G^{-\top}k_0) \neq 0$, then by the continuity of $\hat{\phi}$, for any ω:

$$\lim_{j\to\infty} F_{h_j}(\omega) \geq \lim_{j\to\infty} |\hat{\phi}(h_j\omega + G^{-\top}k_0)|^2 > 0,$$

and we get a contradiction. This achieves the proof for the necessary condition. □

The proposition above is general. Let's take the 2D Cartesian lattice $G = Id$ as example to see its implication on blob ϕ. The condition (5.27) implies that the profile function $b_{\hat{\phi}}(t)$ vanishes at all non zero positions of form $t = \sqrt{m^2+n^2}, m, n \in \mathbb{N}$. Particularly, this is not the case for Gaussian blob, so the limit of the shift invariant space X_h is not dense in $L^2(\mathbb{R}^d)$, unlike the well known result for pixel basis. While this density problem doesn't seem to be a drawback in real applications: the numerical experiences in Chapter 8 confirm that the blob reconstruction, compared with the pixel one, is less sensitive to the sampling step and offers better visual quality.

Remark 5.3.1. A possible solution to have the density is to band-limit the Gaussian blob ϕ as $\mathcal{F}^{-1}(\mathbb{1}_{\{G^{-\top}x, \|x\|_\infty \leq 1/2\}}(\omega)\hat{\phi}(\omega))$, then the condition (5.27) is fulfilled. Nevertheless, this will complicate the expression of ϕ in spatial domain, and reduce the numerical efficiency of the Gaussian blob in parallel computations.

5.3.3 Limitation of the image model by Gaussian blob

Besides the density question, one might ask whether the dyadic approximation spaces $X_{2^j}, j \in \mathbb{Z}$ are nested, *i.e.*, $X_{2^{j+1}} \subset X_{2^j}$.

Proposition 5.3.5. *For a non zero radial function $\phi(x)$, the space X_1 is not included in $X_{1/2}$ if $|\hat{\phi}(\omega)/\hat{\phi}(\omega/2)| \to 0$ as $\|\omega\| \to +\infty$.*

Proof. Suppose that $X_1 \subset X_{1/2}$, then we can write $\phi(x) = \sum_k f_k \phi(2x - x_k)$ for some $\{f_k\} \neq 0$. This is equivalent to $\hat{\phi}(\omega) = \hat{\phi}(\omega/2)\hat{g}(\omega)$, with $\hat{g}(\omega) = 2^{-d}\sum_k f_k \exp(-2\pi i\langle\omega, x_k/2\rangle)$. Remark that $\hat{g}$ is a periodic function, and on the same time $\hat{g}(\omega)$ is radial and tends to 0 as $\|\omega\| \to \infty$. Thus we must have $\hat{g}(\omega) \equiv 0$, which is in contradiction with $\{f_k\} \neq 0$. □

Applying this proposition to the Gaussian blob, the answer is again negative. In regard of these results, we conclude that one can not build a *Multiresolution Analysis* (MRA) in the sense of [108] with a single Gaussian blob. In order to overcome this theoretical limitation and build an efficient image representation model, in the next we will extend the single blob to multiscale ones. The multiscale blob system gives a redundant and compressible representation of $L^2(\mathbb{R}^d)$, which is essential to solve the incomplete data problem.

5.4 Tight frame by a multiscale blob system

We introduce the blob family $\{\psi_j(x)\}_{j\in\mathbf{Z}}$, where each $\psi_j(x)$ is a blob. Typically, this family is constituted by band-pass functions of different frequency selectivity, or a mixture of low-pass and band-pass ones. The scalar products between $L^2(\mathbb{R}^d)$ function f with the translations of $\psi_j(x)$ are called the *analysis coefficients* and denoted by: $\Psi f(x,j) \triangleq \langle f(\cdot), \psi_j(\cdot - x)\rangle$.

Partition of unity In order to synthesize f from its analysis coefficients, we will require the *partition of unity* (PU) property on the blob family $\{\psi_j(x)\}$, which is expressed as:

$$\sum_j |\hat{\psi}_j(\omega)|^2 = \sum_j b_{\hat{\psi}_j}(\|\omega\|)^2 = c_0, \text{ for a.e. } \omega \in \mathbb{R}^d, \tag{5.28}$$

for some constant $c_0 > 0$.

Theorem 5.4.1 (Chapter 5, [14])**.** *Suppose that the PU property holds for $\{\psi_j\}_{j\in\mathbf{Z}}$. Then one can use the analysis coefficients to synthesize f as following:*

$$f(x) = c_0^{-1} \sum_j \Psi f(\cdot, j) * \psi_j(x) \tag{5.29}$$

A direct application of this theorem is difficult since the analysis coefficient $\Psi f(\cdot, j)$ here is defined on the continuous domain $\mathbb{R}^d$. To make (5.29) numerically feasible, we will build a discrete *tight frame* by sampling $\Psi f(\cdot, j)$. The following lemma will be useful:

Lemma 5.4.2. *Let $f \in L^2(\mathbb{R}^d)$ and G an invertible matrix. The Fourier transform of function $f_d(x) \triangleq \sum_{k\in\mathbf{Z}^d} f(Gk)\delta(x - Gk)$ reads:*

$$\hat{f}_d(\omega) = |\det G|^{-1} \sum_{k\in\mathbf{Z}^d} \hat{f}(\omega - G^{-\top}k) \tag{5.30}$$

Proof. Omitted. □

Sampling condition for a tight frame Now let $\mathcal{L}_j$ be a lattice generated by matrix G_j, and we translate $\psi_j(x)$ on $\mathcal{L}_j$ to obtain:

$$\psi_{j,k}(x) \triangleq |\det G_j|^{1/2}\psi_j(x - x_k^j), \quad \text{with } x_k^j = G_j k \tag{5.31}$$

The next proposition provides a simple way to make $\{\psi_{j,k}(x)\}$ a tight frame.

Proposition 5.4.3. *Suppose that for all $j \in \mathbb{Z}$, the following conditions hold:*

1. *ψ_j are band-limited functions satisfying (5.28) with $c_0 = 1$,*
2. *The support of $\hat{\psi}_j$ is included in a fundamental domain Γ_j of the dual lattice $\mathcal{L}_j^*$.*

Then the set $\{\psi_{j,k}(x)\}_{j\in\mathbf{Z},k\in\mathbf{Z}^d}$ constitutes a tight frame of $L^2(\mathbb{R}^d)$:

$$f(x) = \sum_{j\in\mathbf{Z}}\sum_{k\in\mathbf{Z}^d} \langle f, \psi_{j,k}\rangle \psi_{j,k}(x), \ \forall f \in L^2(\mathbb{R}^d) \tag{5.32}$$

Proof. We define the sampled function of continuous coefficients:

$$\Psi_d(x, j) \triangleq \sum_{k\in\mathbf{Z}^d} \Psi f(G_j k, j)\delta(x - G_j k), \tag{5.33}$$

and the reconstruction: $g(x) = \sum_j \Psi_d(\cdot, j) * \psi_j(x)|\det G_j|$. Then by lemma 5.4.2:

$$\begin{aligned}\hat{g}(\omega) &= \sum_j \widehat{\Psi_d}(\omega, j)\hat{\psi}_j(\omega)|\det G_j| \\ &= \sum_j \hat{\psi}_j(\omega) \sum_{k\in\mathbf{Z}^d} \hat{f}(\omega - G_j^{-\top}k)\hat{\psi}_j^*(\omega - G_j^{-\top}k)\end{aligned}$$

Since ψ_j is band-limited and $\operatorname{supp}\hat{\psi}_j \subset \Gamma_j$, no aliasing is introduced in the sum above, therefore: $\hat{g}(\omega) = \sum_j |\hat{\psi}_j(\omega)|^2 \hat{f}(\omega) = \hat{f}(\omega)$, using the partition of unity property. This proves that $\{\psi_{j,k}(x)\}_{j,k}$ constitutes a tight frame of $L^2(\mathbb{R}^d)$. □

Taking the solution space $X = L^2(\mathbb{R}^d)$, the above proposition says that any function $f \in X$ can be synthesized from a $\ell^2(\mathbb{Z})$ sequence $\{f_{j,k}\}$:

$$f(x) = \sum_{j\in\mathbf{Z}}\sum_{k\in\mathbf{Z}^d} f_{j,k}\psi_{j,k}(x) \tag{5.34}$$

The question remains to known if the system $\{\psi_{j,k}(x)\}$ can give a sparse or compressible representation, for the typical images encountered in CT applications. Since this system is generally redundant, there are infinite ways to represent f, and we will seek the sparsest representation from all $\{f_{j,k}\}$ satisfying (5.34) through the algorithm such as

the ℓ_1 minimization or the greedy algorithm discussed in precedent chapter. By the tight frame property of $\{\psi_{j,k}\}$, it suffices now to choose the ψ_j in such a way that the analysis coefficients $\langle f, \psi_{j,k}\rangle$ have a fast decay, in order to guarantee the existence of a sparse solution of the ℓ^1 solver.

5.4.1 Construction of multiscale blob system

The construction proposed here follows the same line as the classical Wavelet theory. It consists in three steps:

1. We choose first a band-limited *mother blob* $\psi(x)$ which has $n > 0$ vanishing moments, *i.e.*, $\psi(x)$ is orthogonal to any d-variables polynomial of order less than n. This means that for any positive indexes $0 \leq k_1 + \cdots + k_d < n$:

$$\int_{\mathbb{R}^d} \psi(x) x^k dx = 0, \text{ with } x^k \triangleq x_1^{k_1} \cdots x_d^{k_d} \tag{5.35}$$

$$\text{or when } \hat{\psi}(\omega) \text{ is smooth, } \partial_1^{k_1} \cdots \partial_d^{k_d} \hat{\psi}(0) = 0 \tag{5.36}$$

   We generate also the lattice $\mathcal{L}_0$ from a matrix G_0, such that $\operatorname{supp} \hat{\psi}$ is supported in a fundamental domain of the dual lattice $\mathcal{L}_0^*$.

2. From such a $\psi(x)$, we define the family $\{\psi_j(x)\}_{j \in \mathbf{Z}}$ as

$$\psi_j(x) = \beta^{-jd} \psi(\beta^{-j} x) \tag{5.37}$$

   with the $\beta > 1$ the dilation parameter carefully chosen to fulfill the partition of unity (5.28). As the index j decreases, the shift invariant space generated by ψ_j represents higher frequency information, and we call them *fine scale*.

3. We translate each $\psi_j(x)$ on an individual hexagonal lattice $\mathcal{L}_j$, which is generated from the matrix $G_j = \beta^j G_0$. Then the sampling condition of Proposition 5.4.3 is fulfilled and the resulting system $\{\psi_{j,k}(x)\}$ is then a tight frame.

We name this construction the *multiscale blob system*.

Vanishing moments One may wish that the condition (5.36) has an equivalence on the profile function of $b_{\hat{\psi}}$, which would be easier to verify. We establish an intermediate result in this direction:

Lemma 5.4.4. *Define $\psi(x) = b(\|x\|)$, with $b : \mathbb{R} \to \mathbb{R}_+$ which is even, $C^n(\mathbb{R})$ smooth and $b^{(k)}(0) = 0$ for $k = 0, 1, \dots n$. Note ∂_i^k the i-th partial derivative of order k. Then:*

$$\partial_i^k \psi(0) = 0, \quad \text{for } k = 0, 1, \dots n$$

Proof. We note $N(x) = \|x\|$. Remark that for $x \neq 0$ and $k \leq n$, $\partial_i^k \psi(x)$ is well defined and given by the Faà di Bruno formula:

$$\partial_i^k \psi(x) = \sum_{P \in \mathbf{P}_k} b^{(|P|)}(\|x\|) \prod_{p \in P} \partial_i^{|p|} N(x) \tag{5.38}$$

Here $\mathbf{P}_k$ denotes all possible partitions of the set $\{1, 2, \dots k\}$. $P \in \mathbf{P}_k$ is one such partition, and $|P|$ is the number of disjoint "pieces". $p \in P$ is then a "piece" (a subset of $\{1, 2, \dots k\}$), and $|p| > 0$ is the size of p.

Clearly we have $\psi(0) = 0$. Now suppose that $\partial_i^k \psi(0) = 0$. We calculate the derivative in direction i of $\partial_i^k \psi$ taken at 0. For this, remark that for $t > 0$:

$$\partial_i^k \psi(te_i) = \sum_{P \in \mathbf{P}_k} b^{(|P|)}(t) \prod_{p \in P} \partial_i^{|p|} N(te_i) = b^{(k)}(t)$$

The last equality above comes from the simple fact that, for $t > 0$:

$$\partial_i^m N(te_i) = \begin{cases} 1 & \text{for } m = 1 \\ 0 & \text{for } m > 1 \end{cases}$$

Then by definition:

$$\partial_i^{k+1} \psi(0) = \lim_{t \to 0^+} \frac{\partial_i^k \psi(te_i) - \partial_i^k \psi(0)}{t} = b^{(k+1)}(0) = 0$$

where we have used the hypothesis $\partial_i^k \psi(0) = 0$. The conclusion now follows by induction. □

Based on this lemma we conjecture the following result, which provides a sufficient condition on the vanishing moments of the blob ψ from the $b_{\hat{\psi}}$.

Conjecture 5.4.1 (Vanishing moments)**.** If ${b_{\hat{\psi}}}^{(m)}(0) = 0$ for $m = 0 \dots n-1$, then:

$$\partial^k \hat{\psi}(0) = 0$$

for all multi-index k such that $|k| < n$. In other words, the blob ψ has n vanishing moments.

Decaying rate of the blob coefficients Given a function f, the decaying rate of its blob coefficients will depend on the vanishing moment of ψ, and also on the smoothness of f. If f is $n-1$ order piecewise polynomial, then (5.35) implies that the blob $\psi_{j,k}$ located inside a polynomial region has its analysis coefficients $|\langle f, \psi_{j,k}\rangle|$ decaying at the rate $O(\beta^{nj})$ [14], and at fine scales only those located near the discontinuities of f have significant non zero coefficients.

Two concrete examples of multiscale blob system are given in sections 5.4.2 and 5.4.3. We emphasize here that none of them fulfils the sampling condition of the Proposition 5.4.3, since their mother blobs ψ are not band-limited, therefore they cannot be claimed as tight-frame. Nevertheless, in the numerical applications we can treat them safely as band-limited function, due to the exponential decay of $\hat{\psi}$ in these two examples.

5.4.2 Diff-Gaussian blob

From the Gaussian blob $\phi(x)$ (5.4), we define $\psi(x)$ in the frequency domain as:

$$\begin{aligned} |\hat{\psi}(\omega)|^2 &= \hat{\phi}(\omega/2) - \hat{\phi}(\omega) \\ &= (\pi/\alpha)^{d/2}(e^{-\pi^2\|\omega\|^2/(4\alpha)} - e^{-\pi^2\|\omega\|^2/\alpha}) \end{aligned} \tag{5.39}$$

A close form expression of $\psi(x)$ is difficult to find. Nevertheless, it's possible to establish the asymptotic expansion, with the aid of the following lemma:

Lemma 5.4.5. *The mono-dimensional function*

$$f(t) \triangleq (\exp(-at^2) - \exp(-bt^2))^{1/2}, \quad \textit{for } 0 < a < b \tag{5.40}$$

has the asymptotic expansion:

$$f(t) = \sum_{k=0}^{\infty} C_k \exp(-(kb - ka + a/2)t^2), \quad \textit{with } C_k = \frac{(2k)!}{4^k(k!)^2(1-2k)} \tag{5.41}$$

Proof. We take the Taylor development of $\sqrt{1-x}$ around 0: $\sum_{k\geq 0} C_k x^k$, with the coefficient C_k given by:

$$C_k = \frac{2^{-k}}{(1-2k)k!}\prod_{m=1}^{k}(2m-1) = \frac{(2k)!}{4^k(k!)^2(1-2k)}$$

(5.41) now follows by rewriting $f(t)$ as: $f(t) = e^{-at^2/2}\sqrt{1-e^{(a-b)t^2}}$, and substituting x by $e^{(a-b)t^2}$ in the development. □

Applying Lemma 5.4.5 on $\hat{\psi}$ defined in (5.39) gives:

$$\hat{\psi}(\omega) = (\pi/\alpha)^{d/4} \sum_{k\geq 0} C_k \exp\left(-\frac{3k+1/2}{4\alpha}\pi^2\|\omega\|^2\right) \tag{5.42}$$

The expression of ψ in spatial domain now follows easily:

Proposition 5.4.6 (Diff-Gaussian blob)**.** *The function $\psi(x)$ defined in (5.39) has the asymptotic expression:*

$$\psi(x) = 2^d(\pi/\alpha)^{-d/4} \sum_{k=0}^{\infty} \frac{C_k}{(3k+1/2)^{d/2}} \exp\left(-\frac{4\alpha}{3k+1/2}\|x\|^2\right) \tag{5.43}$$

The equality holds in L^2 sense.

Proof. We note $\hat{\psi}_N(\omega)$ the sum of N first terms in the series (5.42), then $\hat{\psi}_N(\omega)$ converges (uniformly) to $\hat{\psi}(\omega)$ for all ω. Remark that $\sum_{k\geq 0}|C_k| = 2$, and for all N, $\hat{\psi}_N(\omega)$ can be bounded by:

$$\hat{\psi}_N(\omega) \leq C\exp(-\pi^2\|\omega\|^2/(8\alpha)) \in L^2(\mathbb{R}^d)$$

with $C > 0$ a constant. Applying the Dominated Convergence Theorem (the L^2 version), we see that $\hat{\psi}_N(\omega)$ converges to $\hat{\psi}(\omega)$ in $L^2(\mathbb{R}^d)$. Now taking the Fourier transform term by term on $\hat{\psi}(\omega)$ and we obtain (5.43).

□

From $\psi(x)$ the blob family is defined as

$$\psi_j(x) = 2^{-jd}\psi(2^{-j}x) \tag{5.44}$$

then $\hat{\psi}_j(\omega) = \hat{\psi}(2^j\omega)$. Remark that by construction,

$$\begin{aligned}\sum_{j=-S}^{S}|\hat{\psi}_j(\omega)|^2 &= \sum_{j=-S}^{S}\hat{\phi}(2^{j-1}\omega) - \hat{\phi}(2^j\omega)\\ &= \hat{\phi}(2^{-(S+1)}\omega) - \hat{\phi}(2^S\omega)\end{aligned}$$

Now by letting $S \to \infty$, we see that the PU property (5.28) is fulfilled by this family:

$$\sum_{j\in\mathbf{Z}}|\hat{\psi}_j(\omega)|^2 = \hat{\phi}(0) - \hat{\phi}(\infty) = (\pi/\alpha)^{d/2}$$

We name (5.43) the *Diff-Gaussian* blob. Constructed in this way, ψ has one vanishing moment. Figure 5.1 shows the 2D Diff-Gaussian blob $\psi(x)$ with $\alpha = 1$.

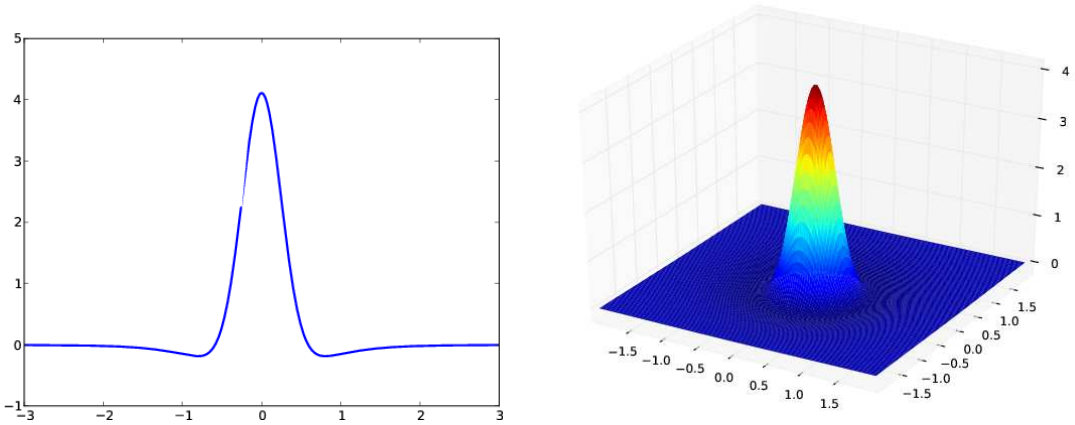

(a) 2D Diff-Gaussian blob profile

(b) 2D Diff-Gaussian blob

FIGURE 5.1: 2D Diff-Gaussian blob ψ with parameter $\alpha = 1$. (a): Profile function b_ψ. (b): 3D visualization.

Multiscale blob system Given a number $S > 0$, we truncate the sequence $\{\psi_j\}$ defined in (5.44) by keeping only the indexes $|j| \leq S - 1$, and modify the blob of the finest scale $-S$ to:

$$|\hat{\psi}_{-S}(\omega)|^2 = (\pi/\alpha)^{d/2} - \hat{\phi}(2^{-S}\omega) \geq 0,$$

which is a high pass blob; and modify also the blob of the coarsest scale S to:

$$|\hat{\psi}_S(\omega)|^2 = \hat{\phi}(2^{S-1}\omega),$$

which is a low pass blob. The scales $|j| > S$ of the family $\{\psi_j\}$ are dropped. With the modified system, the partition of unity property still holds:

$$\sum_{j=-S}^{S} |\hat{\psi}_j(\omega)|^2 = (\pi/\alpha)^{d/2} - \hat{\phi}(2^{-S}\omega) + \ldots + \hat{\phi}(2^{S-1}\omega) = (\pi/\alpha)^{d/2}$$

Figure 5.2 shows the frequency tiling created by $\hat{\psi}_j$ of 5 different scales. Except for the high pass blob $\hat{\psi}_{-S}$, we have spatial expressions (in asymptotic forms) for all other blobs ψ_j, which make the numerical evaluation straight forward. In practice the high pass blob is simply removed from this system, and finally we get $\{\psi_{-S+1}, \ldots, \psi_S\}$.

Remark 5.4.1. In practice it's enough to sum the first 100 terms in (5.43) for an accurate approximation: the truncation error (up to a constant factor) is bounded by $\sum_{k=100}^{\infty} |C_k|(3k + 1/2)^{-d/2}$, which is of order 10^{-6} by numerical evaluation.

Remark 5.4.2. The Difference of Gaussian (DOG) is a mother wavelet often employed in the image edge detection tasks. DOG is defined in spatial domain as the difference between a narrow and a wide Gaussian distribution (L^1-normalized), which results in

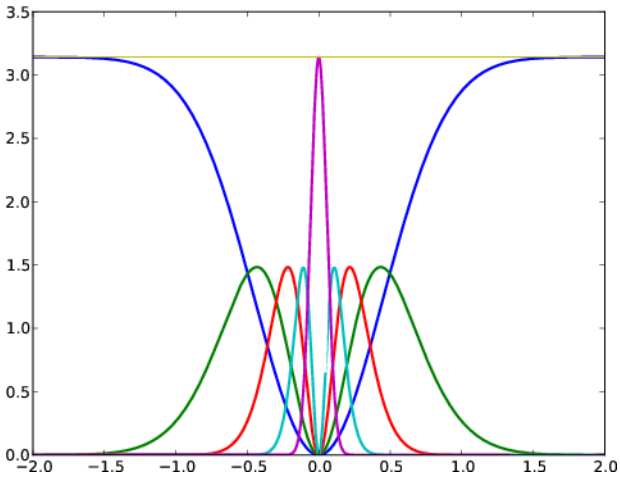

FIGURE 5.2: Multiscale Diff-Gaussian blob system: frequency tiling created by $\hat{\psi}_j(\omega)$ for $j = -2 \dots 2$.

frequency domain a band pass filter. Our Diff-Gaussian blob differs from DOG in that the difference is made in frequency domain to keep the PU property.

5.4.3 Mexican hat blob

A much easier way to build the multiscale blob system is to use the Mexican hat, *i.e.*, the second derivative of the Gaussian function, which will be named the *Mexican hat* blob. For this, we define first the profile function in frequency domain as

$$b_{\hat{\psi}}(s) = c_0 s^2 \exp(-c_1 s^2) \tag{5.45}$$

with the constant $c_0 > 0, c_1 > 0$ to be specified. Now use the Proposition 5.1.1, we only have to solve $\mathcal{A}^{d-1} b_{\hat{\psi}}(s) = \widehat{b_\psi}(s)$.

Lemma 5.4.7 (2D Mexican hat blob)**.** *We have the following 2D Fourier transform pairs:*

$$\psi(x) \triangleq (1 - \alpha\|x\|^2) \exp(-\alpha\|x\|^2) \tag{5.46}$$

$$\hat{\psi}(\omega) \triangleq \pi^3 \alpha^{-2} \|\omega\|^2 \exp(-\pi^2 \alpha^{-1} \|\omega\|^2) \tag{5.47}$$

Proof. The Abel transform of (5.45) reads:

$$\mathcal{A} b_{\hat{\psi}}(s) = c_0 \sqrt{\pi / c_1} (s^2 + (2c_1)^{-1}) \exp(-c_1 s^2)$$

Taking the 1D Fourier transform on $\mathcal{A} b_{\hat{\psi}}$ and by Proposition 5.1.1, we obtain:

$$b_\psi(t) = c_0 \pi c_1^{-2} (1 - \pi^2 t^2 / c_1) \exp(-\pi^2 / c_1 t^2)$$

The transform pair (5.46) and (5.47) now follows by setting $c_1 = \pi^2/\alpha$ and $c_0 = \pi^3/\alpha^2$. □

Lemma 5.4.8 (3D Mexican hat blob)**.** *We have the following 3D Fourier transform pairs:*

$$\psi(x) \triangleq (3\alpha(2\pi^2)^{-1} - \alpha\|x\|^2)\exp(-\alpha\|x\|^2) \tag{5.48}$$

$$\hat{\psi}(\omega) \triangleq (\pi/\alpha)^{3/2}\|\omega\|^2\exp(-\pi^2\alpha^{-1}\|\omega\|^2) \tag{5.49}$$

The Mexican hat blob has two vanishing moments. Using $\psi(x)$ and with a dilation factor $\beta > 1$, the blob family is constructed as $\psi_j(x) = \beta^{-jd}\psi(\beta^{-j}x)$. Figure 5.3 shows the 2D Mexican hat blob of the parameter $\alpha = 1$. Compared with the Diff-Gaussian blob (Figure 5.1), it can be seen that the Mexican hat blob has a better spatial localization.

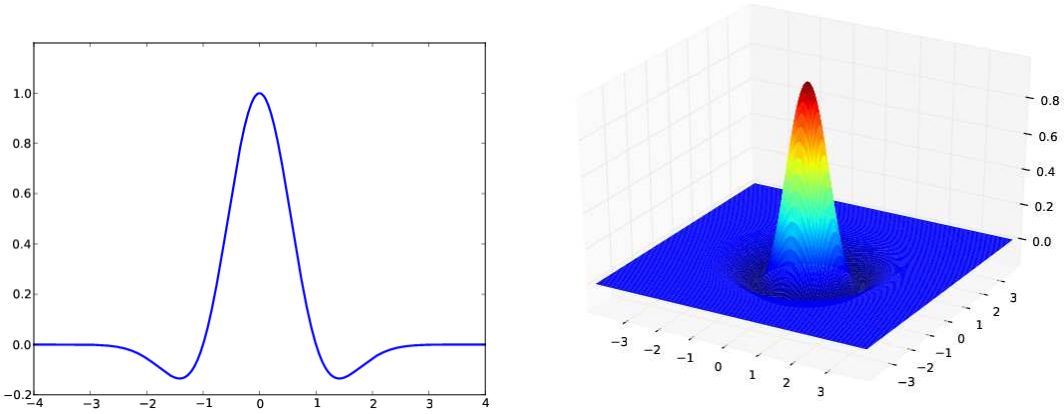

(a) 2D Mexican hat blob profile

(b) 2D Mexican hat blob

FIGURE 5.3: 2D Mexican hat blob ψ with parameter $\alpha = 1$. (a): Profile function b_ψ. (b): 3D visualization.

PU of Mexican hat blob It's a classical result that the 1D Mexican hat function constitutes a frame of $L^2(\mathbb{R})$ if some appropriate dilation and translation parameters are used [109]. In practice, the partition of unity property (5.28) can be verified through a numerical procedure. For a given dilation factor β, we evaluate numerically the maximum and the minimum value of $\sum_{j\in\mathbf{Z}} b_{\hat{\psi}_j}(\|\omega\|)^2$ on interval $[1, \beta]$, noted by v_{min}, v_{max} respectively, and calculate the error $\epsilon = (v_{max} - v_{min})/(v_{max} + v_{min})$ which reflects the deviation from a constant value. It can be observed that ϵ is bounded by 10^{-4} as long as $\beta \leq \sqrt{2}$. Remark that taking β too small yields very redundant multiscale system so reduces the numerical efficiency. The related numerical experiments in Chapter 7 and Chapter 8 are obtained with $\beta = 2$ in order to reduce the redundancy.

5.5 Parameters of blob image

The blob parameter α together with the lattice sampling step h can greatly change the image visual quality and the convergence speed of reconstruction algorithms. We provide some guidelines here on the choice of these parameters for the Gaussian blob $\phi(x) = \exp(-\alpha\|x\|^2)$. With some straightforward modifications, the arguments below apply also on the multiscale blob system. We recall that in numerical implementations the blob is truncated as $\phi(x)\mathbb{1}_{\|x\|\leq r_{cut}}$ with the radius r_{cut} as a free parameter.

Choice of blob parameter α, r_{cut} Let w_D be the essential bandwidth of the unknown function f to be reconstructed (in the sense that $|\hat{f}(\omega)|$ outside the ball of radius w_D is very small). By identifying the FWHM of $\hat{\phi}(\omega)$ as w_D: $\hat{\phi}(w_D) = \hat{\phi}(0)/2$, we deduce $\alpha = \pi^2 w_D^2 / \ln 2$. The blob radius r_{cut} is set using a cut-off error of ε, by $\phi(r_{cut}) = \varepsilon\phi(0)$. We have observed in numerical experiments that the radius r_{cut} has no visible impact on image quality, as long as the cut-off error $\varepsilon \leq 10^{-3}$.

Choice of lattice sampling step h With the parameter α fixed, it's however delicate to determine the hexagonal lattice sampling step h, due to the trade-off between the numerical efficiency and the image visual quality. Decreasing the sampling step can improve the approximation quality of the shift-invariant space X, but at the price of a slower convergence rate of reconstruction algorithms, since the Riesz basis bounds deteriorate and the system becomes ill-conditioned. The criterion we take here is based on a frequency argument for the expression (5.18). Since $\hat{\phi}$ decays exponentially, we can choose a disk of radius R_{cut} on which $\hat{\phi}$ is essentially supported, in the sense that $\hat{\phi}(R_{cut}) = \hat{\varepsilon}\hat{\phi}(0)$ for a given cut-off error $\hat{\varepsilon}$. In order to reduce the aliasing error introduced by the sum in (5.18), the disk of radius R_{cut} should not contain any non zero nodes of the dual hexagonal lattice, which implies $h \leq 1/(\sqrt{3}R_{cut})$. In our numerical experiments we have used the cut-off error $\hat{\varepsilon} = 10^{-1}$. Remark that a smaller $\hat{\varepsilon}$ yields a denser lattice and reduces furthermore the aliasing artifacts caused by the sampling, at the price of a heavier computation charge.

Finally, it's easy to see that the blob size and the lattice sampling step are simultaneously determined by the user-specified reconstruction bandwidth w_D: for the bandwidth $cw_D, c > 0$, the blob cut-off radius becomes r_{cut}/c and the lattice sampling step becomes h/c. In practice, w_D can be chosen according to the detector sampling step, as a consequence of the Projections Slice Theorem.

5.6 Wavelet-Vaguelette Decomposition by blob

The *Wavelet-Vaguelette Decomposition* (WVD) is a principle proposed by Donoho [110] to substitute the classical singular value decomposition (SVD) for solving the linear inverse problem whose operator is homogeneous with respect to dilations, *e.g.*the Radon transform. Let X, Y be two Hilbert spaces and $K : X \to Y$ be an invertible compact operator, whose domain and range are respectively X and Y. We note $Kf = g$, for $f \in X, g \in Y$. The SVD of K finds two singular systems (orthonormal bases) of both X and Y such that the application of K on $f \in X$ is diagonalized with respect to these bases. Nonetheless for general function f, its energy spread with respect to the singular system rarely follows the decay rate of the singular values, consequently f cannot be efficiently represented by its decomposition coefficients. On the other side, a wavelet basis $\psi_\lambda \in X$ can provide sparse representation of f but it doesn't diagonalize K, that is:

$$\langle Kf, K\psi_\lambda \rangle \neq \langle f, \psi_\lambda \rangle \tag{5.50}$$

Wavelet-Vaguelette Decomposition Suppose that the wavelets ψ_λ are compactly supported and have sufficiently large vanishing moments. The *vaguelette* $\{\tilde{\psi}_\lambda\}, \tilde{\psi}_\lambda \in Y$ is a wavelet-like system, and is related to ψ_λ through the operator K as following:

$$\langle Kf, \tilde{\psi}_\lambda \rangle = \langle f, \psi_\lambda \rangle, \ \forall f \in X \tag{5.51}$$

Particularly, $K^* \tilde{\psi}_\lambda = \psi_\lambda$. In light of (5.51), f can be recovered by:

$$f = \sum_\lambda \langle Kf, \tilde{\psi}_\lambda \rangle \psi_\lambda \tag{5.52}$$

Therefore with the wavelet system $\{\psi_\lambda\}$ in X and the vaguelette system $\{\tilde{\psi}_\lambda\}$ in Y, the WVD offers a SVD-like diagonlization of K while at the same time retains the sparsity of the decomposition coefficients $\langle Kf, \tilde{\psi}_\lambda \rangle$. In case that the observation is corrupted by noise, *i.e.*$g = Kf + \epsilon$, one can apply the shrinkage operator on the coefficients $\langle g, \tilde{\psi}_\lambda \rangle$ in the same way as on the wavelet coefficients, and this improves considerably the classical SVD-based linear inversion method [110]. The existence of vaguelette system for some specific operators, especially the Radon transform, has been proved in [110], and its applications in tomography can be found in [111–113].

Vaguelette of the multiscale blob system Here we aim in extending the WVD paradigm to the multiscale blob system. Now let $\{\psi_{j,k}\}_{j \in \mathbf{Z}, k \in \mathbf{Z}^d}$ be a tight frame multiscale blob system constructed as in section 5.4. We need to find a vaguelette system

$\{\tilde{\psi}_{j,k}\}$ in the sinogram domain, such that

$$\mathcal{P}^*\tilde{\psi}_{j,k} = \psi_{j,k}, \text{ for all } j \in \mathbb{Z}, k \in \mathbb{Z}^d \tag{5.53}$$

Then for any function $f \in L^2(\mathbb{R}^d)$ we have $\langle f, \psi_{j,k}\rangle = \langle \mathcal{P}f, \tilde{\psi}_{j,k}\rangle$, and f can be reconstructed by:

$$f = \sum_{j\in\mathbb{Z}} \sum_{k\in\mathbb{Z}^d} \langle \mathcal{P}f, \tilde{\psi}_{j,k}\rangle \psi_{j,k} \tag{5.54}$$

Remark that the decomposition coefficients $\langle \mathcal{P}f, \tilde{\psi}_{j,k}\rangle$ has a fast decay since it's the case of $\langle f, \psi_{j,k}\rangle$, by construction of the multiscale blob system. This property provides a sinogram domain based approach for exploiting the sparsity of f that we will detail in Chapter 9. In the following we will call $\{\tilde{\psi}_{j,k}\}$ the *vaguelette blob*.

Calculate the vaguelette blob $\{\tilde{\psi}_{j,k}\}$ The expression of $\{\tilde{\psi}_{j,k}\}$ corresponded to the blob $\tilde{\psi}_{j,k}$ can be found using the FBP formula and eq. (5.53):

$$\tilde{\psi}_{j,k}(\theta, y) = \frac{1}{|\mathcal{S}^{d-2}|}(\mathcal{I}^{-1}\mathcal{P}\psi_{j,k})(\theta, y), \text{ for } y \in \theta^\perp \tag{5.55}$$

with $\mathcal{I}^{-1}$ the Riesz potential: $\widehat{\mathcal{I}^{-1}f}(\omega) = \|\omega\|^{-1}\hat{f}(\omega)$. In frequency domain we have equivalently:

$$\hat{\tilde{\psi}}_{j,k}(\theta, \omega) = \frac{1}{|\mathcal{S}^{d-2}|}\|\omega\|\hat{\psi}_{j,k}(\omega), \text{ for } \omega \in \theta^\perp \tag{5.56}$$

Remember that the multiscale blob $\psi_{j,k}$ are constructed from a common mother blob ψ as $\psi_{j,k}(x) = \beta^{jd}\psi(\beta^j x - k)$, for $\beta > 0$ some dilation factor. Now if we define the mother vaguelette blob by:

$$\tilde{\psi}(\theta, y) = \frac{1}{|\mathcal{S}^{d-2}|}\int_{\theta^\perp} \|\omega\|\hat{\psi}(\omega)\exp(2\pi i\langle y, \omega\rangle)d\omega \tag{5.57}$$

then it follows easily that the vaguelette blob system are in fact dilations and translations of $\tilde{\psi}$:

$$\tilde{\psi}_{j,k}(\theta, y) = \beta^{jd}\tilde{\psi}(\theta, \beta^j y - \Pi_{\theta^\perp}k) \tag{5.58}$$

Note that the spatial expression $\tilde{\psi}(\theta, y)$ (and that of $\tilde{\psi}_{j,k}(\theta, y)$) is difficult to find in general, so for the numerical evaluation of $\langle \mathcal{P}f, \tilde{\psi}_{j,k}\rangle$ we really rely on the frequency expression (5.56). See Section 9.1.3 for more details.

5.7 Concluding remarks

In this chapter we developed new image representation models based on radial blobs. Compared to the standard pixel basis, the new method benefits from some theoretical advantages such as the fast X-ray projection and the better control on the image bandwidth. Whether or not the new method performs better than pixel in few projections CT image reconstruction remains a question, and it clearly depends on the regularization methods and related numerical algorithms applied on the new image model. This will be the subject of the next chapter.

Chapter 6

Reconstruction Methods for Blob Image

Based on the blob image representation models set up in previous chapters, we are now in position to propose some reconstruction methods for these models. As pointed out in Chapter 4, the "good" reconstruction algorithm which reaches the theoretical limit of performance is nonlinear in nature and exploit the sparsity of the image model. In this chapter we focus on the reconstruction methods which are numerically efficient in the CT context and easily adaptable to the blob image models, namely:

1. the minimization of the blob image's total variation
2. the minimization of the ℓ^1 norm of blob coefficients
3. the hybrid of TV and ℓ^1 minimization

Actually, these methods could have failed to be "efficient" without the remarkable progress achieved recently in the dedicated numerical algorithms. Other reconstruction strategies, like the greedy algorithms, can also be applied to our image model but will not be pursued here.

Notations In the following we note $\mathbf{f} \triangleq \{f_n\}_{n\in\mathbf{Z}}$ a coefficient vector of the blob image, $\mathbf{b}$ the sinogram data vector, and A the X-ray projection operator applying on blob coefficients $\mathbf{f}$ (see Annexe A). Note that all information about the acquisition system is contained in A. We assume the following data generation model:

$$\mathbf{b} = A\mathbf{f} + \mathbf{n} \tag{6.1}$$

with $\mathbf{n}$ a Gaussian noise vector: $n_k \sim \mathcal{N}(0, \sigma^2)$ i.i.d. In practice, the number of scales in the multiscale blob image model is prefixed, and the image support Ω is bounded, therefore all the vectors and operators become finite dimensional. Hereafter we suppose $\mathbf{f} \in \mathbb{R}^N$ and drop the dimensional dependency in notations.

6.1 Total Variation minimization of blob image

The single scale Gaussian blob image model

$$f(x) = \sum_{k \in \mathbf{Z}^d} f_k \phi(x - x_k) \tag{6.2}$$

represents essentially the low frequency information, and it is well known that the usual reconstruction will suffer from its over-smooth character. As a remedy, we propose the minimization of the Total Variation for the blob image, which is known to preserve the constant regions and sharp edges in reconstruction as it does on the pixel image[1], and also reduce the streak artifacts and the noise caused by the incomplete and low dose photon data.

6.1.1 Discrete TV norm of a blob image

Let's recall the definition of the TV semi-norm of a differentiable function f:

$$TV(f) \triangleq \int_{\mathbb{R}^d} \|\nabla f(x)\| dx \tag{6.3}$$

On a blob image the numerical evaluation of the gradient $\nabla f(x)$ as well as (6.3) need to be done in an appropriate manner. For this, we recall the blob-driven discrete gradient operator $D : X \to \mathbb{R}^{d \times |\mathcal{L}'|}$ defined in Section 5.2.2.1:

$$Df \triangleq \begin{pmatrix} D^1 f \\ \vdots \\ D^d f \end{pmatrix} \in \mathbb{R}^{d \times |\mathcal{L}'|}$$

where $D^i : X \to \mathbb{R}^{|\mathcal{L}'|}$ yields the i-th directional derivative of f taken on the lattice $\mathcal{L}'$:

$$(D^i f)_k = \partial_i f(x'_k), \; x'_k \in \mathcal{L}'$$

[1] We refer the reader to Chapter 3 for the literature review on the TV minimization.

Using the trapezoidal rule, we approximate $TV(f)$ on $\mathcal{L}'$ as (up to a constant factor) $\sum_{x'_k \in \mathcal{L}'} \|\nabla f(x'_k)\|$, and define the discrete total variation on coefficient vector $\mathbf{f}$:

$$\|\mathbf{f}\|_{TV} \triangleq \sum_{k \in \mathbf{Z}^d} \sqrt{(D^1 f)_k^2 + \cdots + (D^d f)_k^2} \tag{6.4}$$

In practice, the sampling step of the lattice $\mathcal{L}'$ should be taken reasonably small, *e.g.*, smaller than that of blob lattice $\mathcal{L}$, to make (6.4) a good approximation of (6.3). This would require fast implementations for the operators $D^1, \ldots D^d$.

6.1.1.1 Numerical implementation of operator D

A first solution consists in parallelizing these operators on GPU platform, which has been discussed in the section 2 of Chapter 5. Another possible solution is to compute D^i through FFT technique. We prove here some results on a 2D blob image of type $f(x) = \sum_{k,l} f_{k,l}\phi(x - x_{k,l})$ which can be easily generalized to 3D.

For this, we suppose that the lattice $\mathcal{L}$ generated by matrix G has $N \times N$ nodes, and $\mathcal{L}'$ is also generated by G, but upsampled by a integer factor $s \geq 1$ (so has $sN \times sN$ nodes). Let's denote by $\mathcal{F}_N$ the 2D DFT of size $N \times N$:

$$\mathcal{F}_N \mathbf{f}(m,n) = \sum_{k=0}^{N-1} \sum_{l=0}^{N-1} f_{k,l} \exp(-2\pi i(mk + nl)N^{-1})$$

and introduce the matrix $\mathbf{Y}$, defined by $\mathbf{Y}_{u,v} = \partial_1 \phi(s^{-1}G(u,v))$.

Proposition 6.1.1. *The 2D discrete Fourier transform of D^1, its adjoint D^{1*}, and $D^{1*}D^1$ are :*

$$\mathcal{F}_{sN}(D^1\mathbf{f})(m,n) = \mathcal{F}_N\mathbf{f}(m,n)\mathcal{F}_{sN}\mathbf{Y}(m,n) \tag{6.5}$$

$$\mathcal{F}_N(D^{1*}\mathbf{g})(k,l) = \frac{1}{s^2}\sum_{t=0}^{s-1} \overline{\mathcal{F}_{sN}\mathbf{Y}}(tN+k, tN+l)\mathcal{F}_{sN}\mathbf{g}(tN+k, tN+l) \tag{6.6}$$

$$\mathcal{F}_N(D^{1*}D^1\mathbf{f})(k,l) = \frac{1}{s^2}\mathcal{F}_N\mathbf{f}(k,l)\sum_{t=0}^{s-1} |\mathcal{F}_{sN}\mathbf{Y}|^2(tN+k, tN+l) \tag{6.7}$$

All indexes above are understood as modulo the size of array that they are bound to. Similar expressions hold for the operator D^2.

Proof. Let's rewrite $D^1\mathbf{f}$ as:

$$(D^1\mathbf{f})(m,n) = \partial_1 f(s^{-1}G(m,n)) = \sum_{k,l} f_{k,l}\mathbf{Y}(m - sk, n - sl)$$

Taking 2D DFT of size $sN \times sN$ on $D^1\mathbf{f}$, we get the equation (6.5). The adjoint operator $D^{1*} : \mathbb{R}^{sN\times sN} \to \mathbb{R}^{N\times N}$ reads:

$$(D^{1^*}\mathbf{g})_{k,l} = \sum_{m,n} g_{m,n}\mathbf{Y}(m - sk, n - sl)$$

for any $\mathbf{g} \in \mathbb{R}^{N\times N}$. Use the Parseval identity:

$$\langle D^{1^*}\mathbf{g}, \mathbf{f}\rangle = \frac{1}{N^2}\langle \mathcal{F}_N(D^{1^*}\mathbf{g}), \mathcal{F}_N\mathbf{f}\rangle \tag{6.8}$$

While on the other hand:

$$\begin{aligned}
\langle \mathbf{g}, D^1\mathbf{f}\rangle &= \frac{1}{s^2N^2}\langle \mathcal{F}_{sN}\mathbf{g}, \mathcal{F}_{sN}(D^1\mathbf{f})\rangle, \text{ and by (6.5)},\\
&= \frac{1}{s^2N^2}\sum_{m=0}^{sN}\sum_{n=0}^{sN} \mathcal{F}_{sN}\mathbf{g}(m,n)\overline{\mathcal{F}_N\mathbf{f}}(m,n)\overline{\mathcal{F}_{sN}\mathbf{Y}}(m,n)\\
&= \frac{1}{N^2}\sum_{k=0}^{N}\sum_{l=0}^{N} \overline{\mathcal{F}_N\mathbf{f}}(k,l)\times\\
&\left(\frac{1}{s^2}\sum_{t=0}^{s-1} \overline{\mathcal{F}_{sN}\mathbf{Y}}(tN+k, tN+l)\mathcal{F}_{sN}\mathbf{g}(tN+k, tN+l)\right)
\end{aligned}$$

Compare the last term with (6.8), we get (6.6). Equation (6.7) is a consequence of (6.5) and (6.6). □

Since the FFT of $\mathbf{Y}$ can be computed off-line, one needs only two 2D FFTs for the evaluation of $D^1\mathbf{f}$. Furthermore, the relations (6.6) and (6.7) confirm that the system like $D^{1*}D^1\mathbf{f} = D^{1*}\mathbf{g}$ can be solved by means of FFT.

Remark 6.1.1. We've observed in numerical experiments that the direct evaluation on GPUs is better than the FFT based method, since it avoids introducing aliasing errors. The results presented in the next chapters are based on the GPU implementation. Nonetheless, the FFT based method can still be useful in solving the problems of very high dimension, where even the parallelization becomes time demanding.

6.1.2 Reconstruction by TV minimization

The TV minimization problem on the blob image (6.2) reads:

$$\min_{\mathbf{f}} \|\mathbf{f}\|_{TV}, \quad \text{s.t. } \|A\mathbf{f} - \mathbf{b}\|^2 \le \varepsilon^2, \quad \text{for } \mathbf{f} \in \mathbb{R}^N \tag{6.9}$$

with ε the noise level, or in an equivalent form:

$$\min_{\mathbf{f}} \frac{1}{2}\|A\mathbf{f} - \mathbf{b}\|^2 + \mu\|\mathbf{f}\|_{TV}, \quad \text{for } \mathbf{f} \in \mathbb{R}^N \tag{6.10}$$

with $\mu > 0$ a penalty constant. These formulations are totally parallel to the TV minimization problems for pixel image formulated in section 1.3.2 of Chapter 3, On a Gaussian blob image, it's possible to incorporate a positive constraint on $\mathbf{f}$, and in this way we restraint the solution space to the functions generated by positive Gaussian blobs.

Numerical algorithm We remark that both (6.9) and (6.10) have exactly the same form as the TV minimization for pixel image proposed in the literature, with the only nuance that the underlying discrete gradient operator D defined as (6.4). This suggests that many state-of-art optimization algorithms can be applied without modification. This is the case for the *TVAL3* algorithm [48], which has already been used in Section 3.1.3. The technical details about this algorithm can be found in Annexe B.3.1.1 and in the original report [48].

Choice of penalty constant μ While the noise level ε in (6.9) can be estimated through physical experiments, the penalty parameter μ is much more difficult to determine: it balances the data fitting term $\|A\mathbf{f} - \mathbf{b}\|^2$ and the TV term $\|\mathbf{f}\|_{TV}$, and should be adjusted in function of the noise level, the dimensions of data and the unknowns. We use a simple manual method to choose μ. With the sinogram simulated from a phantom image and with A, $\mathbf{b}$ fixed (so does the noise level), we solve (6.10) for a wide range of μ, and choose the one which gives the best reconstruction result by comparing with the phantom image. Then this choice of μ is used for (6.10) on other data of the same noise level.

6.2 ℓ_1 norm minimization of blob coefficients

As already pointed out in Chapter 5, the image representation using a single scale Gaussian blob is not fundamentally different to that of the pixel basis, since the blob coefficients do not have a fast decay. While for the multiscale blob system developed in Section 5.4 which gives compressible image representation, we can follow the Compressed Sensing theory (see Chapter 4) and use the ℓ^1 minimization as *decoder*, which promotes the sparsity of the blob coefficients.

Modified multiscale blob image model For numerical feasibility, the multiscale blob image model developed in Section 5.4 need to be modified by keeping only a finite number of scales composed of low-pass or bandpass blobs. For the Mexican hat blob model, this is done by dropping all fine scales of index smaller than $-S$ and add a coarse scale made by Gaussian blob ϕ_0 which covers the low frequency. Finally, we have a finite scale image model:

$$f(x) = \sum_{k\in\mathbf{Z}^d} f_{0,k}\phi_0(x - x_k^0) + \sum_{j=-S}^{-1}\sum_{k\in\mathbf{Z}^d} f_{j,k}\psi_j(x - x_k^j) \tag{6.11}$$

The ℓ^1 minimization problem for (6.11) announces:

$$\min_{\mathbf{f}} \|\mathbf{f}\|_1 \quad \text{s.t.} \quad \|A\mathbf{f} - \mathbf{b}\|_2^2 \le \varepsilon^2, \quad \text{for } \mathbf{f} \in \mathbb{R}^N \tag{6.12}$$

where $\mathbf{f}$ is the blob coefficients in (6.11), and $\|\mathbf{f}\|_1 \triangleq \sum_k |f_k|$. Again, we have the equivalent constraint-free form:

$$\min_{\mathbf{f}} \frac{1}{2}\|A\mathbf{f} - \mathbf{b}\|^2 + \mu\|\mathbf{f}\|_1, \quad \text{for } \mathbf{f} \in \mathbb{R}^N \tag{6.13}$$

with μ determined in the same manner as in TV case. Eq. (6.13) is also known under the name of *Basis Pursuit Denoising* (BPDN), or *Basis Pursuit* (BP) for $\varepsilon = 0$ in (6.12) [114], in the sparsity-related image processing literature. In solving linear inverse problem with the pixel basis, BP is usually combined with a sparsifying transform W, *e.g.*, the Wavelet or the Curvelet transform, and becomes:

$$\min_{\mathbf{c}} \frac{1}{2}\|AW\mathbf{c} - \mathbf{b}\|^2 + \mu\|\mathbf{c}\|_1, \quad \text{for } \mathbf{c} \in \mathbb{R}^N \tag{6.14}$$

where W synthesize a pixel image from the coefficient vector $\mathbf{c}$, and the system operator A applies on $W\mathbf{c}$ (see Section 3.1.4). While in (6.12) and (6.13) the projector A operates directly on the blobs and the ℓ_1 norm is applied on the blob coefficients, consequently no *ad hoc* sparsifying transform is needed.

Comparison between (6.13) and (6.14) Although based on the same sparsity-promoting idea, the formulation (6.13) can be more beneficial than (6.14) from computational standpoint. We consider here a simple problem to illustrate the situation. Let $A \sim M \times N$, and suppose that the image to be reconstructed can be expressed using the wavelet coefficients $\mathbf{c}$ which is supported on the index set I, with $|I| \ll N$ and $|I| < M$. The reconstruction of $\mathbf{c}$ from noiseless data $\mathbf{b}$ is then reduced to solving the equation $AWS_I\mathbf{c} = \mathbf{b}$, with $S_I : \mathbb{R}^{|I|} \to \mathbb{R}^N$ the embedding operator. The pseudo

inverse solution reads:

$$\mathbf{c}^\dagger = (S_I^* W^* A^* A W S_I)^{-1} S_I^* W^* A^* \mathbf{b} \tag{6.15}$$

The solution to the linear system (6.15) is commonly computed by the Conjugate Gradient method, which terminates within $|I|$ iterations under favorable conditions on A. Although there is only $|I|$ unknowns to be recovered, the computation complexity in (6.15) is $O(MN|I|)$, for the simple reason that the projector A applies on the pixel image $W\mathbf{c}$ which is full. This is in contrast with the blob image case. Suppose that we want to recover an image represented by $|I|$ blobs supported on I, then the pseudo inverse solution reads:

$$\mathbf{f}^\dagger = (S_I^* A^* A S_I)^{-1} S_I^* A^* \mathbf{b}, \tag{6.16}$$

and the computation complexity of (6.16) is $O(M|I|^2)$, since A operates only on the non zero blobs.

Numerical algorithm A simple way to solve (6.13) is the iterative soft-threshold[2] (IST) method, as summarized in Algorithm 3. The convergence rate of IST is $O(1/n)$ with n the number of iterations. A popular variant to IST is the *Fast IST Algorithm*

Algorithm 3 Iterative Soft-Threshold for solving (6.13)

Initialization: $\mathbf{f}^0, n \leftarrow 0$
while not converged **do**
1. $g \leftarrow A^\top (A\mathbf{f}^n - \mathbf{b})$
2. update the gradient step λ using the steepest descent with line search
3. $\mathbf{f}^{n+1} \leftarrow \text{SoftThresh}_{\lambda\mu}(\mathbf{f}^n - \lambda \mathbf{g})$
4. $n \leftarrow n + 1$

end while

(FISTA) [115], which accelerates the convergence rate to $O(1/n^2)$. While for (6.12) (including the equality case $\varepsilon = 0$), one can use the *Primal Alternating Direction Method* (PADM) [116]. We refer the reader to the Annexe B and the original papers for the technical details of FISTA and PADM.

Heuristic acceleration of IST/FISTA In practice, the computation time of the ℓ^1 minimization problem (6.13) on a multiscale blob image can be much longer[3] than the TV minimization of a single scale Gaussian blob image, therefore seriously restraints its usefulness in real applications. This is mainly due to the X-ray projector's concurrent

[2] The operator $\text{SoftThresh}_\mu(\cdot)$ is defined in Annexe (B.2).

[3] We have observed with simulated data (see Chapter 8) that FISTA algorithm takes usually more than 1000 iterations to converge.

memory access operations raised by the blobs of different radius in the multiscale blob system. The situation could have been improved if one could know priorly the support set I of the true solution, since in this case one only has to solve $\min_{\mathbf{f}} \|AS_I\mathbf{f} - \mathbf{b}\|^2$, where AS_I applies only on a small number of nonzero blobs, therefore much faster than on the whole vector $\mathbf{f}$. Although knowing I in advance is clearly impossible, we can indeed accelerate the computation in solving (6.13) with the IST/FISTA algorithm. We make two observations:

- The problem (6.13) is easier to solve for μ large, because the sparsity of the solution is overly promoted so the computation time is reduced. The *homotopy* method [117–120] solves (6.13) in multiple times: it starts with a μ much bigger than the desired value μ^*, and decreases it gradually to μ^*, by using the last solution as the initialization of the next iteration. See Algorithm 4.

- At n-th iteration of the IST/FISTA algorithm, the soft-threshold operation (step 3 of Algorithm. 3) yields a sparse vector $\mathbf{f}^n$. Let $s > 0$ (a small number) be the support size that one expects on the unknown, and I_n^s be the support of the s largest terms of $\mathbf{f}^n$. It can be observed that for s small, I_n^s stablizes much faster than the overall IST/FISTA algorithm, *i.e.*, $|I_{n+1}^s \triangle I_n^s| \to 0$ rapidly with n, as illustrated in Figure 6.1. Further iterations are needed by IST/FISTA to reduce the residual error $\|A\mathbf{f}-\mathbf{b}\|^2$ using the gradient descent step (step 2 of Algorithm. 3), which is known to have a slow convergence [23]. This suggest us to terminate the IST/FISTA algorithm prematurely as soon as the support set of first s largest term is found. Then we apply a CG debiasing step on the support of the solution to reduce the residual error, which is more efficient than the gradient descent step, and computationally cheap since there is only a small number of coefficients to be identified.

Algorithm 4 Acceleration of IST/FISTA by homotopy

Initialization: $\mathbf{f}^0 \leftarrow 0, t \leftarrow 0, \tau > 1, T \geq 1, \mu^0 = \mu\tau^T$
while $t < T$ **do**
1. Solve (6.13) with parameter μ^t using IST/FISTA, initialized by $\mathbf{f}^t$.
2. $\mathbf{f}^{t+1} \leftarrow$ the solution of step 1.
3. $\mu^{t+1} \leftarrow \mu^t/\tau$.
4. $t \leftarrow t + 1$

end while

Based on these observations, we propose an acceleration method for IST/FISTA by combining the homotopy method and the CG debiasing step, resumed in Algorithm 5. We call it *heuristic* since we do not have the convergence proof of this algorithm. Particularly, the new algorithm 5 does not solve the problem (6.13) exactly due to the

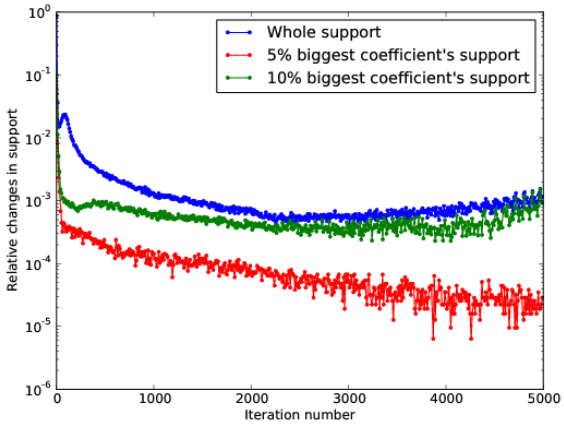

FIGURE 6.1: An example of the convergence rate of the FISTA algorithm in terms of changes in the support set. The vertical axis is in logarithmic scale. The curves of different colors represent the value $|I^s_{n+1} \triangle I^s_n|/N$, with n the iterations number and $N = 3 \times 10^5$ the dimension of vector $\mathbf{f}$. I^s_n is the index set of s largest coefficients of the n-th iteration solution $\mathbf{f}^n$. Blue curve: $s = N$, green curve: $s = 10\% \times N$, red curve: $s = 5\% \times N$.

Algorithm 5 Heuristic acceleration of IST/FISTA by homotopy and debiasing

Initialization: $\mathbf{f}^0 \leftarrow 0, t \leftarrow 0, \tau > 1, T \geq 1, \mu^0 = \mu\tau^T, \epsilon > 0, s > 0$

while $t < T$ **do**

1. Solve (6.13) with parameter μ^t. Initialize IST/FISTA by $\mathbf{f}^t$ and terminate when $|I^s_{n+1} \triangle I^s_n|/N \leq \epsilon$.
2. $\mathbf{f}^{t+1/2} \leftarrow$ the solution returned by IST/FISTA, and let I be the support of $\mathbf{f}^{t+1/2}$.
3. Debiasing: solve $\min_{\mathbf{f}} \|AS_I\mathbf{f} - \mathbf{b}\|^2$ using CG, initialized by $\mathbf{f}^{t+1/2}$.
4. $\mathbf{f}^{t+1} \leftarrow$ the solution returned by step 3.
5. $\mu^{t+1} \leftarrow \mu^t/\tau$.
6. $t \leftarrow t + 1$

end while

premature termination of IST/FISTA iterations, and its solution is often slightly worse than that of the original IST/FISTA algorithm. In Figure 6.2 we plot the acceleration achieved by this method over FISTA in the first 500 iterations. The heuristic algorithm terminates after 230 iterations spending 173 seconds, and the SNR of the final image is 19.50dB. FISTA algorithms terminates after 1000 iterations spending 1200 seconds, and the final SNR is 19.73 dB.

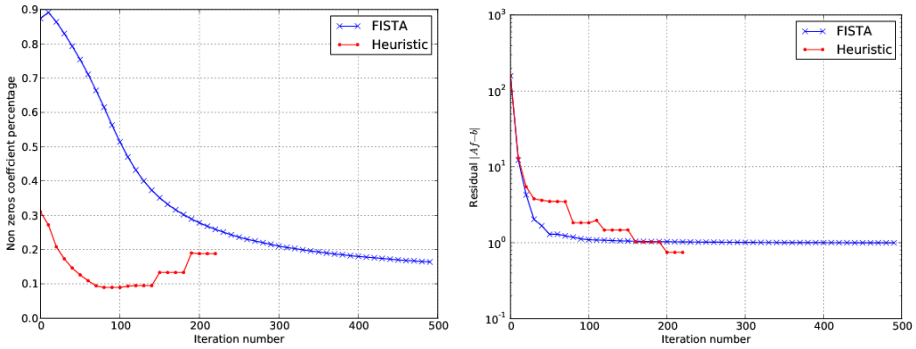

(a) Sparsity $\|\mathbf{f}\|_0/N$ (b) Residual $\|A\mathbf{f}-\mathbf{b}\|$

FIGURE 6.2: An example of the convergence rate of FISTA and the heuristic acceleration algorithms applied to a reconstruction problem. The horizontal axis is the total number that the X-ray projector $A, A^\top$ has been applied. The heuristic algorithm uses $T = 4$ homotopy iterations, with parameters $\tau = 0.5, \epsilon = 5 \times 10^{-3}, s = N$. The jumps in the red curve corresponds to the CG debiasing steps of 25 iterations. Figure (a): the percentage of non zero coefficients at the n-th iteration. (b): the residual $\|A\mathbf{f}-\mathbf{b}\|$ at the n-th iteration.

6.3 Reweighted iterative TV and ℓ^1 minimizations

Both the TV and the ℓ^1 minimizations can be improved by their reweighted versions. The reweighted TV minimization reads:

$$\min_{\mathbf{f}} \|\mathbf{f}\|_{TV(\mathbf{w})} \quad \text{s.t.} \quad \|A\mathbf{f}-\mathbf{b}\|_2^2 \leq \varepsilon^2 \tag{6.17}$$

where $\mathbf{w}$ is a positive weight vector and

$$\|\mathbf{f}\|_{TV(\mathbf{w})} \triangleq \sum_k w_k \sqrt{(D^1 f)_k^2 + \ldots + (D^d f)_k^2} \tag{6.18}$$

The reweighted ℓ^1 minimization reads:

$$\min_{\mathbf{f}} \|\mathbf{w} \odot \mathbf{f}\|_1 \quad \text{s.t.} \quad \|A\mathbf{f}-\mathbf{b}\|_2^2 \leq \varepsilon^2 \tag{6.19}$$

with $\mathbf{w} \in \mathbb{R}_+^N$ a weight vector and $\mathbf{w} \odot \mathbf{f}$ be the element-wise product between two vectors. These formulations are to be incorporated into an iterative framework, where we solve (6.17) or (6.19) for several times by updating at each new iteration the weight $\mathbf{w}$ according to the solution $\mathbf{f}$ of the last reconstruction, see Algorithm 6. One possibility for updating $\mathbf{w}$ in reweighted TV minimization is to calculate the *gradient map* $\|(D\mathbf{f})_k\|$ on the lattice $\mathcal{L}'$[4], and take the k-th entry of $\mathbf{w}$ as:

$$w_k = (\|(D\mathbf{f})_k\| + \epsilon)^{-1} \tag{6.20}$$

[4]See Section 3.1.3.1 for definition of lattice $\mathcal{L}'$.

for $\epsilon > 0$ some small constant. Similarly for reweighted ℓ^1 minimization we can use:

$$w_k = (|f_k| + \epsilon)^{-1} \tag{6.21}$$

Algorithm 6 Reweighted iterative TV/ℓ^1 minimization

Initialization: $t \leftarrow 0, T > 0$, $\mathbf{w} \leftarrow \mathbf{1}$, the constant vector of value 1.
while $t < T$ **do**
1. $\mathbf{f} \leftarrow$ the solution of (6.17) (or the reweighted ℓ^1 problem) with the weight $\mathbf{w}$
2. update the weight $\mathbf{w}$ according to (6.20) or (6.21)
3. $t \leftarrow t + 1$

end while

Generally speaking, the reweighted iterative TV/ℓ^1 minimization method performs better than the standard scheme. The reason for the case of TV minimization is rather intuitive. The map $\|(D\mathbf{f})_k\|$ has large value mainly near the discontinuities, therefore the weight $w_k = (\|(D\mathbf{f})_k\| + \epsilon)^{-1}$ is small at these positions. Consequently, the blobs which contribute to the discontinuities are much less penalized than those inside constant regions. Using the iterative scheme, the information about discontinuities found by the last solution is recycled to a new iteration, and hopefully edges become more sharp and constant regions become more flat. See [121, 122] and the references therein.

Recently, [122–124] brought more insights to the theoretical understanding of the reweighted iterative ℓ^1 minimization. Actually, the reweighting iterations approximate the $\ell^p, p < 1$ minimization problem, which is non convex and the solution may not be globally optimal. The ℓ^p minimization with $p < 1$ is more adapted to signals of fast decay (*e.g.*, those of weak ℓ^p ball for $p < 1$, see Chapter 4) and has better sparsity enhancing capability than ℓ^1 [125, 126]. Therefore solving the reweighted ℓ^1 problem several times can effectively improve the reconstruction of a single ℓ^1 minimization.

6.4 Hybrid of TV and ℓ^1 minimizations

As already pointed out in Section 3.1.1, by the TV minimization (6.9) the number of projections can be greatly reduced, but the low contrast regions and small objects are often smoothed out in favor of constant regions, which can be harmful in the context like medical imaging. On the contrary the ℓ^1 minimization reconstructs well these characters but would require more projections, otherwise the image quality drops fast: the reconstruction suffers from the "salt and pepper" noise, and the homogeneous regions and the edges are not preserved (see Chapter 7 for numerical evidences).

These observations suggest us to use an hybrid model in the hope of combining the advantageous of both parts. For this, we consider the TV-ℓ^1 reconstruction method [70, 120, 127], whose regularization term is the sum of the TV and the ℓ^1 norm:

$$\min_{\mathbf{f}} \ \mu_1\|\mathbf{f}\|_1 + \mu_2\|\mathbf{f}\|_{TV}, \quad \text{s.t. } \|A\mathbf{f}-\mathbf{b}\|^2 \leq \varepsilon^2 \tag{6.22}$$

Or in the equivalent constraint-free form:

$$\min_{\mathbf{f}} \frac{1}{2}\|A\mathbf{f}-\mathbf{b}\|^2 + \mu_1\|\mathbf{f}\|_1 + \mu_2\|\mathbf{f}\|_{TV} \tag{6.23}$$

for μ_1 and μ_2 two positive penalty constants. In practice we set $\mu_1 \gg \mu_2$ thus (6.22) and (6.23) are understood as the ℓ^1 minimization augmented by an extra TV term, and their solutions are expected to be sparse (small ℓ^1 norm) as well as geometrically simple (small TV norm). These formulations improves the standard ℓ^1 minimization by reducing effectively the "salt and pepper" noise and preserving homogeneous regions and edges, and has less "texture killer" default of the standard TV minimization. We refer the reader to next chapter for numerical evidences.

Numerical algorithm The problems (6.23) and (6.22) are numerically challenging, due to the non-smooth regularization term $\mu_1\|\mathbf{f}\|_1 + \mu_2\|\mathbf{f}\|_{TV}$ which can not be handled by neither the TVAL3 nor the IST algorithm discussed previously. Efficient algorithms [120, 127] based on the *alternating direction method* (ADM) and the *penalization* technique [127] (or the *operator splitting* technique [120]) have been proposed for (6.23). Using the same ADM idea, in Annexe we propose an algorithm for both (6.22) and (6.23) but based on an augmented Lagrangian formulation. Similar to the algorithms in [120, 127], the soft-thresholding operators used in both TVAL3 and IST are preserved in our new algorithm, which is a crucial point for its numerical efficiency.

Chapter 7

2D Numerical Experiments - Simulated data

In this chapter we present 2D reconstructions results using simulated data based on the blob image models and the reconstruction methods discussed in previous chapters. In order to demonstrate their effectiveness, we shall confront the methods based on blob with equivalent approaches based on pixel. Since the efficiency of a reconstruction method depends on the application context, *e.g.*, medical (low contrast objects) or industrial (piecewise homogeneous objects) oriented, we shall also make a comparison on different phantom images to bring out their pros and cons. The data have been simulated from pixel phantom images, which allow precise quality assessment on the reconstructions.

Phantom images The phantoms images used in this chapter are shown in Figure 7.1. Particularly, the disk and the Shepp-Logan phantoms are piecewise constant, while the other phantoms are medical oriented and may contain low contrast regions and textures.

Sinogram data simulation Unless specified, the simulated data are acquired as follows. The parallel beam is equally distributed between $[0, \pi)$ (or $[0, 2\pi)$ for fan beam source), and the linear detector is perpendicular to the source-rotation center axis. The other parameters are:

- Rotation axis to source distance: 608.28mm (for fan beam case)
- Rotation axis to detector distance: 608.28mm (for fan beam case)
- Detector Length: 405.52mm

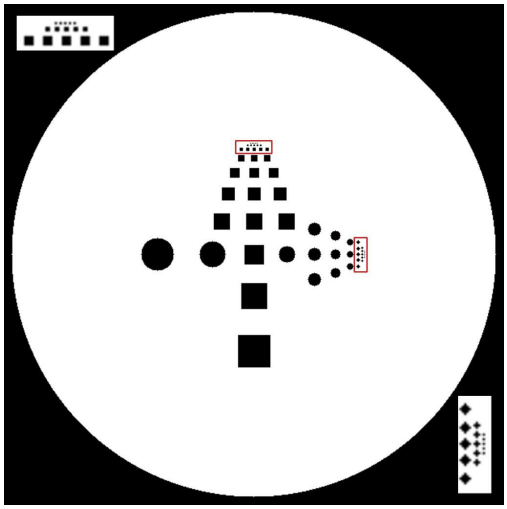

(a) Disk

(b) Shepp-Logan 512×512

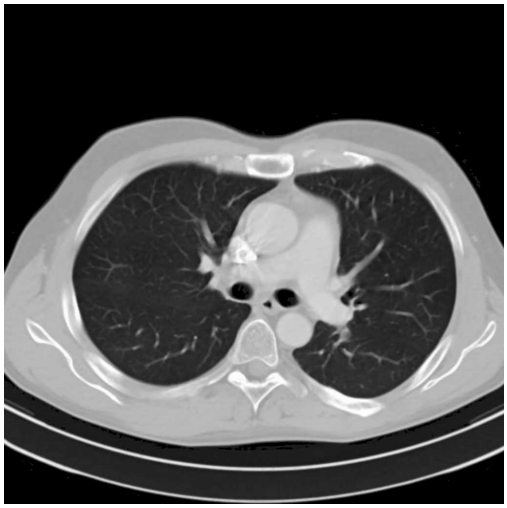

(c) Thorax 512×512

(d) Abdomen 512×512

(e) Lung 334×512

FIGURE 7.1: Phantom images and their dimension. The Disk phantom (a) is a CAD object. Figure (b) (c) (d) and (e) are pixel images with gray level normalized in $[0, 1]$.

- Pixel number of detector: 512

For data simulation, we apply the ray-tracing (Siddon) projector A on the phantom image $\mathbf{f}$ to get a vector $\mathbf{y} = A\mathbf{f}$. The photon number at i-th detector pixel can be considered as a Poisson variable of mean value $I_0 \exp(-y_i)$, with I_0 being the mean value of photon number at source. So we sample a Poisson distribution of mean $I_0 \exp(-y_i)$ and generate in this way the photon data N_i, and the final noisy sinogram $\mathbf{b}$ is obtained by taking $b_i = \log I_0 - \log N_i$. We define the *Signal-to-Noise Ratio* (SNR) of the sinogram as:

$$\mathrm{SNR}(\mathbf{b}) \triangleq 10 \log_{10} \left(\frac{\mathbb{E}\|\mathbf{y}\|^2}{\mathbb{E}\|\mathbf{y} - \mathbf{b}\|^2} \right) \tag{7.1}$$

Using the fact that for y_i large (see Section 2.2.1.1):

$$\mathbb{E}\|\mathbf{y} - \mathbf{b}\|^2 \simeq I_0^{-1} \sum_i \exp(y_i)$$

we deduce that:

$$\mathrm{SNR}(\mathbf{b}) \simeq 10 \log_{10} I_0 + \mathrm{cst} \tag{7.2}$$

Typically in our experiments setting $I_0 = 10^7$ will yield a sinogram of SNR larger than 50dB.

Image display By the property of blob image models, we can re-sample a reconstructed blob image arbitrarily without using any *ad hoc* interpolation method. All our reconstructions are re-sampled to the dimension of the original phantom image, and the same linear window $[0, 1]$ is applied to all output images by default.

Image quality assessment A single index can not give an objective apprehension of image quality. Beside the standard *Signal-to-Noise Ratio*, we use also the *Streak Index* (SI) [5] as the image quality metric. Let $\mathbf{f}$ be the reconstructed pixel image and $\mathbf{g}$ be the reference phantom. The SNR between $\mathbf{f}, \mathbf{g}$ is defined as:

$$\mathrm{SNR}(\mathbf{f}, \mathbf{g}) \triangleq 20 \log_{10} \left(\frac{\|\mathbf{g} - N^{-1} \sum_i g_i\|}{\|\mathbf{f} - \mathbf{g}\|} \right) \tag{7.3}$$

The Streak Index between $\mathbf{f}, \mathbf{g}$ is defined as:

$$\mathrm{SI}(\mathbf{f}, \mathbf{g}) \triangleq N^{-1} \|\mathbf{f} - \mathbf{g}\|_{TV} \tag{7.4}$$

where the discrete TV norm as defined in (3.23) is assumed, and N is the number of pixels in image. SI is well suited for measuring the errors such as the fluctuation of the non constant region or the imprecision of edges, typically caused by the streak artifacts in the reconstruction.

Computation platform All the numerical experiments hereafter are made on a Intel Xeon CPU at 2.50GHz system of 32 Gbyte memory integrating a NVIDIA Tesla C2070 GPU card of 4 Gbyte memory.

Notations We adopt following notations for this and the next chapter.

- P: the number of projections
- D: the number of pixels in the linear detector
- Δ: the reconstruction method in use, *e.g.*, $\Delta = \ell^1$ means the solution is obtained by the ℓ^1 minimization
- N: the dimension (number of blobs or pixels) of the coefficient vector $\mathbf{f}$
- τ: the sparsity level, *e.g.* the percentage of the nonzero entries (blobs).
- $w = [a, b]$: the linear window which is used for image visualization. The gray level beyond (above) b (a) is set to b (a).
- T: the computation time in seconds.
- SNR: the SNR of the reconstruction compared to the original phantom, *i.e.*, (7.3).
- SI: the SI of the reconstruction compared to the original phantom, *i.e.*, (7.4).
- SNR($\mathbf{b}$): the SNR of the sinogram data, *i.e.*, (7.1).
- Mex-4: 4 scales Mexican hat blob system.
- GS: (single scale) Gaussian blob.
- Daub-6: Daubechies wavelet of order 6.

7.1 TV reconstruction results

Unless specified, all reconstructions in the following are obtained by solving the TV minimization problem:

$$\min_{\mathbf{f}} \frac{1}{2}\|A\mathbf{f} - \mathbf{b}\|^2 + \mu\|\mathbf{f}\|_{TV} \tag{7.5}$$

for $\mathbf{f}$ the coefficient of a Gaussian blob image model:

$$f(x) = \sum_{k\in\mathbf{Z}^2} f_k \phi(x - x_k) \tag{7.6}$$

See Chapter 5 for details about this image model and the choice of parameters.

7.1.1 Reconstruction of piecewise constant images

In the first experiment we aim to show that combined with TV minimization (7.5), the Gaussian blobs can well represent small objects, sharp edges and constant regions, which is a point for what blob is often criticized.

The CAD disk phantom with round and square holes of variant size was created for this purpose (see Figure 7.1 (a)). The disk has the uniform attenuation value 1. The diameters of the disk, the largest and the smallest holes are 120mm, 8mm and 0.2mm respectively (the round holes in the vertical rectangular of Figure 7.1(a) appear in diamond form due to the pixelization effect). A noiseless sinogram of 96 projections has been generated using the CIVA simulation platform [128]. The hexagonal lattice sampling step is $h = 0.15$mm, and the parameters of Gaussian blob are $\alpha = 66.96$, $r_{cut} = 0.32$mm.

Reweighted iterative TV reconstruction We solve the reweighted iterative TV minimization problem (6.17) with 3 iterations[1], and display in Figure 7.2 the weighting map $\mathbf{w}$ (see Section 6.3) after these iterations. It can be seen that after the first iteration, most constant regions and the large holes have been already recovered. The streak artifacts appeared in Figure 7.2.(a) are removed and the resolution of small details are improved after the last reweighted iteration. The reconstructed image and the profiles are shown in Figure 7.3 (a), (b), (c) and in Figure 7.4. Compared with the original disk phantom, it can be seen that the constant regions and the contour discontinuities are well preserved. Nevertheless, due to the large size and the smoothness of Gaussian blob, the holes of diameter smaller than 0.4mm are blurred or even missed in the reconstruction. The blob of smaller radius would be necessary to recover these details.

[1] The noise level ϵ is set manually.

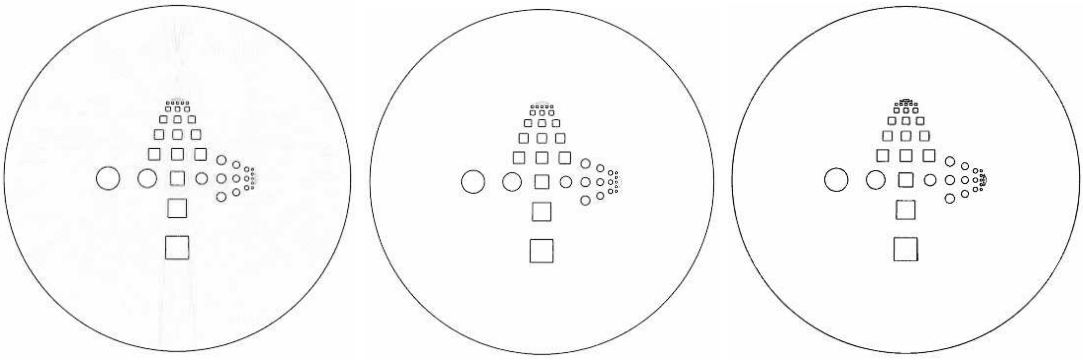

(a) Reweighted iteration 1 (b) Reweighted iteration 2 (c) Reweighted iteration 3

FIGURE 7.2: Disk phantom: P=96, Δ=Reweighted TV with 3 iterations. Figures (a), (b), (c): the reweighting map $\mathbf{w}$ after each iteration.

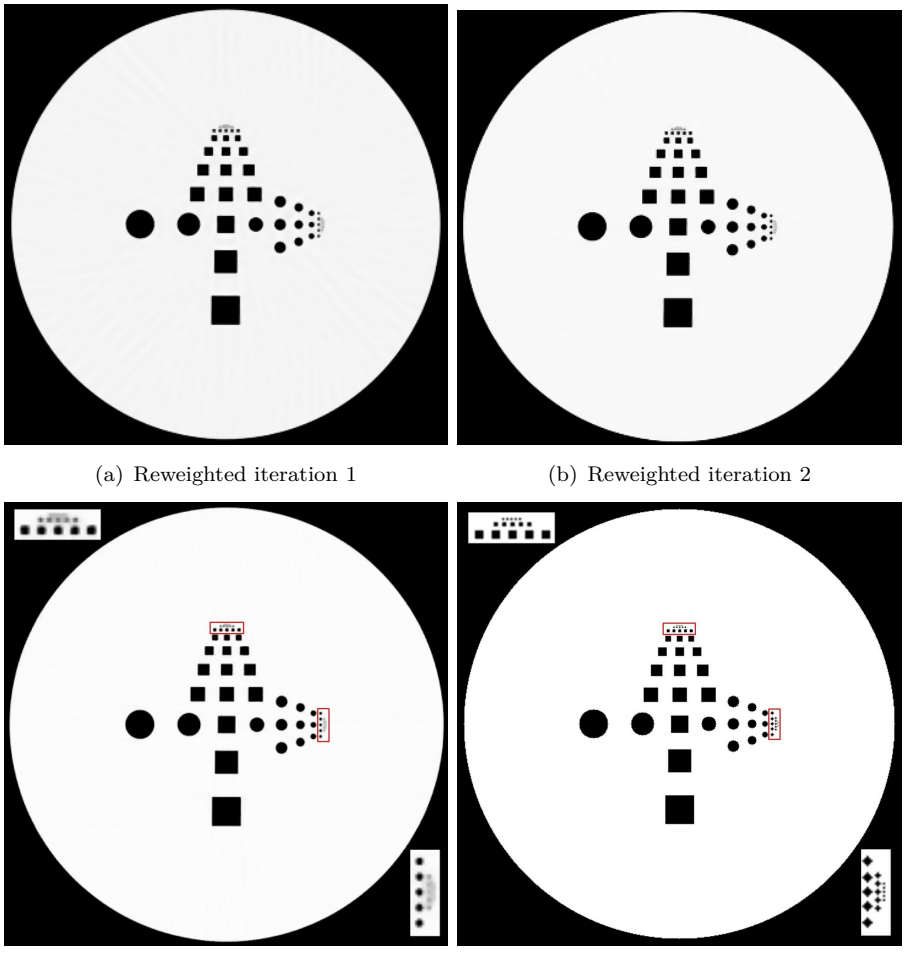

(a) Reweighted iteration 1 (b) Reweighted iteration 2

(c) Reweighted iteration 3 (d) Disk phantom

FIGURE 7.3: Disk phantom: P=96, Δ=Reweighted TV with 3 iterations, $w = [0, 1]$. Figures (a), (b), (c): the reconstructed images after the first, the second and the last iteration. Figure (d): disk phantom. The two corners in (c) and (d) are the zoomed view on the rectangular ROI regions.

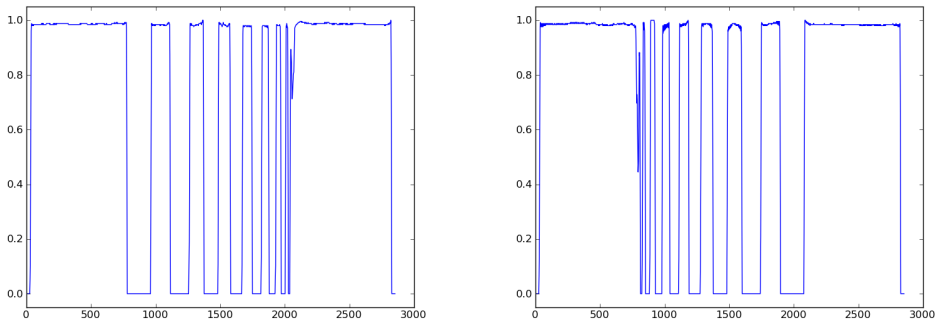

(a) Horizontal central profile

(b) Vertical central profile

FIGURE 7.4: Disk phantom: central profiles of the reconstruction Figure 7.3 (c)

High frequency components Here we test the TV reconstruction method on the Shepp-Logan phantom (Figure 7.1 (b)) using $P = 32$ and SNR($\mathbf{b}$) = 50dB. The local high frequency components contained in image result strong artifacts in reconstruction, which can be observed from Figure 7.5 (b): the square oscillating pattern and the fissure caused some high frequency aliasings in the tangent direction. These artifacts are removed after the reweighted TV minimization, and the image resolution in the low contrast regions are also improved. See also Figure 7.6.

7.1.2 Reconstruction quality vs. lattice sampling step h

In this experiment we study the reconstruction quality as a function of the hexagonal lattice's sampling step h. The Lung phantom (Figure 7.1 (e)) is used here, with the physical size of $167.51 \times 109.27\text{mm}^2$, and its gray level is normalized into $[0, 1]$. The number of projections here is fixed to 64.

Comparison with pixel reconstruction As a comparison, we provide the TV reconstructions with pixel basis at different dimensions, obtained by solving the same minimization problem (7.5) (we use a GPU-implemented Siddon ray-tracing projector A, and the discrete TV norm as defined in (3.23)). The sampling step (or the pixel size) is chosen such that the Cartesian lattice has the dimension 128×84, 170×112 and 256×168 respectively, *i.e.*, the number of unknowns to be recovered equals to 1/16, 1/9 and 1/4 of the original phantom image's pixel number. Figure 7.7 (b), (d), and (f) show the pixel reconstruction results which are zoomed to original dimension 512×334 using the nearest interpolation method.

To make a fair comparison, the sampling step of the blob image is also chosen such that the number of active nodes (those located inside the FoV of acquisition system)

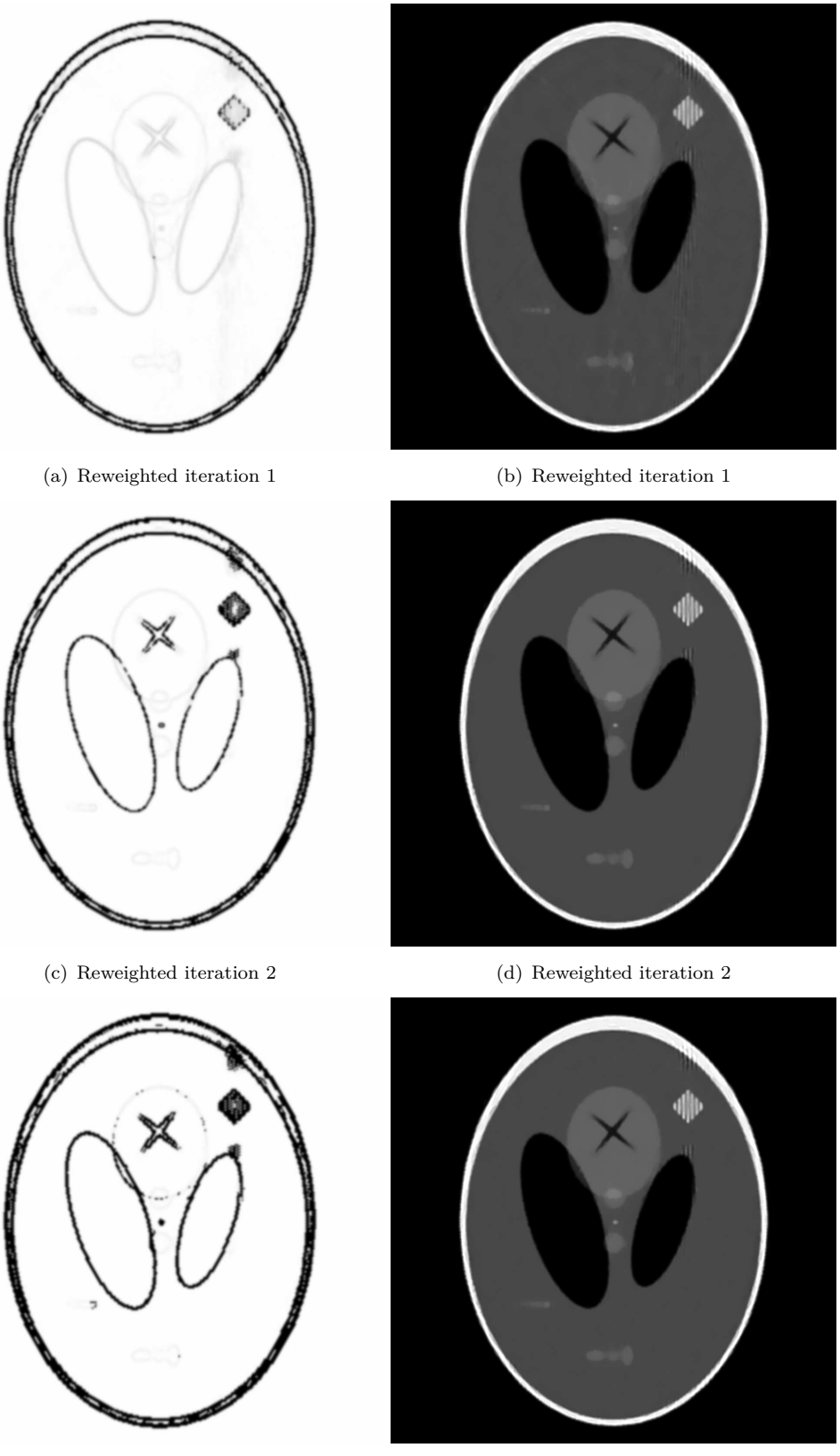

(a) Reweighted iteration 1

(b) Reweighted iteration 1

(c) Reweighted iteration 2

(d) Reweighted iteration 2

(e) Reweighted iteration 3

(f) Reweighted iteration 3, SNR=14.50 dB

FIGURE 7.5: Shepp-Logan phantom: P=32, Δ =Reweighted TV with 3 iterations, SNR($\mathbf{b}$)=50dB, $w = [0, 1]$. Figures (a), (c), (e): the reweighting map $\mathbf{w}$ after the first and the third, and the last iteration. Figures (b), (d), (f): the reconstructed images after the first, the second and the last iteration.

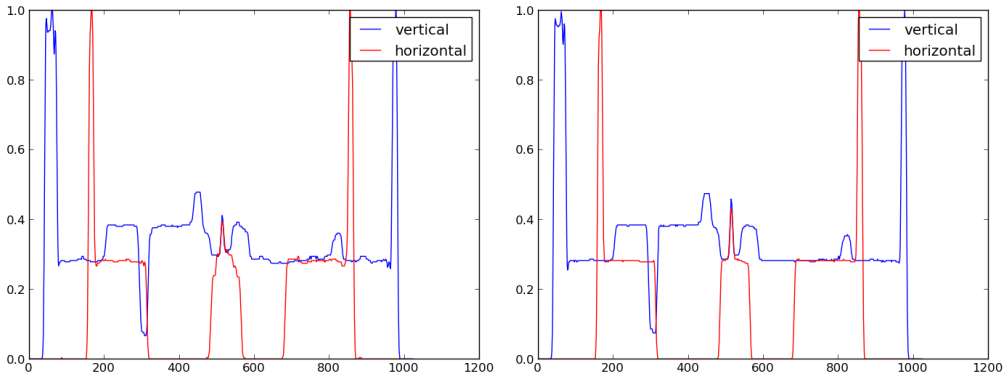

(a) Reweighted iteration 1 (b) Reweighted iteration 3

FIGURE 7.6: Shepp-Logan phantom: central profiles of reconstructed images after the first and the last reweighted TV iterations. Left: Figure 7.5 (b). Right: Figure 7.5 (f).

in the resulting hexagonal lattice is close to 1/16, 1/9 and 1/4 of the original phantom image's pixel number. We recall that by changing h the blob radius r_{cut} is also dilated proportionally (see Section 5.5 for details). The reconstructed images based on blob are shown in Figure 7.7(a), (c), (e) respectively.

We can see that when the sampling step h increases, both the blob and the pixel reconstruction take less computation time since there are less unknowns to recover, at the price of a worse image quality. Nevertheless, the degradation in the pixel reconstruction is more visible than the corresponding blob one, due to the annoying "zig-zag" effects.

Advantages of blob over pixel The same comparison between the blob and the pixel on the phantom Lung has been realized on a wider range of the sampling step h. In Figure 7.8 we plot the results of SNR, SI and computation time in function of the number of unknowns N, which is uniquely determined from h and increases with h^{-1}. The results of the same experiments with phantoms Abdomen and Thorax are shown in Figures 7.9 and 7.10 are respectively. We make the following observations.

- Compared to pixel, the blob reconstruction is less sensitive to the variation of h. Particularly, for the range of h yielding N from 5×10^4 to 2×10^5, the SNR and SI of the blob reconstruction is almost constant.
- At the same number of unknowns, blob is always better than pixel if measured by SI, so one may achieve the same visual quality with less blobs. This suggests that the shift invariant space generated by blob has better approximation quality. It is worthy of note that the higher SNR of the pixel reconstruction for $N > 2 \times 10^5$ does not mean a better image quality, since it contains more streak artifacts than the blob reconstruction as revealed by its SI value.

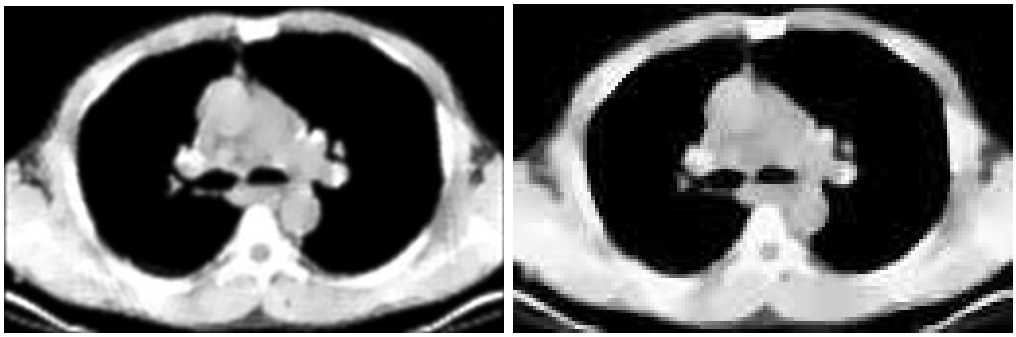

(a) Blob, h=1.460, SNR=16.28dB, SI=0.0217, T=63.14s

(b) Pixel, h=1.309, SNR=13.74dB, SI=0.0348, T=12.47s

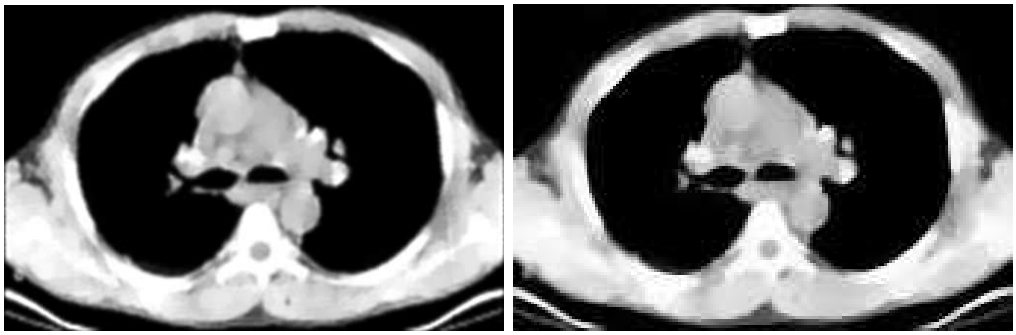

(c) Blob, h=1.096, SNR=17.77dB, SI=0.0194, T=86.36s

(d) Pixel, h=0.985, SNR=14.32dB, SI=0.033, T=18.06s

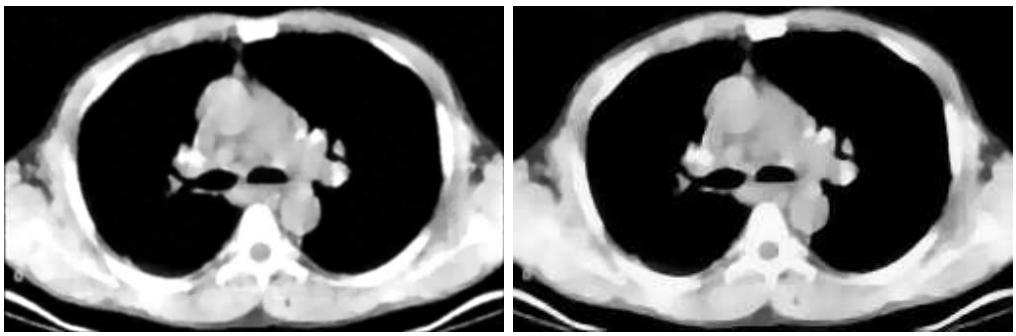

(e) Blob, h=0.730, SNR=18.98dB, SI=0.017, T=98.91s

(f) Pixel, h=0.654, SNR=15.71dB, SI=0.0289, T=51.89s

FIGURE 7.7: Lung phantom: P=64, Δ = TV with different sampling step h, $w = [0, 0.9]$. First column: blob reconstructions. Second column: pixel reconstructions. The number of unknowns in image pairs (a,b), (c,d) and (e,f) is respectively close to 1/16, 1/9 and 1/4 of the original phantom's dimension 512×334.

- The computation time with blob is close to the pixel for the dimension $\geq 10^5$. Remark the computation time in high dimension is very prohibitively high, and practically it's more interesting to use blob which yields better image quality than pixel in middle dimension.

- The optimal choice for N is around 10^5, where blob is superior to pixel with a comparable computation time. Beyond the dimension 2×10^5, there is no more improvement in the reconstruction quality (and even a slight drop for both pixel and blob). This can be explained by the fact that modeling the reconstruction

in a dimension much higher than that of the phantom image (about 1.7×10^5) brings no more information but probably results an ill-conditioned system. In real applications it is hard to find *a priori* the optimal reconstruction dimension (some upper bound can be established based on the Shannon sampling theory [2], but it is simply too pessimistic), therefore the stability of blob can tolerate more upstream modeling error.

7.1.3 Reconstruction from few projections

In this experiment we compare the reconstruction qualities by varying the number of projections. We have simulated 4 groups of data using 32, 48, 64, 96 projections. Figure 7.11 shows the corresponding reconstruction on Lung phantom, obtained with the sampling step $h = 0.292$mm. The reconstruction central profiles with 32 and 96 projections are displayed in Figure 7.12. It can be seen that the visual quality of reconstructed image is improved as the number of projections increases. As a comparison, in Figure 7.11(e) we show the reconstruction from 96 projections by minimizing simply the squared error $\min_{\mathbf{f}} \|A\mathbf{f} - \mathbf{b}\|^2$ using the Conjugated Gradient method. The streak artifacts in the background is typical to the reconstructions with incomplete data. TV minimization removes efficiently these artifacts and all the reconstructions have smaller SI than the Figure 7.11(e). Similar results with the Abdomen phantom are shown in figure 7.16 (a), (b), and (c), and the profiles are in figure 7.17.

As we have already seen in Chapter 3 with the pixel image, TV minimization sets to constant the textures and the low contrast regions in image. With the blob image we have observed exactly the same behavior, and the cartoon effect is particularly visible when the number of projections is very limited, typically less than 64. This character of TV minimization could be harmful and considerably reduce the reliability of the reconstructed image, particularly in applications such as the tumors detection.

Reconstruction quality vs. number of projections We carry out the same test on different phantoms: Shepp-Logan, Thorax and Abdomen (Figure 7.1 (b), (c) and (d)), with P varying from 8 to 256. The SNR and the SI are plotted in Figure 7.13. We make the following remarks.

- For each phantom, we can distinguish a sharp transition in its SNR plot, which indicates roughly the minimum number of projections necessary for an acceptable TV reconstruction. The plots suggest the value between 20 and 40 for Shepp-Logan, between 40 and 60 for Abdomen, and between 60 and 80 for Thorax.

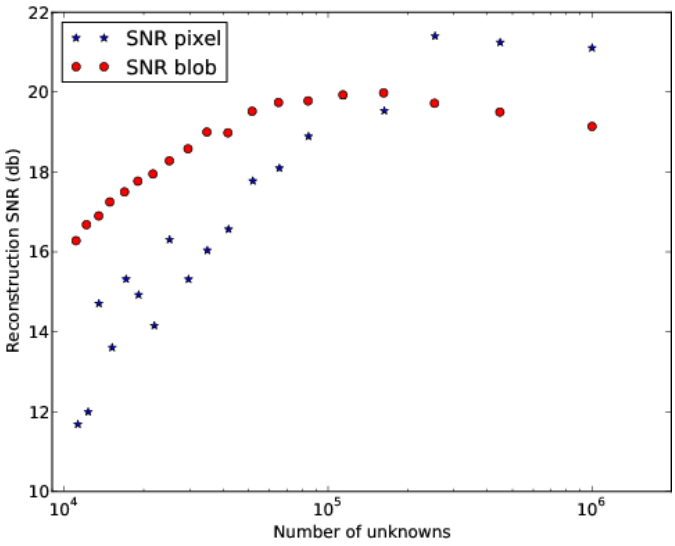

(a) Reconstruction SNR

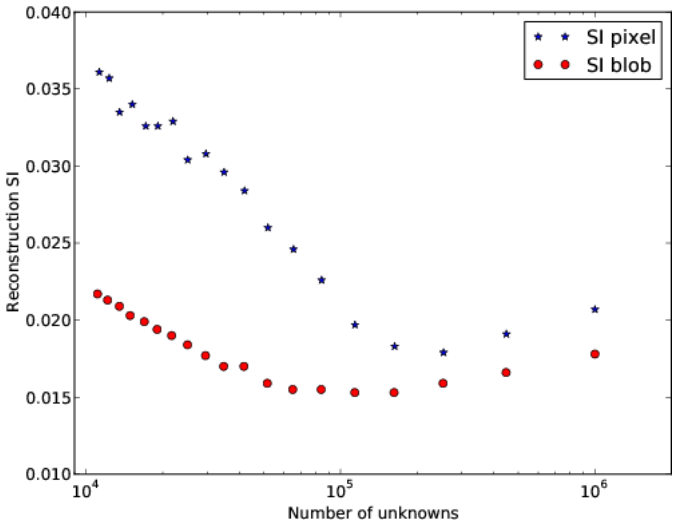

(b) Reconstruction SI

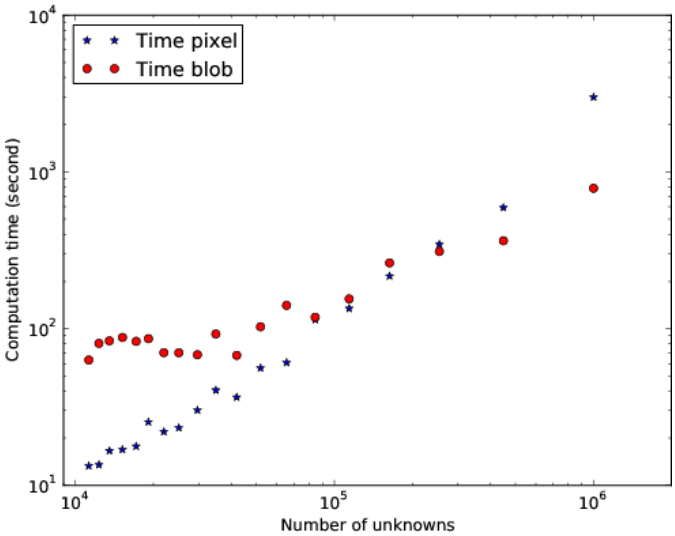

(c) Computation time

FIGURE 7.8: Lung phantom: comparison between blob and pixel in function of the number of unknowns. Blob reconstructions are generally better than pixel ones in terms of visual quality, and it takes less computation time than pixel in high dimension reconstruction.

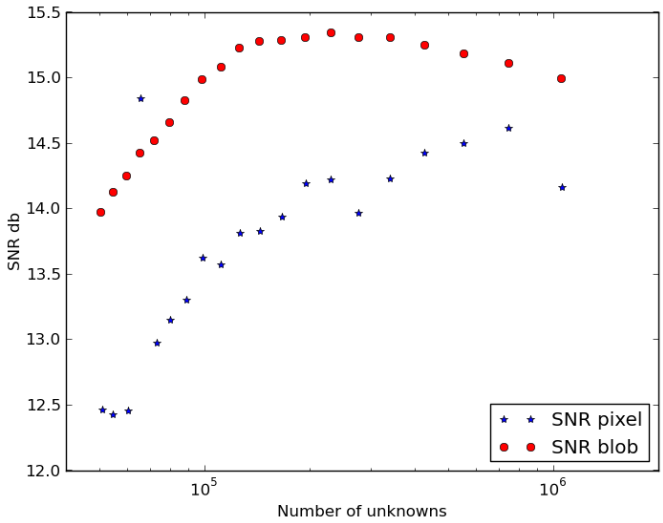

(a) Reconstruction SNR

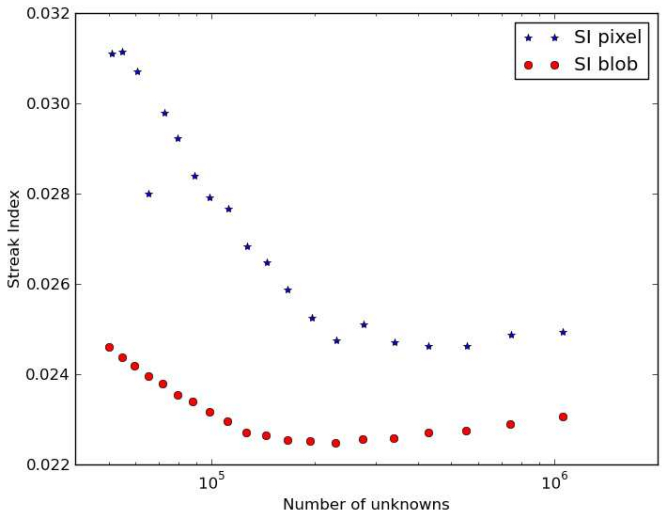

(b) Reconstruction SI

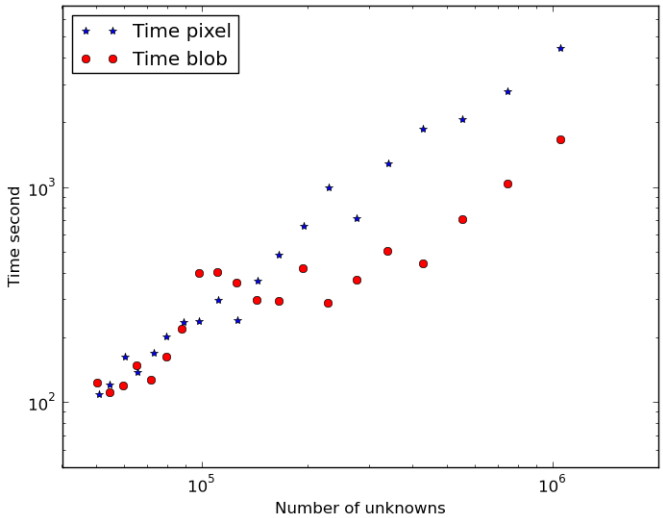

(c) Computation time

FIGURE 7.9: Abdomen phantom: same experiment as in Figure 7.8.

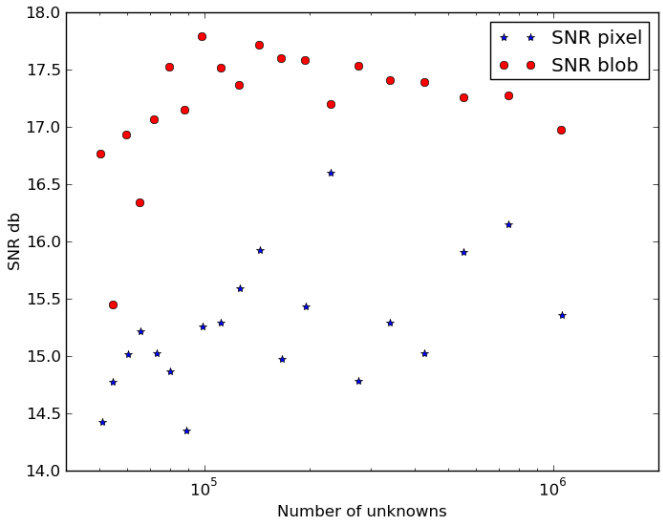

(a) Reconstruction SNR

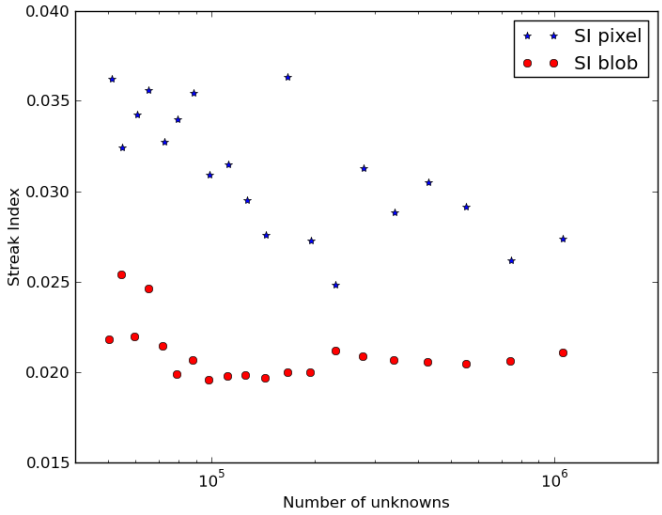

(b) Reconstruction SI

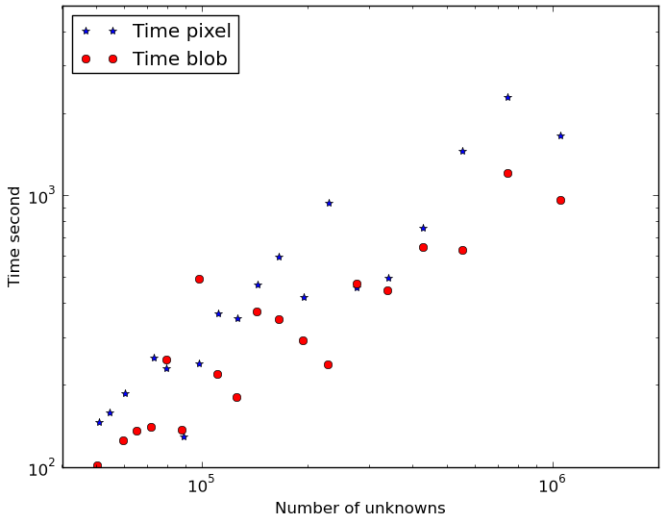

(c) Computation time

FIGURE 7.10: Thorax phantom: same experiment as in Figure 7.8.

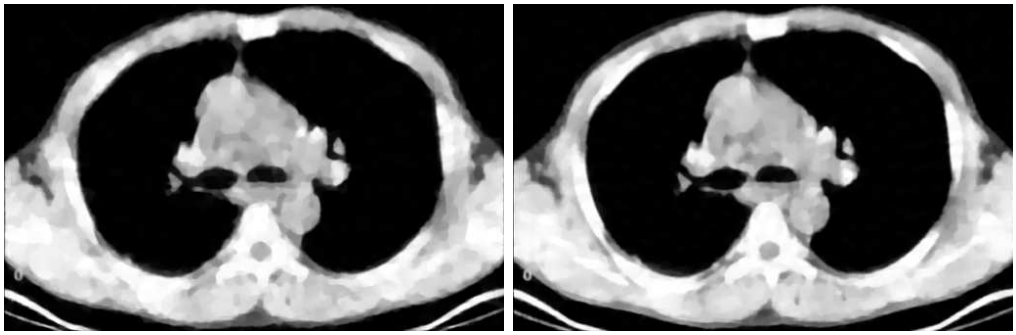

(a) TV, P=32, SNR=17.65dB, SI=0.019

(b) TV, P=48, SNR=19.33dB, SI=0.018

(c) TV, P=64, SNR=19.78dB, SI=0.016

(d) TV, P=96, SNR=20.57dB, SI=0.014

(e) CG, P=96, SNR=18.93dB, SI=0.027

(f) Lung phantom

FIGURE 7.11: Δ = TV with different number of projections P, $w = [0, 0.9]$. For all the reconstructions, the hexagonal lattice sampling step is fixed to $h = 0.292$, yielding the number of blobs 253383. Figure (e) is the reconstruction by CG method.

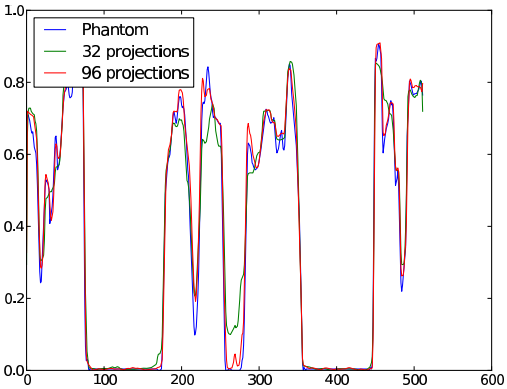

(a) Horizontal central profile

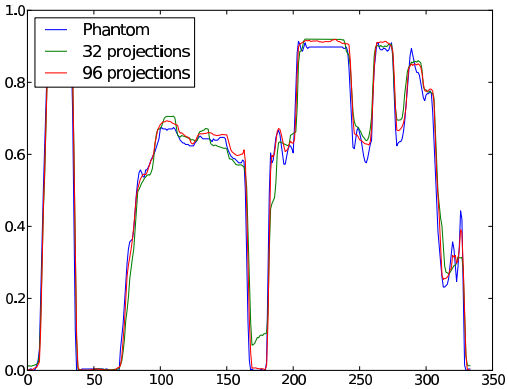

(b) Vertical central profile

FIGURE 7.12: Lung phantom: central profiles of Figure 7.11(a), (d) and (f)

- We are not very surprised to see that the Shepp-Logan and the Abdomen phantoms have similar curves (although the SI of the Shepp-Logan phantom is much smaller), since the later is blocky and almost piecewise constant.
- More projections are needed for the Thorax phantom since it contains a large low contrast and texture regions which are difficult to reconstruct by TV minimization, and yields a non monotone behavior in the reconstruction quality.

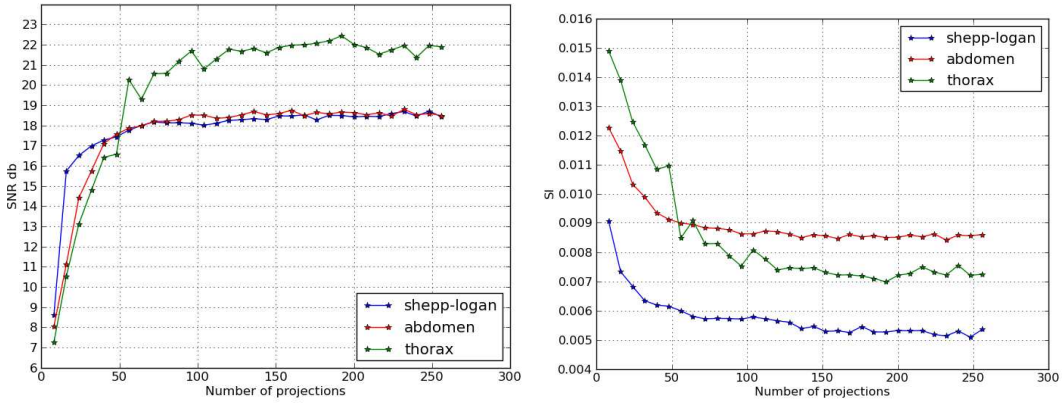

(a) SNR (b) SI

FIGURE 7.13: TV reconstruction quality vs number of projections on different phantoms: Shepp-Logan, Abdomen, and Thorax. Figure (a) and (b) show the SNR and the Streak Index of reconstructions.

7.1.4 Reconstruction with noisy data

We demonstrate here the stability of the TV minimization with respect to noise. In Figure 7.14 we plot the SNR and SI of reconstruction from different number of projections, by varying the noise level in the range of 10 to 50dB. The parameters for blob image are the same as in previous section, and the parameter μ has been chosen manually to maximize the output SNR.

It can be seen that for more than 64 projections, the reconstruction quality is monotonically improved when the noise level in data decreases, and the improvement is more important on the interval $[20, 35]$dB than on the interval $[35, 50]$dB. This suggests that the TV minimization method can "tolerate" the noise up to a certain level, after which the reconstruction quality drops very rapidly. Empirically speaking (see Eq. (7.2)), reducing the source's photon intensity by a factor of 10 results a lose of 10dB in the output sinogram, so these results suggest that the very high dose (*e.g.*, those with SNR($\mathbf{b}$) larger than 40dB) is not necessary for TV minimization.

Figure 7.15 are the reconstructions of Lung phantom from 64 projections using the data of SNR 20 30, 40, and 50dB, simulated by following the method described at the

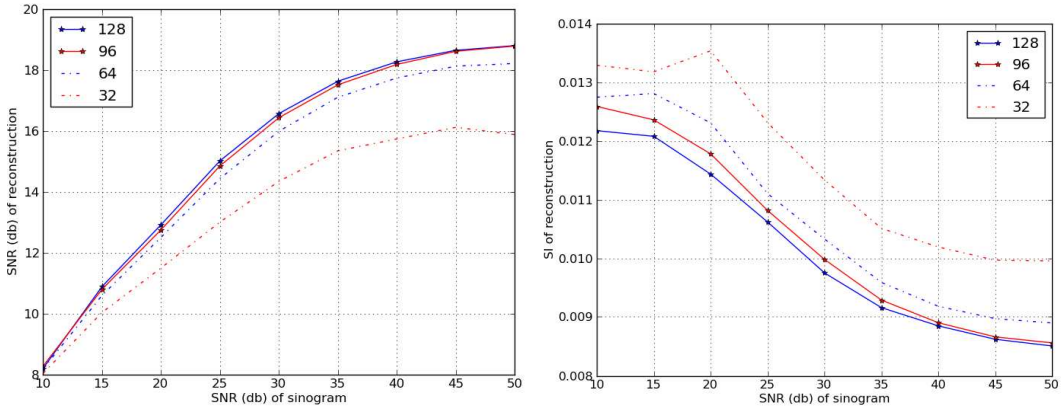

(a) SNR (b) SI

FIGURE 7.14: Abdomen phantom: reconstructions with $\Delta = \text{TV}$on data of SNR($\mathbf{b}$) in the range $[10, 50]$dB, $P = 32, 64, 96, 128$.

beginning of this chapter. The results of the same experiment on the Abdomen phantom are shown in figures 7.16 (d), (e) and (f).

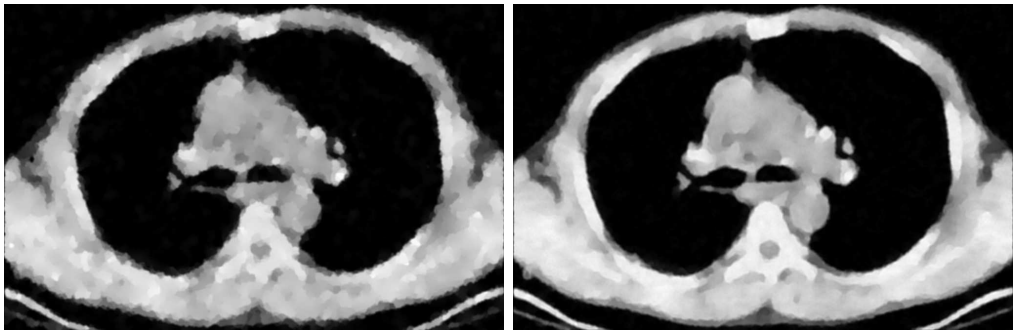

(a) SNR($\mathbf{b}$) = 20dB, SNR=16.13dB, SI=0.020 (b) SNR($\mathbf{b}$) = 30dB, SNR=18.75dB, SI=0.019

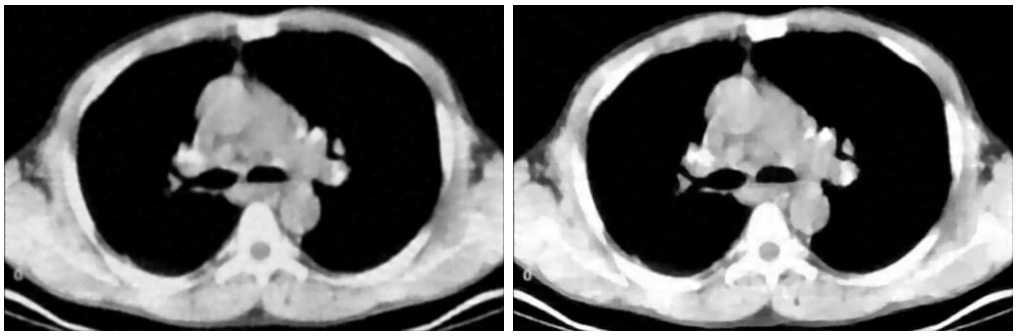

(c) SNR($\mathbf{b}$) = 40dB, SNR=19.80dB, SI=0.017 (d) SNR($\mathbf{b}$) = 50dB, SNR=19.78dB, SI=0.016

FIGURE 7.15: $\Delta = \text{TV}$, $P = 64$, $w = [0, 0.9]$ using the sinogram data of SNR 20dB (a), 30dB (b), 40dB (c) and 50dB (d).

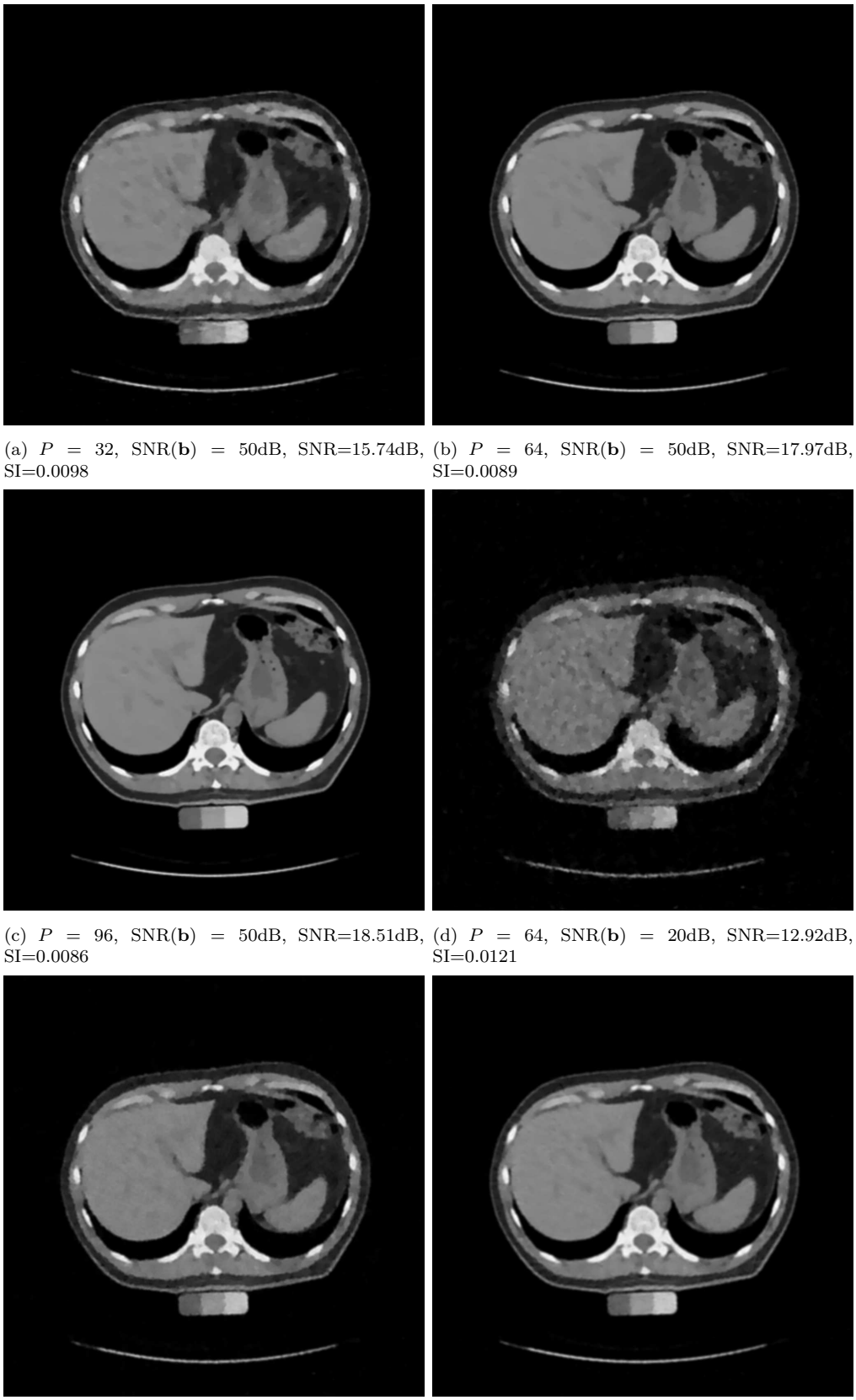

(a) $P = 32$, SNR($\mathbf{b}$) = 50dB, SNR=15.74dB, SI=0.0098

(b) $P = 64$, SNR($\mathbf{b}$) = 50dB, SNR=17.97dB, SI=0.0089

(c) $P = 96$, SNR($\mathbf{b}$) = 50dB, SNR=18.51dB, SI=0.0086

(d) $P = 64$, SNR($\mathbf{b}$) = 20dB, SNR=12.92dB, SI=0.0121

(e) $P = 64$, SNR($\mathbf{b}$) = 30dB, SNR=15.82dB, SI=0.0102

(f) $P = 64$, SNR($\mathbf{b}$) = 40dB, SNR=16.65dB, SI=0.0097

FIGURE 7.16: $\Delta =$ TVfor various P and data SNR, $w = [0, 1]$.

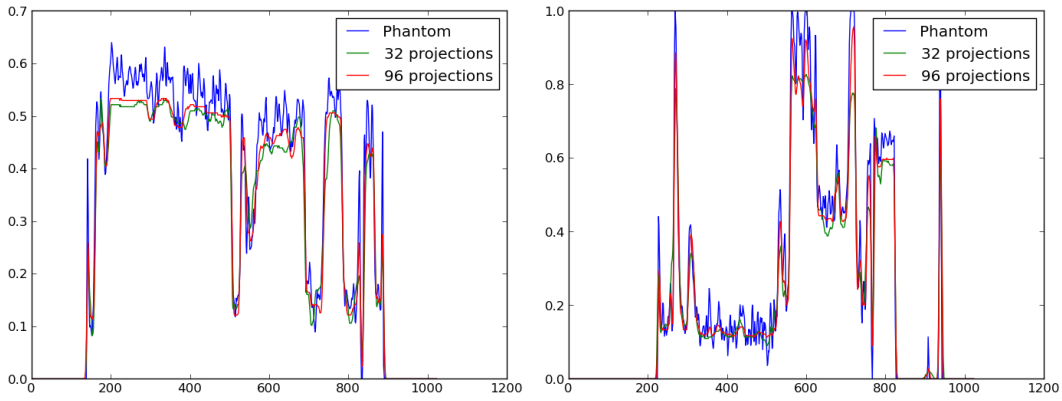

(a) Horizontal central profile (b) Vertical central profile

FIGURE 7.17: Abdomen phantom: central profiles of Figure 7.16(a), (c) and the original phantom.

7.2 ℓ^1 reconstruction results

Unless specified, the results presented in this section are obtained by solving the ℓ^1 minimization problem:

$$\min_{\mathbf{f}} \frac{1}{2}\|A\mathbf{f} - \mathbf{b}\|^2 + \mu\|f\|_1 \tag{7.7}$$

with the multiscale blob system (see Chapter 5, section 4):

$$f(x) = \sum_{j\in\mathbf{Z}} \sum_{k\in\mathbf{Z}^2} f_{j,k}\psi_j(x - x_k^j) \tag{7.8}$$

We present only the results with the Mexican hat multiscale blob system. In fact, the Diff-Gaussian and the Mexican hat multiscale blob systems give very close results on our test phantom, but the computation time of the Mexican hat blob is generally 2 or 3 times less than that of Diff-Gaussian blob, due to its much simpler mathematical expression and its better spatial localization.

7.2.1 Sparsity of the ℓ^1 reconstruction

Figure 7.18 shows the reconstruction with 128 projections using a 4 scales model. Figure 7.18(a) is the first scale image represented by the Gaussian blob on a very coarse lattice. It contains only the low frequency information, and the black background value is zero. Figure 7.18(b), (c), and (d) are respectively the scales -1, -2, -3 represented by the Mexican hat blob on the gradually refined lattices. The gray, black and white correspond respectively to zero, negative and positive values. At the fine scales, there are only a small percentage of significant non zero blobs, located around the edges and the isolated

discontinuities. In total there are less than 8.9% of non zero blobs. The final image in Figure 7.18(e) is the sum of the 4 scales.

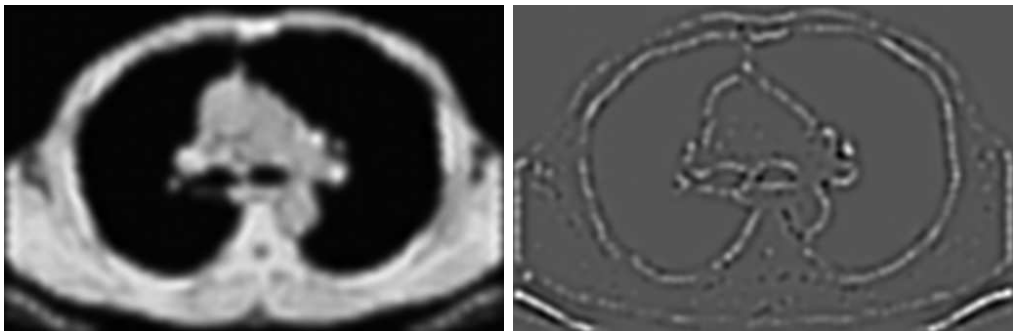

(a) Scale 0, τ=84.7%

(b) Scale -1, τ=20.7%

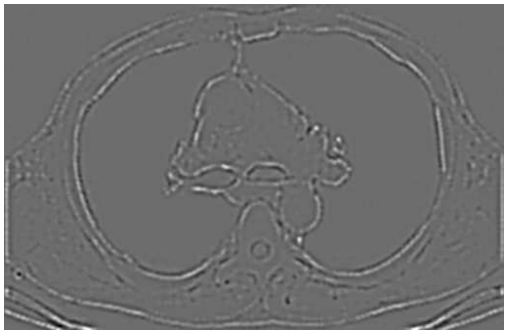

(c) Scale -2, τ=16.3%

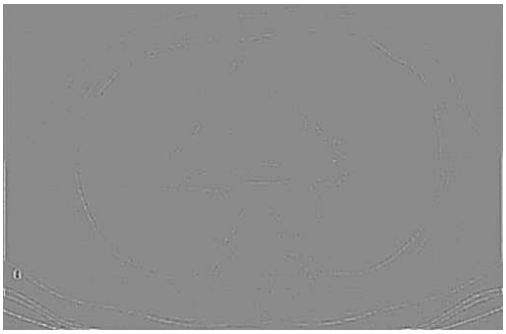

(d) Scale -3, τ=4.9%

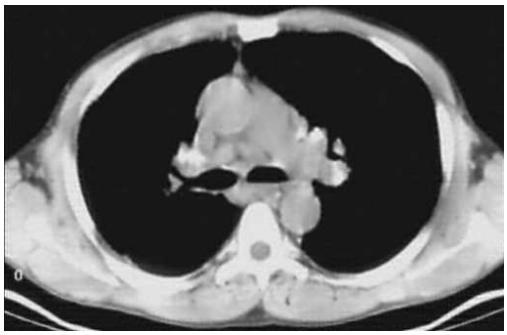

(e) $\Delta = \ell^1$, τ=8.9%, SNR=20.36dB, SI=0.0159, T=1155s

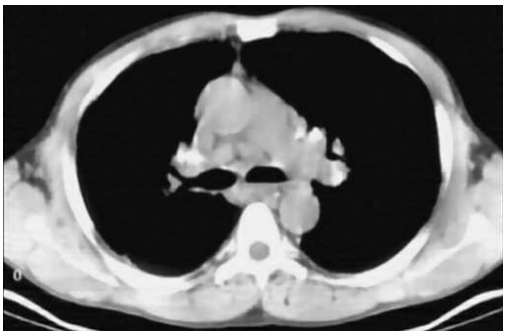

(f) Δ = TV, τ=100%, SNR=20.60dB, SI=0.0149, T=760s

FIGURE 7.18: $\Delta = \ell^1$, P=128, using a 4 scales Mexican hat blob system with N = 289243. The percentage in figure (a)-(d) indicates the sparsity level (proportion of non zero blobs) in each scale, and the global sparsity level is less than 8.9%. Note that in (f) by Δ = TVwith the same 4 scales system, the reconstructed coefficient vector is full.

TV reconstruction on the multiscale blob system In place of the ℓ^1 norm, we can apply the TV minimization on the same multiscale blob system. The reconstructed images are shown in Figure 7.18 (f). Remark that the TV minimization does not promote the sparsity of the solution and the reconstructed coefficients vector is full, *e.g.*, there is no zero blobs. The figure 7.18 (e) and (f) are visually very close, although the TV result has a slightly better SNR and SI, thanks to its edge preserving ability which is absent

in ℓ^1 minimization. Nevertheless, ℓ^1 minimization avoids the stair-wise effect of TV and recovers better the low contrast regions. This can be clearly seen from the zoomed image in Figure 7.19. In figure 7.20 we show the ROI view on the reconstructions of Abdomen phantom with 256 projections, which confirms also the superiority of the ℓ^1 minimization over TV in recovering low contrast and texture objects.

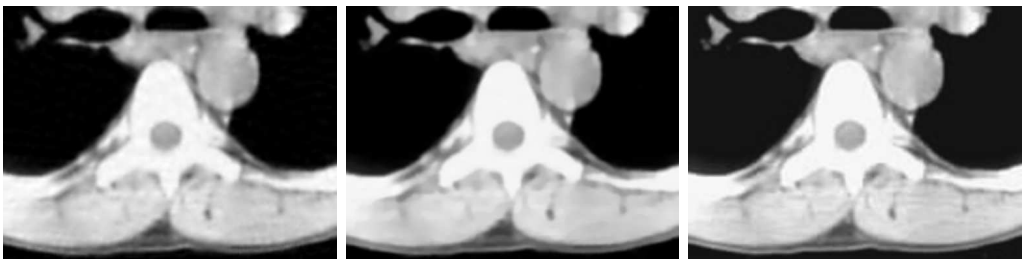

(a) $\Delta = \ell^1$, P=128 (b) Δ = TV, P=128 (c) Phantom

FIGURE 7.19: Lung phantom: zoomed view on the ROI of figures 7.18(e), 7.18(f) and the original phantom.

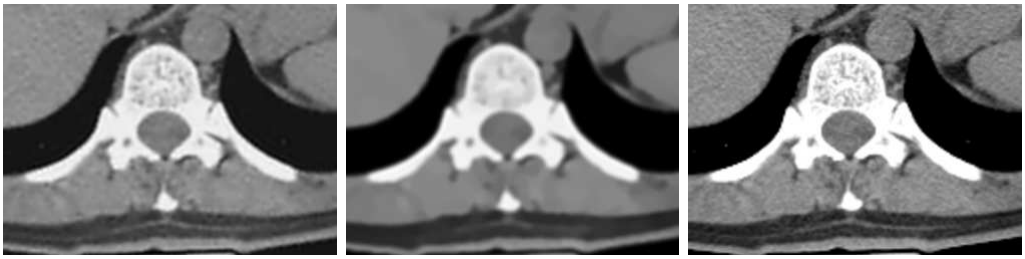

(a) $\Delta = \ell^1$, P=256 (b) Δ = TV, P=256 (c) Phantom

FIGURE 7.20: Abdomen phantom: zoomed view on the ROI of the ℓ^1 and the TV reconstructions and the original phantom.

7.2.2 ℓ^1 reconstruction using few projections

The reconstructions using 48, 64 and 96 projections with the Mexican hat multiscale blob system are shown in Figure 7.24 (a), (c), and (e). Compared to the TV results in Figure 7.11, it seems that the ℓ^1 minimization is far less efficient when the number of projections decreases. Indeed, these results suffer severely from the streak artifacts, contaminating even the low frequency scale when the number of projections is highly insufficient, see Figure 7.21. The magnitude of these artifacts are often close to that of meaningful image contents, consequently, it is difficult for the ℓ^1 solver which employs a soft shrinkage operation on the blob coefficients, to remove these artifacts without damaging the reconstruction image quality.

Reconstruction quality vs. number of projections We carry out the same test on different phantoms: Shepp-Logan, Thorax and Abdomen (Figure 7.1 (b), (c) and

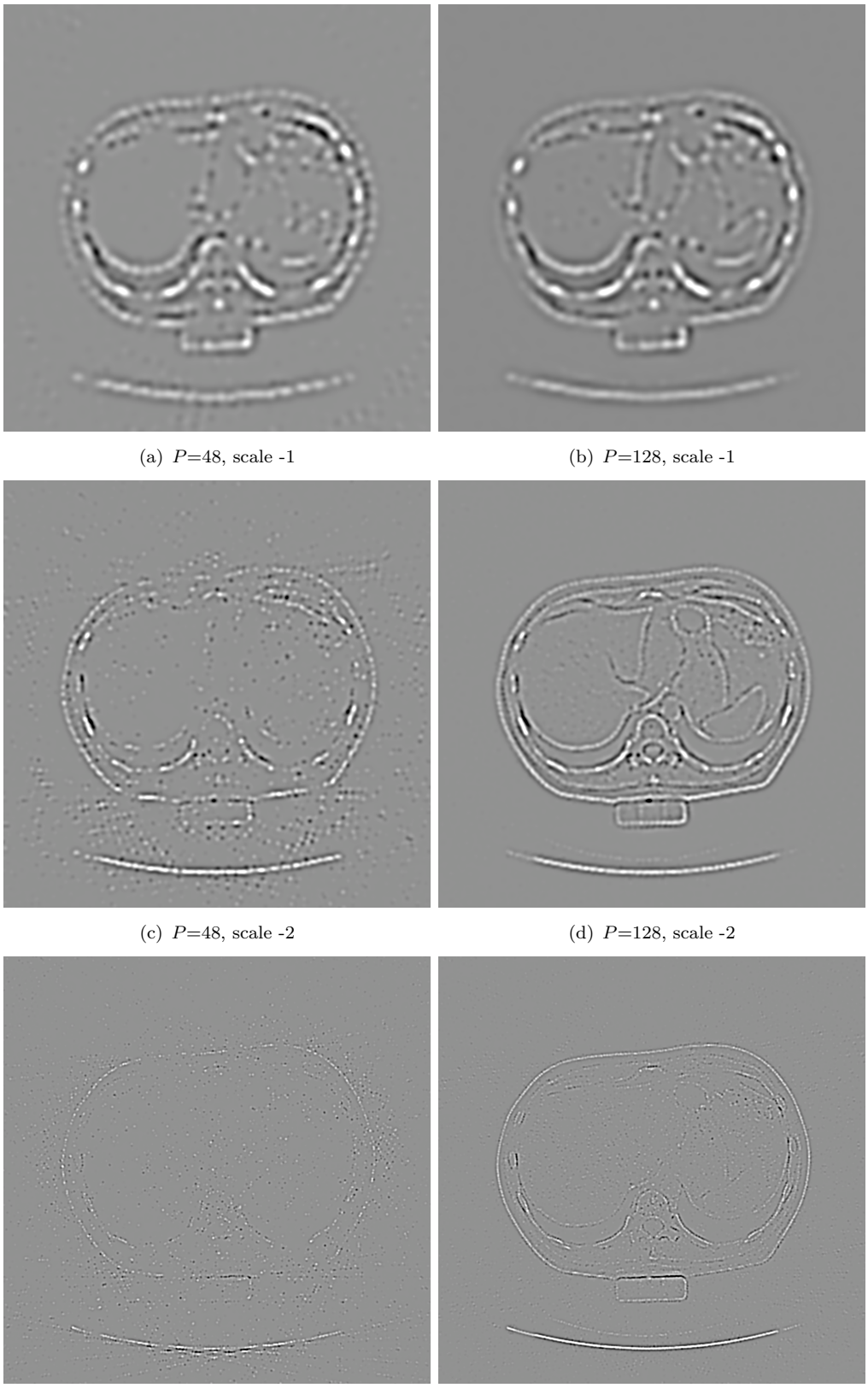

(a) P=48, scale -1

(b) P=128, scale -1

(c) P=48, scale -2

(d) P=128, scale -2

(e) P=48, scale -3

(f) P=128, scale -3

FIGURE 7.21: Abdomen phantom: fine scales of ℓ^1 reconstruction using the same 4 scales Mexican hat blob system. P=48 (first column) and P=128 (second column), $w = [-0.3, 0.3]$. Background gray color represents zero. The streak artifacts corrupt even the coarse scale when P is small.

(d)), with P varying from 8 to 256. The SNR and the SI are plotted in Figure 7.22. We can compare these results with those of the TV reconstruction presented in figure 7.13, and find that the ℓ^1 minimization has very different behavior, see Figure 7.23:

- The image quality improves monotonically as the number of projections increases. This is particularly the case of the Thorax phantom, on which the TV reconstruction behaves irregularly, see Figure 7.13.
- Unlike the TV case where the reconstruction quality remains constant when P is larger than certain number (*e.g.*, 130 projections), the ℓ^1 reconstruction continues to improve substantially with P. For Thorax and Abdomen phantoms, the ℓ^1 results are superior to the TV results for $P \geq 100$ in terms of SNR, and for $P \geq 170$ in terms of SI.

These observations reveal the fundamental difference between the TV and the ℓ^1 minimization. As the analysis given in Chapter 3, section 1.3, the TV minimization solution is a kind of projection onto the "texture free" space, and is always different to the true object. Particularly, the reconstruction error can not be arbitrarily reduced as long as the original image contains textures. On the other hand, Compressed Sensing theory (see Chapter 4) gives a quantitative estimation of the reconstruction error of the ℓ^1 minimization problem:

$$\min_{\mathbf{f}} \|\mathbf{f}\|_1 \text{ s.t. } \|A\mathbf{f} - A\mathbf{g}\|^2 \leq \varepsilon^2 \tag{7.9}$$

It says that if the measurement matrix satisfies the RIP condition of order $2S$, *e.g.*, $\delta_{2S} < \sqrt{2} - 1$, then the solution f of Eq. (7.9) fulfills

$$\|\mathbf{f} - \mathbf{g}\|_2 \leq c_1 \frac{\|\mathbf{g} - \mathbf{g}_S\|_1}{\sqrt{S}} + c_2 \varepsilon \tag{7.10}$$

with ε the noise level contained in data, and $\mathbf{g}_S$ the best S term approximation. For a good sensing matrix (see Chapter 4), the RIP condition is improved as the number of measurements increases, in the sense that the sparsity level S in the RIP condition behaves as

$$S \lesssim \frac{M}{\log(N/M)} \tag{7.11}$$

with M the number of measurements and N the dimension of $\mathbf{g}$. As a consequence of (7.10), if $\mathbf{g}$ is compressible (*e.g.*, the S-term approximation error decreases faster than $\sqrt{S}$), the reconstruction error continues to improve as the number of measurements increases, until being dominated by the noise level.

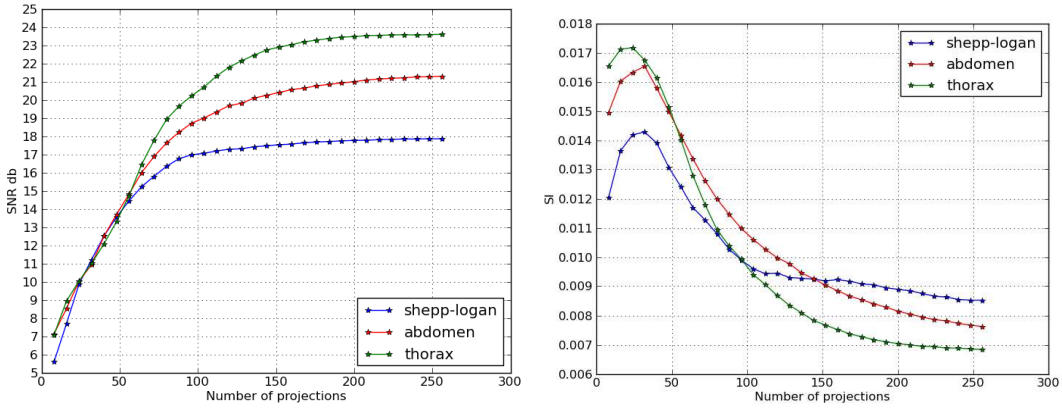

(a) SNR (b) SI

FIGURE 7.22: Shepp-Logan, Abdomen, and Thorax phantoms: ℓ^1 reconstruction quality vs. number of projections. Remark that the small SI value of the reconstructions with fewer than 20 projections are meaningless, since these reconstructions have been totally failed.

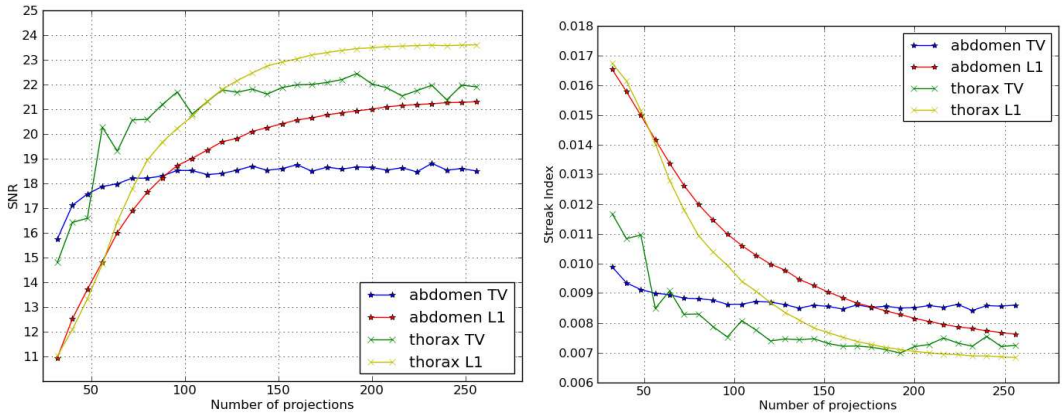

(a) SNR (b) SI

FIGURE 7.23: Abdomen and Thorax phantoms: comparison between the TV and the ℓ^1 reconstructions, for P varying in $[32, 256]$.

7.2.3 Comparison with wavelet reconstruction

In order to reveal the advantages of the multiscale blob system, we compare its reconstructions with those based on the orthogonal Daubechies wavelet basis, also formulated through the ℓ^1 minimization problem:

$$\min_{\mathbf{f}} \frac{1}{2}\|AD\mathbf{f} - \mathbf{b}\|^2 + \mu\|\mathbf{f}\|_1, \ \mathbf{f} \in \mathbb{R}^N, \tag{7.12}$$

which is solved using the same IST algorithm. Here $\mathbf{f}$ denotes the wavelet coefficients and D is a wavelet synthesis operator. In this example we use the Daubechies wavelet of order 6 and D is the associated decimated discrete wavelet transform (DWT). A is a Siddon ray-tracing projector implemented on GPU and applies on the pixel image $D\mathbf{f}$.

The parameter μ is determined as precedent, *i.e.*, we choose manually the value which maximizes the reconstruction quality. By solving (7.12), one recovers the wavelet coefficient $\mathbf{f}$, then the final image is synthesized as $D\mathbf{f}$. In order to make a fair comparison, we set the dimension of $\mathbf{f}$ in the wavelet reconstructions to the one of the phantom image, and choose the blob image parameter to keep the number of blobs as close as possible to their counterparts. The number of scales in the wavelet decomposition and in the blob system are respectively 8 and 4.

The reconstructions from 48, 64 and 96 projections are shown in Figure 7.24 and 7.25, where the first and the second row are respectively the blob and the wavelet results. It can be seen that, at the same number of projections, the blob reconstruction is always better than the wavelet one, which suffers from the high frequency oscillation patterns in the background. There are two possible reasons for the superiority of blob. First, our multiscale blob system is redundant therefore less concerned by the pseudo Gibbs artifacts, which is a typical problem when thresholding under an orthogonal wavelet basis, see Figure 7.26. Secondly, although the number of unknowns is almost the same in two approaches, the blob reconstruction works in a lower bandwidth than the wavelet reconstruction does, therefore avoids the high frequency artifacts without compromising the image quality, thanks to the better space-frequency localization property.

7.2.3.1 Drawbacks of ℓ^1 minimization

On the images which contains low contrast regions and oscillating patterns (*e.g.*medical oriented), our results in section 7.2.2 suggests that the multiscale blob coupled with ℓ^1 minimization would be the preferred reconstruction method over the TV minimization since they preserve these characters while TV removes them, under the condition that the number of projections is relatively important, typically $P \geq 150$. If the number of projections is highly insufficient, typically $P \leq 80$, the reconstruction of ℓ^1 minimization suffers severely from high frequency artifacts, and the visual quality is largely inferior to the TV counterpart. Apart of the streak artifacts (see Figure 7.21), we also distinguish from the zoomed view in Figure 7.26, a kind of "salt and pepper" noisy pattern on the low contrast regions which are mainly due to isolated blobs of fine scales, which can be easily confused with the true porous structures. In light of the inequality (7.11), we see that when the number of data M is small, the ℓ^1 minimization which does not distinguish the coefficients of different scales, makes more approximation errors by favoring energy transfer between scales and using isolated blobs of fine scales in order to match the local minima/maxima of the phantom image. Reducing these noisy pattern can make the ℓ^1 minimization more adequate for P in a middle range.

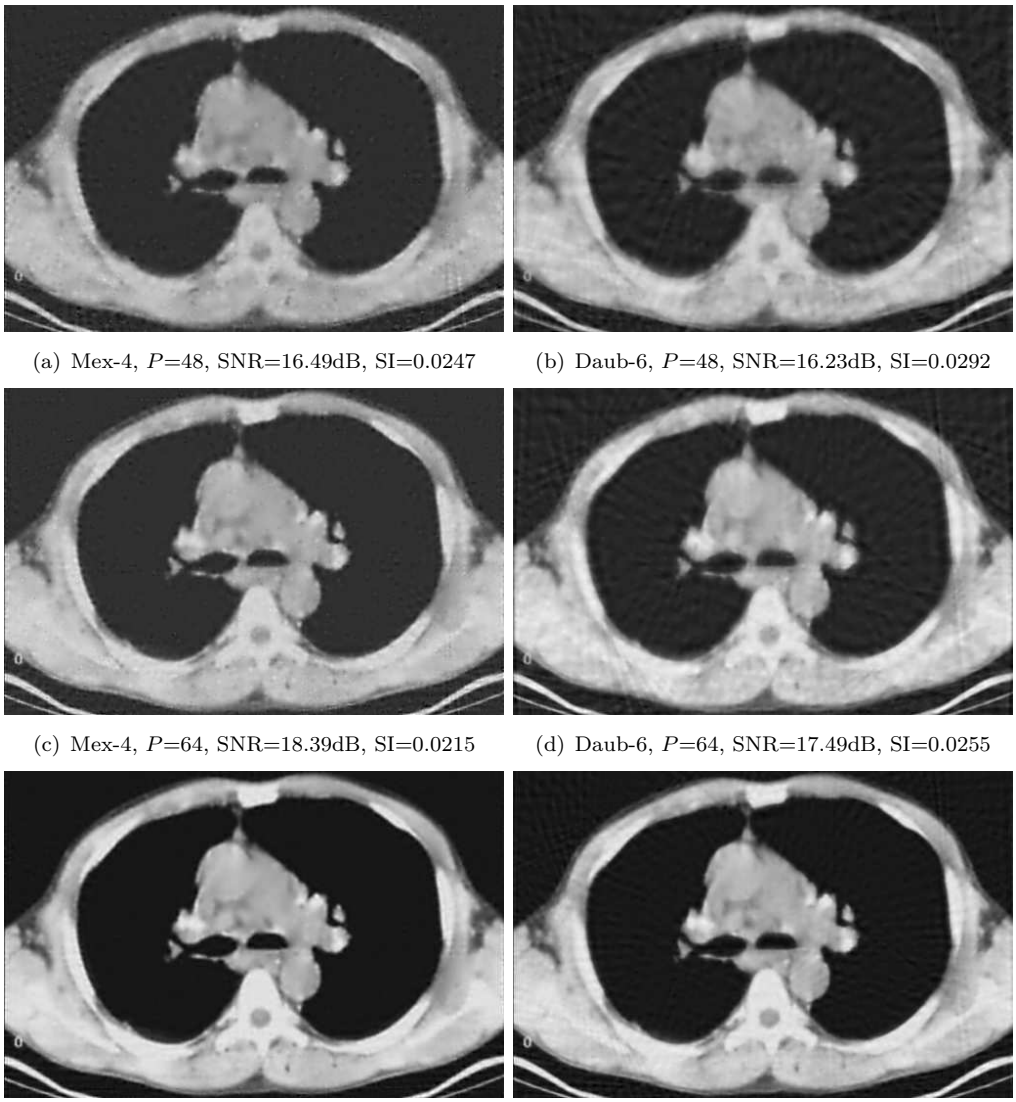

(a) Mex-4, P=48, SNR=16.49dB, SI=0.0247 (b) Daub-6, P=48, SNR=16.23dB, SI=0.0292

(c) Mex-4, P=64, SNR=18.39dB, SI=0.0215 (d) Daub-6, P=64, SNR=17.49dB, SI=0.0255

(e) Mex-4, P=96, SNR=20.04dB, SI=0.0173 (f) Daub-6, P=96, SNR=18.59dB, SI=0.0211

FIGURE 7.24: $\Delta = \ell^1$with P=48, 64, 96, $w = [-0.2, 1.2]$. First column: using 4 scales Mexican hat blob system. Second column: using Daubechies wavelet of order 6.

7.2.4 Reweighted iterative ℓ^1 minimization reconstruction

In Section 6.3 we argued why the standard ℓ^1 minimization problem can be improved by its reweighted iterative version:

$$\min_{\mathbf{f}} \|\mathbf{w} \odot \mathbf{f}\|_1 \quad \text{s.t.} \quad \|A\mathbf{f} - \mathbf{b}\|_2^2 \leq \varepsilon^2 \tag{7.13}$$

where $\mathbf{w} \in \mathbb{R}_+^N$ denotes the weight vector and $\mathbf{w} \odot \mathbf{f}$ is the element-wise product between two vectors. Here we solve (7.13) for 6 iterations using the Algorithm 6. The weight $\mathbf{w}$ is updated at each new iteration by $w_k = (|f_k| + 10^{-3})^{-1}$, with f_k the k-th coefficient of the solution returned by the last iteration. In Figure 7.27 we plot the SNR and the SI of the reconstructions for the phantom Abdomen by varying the number of projections

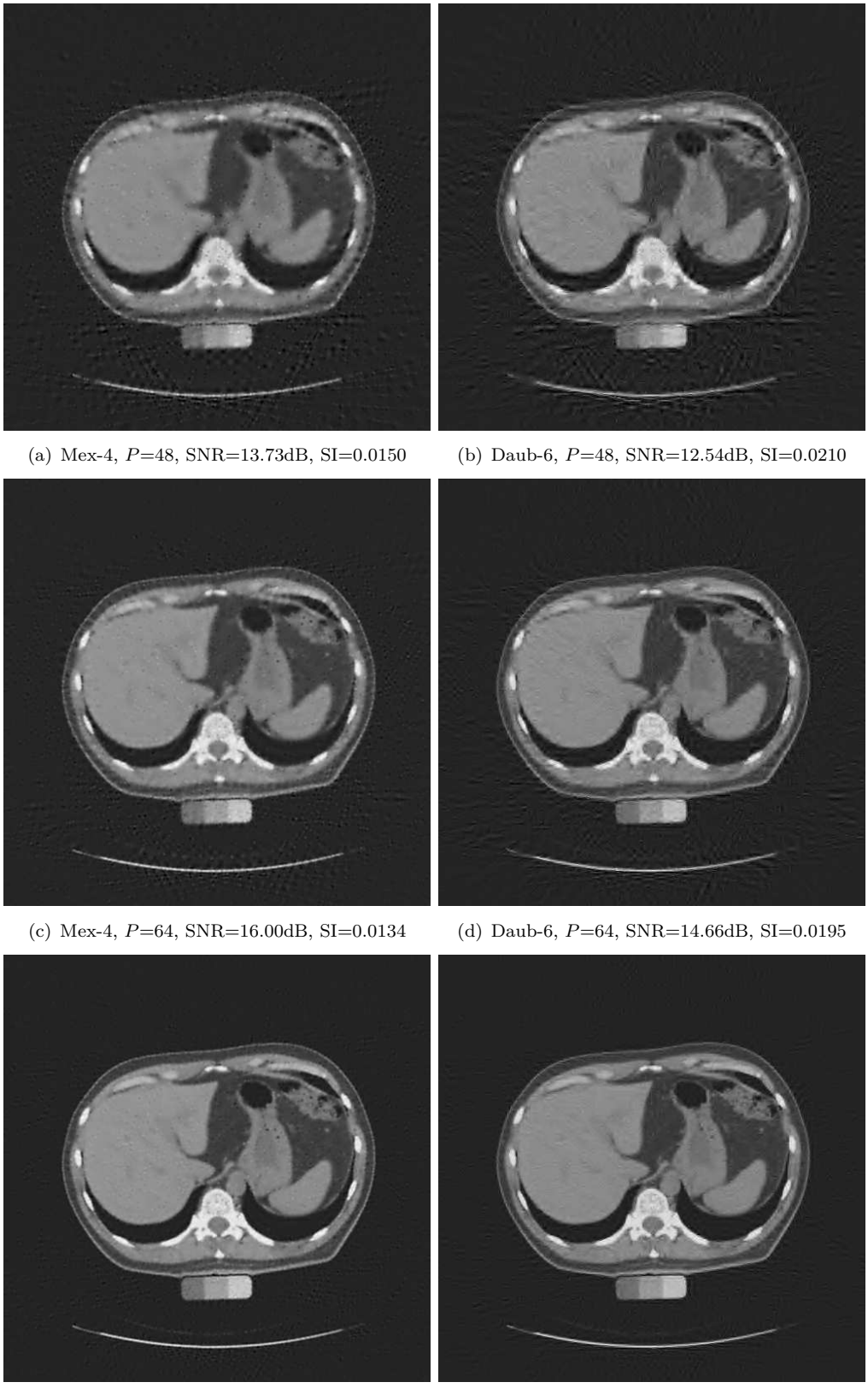

(a) Mex-4, P=48, SNR=13.73dB, SI=0.0150

(b) Daub-6, P=48, SNR=12.54dB, SI=0.0210

(c) Mex-4, P=64, SNR=16.00dB, SI=0.0134

(d) Daub-6, P=64, SNR=14.66dB, SI=0.0195

(e) Mex-4, P=96, SNR=18.53dB, SI=0.0111

(f) Daub-6, P=96, SNR=16.40dB, SI=0.0175

FIGURE 7.25: $\Delta = \ell^1$with P=48, 64, 96, $w = [-0.2, 1.2]$. First column: using 4 scales Mexican hat blob system. Second column: using Daubechies wavelet of order 6.

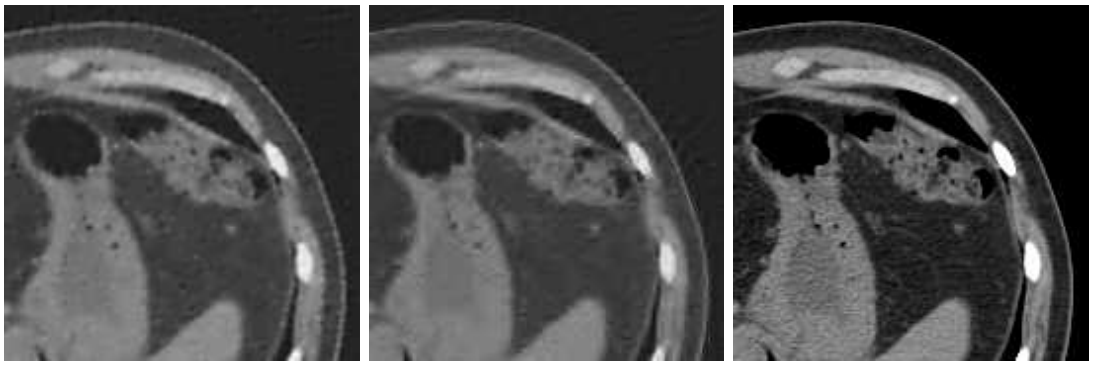

(a) Mexican hat blob (b) Daubechies wavelet (c) Phantom

FIGURE 7.26: Abdomen phantom: zoomed views on the ROI of Figure 7.25 (c), (f) and the original phantom. $w = [-0.2, 1.2]$ for (a) and (b).

between 32 and 256. It can be observed that only very slight improvement in SI has been obtained, which can not even be perceived in the reconstructed image.

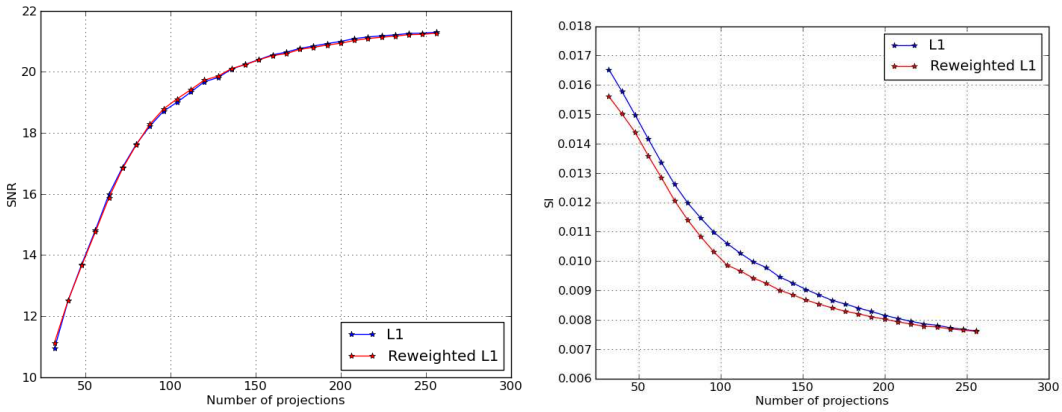

(a) SNR (b) SI

FIGURE 7.27: Abdomen phantom: comparison between the reweighted iterative and the standard ℓ^1 minimization. 6 reweighted iterations has been used. The value ε in (7.13) is chosen manually according to the noise level.

Such a result can be explained as follows. It has been pointed out in [122] that the reweighted iterative ℓ^1 minimization approximates the ℓ^q minimization for $q < 1$, while the later performs significantly better than ℓ^1 decoder only for highly compressible signals, *e.g.* those on weak ℓ^p ball for $p < q$ (See the numerical experiments in [129]). In Figure 7.28 we plot the blob coefficients' decaying rate of the Abdomen phantom using a 4 scales Mexican hat blob system, and through a numerical estimation we obtain the value $p \simeq 1.57$ which indicates that the phantom image is only moderately compressible.

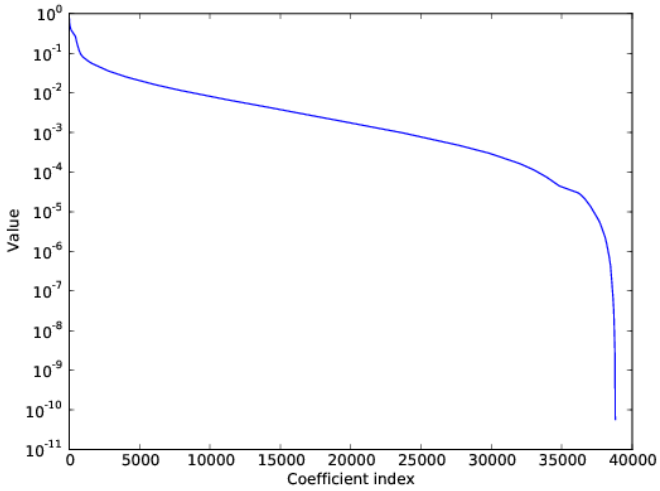

FIGURE 7.28: Abdomen phantom: reconstructed non zero blob coefficients with Mex-4, $P = 256$. Total number of blobs $N = 314302$, the sparsity level of the reconstructed coefficients $\tau = 12.3\%$. The coefficients are sorted such that $|f_{(0)}| \geq |f_{(1)}| \geq \cdots$. The vertical axis is in logarithmic scale. Numerical estimation for the index range in $[5000, 35000]$ reveals that the coefficient vector decays as $n^{-1/p}$ for $p \simeq 1.57$.

7.3 TV-ℓ^1 reconstruction results

As explained in Section 6.3, another way to improve the standard ℓ^1 minimization is to solve the TV-ℓ^1 minimization problem:

$$\min_{\mathbf{f}} \frac{1}{2}\|A\mathbf{f} - \mathbf{b}\|^2 + \mu_1\|\mathbf{f}\|_1 + \mu_2\|\mathbf{f}\|_{TV} \tag{7.14}$$

Here we choose manually the parameters by keeping the ratio $\mu_1/\mu_2 = 100$, and expect to remove the erroneous blobs of fine scales by taking advantage of the TV norm's ability in preserving edges and constant regions.

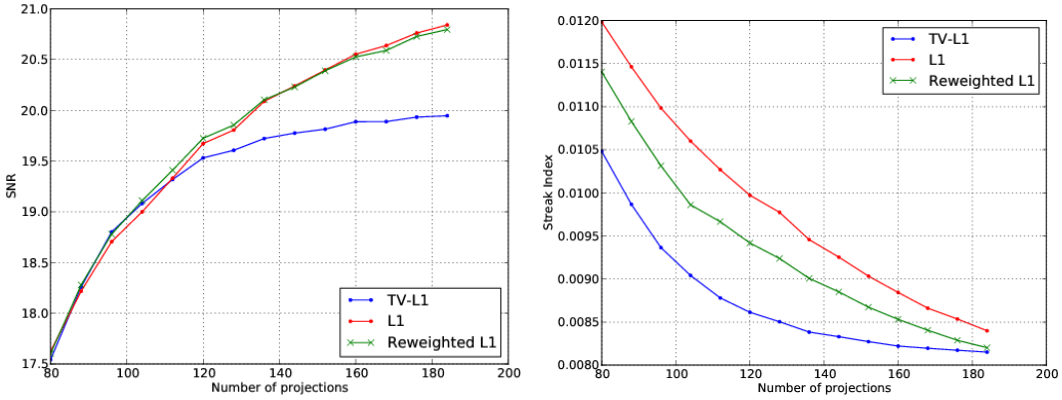

(a) SNR (b) SI

FIGURE 7.29: Comparison between the standard ℓ^1, the reweighted iterative ℓ^1 and the TV-ℓ^1 reconstructions on the phantom Abdomen, for the number of projections varying from 80 to 160. The ℓ^1 and the reweighted ℓ^1 results are the same as in Figure 7.27.

The reconstructions for the number of projections in the range $[80, 180]$ are plotted in Figure 7.29. It can be observed that for the number of projections between 80 and 120, the TV-ℓ^1 model (7.14) has successfully combined the "best part" of the TV and the ℓ^1 methods: the SNR of the TV-ℓ^1 results are very close to that of the standard ℓ^1 results, which indicates that the solution is indeed a sparse one, while their Streak Index values are considerably smaller than the standard ℓ^1 results, which means that the high frequency artifacts are reduced by the TV term. See also Figure 7.30. For the number of projections larger than 150, the ℓ^1 reconstruction is definitely better than the TV-ℓ^1 in terms of SNR, and the smaller SI value of the later suggests that the "texture-killer" behavior of the TV minimization appeared, so a smaller parameter μ_2 in (7.14) should be considered in this case.

In the first column of Figure 7.30 we show the ROI of reconstructions using different methods from 128 projections. The TV-ℓ^1 result is in Figure 7.30 (e). Compared with the standard ℓ^1 reconstruction (Figure 7.30.(a)), the "salt-and-pepper" noise pattern is greatly reduced; while compared with the TV reconstruction (Figure 7.30.(c)) the low contrast regions and small objects are better preserved. The second column of Figure 7.30 shows the finest scale of the 4 scale Mexican hat blob system. It can be seen that the streak artifact of the background which is very abundant in the ℓ^1 and the reweighted ℓ^1 reconstructions (Figure 7.30.(b) and (d)), almost disappears in the TV-ℓ^1 reconstruction (Figure 7.30.(f)), and the isolated blobs on the homogeneous regions inside the object also seem to get to the right place.

7.4 Concluding remarks

Using simulated data, in this chapter we have studied the blob image models and the reconstruction methods by comparing to the equivalent approaches based on pixel/wavelet, and the results in favor of blob have been observed on different phantom images under different scenarios. On the other side, we have also observed that depending on the factors like the object type and the number of available projections, the multiple reconstruction methods and blob image models may have different efficiency. A wide range of scenarios can be covered if we take advantage of the prior information and choose correctly the image model and (or) the reconstruction method. For example, for a piecewise constant object the simple Gaussian blob image coupled with the TV minimization method is fast and robust. For a medical object containing large low contrast regions and textures, the multiscale blob image model coupled with the ℓ^1 minimization method should be considered if the number of projections is relatively large, otherwise the TV or the TV-ℓ^1 method would be more appropriate.

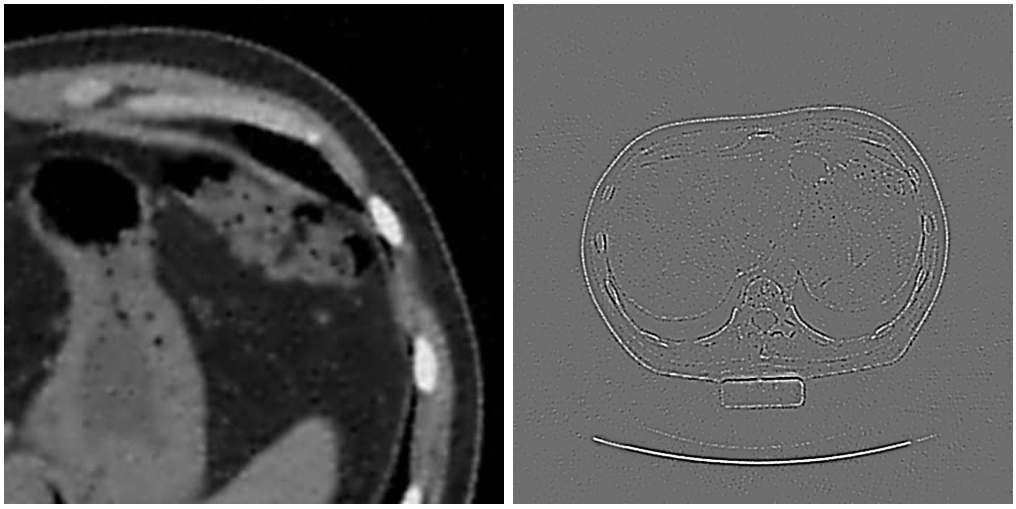

(a) $\Delta = \ell^1$, Mex-4, SNR=19.80dB, SI=0.0097

(b) $\Delta = \ell^1$, Mex-4, τ=12.61%

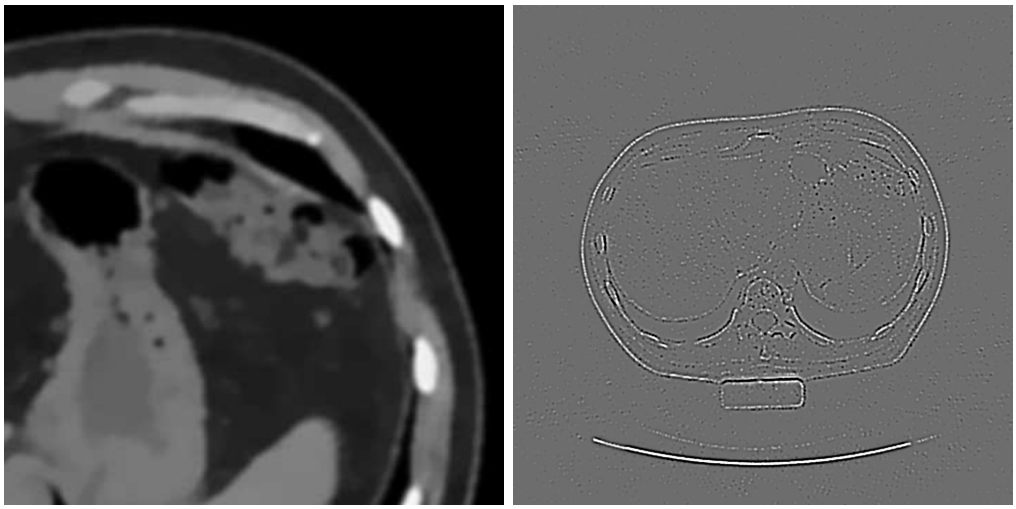

(c) Δ = TV, GS, SNR=18.52dB, SI=0.0086

(d) Δ=Reweighted ℓ^1, Mex-4, τ=8.87%

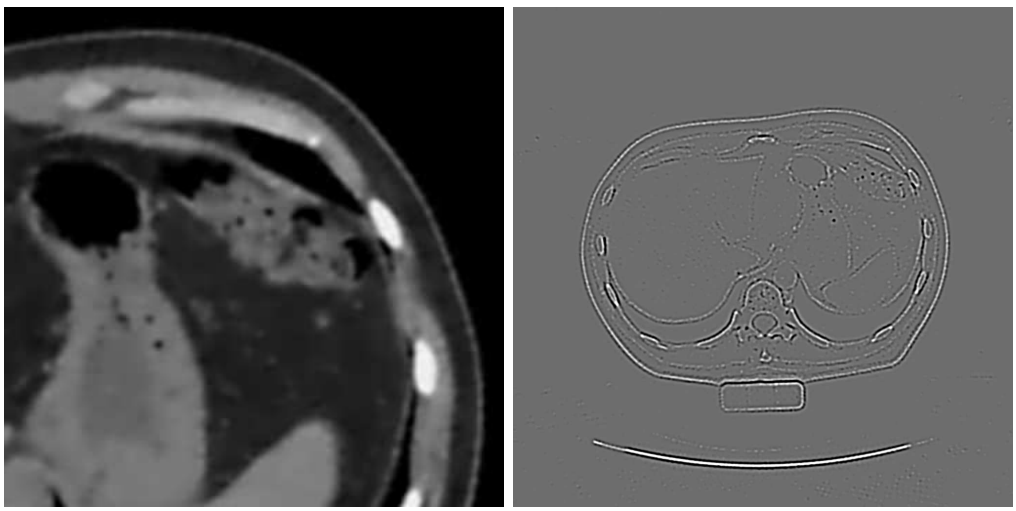

(e) Δ = TV$-\ell^1$, Mex-4, SNR=19.60dB, SI=0.0085

(f) Δ = TV $- \ell^1$, Mex-4, τ=16.33%

FIGURE 7.30: Abdomen phantom: reconstructions obtained using different methods, P=128. First column: zoomed views on the ROI. Second column: the finest scale picture with τ representing the percentage of non zero blobs in that scale.

Chapter 8

2D Numerical experiments - real data

In this chapter we present some preliminary results with real data obtained by our image models and reconstructions methods. The data that we use come from different application domains, and have been acquired independently by collaborators[1] on various non-commercial platforms. The geometrical parameters of the acquisition systems are known only with limited precisions. Unless specified, all the acquisitions are fan beam and *full scan i.e.*, the source is equally distributed on $[0, 2\pi]$. The same notations as Chapter 7 are used in this chapter.

8.1 Medical imaging

The 3D object in consideration is a piece of human spine fixed in epoxy resins of dimension $200 \times 110 \times 100$mm, and a horizontal slice is used as the 2D object to be reconstructed, as shown in Figure 8.1. The resin has much smaller attenuation coefficient than bones therefore can be treated as soft tissue. In Figure 8.1, we can also distinguish some air bubbles enclosed in resins. A possible medical application related to this experiment is the detection of demineralization by estimating the cortex thickness for aged person, where the radiation dose delivered to the patient is proportional to the number of projections.

Acquisition system The data have been acquired on a platform assembled in our laboratory, see Figure 8.2. The X-ray source of current 2.9mA is accelerated at 100kV

[1]The author thanks C.Cai, M.Costin, and G.Haberfehlner for having provided the sinogram data of this chapter.

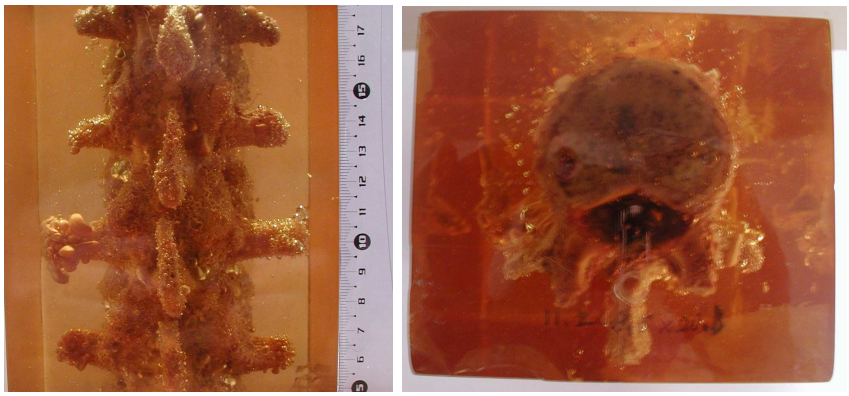

(a) Coronal (b) Transverse

FIGURE 8.1: Human spine fixed in resins

without pre-filtering (polychromatic source), and the exposure time is 1.82ms. We collect 360 fan-beam projections with a linear detector has 1024 pixels. At each angular position, we repeat 512 acquisitions and assign their average as the output in order to improve the signal-to-noise ratio of the sinogram. Other parameters are:

- Source to rotation axis distance: 208.76 mm
- Detector to rotation axis distance: 321.66 mm
- Detector length: 409.6 mm
- X-ray spot size: 0.6 mm

Reconstructions by CG To have a reference image, we solve the least square problem $\min_{\mathbf{f}} \|A\mathbf{f} - \mathbf{b}\|$ using all available data (360 projections and 1024 detector bins for each projection) by CG. The ring artifacts observed in the least square solution Figure 8.3 (a) and (b) are attenuated by the Tikhonov regularization (see Section 3.1.1.1) Figure 8.3 (c). In these reconstructions, one can clearly distinguish the spongy structures inside the spine and the cortex in white color which is much more absorbent. It seems that the cortex has been overly dilated due to the beam-hardening artifact, since the polychromatic source is not handled by our reconstruction algorithm.

Few projections We extract P equally distributed projections, and downsample the X-ray detector by half. The resulting sinogram has dimension $P \times 512$. Figure 8.4 shows the results for $P = 96, 128, 160$ obtained using the TV minimization based on Gaussian blob (second column), and for comparison the Tikhonov regularizations based on pixel are shown in the first column.

FIGURE 8.2: Acquisition system for the spine object. From right to left: X-ray tube, gantry and sample, linear detector.

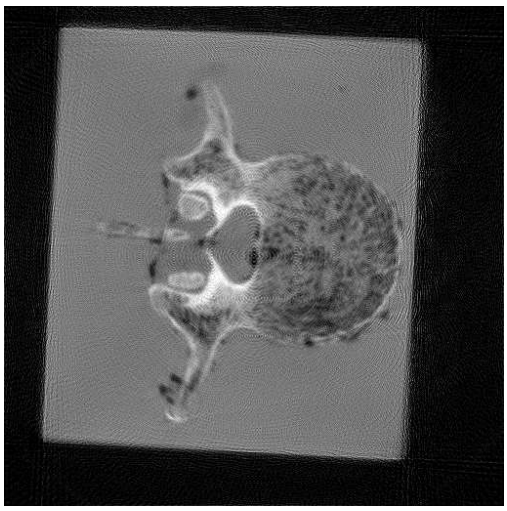

(a) Δ = Least Square, pixel, 25 CG iterations

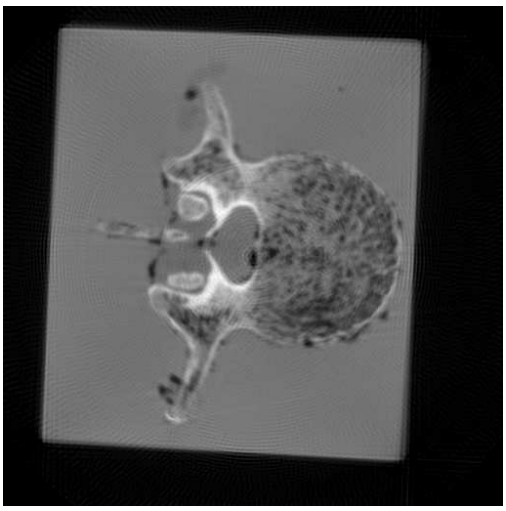

(b) Δ = Least Square, GS, 100 CG iterations

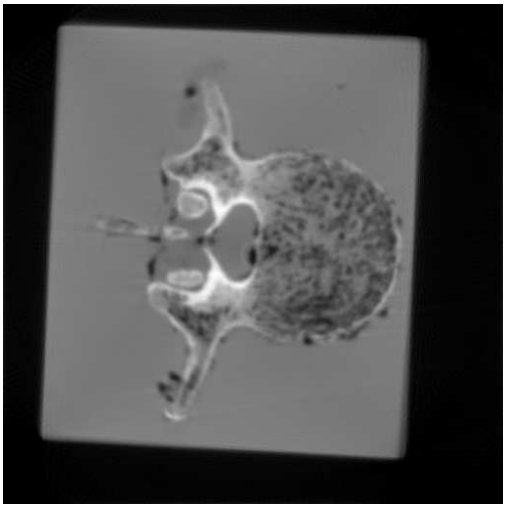

(c) Δ = Tikhonov, pixel, 100 CG iterations

FIGURE 8.3: Reconstructions using 360 projections and 1024 detector bins. Figure (a) and (c) are based on pixel (512×512) of side length 0.25mm. Figure (b) is the same least square solution as (a) but using the Gaussian blob of FWHM 0.406mm. The linear window $[0, 0.049]$ was used for visualization. The black background represents air.

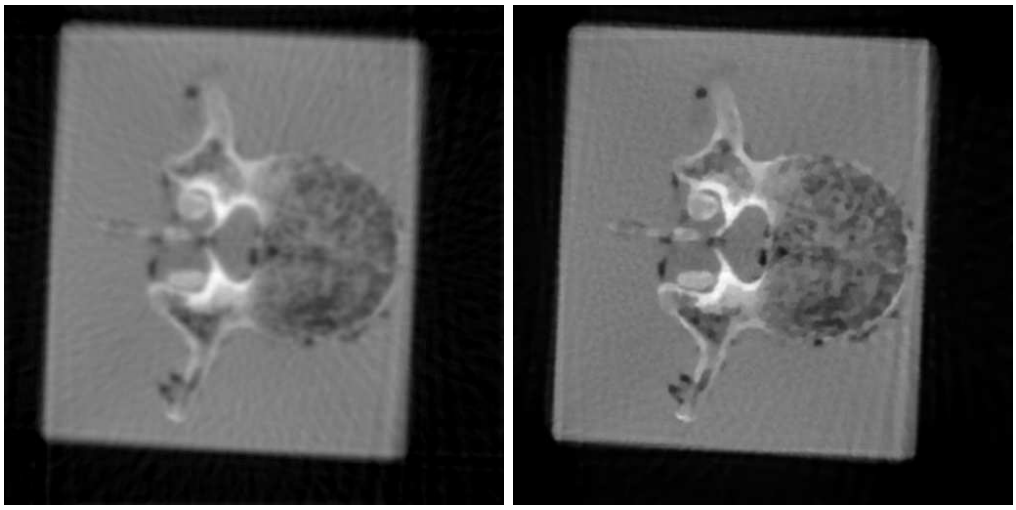

(a) Δ = Tikhonov, pixel, P=96

(b) Δ = TV, GS, P=96

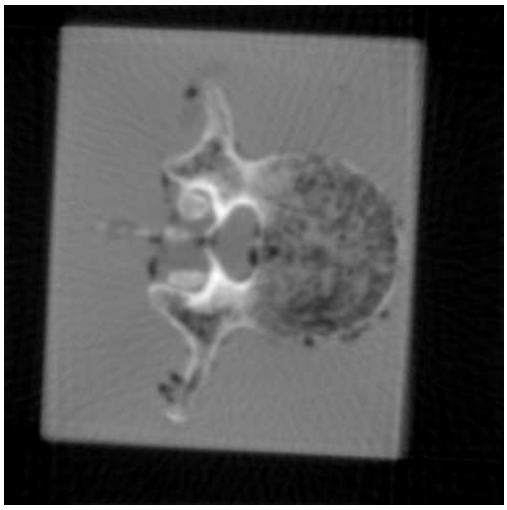

(c) Δ = Tikhonov, pixel, P=128

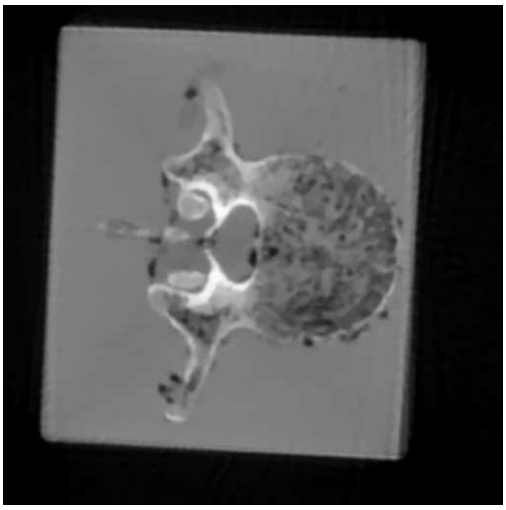

(d) Δ = TV, GS, P=128

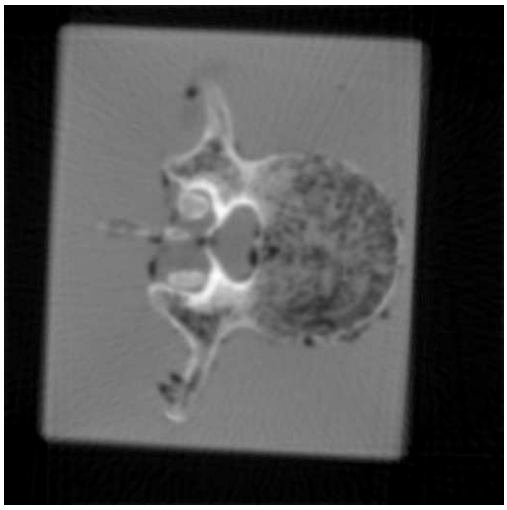

(e) Δ = Tikhonov, pixel, P=160

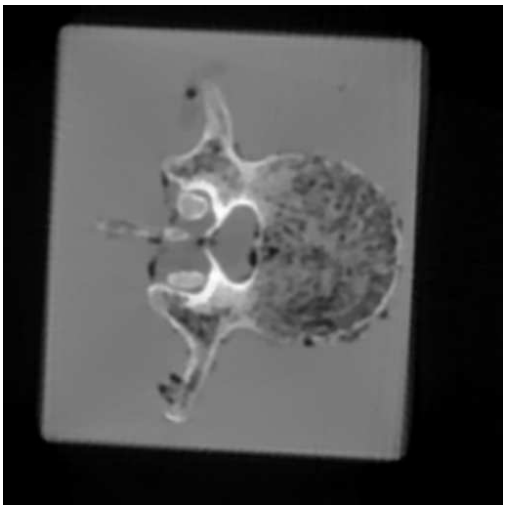

(f) Δ = TV, GS, P=160

FIGURE 8.4: Reconstructions from $P = 96, 128, 160$ by Tikhonov regularization based on pixel (512×512) (first column) and by TV minimization based on Gaussian blob of FWHM 0.812 mm (second column), $w = [0, 0.049]$. Number of blobs $N = 49554$, number of pixels $N = 512 \times 512$. Using smaller Gaussian blobs and a denser lattice will not improve substantially the visual quality of images (b), (d) and (f).

The reconstructions by TV-ℓ^1 minimization using a 4 scales Mexican hat blob system are shown in Figure 8.5. From the zoomed view on the ROIs in Figure 8.6, we can see that the spongy bone structures are better preserved in the TV-ℓ^1 reconstruction. These results confirm that the Spine object can be well reconstructed from about $P \geq 128$ projections and with a detector of 512 pixels, which represents only 17.8% of the whole data set.

8.2 Micro-CT

The term *micro-CT* usually refers to a small scale CT system with the source spot size of a few micrometers. It is useful when high resolution images on small objects are needed, *e.g.*in material science. A cubic sample of dimension 10.00×11.20×7.20 mm taken from a material composed of carbon fibers in a matrix of carbon is shown in Figure 8.7.(a). The objective is to visualize the individual fibers separated from the matrix in a ROI of 5mm diameter. This requires a high resolution reconstruction: typically more than 1500×1500 pixels inside the ROI, see Figure 8.8. Using analytical reconstruction methods, for such a resolution one needs to acquire more than 1400 projections, which is very time consuming and can raise for instance the overheating problem to the micro-CT system. Here we show that with much less projections, one can achieve lower resolution but globally acceptable image quality, and in this way accelerate the acquisition procedure.

Acquisition system The acquisition system is shown in Figure 8.7.(b). The source is made of a micro-focus copper target, accelerated to 60 kV with 35 μA current. In total 360 cone beam projections are collected and at each projection we keep only the central horizontal slice on the flat panel detector, which contains 1536 bins. Other parameters are:

- Source to rotation axis distance: 16.4 mm
- Detector to rotation axis distance: 311.6 mm
- Detector length: 76.8 mm
- X-ray spot size: 5 μm

Figure 8.9.(a) shows the reconstruction using all available data by solving the least square problem with 25 CG iterations. From the reconstructed image it can be deduced that the sinogram data are actually very noisy. Then we extract P equally distributed projections, average the adjacent detector bins and downsample the X-ray detector by

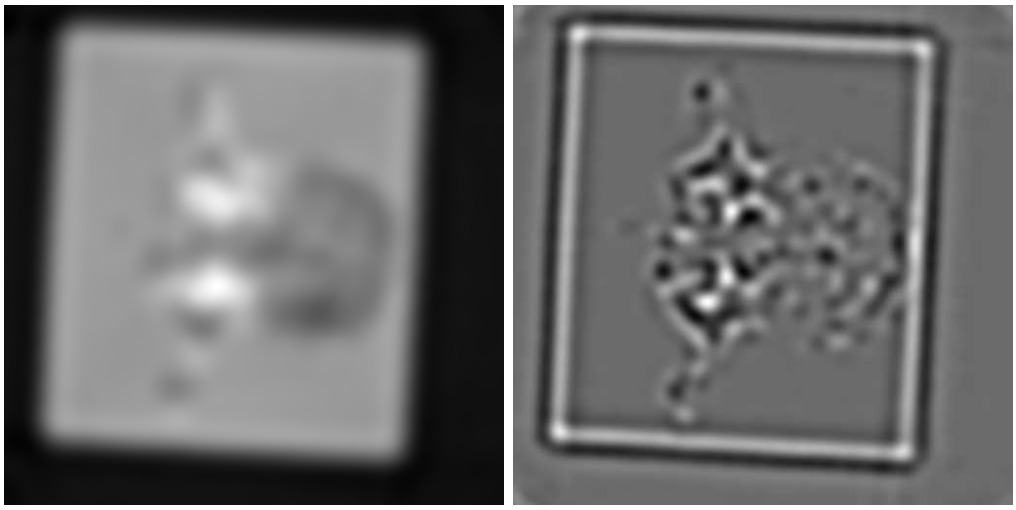

(a) $\Delta = \mathrm{TV} - \ell^1$, P=160, Scale 0, τ =90.28%

(b) $\Delta = \mathrm{TV} - \ell^1$, P=160, Scale -1, τ =35.41%

(c) $\Delta = \mathrm{TV} - \ell^1$, P=160, Scale -2, τ =28.77%

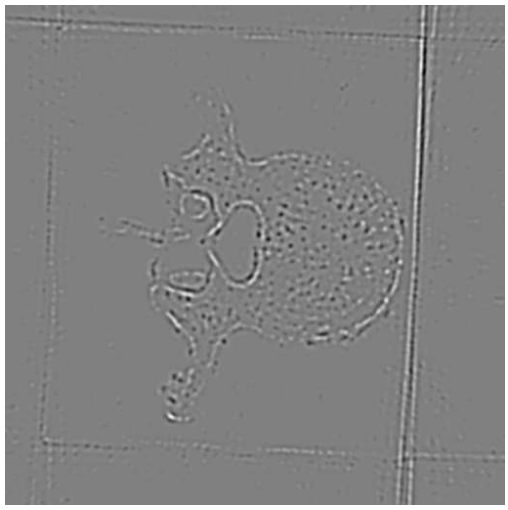

(d) $\Delta = \mathrm{TV} - \ell^1$, P=160, Scale -3, τ =11.34%

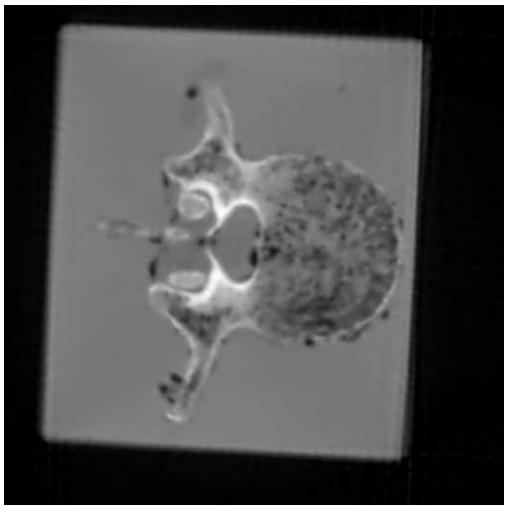

(e) $\Delta = \mathrm{TV} - \ell^1$, P=160, τ=16.40%

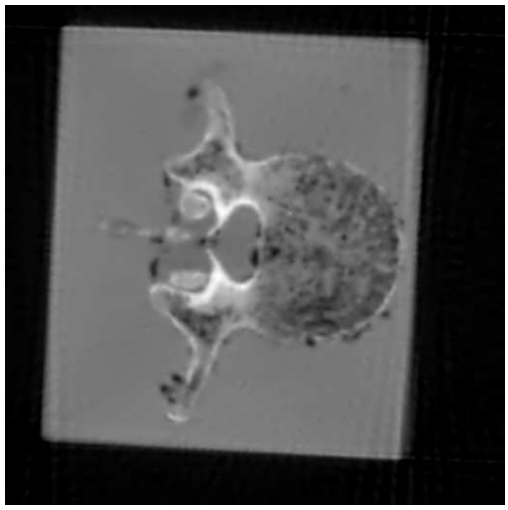

(f) $\Delta = \mathrm{TV} - \ell^1$, P=128, τ=17.73%

FIGURE 8.5: $\Delta = \mathrm{TV} - \ell^1$, Mex-4, from 160 (e) and 128 (f) projections. Figure (a)-(d) are scale decompositions of (e). τ indicates the percentage of non zero blobs in each scale (a-d) or in total (e-f). The gray level in (a-d) are image dependent, with the background gray color representing 0, and white color for positive values. There are 202522 blobs in all 4 scales. In the finest scale (d) the FWHM of the Mexican hat blob is about 0.975mm.

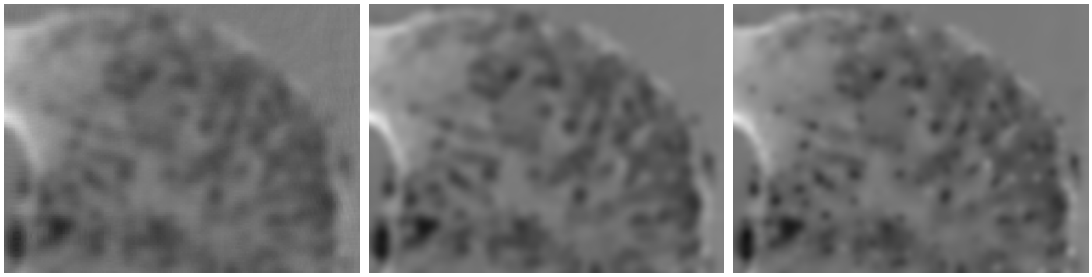

(a) Δ = Tikhonov, Pixel, P=360 (b) Δ = TV, GS, P=160 (c) $\Delta = \text{TV} - \ell^1$, Mex-4, P=160

FIGURE 8.6: Spine: zoomed view on ROI of different reconstructions. Figure (a), (b), and (c) correspond to Figure 8.3 (c), 8.4 (f) and 8.5 (e), respectively.

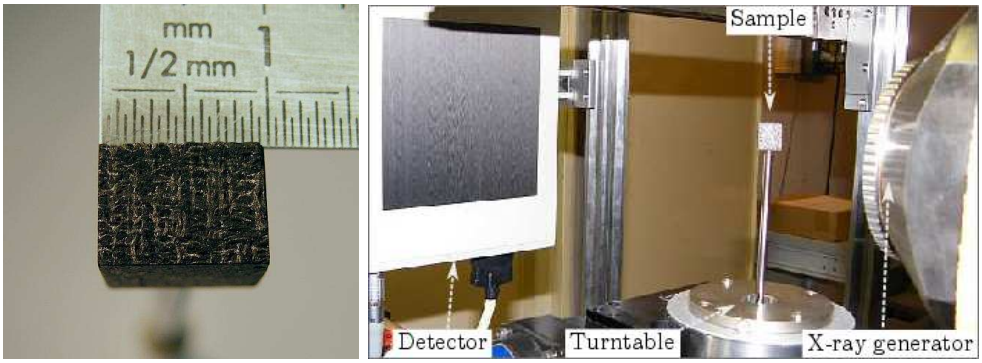

(a) Sample (b) Micro-CT system

FIGURE 8.7: Micro-CT: A cubic sample of a material composed of carbon fibers in a matrix of carbon and the acquisition system. Courtesy of M.Costin.

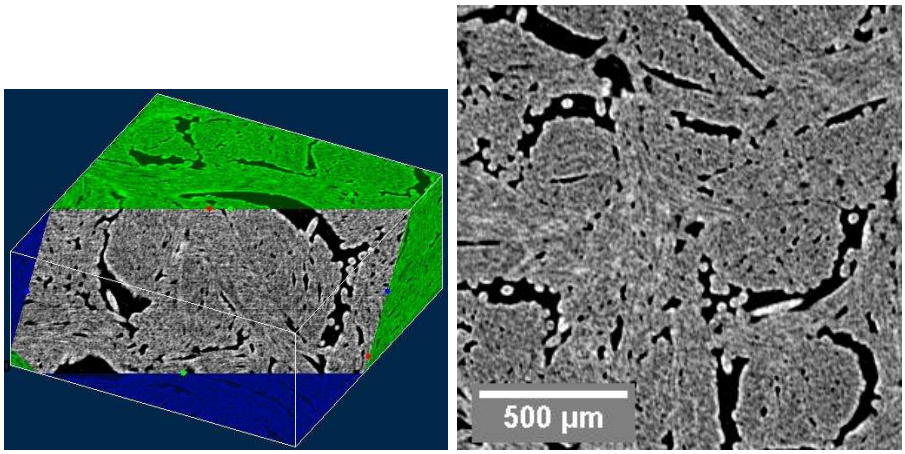

(a) (b)

FIGURE 8.8: Micro-CT: ROI reconstruction from 1440 projections by analytical method *ASDIR*[1]. The isolated white spots inside the black regions are carbon fibers. Courtesy of M.Costin.

a factor 3. The resulting sinogram has dimension $P \times 512$. Figure 8.9 (c) and (e) show the reconstructions for $P = 360$ using TV minimization with Gaussian blob and ℓ^1 minimization with 4 scales Mexican blob system respectively. From the zoomed view (Figure 8.10) on the ROI we see that TV minimization removes better the noise than ℓ^1 minimization does. Nevertheless, the carbon fibers can be distinguished in none of these reconstructions.

Few projections Using the TV reconstruction from 360 projections (Figure 8.9.(c)) as reference image, in Figure 8.11 we plot the SNR and the SI of the reconstructions by TV minimization with the number of projections P varies in the range $[64, 256]$ and with the downsampled detector (512 bins). A visual comparison suggests that the image quality becomes acceptable for $P \geq 192$, see the second column in the Figure 8.9.

8.3 Electron microscopy/tomography

Electron microscopy/tomography (EM) [130] is an imaging technology based on the similar principle as X-ray CT but uses electron flux to probe nanoscale objects. It is widely used in biology and material science and can provide a few tenth nanometer resolution. The specimen to be probed is generally in needle shape, and the electron gun positioned perpendicular to the needle scans one slice from different angles by tilting the needle. For some mechanical reasons of the acquisition system, the angular range of view in practice is often limited. In addition the micro structure of the (biological) specimen can be damaged by the electron flux, therefore reducing the projection number helps to keep their integrality.

The needle shown in Figure 8.12 is extracted from a Silicon surface irradiated by femtosecond laser using Tellurium as dopant [131]. On one slice through the needle, 157 parallel beam projections equally distributed on $[-78°, 78°]$ have been acquired. Figures 8.12 (b) and (c) are reconstructions using FBP and SIRT[2], and different grey levels correspond to different concentrations of Tellurium in Silicon. From these images we can clearly distinguish the streak artifacts due to the limited angle of view, and also the metallic artifacts around the white spot.

Few projections Here we extract P equally distributed projections from the whole data. In order to remove the streak artifacts, we restrict the support of the reconstruction area to a small disk (half of the diameter of the FoV) including the object.

[2]SIRT stands for Simultaneous Iterative Reconstruction Technique [132].

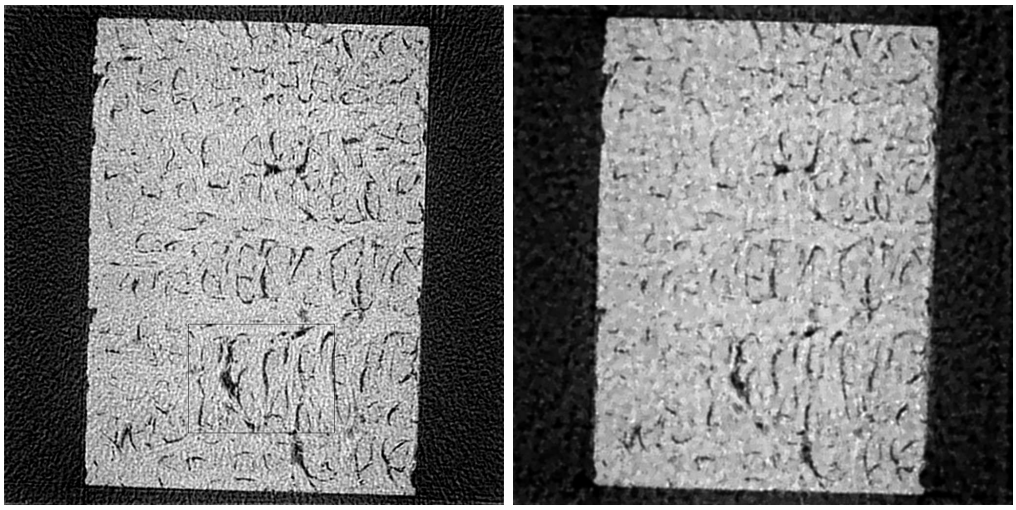

(a) Δ = Least Square, GS, P=360

(b) Δ = TV, GS, P=128

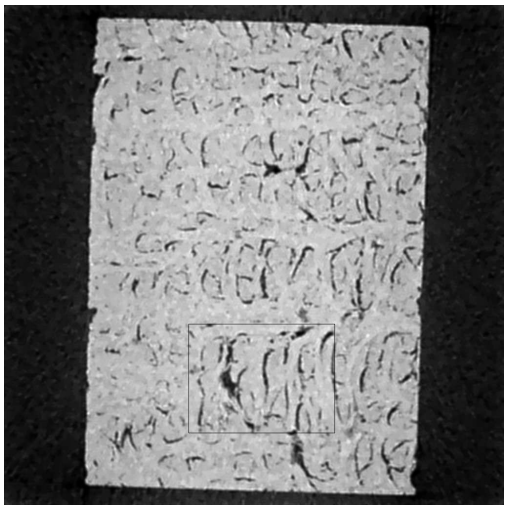

(c) Δ = TV, GS, P=360

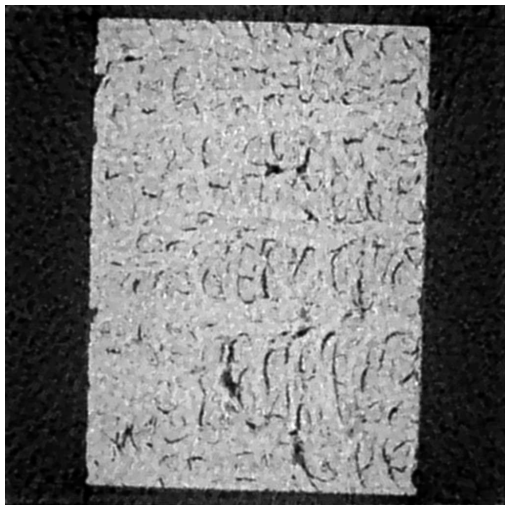

(d) Δ = TV, P=192

(e) $\Delta = \ell^1$, Mex-4, P=360

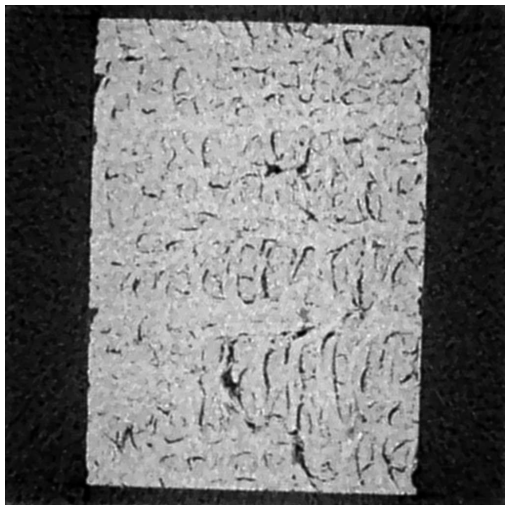

(f) Δ = TV, P=256

FIGURE 8.9: First column: reconstructions using all 1536 detector bins and all 360 projections. Second column: TV minimization for P=128, 192, 256 with the detector downsampled by a factor 3 (D=512). The Gaussian blob in Figure (a)-(d) and (f) has FWHM 0.0148mm, and the finest scale Mexican hat blob in (e) has FWHM 0.0178mm. $w = [0, 0.0067]$.

(a) Least square (b) TV minimization (c) ℓ^1 minimization

FIGURE 8.10: Micro-CT: zoomed view on the ROI marked by rectangles in Figure 8.9.

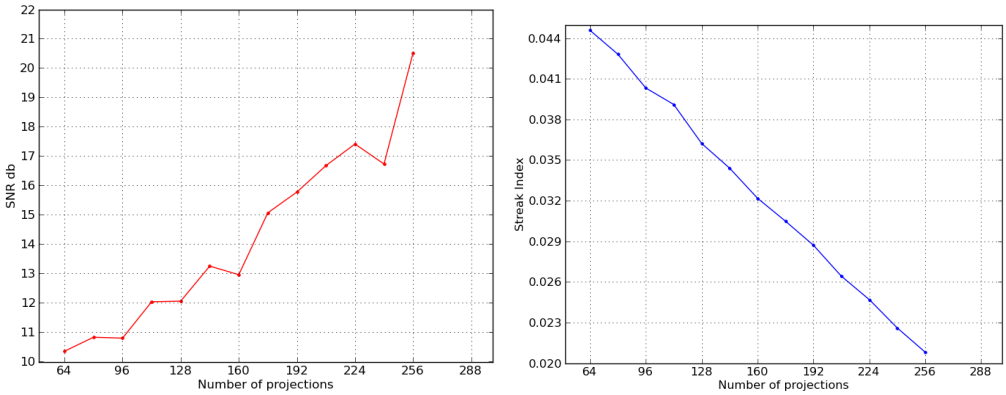

(a) SNR (b) SI

FIGURE 8.11: SNR and SI of the reconstructions from $P \in [64, 256]$ projections by TV minimization based on Gaussian blob, using Figure 8.9.(b) as ground truth.

Figures 8.13 shows the TV reconstructions from different number of projections. Compared with the classical reconstructions (Figure 8.12 (b) and (c)), the streak artifacts are reduced and the details are well preserved even for P small. Figure 8.14 shows the TV-ℓ^1 reconstructions with 4 scales Mexican hat blob system, where the stage-wise artifacts due to the TV minimization are avoided.

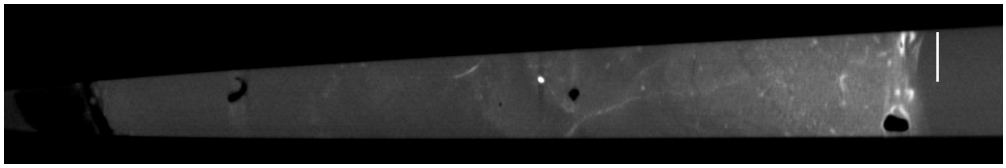

(a) EM object

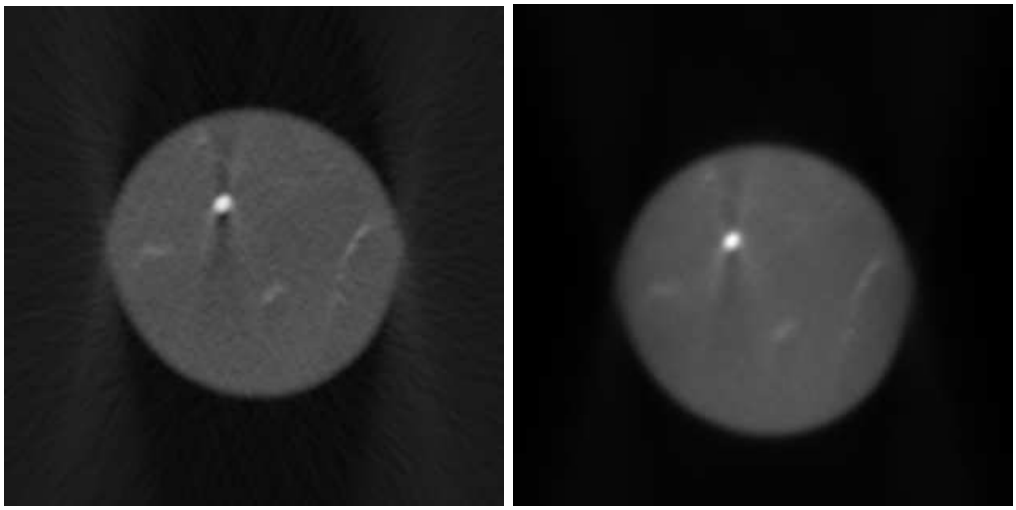

(b) FBP (c) SIRT

FIGURE 8.12: Figure (a): a needle shaped EM object of diameter about 200nm. Figure (b) FBP and (c) SIRT reconstructions from 157 parallel beam projections equally distributed on $[-78°, 78°]$. Courtesy of G.Haberfehlner.

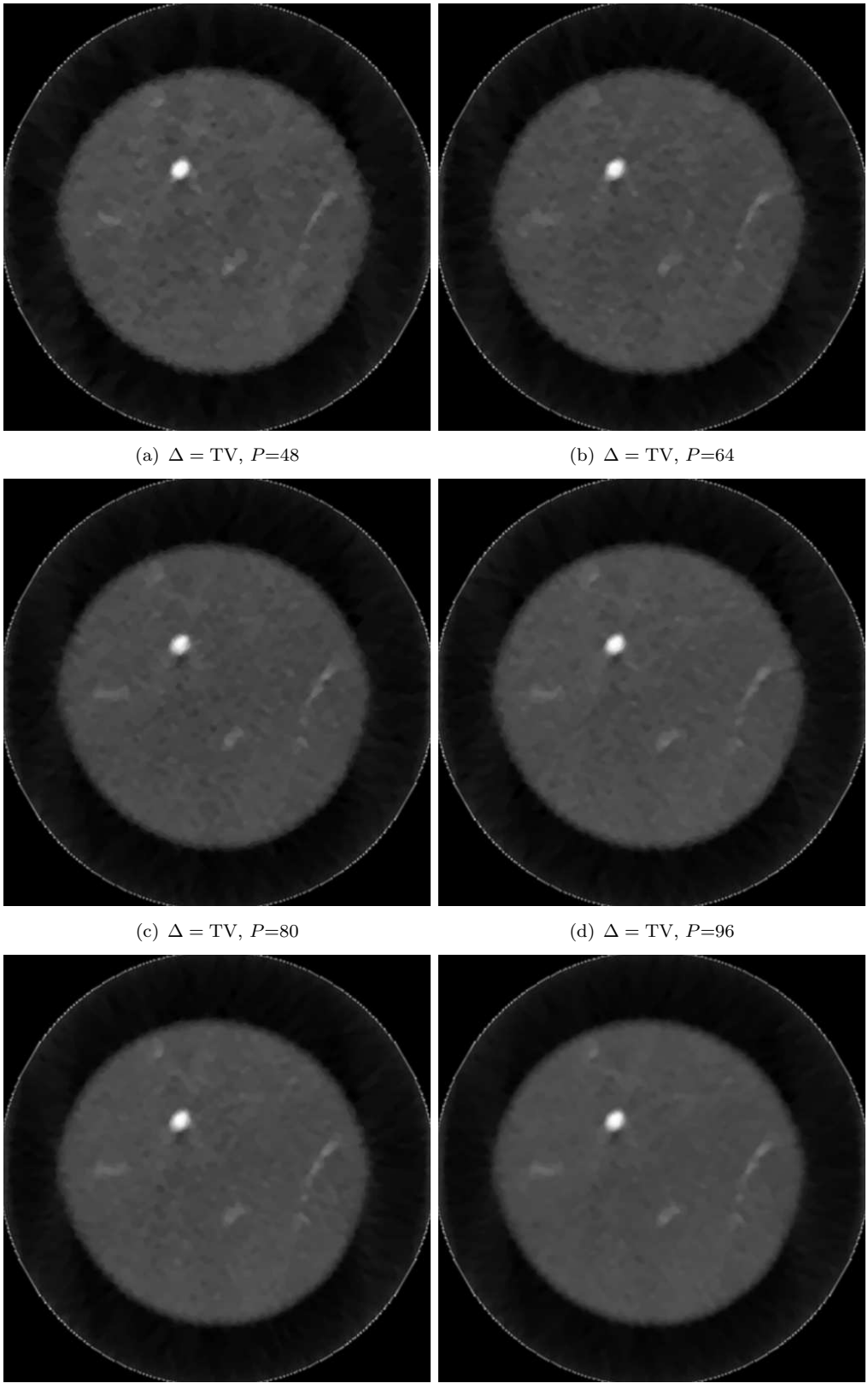

(a) $\Delta = \text{TV}$, P=48 (b) $\Delta = \text{TV}$, P=64

(c) $\Delta = \text{TV}$, P=80 (d) $\Delta = \text{TV}$, P=96

(e) $\Delta = \text{TV}$, P=112 (f) $\Delta = \text{TV}$, P=157

FIGURE 8.13: EM object: TV minimization with Gaussian blob from different number of projections, $w = [0, 0.025]$. The white circles are due to the restriction of the reconstruction area.

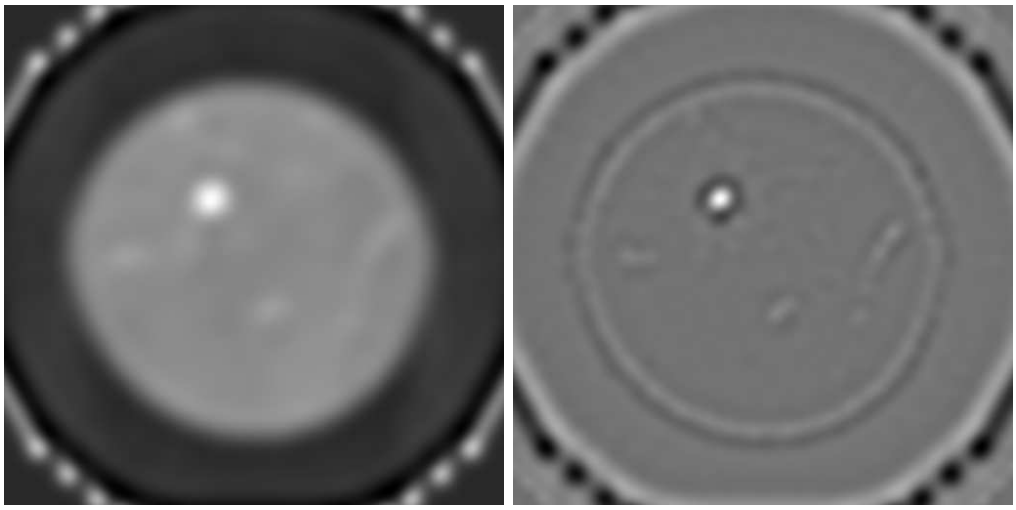

(a) $\Delta = \text{TV} - \ell^1$, P=96, Scale 0

(b) $\Delta = \text{TV} - \ell^1$, P=96, Scale -1

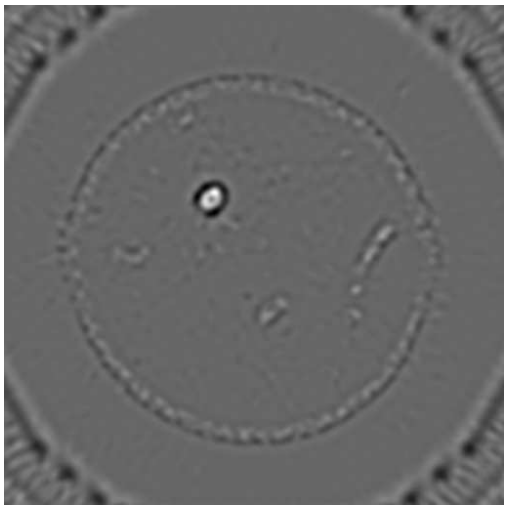

(c) $\Delta = \text{TV} - \ell^1$, P=96, Scale -2

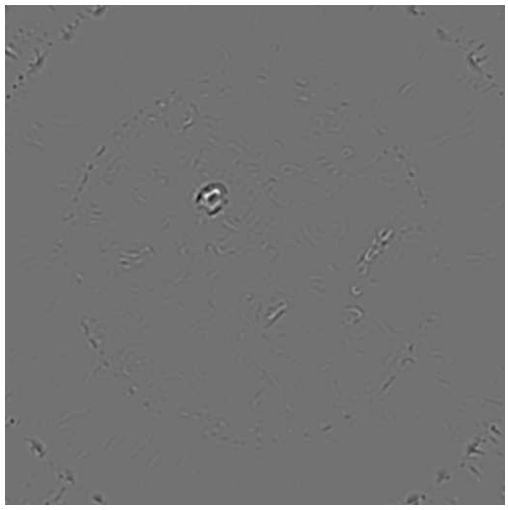

(d) $\Delta = \text{TV} - \ell^1$, P=96, Scale -3

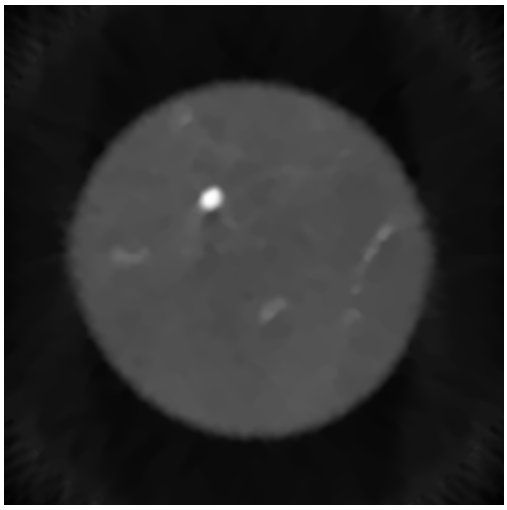

(e) $\Delta = \text{TV} - \ell^1$, P=96

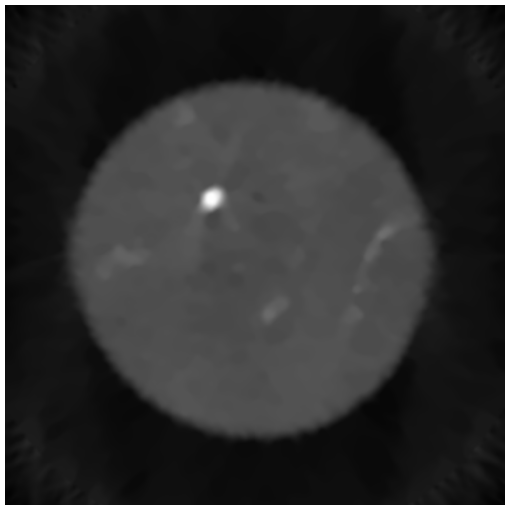

(f) $\Delta = \text{TV} - \ell^1$, P=64

FIGURE 8.14: EM object: Figure (e) and (f) are reconstructions from P=96 and P=64 using $\Delta = \text{TV} - \ell^1$and Mex-4, $w = [0, 0.025]$ for (e) and (f). Figure (a-d) are scale decompositions of (e) where the gray level are scale dependant. The large circles in (a-d) are due to the restriction of the reconstruction area and are canceled out in (e).

Chapter 9

Conclusions and perspectives

In this thesis we have studied the feasibility of CT reconstruction from few projections for *generic* objects (medical or industrial oriented): does a small number of X-ray projections can capture the essential information of an object? And how to reconstruct it?

We have seen the importance of regularizations in a Bayesian framework: some state-of-the-arts regularization methods proposed in the CT literature, particularly those based on the edge preserving prior, the Total Variation and the wavelets, are efficient for the few projections problem. These methods are closely connected with the Compressed Sensing theory. CS explains rigorously the triangular relationship between the sparsity of the unknown, the sampling condition to be fulfilled, and the reconstruction method as well as its error. The general CS framework for the few projections problem is: 1) sparse representation/modeling of the function; 2) reconstruction via specific non-linear algorithms like TV or ℓ^1 minimization. This suggests the widely employed "pixel/voxel + sparsifying basis" scheme: as long as the object is sufficiently sparse, it (more precisely, its representation coefficients) can be reconstructed from a small number of projections.

Nevertheless, such a scheme is not the optimal way for image representation and reconstruction in CT, due to the poor space-frequency localization property of pixel, and to the higher numerical complexity when combining the pixel/voxel based X-ray projector with the *ad hoc* sparsifying basis, *e.g.*, the wavelet transform. These observations has led us to adapt the "CT-friendly" radial bases called *blob* to CS. In particular we have constructed and analyzed the radial basis based on Gaussian family for image representation and reconstruction. They have better space-frequency localization properties than pixel, and many operations, such as the X-ray transform, the gradient or the interpolation, can be analytically evaluated, thus there is no need for discretization or approximation of the X-ray projector. The typical (medical) images in CT represented

by these bases has a compressible form, so the *ad hoc* sparse representation system used in the ordinary CS algorithms is not needed.

By following the classical wavelet theory, we have proposed two image models. The first is the shift invariant space spanned by translating a Gaussian blob ϕ on an hexagonal lattice $\mathcal{L}$. We have proven that it constitutes a Riesz basis but the limit is not dense in $L^2(\mathbb{R}^d)$. The second is the sum of multiscale shift invariant spaces spanned by the blob $\psi_j(x) = \beta^{-jd}\psi(\beta^{-j}x)$ and by translating on the (dyadically) refined lattices $\mathcal{L}_j$. This constitutes a tight frame of $L^2(\mathbb{R}^d)$ if the mother blob ψ is band-limited and if the partition of unity property is satisfied. The Mexican hat blob and the Diff-Gaussian blob can be treated as band-limited due to their exponential decay. The adaptations of the existing TV and ℓ^1 minimization methods to blob images are straightforward, and the main issue is to parallelize (on a GPU platform) the X-ray projector and the interpolator (*e.g.*, the gradient operator) on the blob image.

Through 2D numerical experiments using simulated data, we have shown that the new models indeed have many advantages over the classical pixel and (decimated) wavelet model. Compared with pixel, the TV reconstruction based on the Gaussian blob is much less sensitive to the variation of the underlying lattice's sampling step. On the medical oriented phantoms, the low dimension blob image can achieve the reconstruction quality (measured in SNR and in SI) equivalent to a high dimension pixel image. Working in a lower bandwidth, the blob based reconstruction is more stable than the pixel based one, while the reconstruction still enjoys a nice visual quality. Such a phenomenon can be contributed to the better space-frequency localization, the smoothness and the radial symmetry of blob, and also to the use of hexagonal lattice, which has a higher angular frequency and lower zig-zag artifacts than the Cartesian lattice.

When the number of projections P is large, typically $P > 150$, the multiscale blob model coupled with the ℓ^1 minimization offers a better image quality than the TV minimization. The multiscale blob system is a mimic of the multiresolution wavelet basis, while it is redundant and less concerned by the pseudo Gibbs phenomenon. Using different testing phantoms, we have revealed a fundamental difference between the TV and the ℓ^1 methods. Unlike the TV minimization which removes systematically low contrast regions and oscillating patterns, the ℓ^1 minimization preserves very well these characters, which are essential for medical applications. On the contrary, for P small, typically $P < 80$, the ℓ^1 method is largely inferior to TV, due to the streak artifacts and the erroneous fine scale blobs. The hybrid TV-ℓ^1 minimization combines the best part of each and improves the image quality for P in the middle range. We draw the conclusion that the choice of the image model and the reconstruction method should be made by taking into account the application context and the completeness of data. The

multiscale blob image models and the TV/ℓ^1 or TV-ℓ^1 methods that we have proposed can cover a wide range of the applications and of the number of projections.

At the end we have validated our approaches on real data collected from different application fields, where the reduction of projections can bring real improvements. Although these raw data have limited quality, our preliminary results confirm that the number of projections in these applications can generally be reduced by a factor 2 or 3 without compromising the image quality.

9.1 Perspectives

9.1.1 3D generalization

An important extension is the 3D reconstruction, which has not been presented in this thesis, while the whole theory and the reconstruction methods that we have developed include 3D as a special case. The 2D hexagonal lattice becomes in 3D the *Face Centered Cubic* (FCC) lattice and the related blob-driven X-ray projector and interpolator must be accordingly modified. Nevertheless, more efforts seem to be necessary for the efficient parallelization of these operators on GPU platforms due to the large dimension in 3D.

9.1.2 Contour blob

Recall the following definition of multiscale (Mexican hat) blobs at scale j:

$$\psi_{j,k}(x) = |\det G_j|^{1/2} \psi_j(x - x_k^j), \quad \text{with } x_k^j = G_j k \tag{9.1}$$

with $\beta > 1$ the dilation factor, $G_j = \beta^j G_0$ the generating matrix of the refined lattice $\mathcal{L}_j$, and $\psi_j(x) = \beta^{-jd}\psi(\beta^{-j}x)$ the dilated mother blob. Let $f \in L^\infty(\mathbb{R}^d)$ be a piecewise linear function with the contour/surface Γ which is C^2 smooth. For very fine scale, *i.e.*, $j \ll 0$, the number of blobs which "feel" the contour Γ is about $O(|\Gamma|\beta^{-j(d-1)})$. For one of these blobs $\psi_{j,k}$, it is easy to see that its analysis coefficient is bounded by:

$$|\langle f, \psi_{j,k}\rangle| \leq \|f\|_\infty \|\psi_{j,k}\|_1 \lesssim \beta^{jd/2} \tag{9.2}$$

In other words, at scale j, there are $O(|\Gamma|\beta^{-j(d-1)})$ blobs giving the non zero coefficients of magnitude $O(\beta^{jd/2})$. From this we can deduce that the N-th largest entry in the coefficient vector $\{|\langle f, \psi_{j,k}\rangle|\}$ decays asymptotically as:

$$N^{d/(2-2d)} \tag{9.3}$$

Particularly in 2D we have the decaying rate N^{-1} which is identical to that given by the wavelet basis. In order to reduce the reconstruction error, one would need a representation system which gives faster decay than (9.3) (see Chapter 4). A possible improvement is to use a curvelet-like [92] multiscale blob system, in which the radial symmetry of blob is dropped in favor of the angular orientation which gives it the geometric sensitivity. The blobs of such a system are the anisotropic dilations, the translations and the rotations of a common mother *contour blob* ψ, and they have a elongated shape. In 2D it is the tensorial product of a Gaussian function $g(t) = \exp(-\alpha_1 t^2)$ and a Mexican hat function and $m(t) = \exp(-\alpha_2 t^2)(1 - 2\alpha_2 t^2)$:

$$\psi(x) \triangleq g(x_1)m(x_2) \tag{9.4}$$

Figure 9.1 gives a visual representation of ψ. Although not radial symmetric, the X-ray transform $\mathcal{P}\psi(y, \theta)$ of the contour blob can also be evaluated analytically therefore one keeps the "CT-friendly" characters of the radial blob. Thanks to the Mexican hat

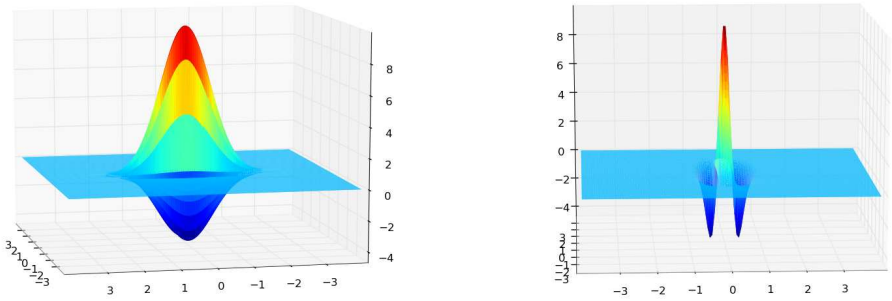

FIGURE 9.1: Two different views on the mother contour blob with $\alpha_1 = 1, \alpha_2 = 10$.

function and the elongated shape, most of the analysis coefficients of the blobs will be cancelled out unless those which are "perfectly" aligned with the contour, thus one can expect that the N-th largest coefficient has a faster decaying rate than the radial blob case.

9.1.3 Sinogram inpainting

Lastly, all the reconstruction techniques studied previously search a solution in the object space X, for the reason that the prior information, *e.g.*the sparsity of $\mathbf{f}$, is easily expressed in X. While another possible way of reconstruction is to restore the entire sinogram[133–135], then proceed by standard algorithms, *e.g.*FBP, as we have pointed out in Chapter 4. Under the new context of few projections problem, we need to restore a highly incomplete sinogram. This is possible by exploiting the sparsity of sinogram

under the *vaguelette blobs* (Section 5.6) using an analysis prior. We give some preliminary investigations by presenting an algorithm on the efficient implementation of this prior.

Data fitting term Let's note $g = \mathcal{P}f$. The X-ray projection is even in θ: $\mathcal{P}f(-\theta, y) = \mathcal{P}f(\theta, y)$, so we can restrict the domain of $\mathcal{P}$ to

$$\mathcal{T}_+ = \{(\theta, y) | \theta \in \mathcal{S}_+^{d-1}, y \in \theta^\perp\} \tag{9.5}$$

with $\mathcal{S}_+^{d-1}$ the half unit sphere of $\mathbb{R}^d$. In practice data are observed only on T, a discrete subset of $\mathcal{T}_+$, and we call *observation mask* $\mathcal{M} : L^2(\mathcal{T}_+) \to \mathbb{R}^M$ the restriction on the observation set T. Then the data fitting term reads: $\|\mathcal{M}g - \mathbf{b}\|^2$.

Sparsity of the sinogram domain Let $\{\psi_{j,k}\}$ be a tight frame of $L^2(\Omega)$, *e.g.*the multiscale blob system, and $\{\tilde{\psi}_{j,k}\}$ the corresponding vaguelette:

$$\langle f, \psi_{j,k} \rangle = \langle g, \tilde{\psi}_{j,k} \rangle$$

Given that $\langle f, \psi_{j,k} \rangle$ has fast decay (see Section 5.4.1), we can regularize the sinogram restoration problem by minimizing the ℓ^1 norm of the coefficient $\langle g, \tilde{\psi}_{j,k} \rangle$.

Consistency constraint A consistency constraint is necessary to enforce the restored g to be a "true sinogram". In 2D, this is described by the Ludwig-Helgason consistency condition [133, 136]. We note $\mathcal{T}_+ = [0, \pi] \times [-1, +1]$ and let $P_n(y)$ be the normalized Legendre polynomial of degree n, $S_{l,1}(\theta) = \cos(l\theta)/\sqrt{\pi}$, and $S_{l,2}(\theta) = \sin(l\theta)/\sqrt{\pi}$, and define

$$J_{l,*}^n = \int_{\mathcal{T}_+} g(\theta, y) S_{l,*}(\theta) P_n(y) dy d\theta$$

Theorem 9.1.1 (Ludwig-Helgason consistency condition[133, 136])**.** *If $g \in L^2(\mathcal{T}_+)$ is a sinogram, then for the index set running through $* = 1, 2$, $l, n = 0, 1 \ldots$, $n < l$, and $n + l$ even:*

$$J_{l,*}^n = 0$$

Putting the different components together, the sinogram inpainting problem announces, in a continuous formulation:

$$\min_{g \in L^2(\mathcal{T}_+)} \frac{1}{2} \|\mathcal{M}g - \mathbf{b}\|^2 + \mu \sum_{j,k} |\langle g, \tilde{\psi}_{j,k} \rangle| \quad \text{s.t. } J_{l,*}^n = 0 \tag{9.6}$$

with $\mu > 0$ the penalty constant, and the index set $l, n, *$ as in Theorem 9.1.1. In practice (9.6) is approximated by a discrete version:

$$\min_{\mathbf{g}\in\mathbb{R}^M} \frac{1}{2}\|\mathcal{M}\mathbf{g} - \mathbf{b}\|^2 + \mu\|\tilde{\Psi}\mathbf{g}\|_1 \text{ s.t. } J^n_{l,*} = 0 \tag{9.7}$$

In this formulation, $\tilde{\Psi}$ is a linear operator such that $\tilde{\Psi}\mathbf{g}$ approximates $\langle g, \tilde{\psi}_{j,k}\rangle$, and the number of constraints $J^n_{l,*} = 0$ is finite. The vector $\mathbf{g}$ is the sample values of the continuous sinogram g taken on the lattice $\mathcal{L}_{\mathcal{T}_+}$:

$$\mathcal{L}_{\mathcal{T}_+} \triangleq \left\{\theta_p \times E_{\theta_p} m/W,\ p = 1, \ldots, P, \text{ and } m \in I\right\} \tag{9.8}$$

where the following notations have been introduced:

- $\{\theta_p\}_{p=1,\ldots,P}$ are P directions equally distributed on $\mathcal{S}^{d-1}_+$.
- $E_\theta \triangleq [e_1, \ldots, e_{d-1}]$ denotes an orthobasis of $\theta^\perp$, and $E^*_\theta E_\theta = \mathrm{Id}$.
- The detector pixel's index set $I \triangleq [\![-L/2, L/2-1]\!]^{d-1}$ with prefixed even number $L > 0$.
- $W^{-1} > 0$ is the sampling step on detector.
- $M = P \times |I|$ is the dimension of the lattice $\mathcal{L}_{\mathcal{T}_+}$ (also that of $\mathbf{g}$).

The observation mask $\mathcal{M}$ in (9.7) is the restriction on a set of observation $T \subset P \times I$. Remark that the X-ray projector, which is a time and memory consuming operation for the iterative algorithm working in image domain, is avoided in (9.7), and the computational charge here is transfered to the scalar product $\tilde{\Psi}\mathbf{g} \simeq \langle g, \tilde{\psi}_{j,k}\rangle$. Although the direct evaluation of $\langle g, \tilde{\psi}_{j,k}\rangle$ (*e.g.*by numerical integration) for all indexes j, k is certainly possible, it could be very expensive due to the large dimension of the multiscale blob system $\{\psi_{j,k}\}$. In the following we give details on how $\langle g, \tilde{\psi}_{j,k}\rangle$ is approximated by $\tilde{\Psi}\mathbf{g}$ and using the Non-Uniform FFT technique for a fast implementation of $\tilde{\Psi}$.

9.1.3.1 Efficient evaluation of $\langle g, \tilde{\psi}_{j,k}\rangle$

First we write:

$$\langle g, \tilde{\psi}_{j,k}\rangle = 2\int_{\mathcal{S}^{d-1}_+}\int_{\theta^\perp} g(\theta, y)\tilde{\psi}_{j,k}(\theta, y)dyd\theta \tag{9.9}$$

We observe that if the the inner integral in (9.9) can approximated by some value $F_j(\theta, k)$, then the outer integral is easily handled by the trapezoidal rule and we get:

$$\langle g, \tilde{\psi}_{j,k} \rangle \simeq C \sum_{p=1}^{P} F_j(\theta_p, k) \tag{9.10}$$

with C an irrelevant constant, and the summation in (9.10) can be parallelized for index j. Now we focus on the approximation of the inner integral.

Evaluation of $F_j(\theta_p, k)$ Let's recall the following fact about the vaguelette blob:

$$\hat{\tilde{\psi}}_{j,k}(\theta, \omega) = \frac{1}{|\mathcal{S}^{d-2}|} \|\omega\| \hat{\psi}_{j,k}(\omega), \quad \text{for } \omega \in \theta^{\perp} \tag{9.11}$$

and by the construction of tight frame blob:

$$\hat{\psi}_{j,k}(\omega) = \hat{\psi}_j(\omega) \exp(-2\pi i \langle \omega, x_k^j \rangle) |\det G_j|^{1/2} \tag{9.12}$$

with $x_k^j = G_j k$. Then the inner integral can be rewritten as:

$$\int_{\theta^{\perp}} g(\theta, y) \tilde{\psi}_{j,k}(\theta, y) dy = \frac{|\det G_j|^{1/2}}{|\mathcal{S}^{d-2}|} \int_{\mathbb{R}^{d-1}} \hat{g}(\theta, E_\theta \omega) \|\omega\| \hat{\psi}_j(E_\theta \omega) e^{2\pi i \langle \omega, E_\theta^* G_j k \rangle} d\omega \tag{9.13}$$

Remark that by construction $\hat{\psi}_j$ is band-limited and one can choose

$$\operatorname{supp} \hat{\psi}_j \subset \Gamma_j = \left\{ G_j^{-\top} \omega, \|\omega\|_\infty \leq 1/2 \right\}$$

then $E_\theta \omega \in \Gamma_j \Leftrightarrow \omega \in E_\theta^* \Gamma_j \subset \mathbb{R}^{d-1}$. For a finite number of scales j and directions θ, all $E_\theta^* \Gamma_j$ can be contained in a cube B:

$$B \triangleq \{\|\omega\|_\infty \leq W/2\} \cap \mathbb{R}^{d-1} \tag{9.14}$$

and W is the width of B taken as:

$$W = \sup_{|j| \leq J} \sup_{\theta \in \{\theta_1, \ldots, \theta_P\}} \{\|E_\theta^* G_j^{-\top}\|_\infty\} \tag{9.15}$$

Now define

$$\hat{F}_j(\theta, \omega) \triangleq \frac{|\det G_j|^{1/2}}{|\mathcal{S}^{d-2}|} \hat{g}(\theta, E_\theta \omega) \|\omega\| b_{\hat{\psi}_j}(\|\omega\|) \tag{9.16}$$

then we get an expression for the inner integral:

$$\int_{\theta^{\perp}} g(\theta, y) \tilde{\psi}_{j,k}(\theta, y) dy = \int_B \hat{F}_j(\theta, \omega) \exp(-2\pi i \langle \omega, E_\theta^* G_j k \rangle) d\omega \tag{9.17}$$

which in turn is approximated using the trapezoidal rule by

$$F_j(\theta,k) \triangleq \left(\frac{W}{L}\right)^{d-1} \sum_{l\in I} \hat{F}_j(\theta,\omega_l) e^{-2\pi i\langle \omega_l, E_\theta^* G_j k\rangle} \tag{9.18}$$

with $\omega_l = Wl/L$. Note that due to the presence of $E_\theta^* G_j$ which maps the regular d dimensional lattice to irregular $d-1$ dimensional one, there is generally no hope calculate (9.18) by FFT and we have to use the Non Uniform FFT(NUFFT).

Evaluation of $\hat{g}(\theta, E_\theta\omega)$ In order to calculate (9.18) by NUFFT, the sample values of $\hat{g}(\theta, E_\theta\cdot)$ for the direction θ and on the nodes $\omega_l = Wl/L$ must be collected. For this, we sample g on the lattice $\mathcal{L}_{\mathcal{T}_+}$ and use again the trapezoidal rule:

$$\begin{aligned}\hat{g}(\theta, E_\theta\omega_l) &= \int_{\mathbb{R}^{d-1}} g(\theta, E_\theta y)\exp(-2\pi i\langle y,\omega_l\rangle)dy \\ &\simeq \left(\frac{1}{W}\right)^{d-1} \sum_{m\in I} g(\theta, E_\theta m/W) e^{-2\pi i\langle m,l\rangle/L}\end{aligned} \tag{9.19}$$

Clearly, (9.19) is to be processed by FFT.

Final algorithm for the operator $\tilde{\Psi}$ and $\tilde{\Psi}^*$ We introduce the following operators:

- FFT $\mathcal{F} : \mathbb{R}^{|I|} \to \mathbb{R}^{|I|}$.
- $D^j : \mathbb{R}^{|I|} \to \mathbb{R}^{|I|}$, defined as:

$$(D^j \mathbf{f})_l \triangleq \frac{|\det G_j|^{1/2}}{|\mathcal{S}^{d-2}|} L^{-d} W\|l\| b_{\hat{\psi}_j}(W\|l\|/L) f_l,\ l\in I$$

- Non-Uniform FFT $\mathcal{F}_\mathcal{N} : \mathbb{R}^{|I|} \to \mathbb{R}^{N_j}$, with N_j the number of nodes at scale j:

$$(\mathcal{F}_\mathcal{N}\mathbf{g})_k = \sum_{l\in I} g_l e^{-2\pi i\langle \omega_l, E_\theta^* G_j k\rangle}$$

  And $\mathcal{F}_\mathcal{N}{}^{j,p}$ to emphasize that the NUFFT depends on j,p.

Now we can put different parts together and get the algorithm for $\tilde{\Psi}$ and $\tilde{\Psi}^*$.

Algorithm 7 Forward operator $\tilde{\Psi}$. Input : sinogram vector $\mathbf{g}$

Initialization: for all scales j, set to zero $S_j \in \mathbb{R}^{N_j}$
for $|j| \leq J$ (parallelization) **do**
  for $p = 1 \dots P$ **do**
    $S_j \leftarrow S_j + \mathcal{F}_{\mathcal{N}}{}^{j,p} D^j \mathcal{F} \mathbf{g}_p$, with $\mathbf{g}_p$ the p-th projection.
  end for
end for

Algorithm 8 Backward operator $\tilde{\Psi}^*$. Input : coefficient vector S

Initialization: for all directions p, set to zero $\mathbf{g}_p \in \mathbb{R}^{|I|}$
for $p = 1 \dots P$ (parallelization) **do**
  for $|j| \leq J$ **do**
    $\mathbf{g}_p \leftarrow \mathbf{g}_p + \mathcal{F}^* D^j \mathcal{F}_{\mathcal{N}}{}^{j,p^*} S_j$, with S_j the coefficients of scale j.
  end for
end for

Appendix A

Blob-driven projector and back-projector

We present in this section an algorithm for the X-ray projector A and the associated back-projector A^*, which are invariant to the lattice structure. Baptized "blob-driven", it has two different forms, distinguished by the way how the contribution coefficient is calculated. Let's note A_{mk} the contribution coefficient of a blob centered at position x_k to the m-th detector bin. We can take A_{mk} as:

1. the linear integral defined by the intersection between the blob and the ray from the source to the center of detector bin, then we have the ray-tracing projector
2. or the area integral defined by the intersection between the blob and the strip region delimited by the source and the detector bin, then we have the strip-integral projector.

These two methods have the same computational complexity. The overall algorithm is parallelized and implemented on GPU. We resume the forward projection *kernel*, *i.e.*, the codes executed in parallel by all processor, in Algorithm 9. Remark that the step 3 is a concurrent operation since multiple kernels try to add their values to the same memory address. This can be correctly handled by the so-called *atomic operation*. The backward projection algorithm is similar to 9, with the step 3 replaced by: $f_k \leftarrow f_k + A_{mk} \times y_m$.

Algorithm 9 Forward projection kernel for the blob ϕ_k and the detector bin m

1: Input: blob coefficient vector $\mathbf{f}$, projection vector $\mathbf{y}$ to be updated.
2: Determine the contribution coefficient A_{mk}
3: Concurrent write: $y_m \leftarrow y_m + A_{mk} \times f_k$
4: Output: updated projection vector $\mathbf{y}$

A.0.4 Ray-tracing projector

The first method for calculating A_{mk} is close to the usual Siddon ray-tracing projector. It discretizes the continuous footprint of blob at the detector's sampling rate. The contribution coefficient A_{mk} is given by the Abel transform and depends only on the distance from the blob center x_k to the m-th ray. We list the Abel transforms of some blobs:

$$\begin{aligned}
\text{Gaussian (5.4):} \quad & \mathcal{A}b_\phi(t) = \sqrt{\pi/\alpha}\exp(-\alpha t^2) \\
\text{2D Diff-Gaussian (5.43):} \quad & \mathcal{A}b_\psi(t) = \sqrt{\pi/\alpha}\sum_{k=0}^{\infty}\frac{2C_k}{\sqrt{3k+1/2}}\exp\left(-\frac{4\alpha t^2}{3k+1/2}\right) \\
\text{2D Mexican hat (5.46):} \quad & \mathcal{A}b_\psi(t) = \sqrt{\pi/\alpha}\exp(-\alpha t^2)(1/2-\alpha t^2)
\end{aligned}$$

Using these analytical expressions A_{mk} can be evaluated on-the-fly, with the only exception of the Diff-Gaussian blob which has a cumbersome asymptotic expression. In this case, we pre-calculate and store its Abel transform, then look up the table on-the-fly to retrieve the contribution coefficient. For a dilated blob $\phi_\lambda(x) \triangleq \phi(\lambda x)$, we have $\mathcal{A}b_{\phi_\lambda}(t) = \lambda^{-1}\mathcal{A}b_\phi(\lambda t)$, and this allows to calculate A_{mk} for all the blobs in the multiscale system.

A.0.5 Strip-integral projector

The second method for calculating the contribution coefficient, can be seen roughly as applying a low-pass filter to the footprint of blob before sampling it. When the detector sampling rate is low, this method can effectively reduce the aliasing artefacts due to the sinogram discretization.

Figure A.1 illustrates the scenario for a blob centered at position x_k, denoted by $\phi_k(x) = \phi(x - x_k)$. The source is located at S, Γ is the m-th detector pixel delimited by the borders D_1 and D_2, and Σ is the strip region defined by the intersection of the blob and X-ray beam. The contribution coefficient A_{mk}, defined as the area integration of ϕ_k on Σ, is difficult to evaluate directly since there's no analytical expression for it. The solution we propose here (already mentioned in [97]), is to pre-calculate a strip-integral table and look up the table on-the-fly.

A.0.5.1 Looking-up table

Let $\theta_1 = SD_1/\|SD_1\|$ be a unitary vector and $\theta_1^\perp$ its orthogonal (defined as the $\pi/2$ clockwise rotation). The orthogonal projection of vector $Sx_k = x_k - S$ onto $\theta_1^\perp$ is

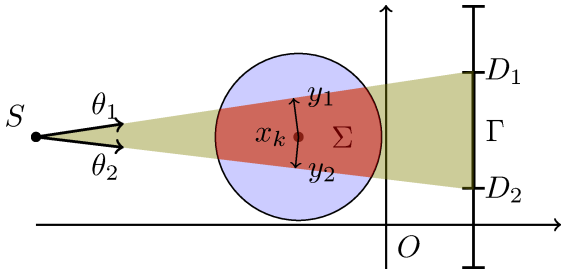

FIGURE A.1: The strip-integral is calculated as the area integration of blob function on the red region Σ.

$y_1 = t_1\theta_1^{\perp}$. Let Θ_1 be the circular segment situated at the opposed side of $\theta_1^{\perp}$. We have:

$$\int_{\Theta_1} \phi_k(x)dx = \int_{-\infty}^{t_1} \int_{\mathbb{R}} \phi_k(t\theta_1^{\perp} + s\theta_1)dsdt \tag{A.1}$$

We note $T(t)$ the pre-calculated table: $T(t) = \int_{-\infty}^{t} \mathcal{A}b_\phi(|r|)dr$, then it's easy to see that (A.1) equals to $T(t_1 - \langle x_k, \theta_1^{\perp}\rangle)$. Similar values and definitions exist for $\theta_2 = SD_2/\|SD_2\|$, *e.g.*, Θ_2 is the circular segment situated at the opposed side of $\theta_2^{\perp}$. Since $\Sigma = \Theta_2 - \Theta_1$, the strip-integral equals to the difference of two area integrals, and can be retrieved by two looking-up table operations:

$$\int_{\Sigma} \phi_k(x)dx = T(t_2 - \langle x_k, \theta_2^{\perp}\rangle) - T(t_1 - \langle x_k, \theta_1^{\perp}\rangle) \tag{A.2}$$

A.0.6 Back-projector

We define the back-projector by transposing the contribution coefficients of projector. For a detector pixel Γ, the contribution coefficient to blob ϕ_k is calculated exactly in the same way as for the projector. It is worth to note that if A is considered as an application from the solution space X to $\mathbb{R}^M$, the back-projector defined in this way is not necessarily the adjoint operator of A. Nevertheless, these two operators are adjoint between them as long as A is treated as an application from sequential space $\ell^2(\mathbb{Z})$ to $\mathbb{R}^M$, and we note:

$$(A\mathbf{f})_m = \sum_{k\in\mathbf{Z}} A_{mk}f_k, \;\; (A^*\mathbf{b})_k = \sum_{m=1}^{M} A_{km}b_m \tag{A.3}$$

Appendix B

Optimization methods

This chapter covers some important algorithms used in this thesis to solve the problems related to TV and ℓ^1 minimizations. An abundant literature exists on this subject (though in most of cases being independent of the CT application), and the methods that we have chosen are commonly considered to be in the state-of-the-art. We only resume these algorithms here for completeness and for reference reasons, and refer readers to the original publications for more advanced technical details.

B.1 Notations

- $\|x\| = (\sum_n |x_n|^2)^{1/2}$, $\|x\|_1 = \sum_n |x_n|$, and $\|x\|_\infty = \max_n |x_n|$
- $\|\cdot\|_{TV}$: discrete TV norm, see Chapter 3 and 6 for the definitions
- C: a convex closed subset of $\mathbb{R}^N$

Some useful results The following lemmas will be useful, and their proofs can be found in [48, 50].

Lemma B.1.1 (ℓ^1-shrinkage)**.** *Let $w, u \in \mathbb{R}^N$. The minimizer of the problem:*

$$\min_u \frac{1}{2}\|w-u\|^2 + \lambda\|u\|_1, \quad \textit{for } u \in \mathbb{R}^N \tag{B.1}$$

is given by the shrinkage formula:

$$u_n = \max\left(|w_n| - \lambda,\ 0\right) \cdot \textit{sign}(w_n), \ \textit{for } n = 1, \ldots, N \tag{B.2}$$

with $\textit{sign}(x) = 1$ if $x \geq 0$, and $\textit{sign}(x) = -1$ if otherwise.

Lemma B.1.2 (ℓ^2-shrinkage)**.** *Let $w, u \in \mathbb{R}^N$, and $\|\cdot\|$ the euclidien norm. The minimizer of the problem:*

$$\min_u \frac{1}{2}\|w-u\|^2 + \lambda\|u\|, \quad \text{for } u \in \mathbb{R}^N \tag{B.3}$$

is given by the shrinkage formula:

$$u = \max\left(\|w\| - \lambda,\ 0\right) \cdot \frac{w}{\|w\|} \tag{B.4}$$

where the convention $0 \cdot \frac{0}{0} = 0$ is followed.

We denote $\text{SoftThresh}\,(w,\lambda)$ and $\text{SoftThresh}_2\,(w,\lambda)$ the solution of (B.1) and of (B.3), respectively.

B.2 General framework for AL and ADM

The augmented Lagrangian(AL) and alternating direction method (ADM) are quite classic algorithms in the numerical optimization theory. In a series of papers [116][48][49] it has been shown that they are very efficient in solving the CS related problems.

Let $f(x) : \mathbb{R}^{N_1} \to \mathbb{R}$ and $g(y) : \mathbb{R}^{N_2} \to R$ be convex functions, and $A \sim M \times N_1, B \sim M \times N_2$ be two matrices. Consider the minimization problem:

$$\min_{x,y} f(x) + g(y) \ \text{ s.t. } \ Ax + By = b, \ \text{ for } x \in \mathbb{R}^{N_1}, y \in \mathbb{R}^{N_2} \tag{B.5}$$

which can be solved by minimizing the augmented Lagrangian function:

$$\max_{\lambda} \min_{x,y} \mathcal{L}_{\mathcal{A}}(x,y;\lambda), \ \text{ for } \ \text{ for } x \in \mathbb{R}^{N_1}, y \in \mathbb{R}^{N_2}, \lambda \in \mathbb{R}^M \tag{B.6}$$

The augmented Lagrangian $\mathcal{L}_{\mathcal{A}}(x,y;\lambda)$ is given by:

$$\mathcal{L}_{\mathcal{A}}(x,y;\lambda) \triangleq f(x) + g(y) + \langle \lambda, Ax + By - b\rangle + \frac{\beta}{2}\|Ax + By - b\|^2 \tag{B.7}$$

where $\lambda \in \mathbb{R}^P$ is the Lagrangian multiplier and $\beta > 0$ is the penalization parameter. The classical AL algorithm for solving (B.6) reads (k-th iteration):

$$\begin{cases} (x^{k+1}, y^{k+1}) & \leftarrow \arg\min_{x,y} \mathcal{L}_{\mathcal{A}}(x,y;\lambda) \\ \lambda & \leftarrow \lambda - \beta(Ax^{k+1} + By^{k+1} - b) \\ k & \leftarrow k+1 \end{cases} \tag{B.8}$$

Remark that the joint minimization of $\min_{x,y} \mathcal{L}_{\mathcal{A}}(x, y; \lambda)$ can be costly, and one can exploit the quasi-separable form of $\mathcal{L}_{\mathcal{A}}(x, y; \lambda)$ in x and y. Namely, at each iteration one solves alternatively x, y before update the Lagrangian multiplier λ. Then we have the general algorithm of ADM for solving eq. (B.6), as resumed in Algorithm 10. For the convergence of ADM see [48, 116] and the references therein. This general framework is powerful since by replacing f, g, one can solve a wide range of optimization problems related to Compressed Sensing, as we shall see in the following.

Algorithm 10 General framework for of ADM for solving (B.6)

Initialization $x^0, y^0, \lambda^0 = 0, k = 0, \beta > 0$
while not converged **do**
  $x^{k+1} \leftarrow \arg\min_x \mathcal{L}_{\mathcal{A}}(x, y^k; \lambda^k)$
  $y^{k+1} \leftarrow \arg\min_y \mathcal{L}_{\mathcal{A}}(x^{k+1}, y; \lambda^k)$
  $\lambda^{k+1} \leftarrow \lambda^k - \beta(Ax^{k+1} + By^{k+1} - b)$
  $k \leftarrow k + 1$
end while

B.3 TV minimization

Consider the following TV minimization problems:

$$\min_x \frac{\mu}{2}\|Ax - b\|^2 + \|x\|_{TV}, \text{ s.t. } x \in C \tag{TV}$$

$$\min_x \|x\|_{TV}, \text{ s.t. } Ax = b \text{ and } x \in C \tag{TV-EQ}$$

$$\min_x \|x\|_{TV}, \text{ s.t. } \|Ax - b\|^2 \leq \epsilon^2, \ x \in C \tag{TV-DN}$$

Recall the definition of discrete TV norm ($d = 2$ or 3, see chapters 3 and 6 for details):

$$\|x\|_{TV} = \sum_{n=1}^{N} \sqrt{(D^1 x)_n^2 + \ldots + (D^d x)_n^2} = \sum_{n=1}^{N} \|D_n x\| \tag{B.9}$$

where $D^i : \mathbb{R}^N \to \mathbb{R}^N$ is the discrete derivative operator in direction i. The element-wise operator $D_n : \mathbb{R}^N \to \mathbb{R}^d$ and the overall operator $D : \mathbb{R}^N \to \mathbb{R}^{d \times N}$ are defined as:

$$D_n x \triangleq \begin{pmatrix} (D^1 x)_n \\ \vdots \\ (D^d x)_n \end{pmatrix}, \ Dx \triangleq \begin{pmatrix} D^1 x \\ \vdots \\ D^d x \end{pmatrix} \tag{B.10}$$

We introduce the variable $u = [u_1^\top \dots u_N^\top]^\top \in \mathbb{R}^{d\times N}$, such that:

$$u_n = D_n x \in \mathbb{R}^d, \quad \text{for } n = 1 \dots N, \text{ and } u = Dx \tag{B.11}$$

i.e., u_n is the gradient of x taken at site n, and clearly $\|x\|_{TV} = \sum_n \|u_n\|$. Let's introduce the penalization parameter $\beta > 0$, the Lagrangian multipliers $\nu_1 \dots \nu_N \in \mathbb{R}^d$ (each ν_n is associated to a constraint $u_n = D_n x$), and $\nu = [\nu_1^\top \dots \nu_N^\top]^\top \in \mathbb{R}^{d\times N}$.

B.3.1 Solving the problem (TV-DN)

We discuss here only the solution of (TV-DN). The problems (TV) and (TV-EQ) can be solved by taking some trivial adaptations therefore omitted. By introducing the variables $y = Ax - b$, $u = Dx$ as in eq. (B.11) and the Lagrangian multipliers ν, λ, the AL function for (TV-DN) reads:

$$\begin{aligned}\mathcal{L}_{\mathcal{A}}(x, u, y; \nu, \lambda) \triangleq\ & \frac{\mu}{2}\|Ax - b - y\|^2 - \langle \lambda, Ax - b - y\rangle \\ & + \frac{\beta}{2}\|Dx - u\|^2 - \langle \nu, Dx - u\rangle + \sum_n \|u_n\|\end{aligned} \tag{B.12}$$

The overall AL iteration (B.8) now becomes:

$$\begin{cases} (x^{k+1}, u^{k+1}, y^{k+1}) & \leftarrow \arg\min_{x,u,y}\{\mathcal{L}_{\mathcal{A}}(x, u, y; \nu, \lambda),\ \|y\| \le \epsilon, x \in C\} \\ \nu & \leftarrow \nu - \beta(Dx^{k+1} - u^{k+1}) \\ \lambda & \leftarrow \lambda - \mu(Ax^{k+1} - b - y^{k+1}) \\ k & \leftarrow k + 1 \end{cases} \tag{B.13}$$

and the minimization of $\mathcal{L}_{\mathcal{A}}(x, u, y; \nu, \lambda)$ w.r.t. x, u, y is carried out by ADM in three steps:

$$y^{k+1} \leftarrow \arg\min_y \{\mathcal{L}_{\mathcal{A}}(x^k, u, y; \nu, \lambda),\ \|y\| \le \epsilon\} \tag{y-step}$$

$$u^{k+1} \leftarrow \arg\min_u \{\mathcal{L}_{\mathcal{A}}(x^k, u, y; \nu, \lambda)\} \tag{u-step}$$

$$x^{k+1} \leftarrow \arg\min_x \{\mathcal{L}_{\mathcal{A}}(x, u^{k+1}, y^{k+1}; \nu, \lambda) \ \text{ s.t. } \ x \in C\} \tag{x-step}$$

y-step The minimization problem in (y-step) can be rewritten as:

$$\min_y \|Ax^k - b - y - \lambda/\mu\|^2, \quad \text{s.t. } \|y\| \le \epsilon \tag{B.14}$$

and the solution is simply given by:

$$y^{k+1} = \epsilon \cdot \Pi_{B_2}(Ax^k - b - \lambda/\mu) \tag{B.15}$$

with B_2 the unit ℓ^2 ball in $\mathbb{R}^M$, and Π_K the convex projection onto set K.

u-step Note that (u-step) is equivalent to solving:

$$\min_u \sum_n \left(\|u_n\| + \frac{\beta}{2}\|D_n x^k - \nu_n/\beta - u_n\|^2 \right) \tag{B.16}$$

and its solution is obtained by applying the shrinkage formula of Lemma B.1.2:

$$u_n^{k+1} = \text{SoftThresh}_2\left(D_n x^k - \nu_n/\beta, \frac{1}{\beta}\right) \tag{B.17}$$

for $n = 1 \dots N$.

Remark B.3.1. If the anisotropic TV is used in place of (B.9):

$$\|x\|_{TV} = \sum_{n=1}^{N} |(D^1 x)_n| + \ldots + |(D^d x)_n| = \sum_n \|D_n x\|_1 \tag{B.18}$$

Then the shrinkage formula (B.17) becomes accordingly (all operations are component-wise):

$$u_n^{k+1} = \max\left(|w_n| - \frac{1}{\beta}, 0\right) \cdot \frac{w_n}{|w_n|} \tag{B.19}$$

x-step The minimization problem in (x-step) is equivalent to:

$$\min_{x \in C} \frac{\mu}{2}\|Ax - b - \lambda/\mu - y^{k+1}\|^2 + \frac{\beta}{2}\|Dx - \nu/\beta - u^{k+1}\|^2 \tag{B.20}$$

If the constraint C is off, its solution is simply given by the linear system:

$$(\mu A^\top A + \beta D^\top D)x = \beta D^\top (u^{k+1} + \nu/\beta) + \mu A^\top (b + y^{k+1} + \lambda/\mu) \tag{B.21}$$

A direct inversion of this system (with CG fox example) can be time-consuming when the dimension of x is high. This motivates the *TVAL3* and the *TVIADM* algorithms resumed in the next, which circumvent (B.21) by different techniques.

B.3.1.1 TVAL3

TVAL3 algorithm [48] solves (x-step) approximately. In place of inverting the system (B.21), it takes simply a gradient descent step:

$$x^{k+1} = x^k + \alpha g^k \tag{B.22}$$

with g^k the gradient of function $\mathcal{L}_\mathcal{A}(x, u^{k+1}, y^{k+1}; \nu, \lambda)$ w.r.t. x taken at x^k:

$$g^k = \mu A^\top (Ax^k - b - \lambda/\mu - y^{k+1}) + \beta D^\top (Dx^k - \nu/\beta - u^{k+1}) \tag{B.23}$$

The step length α is determined by the Barzilai-Borwein (BB) method [137]:

$$\alpha = \frac{\|x^k - x^{k-1}\|^2}{\langle x^k - x^{k-1}, g^k - g^{k-1}\rangle} \tag{B.24}$$

If some constraint set C is used, for example the positivity constraint $x_k \geq 0$, then (B.22) is followed by a projection step Π_C:

$$x^{k+1} = \Pi_C(x^k + \alpha g^k) \tag{B.25}$$

The gradient descent step (B.22) in place of solving exactly (B.21) might cause non convergence of ADM iterations. As a remedy, the TVAL3 algorithm applies ADM iteratively on x, u, y (called inner iteration), the Lagrangian multipliers are updated after the inner iteration. See Algorithm 11. It's worth to point out that there's no

Algorithm 11 TVAL3 for solving (TV-DN)

Initialization $x^0, k = 0$
while not converged **do**
  while inner iteration not converged **do**
    $y^{k+1} \leftarrow \arg\min_y \mathcal{L}_\mathcal{A}(x^k, u, y; \nu, \lambda)$ by (B.15)
    $u^{k+1} \leftarrow \arg\min_u \mathcal{L}_\mathcal{A}(x^k, u, y; \nu, \lambda)$ by shrinkage formula (B.17)
    $x^{k+1} \leftarrow \arg\min_x \mathcal{L}_\mathcal{A}(x, u^{k+1}, y^{k+1}; \nu, \lambda)$ by gradient step (B.25)
  end while
  $\nu \leftarrow \nu - \beta(Dx^{k+1} - u^{k+1})$
  $\lambda \leftarrow \lambda - \mu(Ax^{k+1} - b - y^{k+1})$
  $k \leftarrow k + 1$
end while

known theoretical proof on the convergence of TVAL3 in the literature, nevertheless, this algorithm in practice converges very fast and is competing with the other state-of-art TV solvers. We refer reader to the original report [48] for numerical evidences.

B.3.1.2 TVIADM

TVIADM [50] solves approximately (x-step) by linearizing $\|Ax-b\|^2/2$ around x^k and adding a proximal term $\mu/(2\tau)\|x-x^k\|^2$. The (x-step) is replaced by:

$$\min_x \frac{\beta}{2}\|Dx-\nu/\beta-u^{k+1}\|^2+\frac{\mu}{2\tau}\|x-(x^k-\tau h^k)\|^2 \tag{B.26}$$

with $h^k=A^\top(Ax^k-b-y^{k+1}-\lambda/\mu)$. The solution is given by the linear system:

$$\left(D^\top D+\frac{\mu}{\beta\tau}\,\mathrm{Id}\right)x=D^\top(u^{k+1}+\nu/\beta)+\frac{\mu}{\beta\tau}(x^k-\tau h^k) \tag{B.27}$$

When x is a pixel image, the matrix in eq. (B.27) can be inverted immediately by taking FFT. In Chapter 6 we have adapted this technique to the blob image, see Proposition 6.X. The final TVIADM algorithm is summarized in Algorithm 12.

Algorithm 12 TVIADM for solving (TV-DN)

Initialization $x^0, k=0$
while not converged **do**
  $y^{k+1}\leftarrow \arg\min_y \mathcal{L}_\mathcal{A}(x^k,u,y;\nu,\lambda)$ by (B.15)
  $u^{k+1}\leftarrow \arg\min_u \mathcal{L}_\mathcal{A}(x^k,u,y;\nu,\lambda)$ by shrinkage formula (B.17)
  $x^{k+1}\leftarrow \arg\min_x \mathcal{L}_\mathcal{A}(x,u^{k+1},y^{k+1};\nu,\lambda)$ by inverting (B.27) using FFT
  $\nu\leftarrow\nu-\beta(Dx^{k+1}-u^{k+1})$
  $\lambda\leftarrow\lambda-\mu(Ax^{k+1}-b-y^{k+1})$
  $k\leftarrow k+1$
end while

B.4 ℓ^1-minimization

The ℓ^1-minimization can be one of the following optimization problems:

$$\min_x \frac{\mu}{2}\|Ax-b\|^2+\|x\|_1,\ \text{s.t. } x\in C \tag{ℓ^1}$$

$$\min_x \|x\|_1,\ \text{s.t. } Ax=b \text{ and } x\in C \tag{BP}$$

$$\min_x \|x\|_1,\ \text{s.t. } \|Ax-b\|^2\le\epsilon^2,\ x\in C \tag{BPDN}$$

B.4.1 Solving the problem (BPDN)

Here we solve (BPDN) by the augmented Lagrangian method. Let's introduce the auxiliary variables: $y=Ax-b$, and the penalization parameter $\beta>0$, then the AL

function of (BPDN) reads:

$$\mathcal{L}_{\mathcal{A}}(x, y; \lambda) = \frac{\beta}{2}\|Ax - b - y\|^2 - \langle \lambda, Ax - b - y \rangle + \|x\|_1 \tag{B.28}$$

We need to solve

$$\min_{x,y} \mathcal{L}_{\mathcal{A}}(x, y; \lambda), \text{ s.t. } \|y\| \leq \epsilon$$

Now apply the ADM, at the k-th iteration one needs first to minimize $\mathcal{L}_{\mathcal{A}}(x^k, y; \lambda)$ with respect to y, which amounts to solve:

$$\min_{y} \frac{\beta}{2}\|Ax - b - y - \lambda/\beta\|^2 \text{ s.t. } \|y\| \leq \epsilon \tag{B.29}$$

The solution is simply:

$$y^{k+1} = \Pi_{B_\epsilon}(Ax^k - b - \lambda/\beta) \tag{B.30}$$

Then we need to minimize $\mathcal{L}_{\mathcal{A}}(x, y^{k+1}; \lambda)$ with respect to x. This is equivalent to solve:

$$\min_{x} J(x) + \|x\|_1 \tag{B.31}$$

with $J(x) = \frac{\beta}{2}\|Ax - b - y - \lambda/\beta\|^2$. Instead of solving (B.32) exactly, we solve its approximation by linearizing $J(x)$ around x^k and adding a proximal term:

$$\min_{x} \frac{\tau}{2}\|x - x^k\|^2 + \langle g^k, x - x^k \rangle + \|x\|_1 \tag{B.32}$$

with $g^k = \nabla J(x^k) = \beta A^\top (Ax^k - b - y^{k+1} - \lambda/\beta)$, and $\tau > 0$ the strength of the proximal term. Now one can apply the shrinkage formula (B.2) and get the solution of (B.32):

$$x^{k+1} = \text{SoftThresh}\left(x^k - g^k/\tau, 1/\tau\right) \tag{B.33}$$

If some convex constraint $x \in C$ is used, the above solution is followed by a projections step: $\Pi_C(x^{k+1})$. We resume the final algorithm in 13.

Algorithm 13 ADM for solving (BPDN)

Initialization $x^0, y^0, \lambda^0 = 0, k = 0, \beta > 0, \tau > 0$
while not converged **do**
  $y^{k+1} \leftarrow \arg\min_y \mathcal{L}_{\mathcal{A}}(x^k, y; \lambda)$, s.t. $\|y\| \leq \epsilon$ by (B.30)
  $x^{k+1} \leftarrow \arg\min_x \mathcal{L}_{\mathcal{A}}(x, y^{k+1}; \lambda)$ by (B.33)
  $\lambda \leftarrow \lambda - \beta(Ax^{k+1} - b - y^{k+1})$
  $k \leftarrow k + 1$
end while

Remark B.4.1. The convergence of this algorithm and the choice of the proximal strength τ are discussed in [116].

B.5 TV-ℓ^1 minimization

The hybrid TV-ℓ^1 minimization problem aims in solving:

$$\min_x \frac{1}{2}\|Ax-b\|^2 + \mu_1\|x\|_1 + \mu_2\|x\|_{TV} \tag{B.34}$$

As previously in section B.3.1, we introduce the auxiliary variable $u = Dx$, the lagrangian multiplier ν and the penalization constant $\beta > 0$. The augmented lagrangian function reads:

$$\mathcal{L}_{\mathcal{A}}(x,u;\nu) \triangleq \frac{1}{2}\|Ax-b\|^2 + \mu_1\|x\|_1 + \mu_2\sum_n\|u_n\| - \langle\nu, Dx-u\rangle + \frac{\beta}{2}\|Dx-u\|^2 \tag{B.35}$$

Now we apply the ADM as in section B.3.1. At the k-th iteration we need to solve alternatively the u-step and the x-step.

u-step Minimizing $\mathcal{L}_{\mathcal{A}}(x,u;\nu)$ with respect to u amounts to solve:

$$\min_u \sum_n \left(\mu_2\|u_n\| + \frac{\beta}{2}\|D_n x^k - \nu_n/\beta - u_n\|^2\right) \tag{B.36}$$

and its solution is again given by the shrinkage formula, for $n = 1\dots N$:

$$u_n^{k+1} = \text{SoftThresh}_2\left(D_n x^k - \nu_n/\beta, \frac{\mu_2}{\beta}\right) \tag{B.37}$$

x-step Minimizing $\mathcal{L}_{\mathcal{A}}(x,u;\nu)$ with respect to x is equivalent to:

$$\min_x J(x) + \mu_1\|x\|_1 \tag{B.38}$$

with $J(x) \triangleq \frac{1}{2}\|Ax-b\|^2 + \langle\nu, Dx-u\rangle + \frac{\beta}{2}\|Dx-u\|^2$. Unlike the problem (B.1), there's no close-form soft-thresh formula for (B.38). Instead of solving it exactly, we can solve an approximated version, by linearizing it around the current solution x^k and adding a proximal term $\frac{\tau}{2}\|x-x^k\|^2$:

$$\min_x \frac{\tau}{2}\|x-x^k\|^2 + \langle g^k, x-x^k\rangle + \mu_1\|x\|_1 \tag{B.39}$$

Here $\tau > 0$ is a constant controlling the proximal term strength, and g^k the gradient $g^k \triangleq \nabla J(x^k) = A^\top(Ax^k-b) - D^\top\nu + \beta D^\top(Dx^k-u)$. Now we note x^{k+1} the solution

of (B.39) given by:

$$x^{k+1} = \text{SoftThresh}\left(x^k - g^k/\tau, \mu_1/\tau\right) \tag{B.40}$$

The overall algorithm is resumed in Algorithm 14.

Algorithm 14 ADM for solving (B.34)

Initialization $x^0, u^0, \nu^0 = 0, k = 0, \beta > 0, \tau > 0$
while not converged **do**
  $u^{k+1} \leftarrow \arg\min_x \mathcal{L}_{\mathcal{A}}(x^k, u; \nu)$ by (B.37)
  $x^{k+1} \leftarrow \arg\min_x \mathcal{L}_{\mathcal{A}}(x, u^{k+1}; \nu)$ by (B.40)
  $\nu \leftarrow \nu - \beta(Dx^{k+1} - u^{k+1})$
  $k \leftarrow k + 1$
end while

Remark B.5.1. In order to guarantee the convergence of Algorithm 14, the proximal term constant $\tau > 0$ must be taken strong enough. In the limit case, we can set $\mu_2 = 0$ in (B.34), and the TV-ℓ^1 minimization becomes the ℓ^1 minimization problem. Then the gradient $g^k = A^\top(Ax^k - b)$, and Algorithm 14 is reduced to a simple Iterative Soft-Thresholding (IST) algorithm, *i.e.*,

$$x^{k+1} = \text{SoftThresh}\left(x^k - A^\top(Ax^k - b)/\tau, \mu_1/\tau\right) \tag{B.41}$$

τ is therefore interpreted as the gradient step length. It's known that IST converges if $\tau^{-1} \in (0, 2/\|A\|^2)$. See [116, 120] and [138] (Chapter 7) for more discussions.

Appendix C

Résumé de la thèse

C.1 Introduction

Cette thèse est une contribution aux algorithmes de reconstruction d'images pour le système de la tomographie par rayon X (X-ray CT), qui fonctionne à l'angle de vue complet mais avec un petit nombre de projections. CT est une technologie mature pour représenter visuellement l'intérieur d'un objet physique en utilisant des projections extérieures. Elle a des applications très répandues dans les domaines industriels et médicaux. Quelques exemples bien connus concernant notre vie quotidienne sont les systèmes d'imagerie dentaire ou cardiaque dans les hôpitaux, et les contrôles de bagage dans les aéroports. Un système de CT minimum est composé de deux parties:

- acquisition de données: à différentes positions d'une trajectoire échantillonnée autour de l'objet, la source de rayon X génère des photons qui seront atténués par l'objet, ensuite capturés par le détecteur.
- reconstruction d'images: les coefficients d'atténuation sont reconstitués à partir des données (aussi appelé le *sinogramme*) recueillis sur le détecteur, et représentés en niveau de gris pour la visualisation.

Notons $f : \mathbb{R}^d \to \mathbb{R}$ la fonction d'atténuation à reconstruire. L'expression mathématique pour le modèle de données est la transformée en rayon X:

$$\mathcal{P}f(\theta, y) = \mathcal{P}_\theta f(y) \triangleq \int_{\mathbb{R}} f(y + t\theta)dt, \ y \in \theta^\perp \tag{C.1}$$

avec la direction $\theta \in \mathcal{S}^{d-1}$, la sphère unitaire de $\mathbb{R}^d$. En 2D, cette transformation est équivalente à celle de Radon:

$$\mathcal{R}f(\theta, s) = \mathcal{R}_\theta f(s) \triangleq \int_{y \in \theta^\perp} f(y + s\theta)dy, \ s \in \mathbb{R} \tag{C.2}$$

On a affaire à une situation typique d'un problème inverse mal posé, du au fait que l'inversion $\mathcal{R}^{-1}$ n'est pas bornée.

C.1.1 Condition d'échantillonage

En pratique, les directions $\theta \in \{\theta_1 \dots \theta_P\}$ et les détecteurs $y \in \{y_1 \dots y_D\}$ sont tous les deux des nombres finis. Typiquement, les positions des sources sont équi-distribuées et les détecteurs ont tous la même taille. Ceci définit un schéma d'échantillonnage uniforme sur le domaine $\mathcal{T} = \{(\theta, y), \theta \in \mathcal{S}^{d-1}, y \in \theta^\perp\}$. Supposons que l'inconnue f est essentiellement B bande-limitée ([2], Chapitre 3), par les analyses de Shannon, un échantillonnage standard en 2D nécessite au moins $P \geq B/\pi$ projections et $D \geq B$ détecteurs afin d'obtenir une reconstruction fidèle de f [2]. En langage de pixel, ceci implique que $P \gtrsim 512$ projections seraient nécessaires pour reconstruire une image de dimension 512×512. C'est la condition d'échantillonnage typique exigée par de nombreux algorithmes analytiques comme la rétro-projection filtrée (FBP).

C.1.2 Problème de faible nombre de projections

Le problème de faible nombre de projections désigne la reconstruction en utilisant seulement $P \ll B/\pi$ projections (équitablement réparties), sans compromettre la qualité de l'image. En résolvant ce problème, nous pouvons améliorer à la fois la sécurité (faible dose) et la productivité (acquisition rapide) d'un système de CT. Malheureusement, les algorithmes classiques échouent dans cette situation: un faible taux d'échantillonnage angulaire conduit aux lourds artefacts qui peuvent rendre la reconstruction impossible à interpréter. Par ailleurs, la procédure d'inversion est instable du fait du bruit dans les données et du problème mal posé.

Objectif de cette thèse Dans cette thèse, nous visons à démontrer la faisabilité de la reconstruction à partir d'un faible nombre de projections pour un objet générique (*e.g.* médical ou industriel), et de fournir des algorithmes de reconstruction efficaces et robustes qu'on validera sur des données réelles et simulées.

C.1.3 Travaux précédents

Une méthode viable de traiter le problème de faible nombre de projections (et le problème des données incomplètes en général) consiste à utiliser les algorithmes *algébriques* ou *itératifs* qui permettent d'intégrer des informations préalables dans la procédure de reconstruction. Dans cette direction, des solutions diverses ont été proposées dans la littérature: elles sont basées sur différents modèles d'image et sont orientées vers de différentes applications. Dans le cadre bayésien, la reconstruction peut être réalisée par l'estimation du *maximum de la probabilité a posteriori* (MAP):

$$\hat{f} \triangleq \min_{f \in X} \; F(f, b) + R(f) \tag{MAP}$$

où X est un espace fonctionnel, $F(f, b)$ représente la fidélité aux données et incarne le processus physique de la génération des données b à partir du modèle f, et R est le terme de régularisation caractérisant l'information préalable sur f. Un cas particulier de R est le *prior préservant les bords* (EPP), qui suppose que f est homogène par région, et qu'il contient peu d'information en dehors des bords. Comme une large classe d'objet en CT peut être représentée par ce modèle, cette méthode peut les reconstituer efficacement en utilisant un petit nombre de projections.

Dans la même veine que l'EPP, la méthode de la minimisation TV modélise f dans l'espace de variation bornée et utilise la semi-norme de variation totale comme R. Les propriétés théoriques de cette méthode, telles que la préservation des bords et la perte des régions à faible contraste et des zones d'oscillation, ont été intensivement étudiées dans la littérature. L'efficacité surprenante de la minimisation TV dans le traitement du problème de faible nombre de projections a été signalée dans de nombreuses publications [3–6].

Plutôt que de reconstruire f directement comme un objet visuel, une autre possibilité est de régulariser dans l'espace de Besov: on utilise la norme de Besov comme R via la transformée en ondelette, et reconstruit les coefficients d'ondelette [7, 8]. Cette approche est basée sur le fait que la plus part des images naturelles peut être "compressée", c'est à dire fidèlement représentée par une base multi-résolution d'ondelette avec un petit nombre de coefficients. La capacité de compression et la structure de multi-résolution de la base d'ondelette offrent un moyen efficace pour réduire la dimension inhérente et pour résoudre le problème mal posé.

Le succès des méthodes de TV et d'ondelette peut être expliqué par “représenter une fonction dans un espace où elle est simple”. Par exemple, une fonction homogène par morceaux est simple dans l'espace BV car il n'y a pratiquement pas d'information en dehors des bords. De même, une image naturelle représentée par ses coefficients d'ondelette

a une petite norme Besov, due au fait que l'essentielle de ses informations est concentrée sur seulement quelques plus grands coefficients.

Parcimonie La notion de parcimonie entre alors dans notre champ de vision. Un vecteur est dit *parcimonieux* s'il contient peu de coefficients non nuls, ou *compressible* s'il peut être approché par un vecteur parcimonieux en conservant quelques plus grands coefficients. Pour un problème inverse où le nombre de données disponibles est beaucoup plus petit que la dimension de l'inconnu, chercher l'inconnu dans un espace où il est censé être parcimonieux serait beaucoup plus avantageux que d'autres techniques de régularisation, grâce au fait que la parcimonie réduit la dimension inhérente du système linéaire, et améliore la situation problématique, telles que la non unicité, l'instabilité de la solution par rapport au bruit, etc.

Du point de vue d'échantillonnage du signal, nous demandons si une fonction f peut être identifiée seulement à l'aide de quelques échantillons de son sinogramme en exploitant la parcimonie, et quelles seraient les conditions d'échantillonnage et les méthodes de reconstruction.

Compressed Sensing La théorie émergente de Compressed Sensing (CS) donne des réponses rigoureuses à ces questions. Grosso modo, si f est suffisamment parcimonieuse ou compressible par rapport aux certains systèmes de représentation, alors ses informations peuvent être capturées par quelques mesures aléatoires linéaires dont le nombre est quasi proportionnel au niveau de la parcimonie de f, et la reconstruction de f est posée comme un problème d'optimisation, par exemple, la minimisation de la norme ℓ^1. Par ailleurs, l'erreur de la reconstruction est proche de l'erreur de "compression". CS a également prouvé que la combinaison entre les mesures aléatoires et la minimisation ℓ^1 est en quelque sorte "optimale", car ils atteignent la borne théorique de la performance. Cette théorie nous fournit un cadre général pour le problème de faible nombre de projections. Pour cela, on a besoin de:

- représenter/modéliser f dans un espace qui favorise la parcimonie, par exemple, un système multi-échelle comme l'ondelette ou la curvelette, ou un dictionnaire arbitraire qui peut synthétiser une image avec un petit nombre d'atomes.
- chercher la solution parcimonieuse via des méthodes spécifiques non linéaires comme la minimisation TV ou ℓ^1.

Représentation d'image en CT Il est remarquable que la plupart des méthodes de reconstruction dans le cadre du CS utilise le pixel (ou le voxel en 3D) comme la

base de représentation de l'image. Outre sa simplicité numérique, le pixel est à la base de nombreuses transformées rapides (FFT, DCT, DWT, *etc.*). Cependant, vis-à-vis des algorithmes de reconstruction itérative en CT, le pixel n'est pas la manière optimal pour représenter une fonction pour les raisons suivantes:

- La localisation spatio-fréquentielle du pixel est médiocre. De gros pixels sont nécessaires pour contrôler la bande passante de la reconstruction et pour stabiliser la procédure d'inversion, en revanche la qualité visuelle est considérablement réduite.
- Il nécessite la discrétisation ou l'approximation du projecteur de rayon X, dont la complexité numérique est dominée par la dimension de la discrétisation, non pas par la parcimonie de l'image sous-jacente (par rapport au système de représentation).

De l'autre côté, la fonction radiale appelée Kaisser-Bessel blob qui est meilleure que le pixel pour les raisons mentionnées ci-dessus, a déjà été proposée il y a plusieurs décennies. Toutefois, le blob n'a pas une structure multi-échelle, et sa représentation de l'image n'est pas parcimonieuse. Par ailleurs, la plupart des méthodes de la reconstruction proposées pour le blob Kaisser-Bessel ne sont pas adéquates pour le problème de faible nombre de projections.

C.1.4 Contributions

Inspiré par tous ces éléments, nous développons dans cette thèse des bases radiales de la famille gaussienne toujours baptisés blobs, et nous les utilisont pour la représentation et la reconstruction d'image. Les blobs ont de meilleures propriétés de localisation spatio-fréquentielle que le pixel, et de nombreuses opérations, telles que la transformée en rayon X, le gradient ou l'interpolation, peuvent être analytiquement évaluées, ainsi on évite la discrétisation ou l'approximation dans le calcul du projecteur de rayon X. Une image représentée par blobs est compressible, de sorte que le système *ad hoc* de la représentation parcimonieuse utilisées dans les algorithmes CS ordinaires n'y est plus nécessaire.

En nous basant sur les blobs, nous allons construire un modèle mono-échelle et un modèle multi-échelle d'image, qui peuvent être qualifiés respectivement comme d'imitation du pixel ou de l'ondelette de multi-résolution, et nous étudierons certaines propriétés d'approximation de ces modèles.

Une fonction est représentée dans l'espace invariant par translation généré par blobs sur une grille hexagonale, et la reconstruction revient à déterminer les coefficients de

blobs par la minimisation de la norme TV ou ℓ^1, qui seront adaptés pour ces nouveaux modèles d'image. En fonction du caractère de l'objet (*e.g.*, constant par morceaux ou avec des régions à faible contraste), et du nombre de projections, ces deux méthodes de minimisation n'ont pas le même comportement.

Les calculs avec le blob, *e.g.* la projection de rayon X, l'interpolation, sont facilement parallélisables sur la plate-forme GPU. On développe un projecteur de rayon X baptisé *blob-driven* qui est implementé sur le GPU. Pour démontrer les efficacités des nouveaux modèles d'image et celles des algorithmes de reconstruction, nous les comparerons, à travers différentes expériences numériques, aux approches équivalentes basées sur la base de pixel / ondelette.

C.2 Linear data model and Bayesian framework

La reconstruction d'un objet spatial à partir d'un faible nombre de projections est un problème inverse mal posé, et les méthodes analytiques n'y sont pas adaptées [2]. Au contraire, les méthodes *itératives* (ou *algébriques*), qui exploitent l'information *a priori* de l'objet, peuvent stabiliser l'inversion et fournir des solutions satisfaisantes. Dans ce chapitre, nous introduisons un modèle de donnée linéaire largement accepté dans la littérature du CT. Ce modèle qui est fondamental pour tous nos futures études, décrit la relation linéaire entre l'observation et l'objet inconnu. Puis nous préparons un cadre général bayésien, dans lequel l'information *a priori* peut s'introduire facilement, et nous transformons le problème de la reconstruction sous la forme d'un problème d'optimisation.

C.3 Revue sur la régularisation et les méthodes itératives

L'utilisation de l'information *a priori* peut considérablement améliorer la qualité de la reconstruction, surtout quand les données observées sont incomplètes ou corrompues par du bruit. Dans le cadre bayésien, la régularisation R représente notre connaissance *a priori* sur la fonction inconnue f, principalement en terme de régularité. Une image de pixel est traitée comme un champ aléatoire de Markov, ainsi sa régularité est exprimée par une fonction de potentiel qui agit sur les cliques. L'espace à variation borée et l'espace de Besov sont des espaces de régularité très utiles pour la reconstruction en tomographie. Il existe aussi des méthodes non bayésiennes pour la régularisation des problèmes inverses, où l'information *a priori* n'est pas exprimée comme une distribution de probabilité. Dans ce chapitre, nous récapitulons les techniques de régularisation

ainsi que les méthodes itératives proposées dans le la littérature, et nous détaillons en particulier celles qui concernent directement le problème de faible nombre de projections.

C.4 Compressed Sensing et CT

Compressed Sensing (CS) est une théorie émergente sur l'acquisition et la reconstruction du signal, avec le double objectifs de capter les informations essentielles du signal en utilisant un petit nombre de mesures, et de reconstruire le signal original de façon fidèle. La mesure utilisée par CS est souvent aléatoire, ce qui permet de "compresser" les informations dans un petit nombre de mesures, tandis que le processus de la reconstruction est non linéaire, et son erreur peut être quantifiée en fonction de la complexité du signal et le nombre de mesures. Le cadre du CS est particulièrement utile dans les situations où une acquisition complète du signal est coûteuse ou même impossible, comme l'IRM et l'échantillonage du signal de bande extra-large. En adaptant le protocole d'acquisition au principe de CS, on peut réduire le taux d'échantillonnage au dessous de celui prédit par le théorème de Shannon-Nyquist. Dans la situation où la mesure est déterministe mais en petit nombre, on peut toujours utiliser le processus de reconstruction du CS pour stabiliser la reconstruction et aussi pour réduire l'erreur.

C.5 Blob radial pour la représentation de l'image

Une base radiale nommée *(Kaisser-Bessel) blob* et ses techniques de reconstruction dédiées ont déjà été proposées il y a plusieurs décennies. Limité par le charge du calcul, il semble que le potentiel derrière cette ligne de recherche reste inexploité par la communauté du CT, et qu'auncun effort n'a été réalisé pour l'adapter au problème de faible nombre de projections, où la notion de la parcimonie et les algorithmes de reconstruction non-linéaires deviennent incontournable. Le but de ce chapitre est d'introduire les blobs de la famille gaussienne, et de développer deux modèles de représentation d'images basées sur blobs: un modèle mono-échelle et un multi-échelle, qui peuvent être vus respectivement comme les imitations du pixel et des ondelettes de multirésolution, alors qu'ils possèdent de meilleures propriétés pour les applications du CT.

C.6 Méthodes de reconstruction pour l'image de blob

Basés sur les modèles d'image de blob mis en place dans les chapitres précédents, nous sommes maintenant en position de proposer des méthodes de reconstruction. Comme on

a souligné dans le chapitre 4, un “bon” algorithme de reconstruction qui atteint la limite théorique de la performance est non linéaire, et il exploite la parcimonie de l'image. Dans ce chapitre, nous nous concentrons sur les méthodes de reconstruction qui sont numériquement efficaces dans le contexte du CT et facilement adaptables aux modèles d'image blob, à savoir:

1. la minimisation de la variation totale de l'image blob
2. la minimisation de la norme ℓ^1 des coefficients de blob
3. l'hybride de la variation totale et le ℓ^1

C.7 Expériences numériques 2D - Données simulées

Dans ce chapitre, nous présentons les résultats des reconstructions 2D basées sur les modèles d'image blob et les méthodes de reconstruction présentées dans les chapitres précédents. Afin de montrer leur efficacité, nous allons les confronter aux approches équivalentes mais basées sur pixel. Comme l'efficacité d'une méthode de reconstruction dépend du contexte d'application, nous allons aussi comparer différentes images de fantôme. Les données ont été simulées à partir des images de pixel, ce qui permet d'avoir une évaluation précise de l'erreur de la reconstruction.

C.8 Expériences numériques 2D - Données réelles

Dans ce chapitre, nous présentons quelques résultats préliminaires avec des données réelles, obtenus par notres modèles d'images et notres méthodes de reconstruction. Les données proviennent de différentes domaines d'application, et ont été acquises de façon indépendante par notres collaborateurs sur diverses plate-formes non commerciales. Les paramètres géométriques des systèmes d'acquisition ne sont connues que avec une précision limitée.

C.9 Conclusions et perspectives

Dans cette thèse, nous avons étudié la faisabilité de la reconstruction des objets génériques (médicals ou industriels) en CT à partir d'un faible nombre de projections: est-ce qu'un petit nombre de projections peut capturer les informations essentielles d'un objet? Et comment le reconstruire?

Dans un cadre bayésien, nous avons vu l'importance de la régularisation: certains méthodes proposées dans la littérature, notamment celles fondées soit sur la préservation des bords, soit sur la variation totale ou les ondelettes, sont efficaces pour traiter ce problème. Ces méthodes sont étroitement liées à la théorie de Compressed Sensing. CS explique rigoureusement la relation triangulaire entre la parcimonie de l'inconnu, la condition d'échantillonnage à respecter, et la méthode de reconstruction ainsi que l'erreur entraînée. Le cadre général de CS pour résoudre notre problème est: 1) la représentation / la modélisation parcimonieuse de la fonction; 2) la reconstruction par des algorithmes non linéaires comme la minimisation TV ou ℓ^1. Ceci suggère le schema populaire de "pixel / voxel + base de parcimonie": tant que l'objet est suffisamment parcimonieux, il peut être reconstruit à partir d'un petit nombre de projections.

Néanmoins, un tel schéma n'est pas optimal pour la reconstruction en CT, en raison de la mauvaise localisation spatio-fréquentielle du pixel, mais aussi de la complexité numérique élevée quand on combine le projecteur de rayon X (basé sur pixel / voxel) avec la base *ad hoc* de la parcimonie, *e.g.* la transformée en ondelette. Ces observations nous ont conduit à adopter une base radiale appelée *blob* à CS. En particulier, nous avons construit les bases radiales de la famille gaussienne pour la représentation et la reconstruction de l'image. Leur localisation spatio-fréquentielle est meilleure que le pixel, et de nombreuses opérations, telles que la transformée en rayon X, le gradient ou l'interpolation, peuvent être évaluées analytiquement. Les images médicales typiques en CT sont compressibles par rapport à ces bases, de sorte que le système *ad hoc* de représentation parcimonieuse utilisé dans les algorithmes ordinaires de CS n'est plus nécessaire.

En se servant la théorie des ondelettes classiques, nous avons proposé deux modèles d'image. Le premier est l'espace invariant par translation engendré par un blob ϕ gaussien sur une grille hexagonale $\mathcal{L}$. Nous avons prouvé que ceci constitue une base de Riesz, mais sa limite n'est pas dense dans $L^2(\mathbb{R}^d)$. La seconde est la somme des espaces multi-échelles invariants par translation, et ces espaces sont engendrés par les blobs $\psi_j(x) = \beta^{-jd}\psi(\beta^{-j}x)$ sur les grilles $\mathcal{L}_j$ dyadiquement raffinées. Ceci constitue une trame étroite de $L^2(\mathbb{R}^d)$ à condition que le blob de mère ψ soit de bande limitée, et que la partition d'unité soit satisfaite. Le blob de chapeau mexicain et le blob de Diff-Gaussian peuvent être considérés comme bande limitée grâce à leurs décroissances exponentielles. Les adaptations des méthodes de minimisation du TV et du ℓ^1 aux images de blob sont directes, et le défi technique principal était de paralléliser le projecteur de rayon X et les interpolateurs (*e.g.* l'opérateur de gradient) sur la plate-forme GPU.

Grâce aux expérimentations numériques 2D avec des données simulées, nous avons montré que les nouveaux modèles ont effectivement de nombreux avantages par rapport aux

modèles classiques du pixel et de l'ondelette décimé. Comparée aux pixels, la reconstruction de TV basée sur le blob gaussien est beaucoup moins sensible à la variation du pas d'échantillonnage de la grille sous-jacente. Avec les fantômes médicaux, l'image de blob de faible dimension a la même qualité (mesurée en SNR et en SI) qu'une image de pixel de grande dimension. En travaillant dans une bande passante faible, la reconstruction basée sur le blob est plus stable que celle du pixel, tout en gardant la qualité visuelle d'image. Un tel phénomène peut être du à une meilleure localisation spatio-fréquentielle, la régularité et la symétrie radiale du blob, et aussi à l'utilisation de la grille hexagonale, qui a une fréquence angulaire supérieure, donc réduit des artefacts de zig-zag de la grille cartésienne.

Lorsque le nombre de projections P est grand, par exemple $P > 150$, le modèle du blob multi-échelle couplé avec la minimisation ℓ^1 offre une meilleure qualité d'image que la minimisation TV. Le système des blobs multi-échelles est une analogie de la base d'ondelette de multi-résolution, mais il est redondant donc moins concerné par le phénomène de pseudo Gibbs. En utilisant de différentes fantômes, nous avons révélé une différence fondamentale entre la méthode de TV et de ℓ^1. Contrairement à la minimisation TV qui élimine systématiquement les zones à faible contraste et à l'oscillation, la minimisation ℓ^1 préserve bien ces caractères, qui peuvent être essentiels pour certaines applications médicales. Au contraire, pour un P petit, par exemple $P < 80$, la méthode ℓ^1 est largement inférieure à celle du TV, à cause des artefacts de streaks et des blobs erronées à fine échelle. La minimisation hybride TV-ℓ^1 combine la meilleur partie de chacun et améliore la qualité de l'image pour un P moyennement élevé. Nous tirons la conclusion que le choix du modèle de l'image et la méthode de reconstruction doivent être faites en prenant en compte le contexte d'application et aussi la complétude des données. Le modèle d'image multi-échelle et les méthodes TV/ℓ^1 et TV-ℓ^1 que nous avons proposées peuvent couvrir un large champ d'applications en fonction du nombre de projections.

A la fin, nous avons validé notre approche sur des données réelles provenant de différents domaines où la réduction du nombre de projections a des intérêts réels. Bien que les qualités des données sont limitées, nos résultats préliminaires confirment que, de manière générale, le nombre de projections dans ces applications peut être réduit jusqu'à 50%, sans pour autant compromettre la qualité de l'image.

Bibliography

[1] Marius Costin. *Marius Costin. Multiresolution Image Reconstruction in X-ray Micro- and Nano- Computed Tomography: Application in Materials Non-Destructive Testing.* PhD thesis, L'Institut National des Sciences Appliquées de Lyon, EEA, 2010.

[2] F. Natterer. *The mathematics of computerized tomography.* Society for Industrial Mathematics, 2001.

[3] G. T. Herman and R. Davidi. Image reconstruction from a small number of projections. *Inverse problems*, 24:045011, 2008.

[4] J. Tang, B. E Nett, and G. H Chen. Performance comparison between total variation (TV)-based compressed sensing and statistical iterative reconstruction algorithms. *Physics in Medicine and Biology*, 54:5781, 2009.

[5] J. Bian, J. H Siewerdsen, X. Han, E. Y Sidky, J. L Prince, C. A Pelizzari, and X. Pan. Evaluation of sparse-view reconstruction from flat-panel-detector cone-beam CT. *Physics in Medicine and Biology*, 55:6575, 2010.

[6] E. Y Sidky, C. M Kao, and X. Pan. Accurate image reconstruction from few-views and limited-angle data in divergent-beam CT. *Journal of X-Ray Science and Technology*, 14(2):119–139, 2006.

[7] K. Niinimäki, S. Siltanen, and V. Kolehmainen. Bayesian multiresolution method for local tomography in dental x-ray imaging. *Physics in Medicine and Biology*, 52:6663, 2007.

[8] K. Niinimaki, V. Kolehmainen, and S. Siltanen. Multiresolution local tomography in dental radiology using wavelets. In *Engineering in Medicine and Biology Society, 2007. EMBS 2007. 29th Annual International Conference of the IEEE*, pages 2912–2915. IEEE, 2007. ISBN 1557-170X.

[9] T. M Buzug. *Computed tomography: from photon statistics to modern cone-beam CT.* Springer Verlag, 2008. ISBN 3540394079.

[10] É Barat and T. Dautremer. A nonparametric bayesian approach for emission tomography reconstruction. In *AIP Conference Proceedings*, volume 954, page 381, 2007.

[11] K. Sauer and C. Bouman. A local update strategy for iterative reconstruction from projections. *Signal Processing, IEEE Transactions on*, 41(2):534–548, 1993.

[12] J. Kaipio and E. Somersalo. *Statistical and Computational Inverse Problems. Number 160 in Applied Mathematics*. New York: Springer, 2004.

[13] O. Scherzer. *Variational methods in imaging*, volume 167. Springer Verlag, 2009. ISBN 0387309314.

[14] S. Mallat. *A Wavelet Tour of Signal Processing, The Sparse Way*. Academic Press Professional, Inc., 2009.

[15] Robert L. Siddon. Fast calculation of the exact radiological path for a three-dimensional CT array. *Medical Physics*, 12(2):252–255, March 1985. doi: 10.1118/1.595715. URL http://link.aip.org/link/?MPH/12/252/1.

[16] P. M Joseph. An improved algorithm for reprojecting rays through pixel images. *Medical Imaging, IEEE Transactions on*, 1(3):192–196, 1982.

[17] B. D Man and S. Basu. Distance-driven projection and backprojection in three dimensions. *Physics in medicine and biology*, 49:2463, 2004.

[18] W. Zhuang, S. S. Gopal, and T. J. Hebert. Numerical evaluation of methods for computing tomographic projections. *Nuclear Science, IEEE Transactions on*, 41 (4):1660–1665, 1994.

[19] Y. Z. O'Connor and J. A Fessler. Fourier-based forward and back-projectors in iterative fan-beam tomographic image reconstruction. *Medical Imaging, IEEE Transactions on*, 25(5):582–589, 2006.

[20] S. Matej, J. A. Fessler, and I. G. Kazantsev. Iterative tomographic image reconstruction using fourier-based forward and back-projectors. *IEEE Transactions on medical imaging*, 23(4):401–412, 2004.

[21] Y. Long, J. A Fessler, and J. M Balter. 3D forward and Back-Projection for X-Ray CT using separable footprints. *Medical Imaging, IEEE Transactions on*, 29(11): 1839–1850, 2010.

[22] Per-Erik Danielsson, Maria Magnusson Seger, and Johan Sunnegårdh. Basis and window functions in CT. 2005. URL

http://www.cvl.isy.liu.se/ScOut/Publications/PaperInfo/dms05.html. Welcome to the Computer Vision Laboratory at Linköping University in Linköping, Sweden.

[23] J. Nocedal and S. J. Wright. *Numerical optimization*. Springer Verlag, 1999.

[24] C. Bouman and K. Sauer. A generalized gaussian image model for edge-preserving MAP estimation. *IEEE Transactions on Image Processing*, 2(3):296–310, 1993.

[25] R Casanova, A Silva, and A R Borges. MIT image reconstruction based on edge-preserving regularization. *Physiological Measurement*, 25(1):195–207, February 2004. ISSN 0967-3334. doi: 10.1088/0967-3334/25/1/026. URL http://iopscience.iop.org/0967-3334/25/1/026.

[26] A. Raj, G. Singh, R. Zabih, B. Kressler, Y. Wang, N. Schuff, and M. Weiner. Bayesian parallel imaging with edge preserving priors. *Magnetic Resonance in Medicine*, 57(1):8–21, 2007.

[27] P. Charbonnier, L. Blanc-Feraud, G. Aubert, and M. Barlaud. Deterministic edge-preserving regularization in computed imaging. *IEEE Transactions on image processing*, 6(2):298–311, 1997.

[28] T. Hsiao, A. Rangarajan, and G. Gindi. A new convex edge-preserving median prior with applications to tomography. *IEEE transactions on medical imaging*, 22 (5):580–585, 2003.

[29] N. Villain, Y. Goussard, J. Idier, and M. Allain. 3D edge-preserving image enhancement for computed tomography. *IEEE Trans. Med. Imag*, 22(10):1275–1287, 2003.

[30] A. H Delaney and Y. Bresler. Globally convergent edge-preserving regularized reconstruction: an application to limited-angle tomography. *Image Processing, IEEE Transactions on*, 7(2):204–221, 1998.

[31] M. Nikolova and R. H. Chan. The equivalence of half-quadratic minimization and the gradient linearization iteration. *IEEE Transactions on Image Processing*, 16 (6):1623, 2007.

[32] M. Nikolova. Analysis of the recovery of edges in images and signals by minimizing nonconvex regularized least-squares. *Multiscale modeling and simulation*, 4(3): 960–991, 2005.

[33] P. J. Green. Bayesian reconstructions from emission tomography data using a modified EM algorithm. *IEEE Transactions on Medical Imaging*, 9(1):84–93, 1990.

[34] P. Perona and J. Malik. Scale-space and edge detection using anisotropic diffusion. *Pattern Analysis and Machine Intelligence, IEEE Transactions on*, 12(7):629–639, 1990.

[35] S. A Geman, D. E McClure, and Center for Intelligent Control Systems (US). *Statistical methods for tomographic image reconstruction*. Center for Intelligent Control Systems, 1987.

[36] A. Blake and A. Zisserman. Visual reconstruction. 1987.

[37] D. Geman and C. Yang. Nonlinear image recovery with half-quadratic regularization. *IEEE Transactions on Image Processing*, 4(7):932–946, 1995.

[38] C. A. Bouman and K. Sauer. A unified approach to statistical tomography using coordinate descent optimization. *IEEE Transactions on Image Processing*, 5(3): 480–492, 1996.

[39] S. S Saquib, C. A Bouman, and K. Sauer. A non-homogeneous MRF model for multiresolution bayesian estimation. In *Image Processing, 1996. Proceedings., International Conference on*, volume 1, pages 445–448 vol. 2. IEEE, 1996. ISBN 0780332598.

[40] J. B Thibault, K. D Sauer, C. A Bouman, and J. Hsieh. A three-dimensional statistical approach to improved image quality for multislice helical CT. *Medical physics*, 34:4526, 2007.

[41] L. C Evans and R. F Gariepy. *Measure theory and fine properties of functions*. CRC, 1992. ISBN 0849371570.

[42] L. I Rudin, S. Osher, and E. Fatemi. Nonlinear total variation based noise removal algorithms. *Physica D: Nonlinear Phenomena*, 60(1-4):259–268, 1992.

[43] Y. Meyer. *Oscillating patterns in image processing and nonlinear evolution equations: the fifteenth Dean Jacqueline B. Lewis memorial lectures*, volume 22. Amer Mathematical Society, 2001. ISBN 0821829203.

[44] A. Haddad and Y. Meyer. An improvement of Rudin-Osher-Fatemi model. *Applied and Computational Harmonic Analysis*, 22(3):319–334, 2007.

[45] A. Chambolle. An algorithm for total variation minimization and applications. *Journal of Mathematical Imaging and Vision*, 20(1):89–97, 2004.

[46] E. Candes and J. Romberg. l1-magic: Recovery of sparse signals via convex programming. *URL: www. acm. caltech. edu/l1magic/downloads/l1magic. pdf*, 2005.

[47] S. Becker, J. Bobin, and E. Candes. NESTA: a fast and accurate first-order method for sparse recovery. *Arxiv preprint arXiv:0904.3367*, 2009.

[48] Chengbo Li, Wotao Yin, and Yin Zhang. TV minimization by augmented lagrangian and ALternating direction ALgorithms, 2009. URL http://www.caam.rice.edu/~optimization/L1/TVAL3/.

[49] Y. Wang, J. Yang, W. Yin, and Y. Zhang. A new alternating minimization algorithm for total variation image reconstruction. *SIAM Journal on Imaging Sciences*, 1(3):248–272, 2008.

[50] Y. Xiao and J. Yang. A fast algorithm for total variation image reconstruction from random projections. *Arxiv preprint arXiv:1001.1774*, 2010.

[51] Y. Meyer and D. H. Salinger. *Wavelets and operators*. Cambridge Univ Pr, 1995.

[52] R. DeVore and B. Lucier. Fast wavelet techniques for near-optimal image processing. In *MILCOM*, pages 48–48. Citeseer, 1992.

[53] V. Kolehmainen, A. Vanne, S. Siltanen, S. Järvenpää, J. P Kaipio, M. Lassas, and M. Kalke. Bayesian inversion method for 3D dental x-ray imaging. *e & i Elektrotechnik und Informationstechnik*, 124(7):248–253, 2007.

[54] V. Kolehmainen, S. Siltanen, S. Järvenpää, J. P. Kaipio, P. Koistinen, M. Lassas, J. Pirttilä, and E. Somersalo. Statistical inversion for medical x-ray tomography with few radiographs: II. application to dental radiology. *Physics in Medicine and Biology*, 48:1465, 2003.

[55] M. Rantala, S. Vanska, S. Jarvenpaa, M. Kalke, M. Lassas, J. Moberg, and S. Siltanen. Wavelet-based reconstruction for limited-angle x-ray tomography. *Medical Imaging, IEEE Transactions on*, 25(2):210–217, 2006.

[56] S. Vänskä, M. Lassas, and S. Siltanen. Statistical x-ray tomography using empirical besov priors. *International Journal of Tomography & Statistics*, 11(S09):3–32, 2009.

[57] S.F. Gull and J. Skilling. Maximum entropy method in image processing. *Communications, Radar and Signal Processing, IEE Proceedings F*, 131(6):646–659, 1984. ISSN 0143-7070. doi: 10.1049/ip-f-1:19840099.

[58] E. T. Jaynes. On the rationale of maximum-entropy methods. *Proc. IEEE*, 70(9): 939–952, 1982.

[59] M. A. Limber, T. A. Manteuffel, S. F. McCormick, and D. S. Sholl. Optimal resolution in maximum entropy image reconstruction from projections with multigrid

acceleration. In *NASA CONFERENCE PUBLICATION*, pages 361–361. Citeseer, 1993.

[60] A. Mohammad-Djafari and G. Demoment. Maximum entropy image reconstruction in x-ray and diffraction tomography. *Medical Imaging, IEEE Transactions on*, 7(4):345–354, 1988.

[61] S. F. Gull and T. J. Newton. Maximum entropy tomography. *Applied optics*, 25 (1):156–160, 1986.

[62] D. L. Donoho, I. M. Johnstone, J. C. Hoch, and A. S. Stern. Maximum entropy and the nearly black object. *Journal of the Royal Statistical Society. Series B (Methodological)*, 54(1):41–81, 1992.

[63] M. I. Reis and N. C. Roberty. Maximum entropy algorithms for image reconstruction from projections. *Inverse Problems*, 8:623–644, 1992.

[64] R. Gordon, R. Bender, and G. T Herman. Algebraic reconstruction techniques (ART) for three-dimensional electron microscopy and x-ray photography* 1. *Journal of theoretical Biology*, 29(3):471–481, 1970.

[65] Cristian Badea and Richard Gordon. Experiments with the nonlinear and chaotic behaviour of the multiplicative algebraic reconstruction technique (MART) algorithm for computed tomography. *Physics in Medicine and Biology*, 49(8):1455–1474, April 2004. ISSN 0031-9155. doi: 10.1088/0031-9155/49/8/006. URL http://iopscience.iop.org/0031-9155/49/8/006.

[66] B. A. Ardekani, M. Braun, B. F. Hutton, I. Kanno, and H. Iida. Minimum cross-entropy reconstruction of PET images using prior anatomical information. *Physics in Medicine and Biology*, 41:2497–2517, 1996.

[67] C. L. Byrne. Iterative image reconstruction algorithms based on cross-entropy minimization. *IEEE Transactions on image processing*, 2(1):96–103, 1993.

[68] D. C. Youla and H. Webb. Image restoration by the method of convex projections: part 1 theory. *IEEE Transactions on Medical Imaging*, 1(2):81, 1982.

[69] J. Duchi, S. Shalev-Shwartz, Y. Singer, and T. Chandra. Efficient projections onto the l 1-ball for learning in high dimensions. In *Proceedings of the 25th international conference on Machine learning*, pages 272–279. ACM, 2008.

[70] E. Candes and J. Romberg. Practical signal recovery from random projections. 2008.

[71] E. J Candès, J. Romberg, and T. Tao. Robust uncertainty principles: Exact signal reconstruction from highly incomplete frequency information. *Information Theory, IEEE Transactions on*, 52(2):489–509, 2006.

[72] D. L. Donoho. Compressed sensing. *IEEE Transactions on Information Theory*, 52(4):1289–1306, 2006.

[73] A. C Hansen. Generalized sampling and infinite dimensional compressed sensing. Technical report, Technical report NA2011/02, DAMTP, University of Cambridge, 2011.

[74] E. J. Candès. Compressive sampling. In *Proceedings of the International Congress of Mathematicians*, volume 1. Citeseer, 2006.

[75] A. Cohen, W. Dahmen, and R. DeVore. Compressed sensing and best k-term approximation. *AMERICAN MATHEMATICAL SOCIETY*, 22(1):211–231, 2009.

[76] R. A. DeVore. Nonlinear approximation. *Acta numerica*, 7:51–150, 2008.

[77] J. A Tropp and A. C Gilbert. Signal recovery from random measurements via orthogonal matching pursuit. *Information Theory, IEEE Transactions on*, 53(12): 4655–4666, 2007.

[78] T. Blumensath and M. E. Davies. Iterative hard thresholding for compressed sensing. *Applied and Computational Harmonic Analysis*, 2009.

[79] D. Needell and J. A. Tropp. CoSaMP: iterative signal recovery from incomplete and inaccurate samples. *Applied and Computational Harmonic Analysis*, 26(3): 301–321, 2009.

[80] E. J Candes and T. Tao. Decoding by linear programming. *Information Theory, IEEE Transactions on*, 51(12):4203–4215, 2005.

[81] E. J Candes. The restricted isometry property and its implications for compressed sensing. *Comptes Rendus Mathematique*, 346(9-10):589–592, 2008.

[82] E. J Candes and T. Tao. Near-optimal signal recovery from random projections: Universal encoding strategies? *Information Theory, IEEE Transactions on*, 52 (12):5406–5425, 2006.

[83] M. Rudelson and R. Vershynin. On sparse reconstruction from fourier and gaussian measurements. *Communications on Pure and Applied Mathematics*, 61(8):1025–1045, 2008.

[84] E. Candès and J. Romberg. Sparsity and incoherence in compressive sampling. *Inverse problems*, 23:969, 2007.

[85] A. C Kak and M. Slaney. Principles of computerized tomographic imaging. 1988.

[86] M. J. Fadili, J. L Starck, and F. Murtagh. Inpainting and zooming using sparse representations. *The Computer Journal*, 52(1):64, 2009.

[87] M. Elad, J. L Starck, P. Querre, and D. L Donoho. Simultaneous cartoon and texture image inpainting using morphological component analysis (MCA). *Applied and Computational Harmonic Analysis*, 19(3):340–358, 2005.

[88] L. Desbat. Efficient sampling on coarse grids in tomography. *Inverse Problems*, 9: 251, 1993.

[89] A. Faridani. Fan-beam tomography and sampling theory. *The radon transform, inverse problems, and tomography: American Mathematical Society short course, January 3-4, 2005, Atlanta, Georgia*, 63:43, 2006.

[90] A. M. Cormack. Sampling the radon transform with beams of finite width. *Physics in medicine and biology*, 23:1141, 1978.

[91] G. Peyré. Best basis compressed sensing. *Signal Processing, IEEE Transactions on*, 58(5):2613–2622, 2010.

[92] Emmanuel J Candès and David L Donoho. New tight frames of curvelets and optimal representations of objects with piecewise c2 singularities. *Communications on Pure and Applied Mathematics*, 57(2):219–266, February 2004. ISSN 1097-0312. doi: 10.1002/cpa.10116. URL http://onlinelibrary.wiley.com/doi/10.1002/cpa.10116/abstract.

[93] H. Rauhut, K. Schnass, and P. Vandergheynst. Compressed sensing and redundant dictionaries. *Information Theory, IEEE Transactions on*, 54(5):2210–2219, 2008.

[94] M. Aharon, M. Elad, and A. Bruckstein. K-SVD: an algorithm for designing overcomplete dictionaries for sparse representation. *Signal Processing, IEEE Transactions on*, 54(11):4311–4322, 2006.

[95] I. Tosic, I. Jovanovic, P. Frossard, M. Vetterli, and N. Duric. Ultrasound tomography with learned dictionaries. In *Acoustics Speech and Signal Processing (ICASSP), 2010 IEEE International Conference on*, pages 5502–5505. IEEE, 2010. ISBN 1520-6149.

[96] R. M. Lewitt. Multidimensional digital image representations using generalized Kaiser-Bessel window functions. *Journal of the Optical Society of America A*, 7 (10):1834–1846, 1990.

[97] R. M. Lewitt. Alternatives to voxels for image representation in iterative reconstruction algorithms. *Physics in Medicine and Biology*, 37:705–716, 1992.

[98] S. Matej and R. M. Lewitt. Image representation and tomographic reconstruction using spherically-symmetric volume elements. In *Nuclear Science Symposium and Medical Imaging Conference, 1992., Conference Record of the 1992 IEEE*, pages 1191–1193, 1992.

[99] M. D. Buhmann. Radial basis functions. *Acta numerica*, 9:1–38, 2001.

[100] J. J. Green. *Approximation with the radial basis functions of Lewitt*. SHEFFIELD UNIV (UNITED KINGDOM) DEPT OF APPLIED MATHEMATICS, 2001.

[101] S. Matej and R.M. Lewitt. Practical considerations for 3-D image reconstruction using spherically symmetric volume elements. *Medical Imaging, IEEE Transactions on*, 15(1):68–78, 1996. ISSN 0278-0062. doi: 10.1109/42.481442.

[102] R. M. Mersereau. The processing of hexagonally sampled two-dimensional signals. *Proceedings of the IEEE*, 67(6):930–949, 2005.

[103] X. He and W. Jia. Hexagonal structure for intelligent vision. In *Information and Communication Technologies, 2005. ICICT 2005. First International Conference on*, pages 52–64. IEEE, 2006. ISBN 0780394216.

[104] J. H Conway, N. J.A Sloane, and E. Bannai. *Sphere packings, lattices, and groups*. Springer Verlag, 1999. ISBN 0387985859.

[105] P Maass. The x-ray transform: singular value decomposition and resolution. *Inverse Problems*, 3(4):729–741, November 1987. ISSN 0266-5611. doi: 10.1088/0266-5611/3/4/016. URL http://iopscience.iop.org/0266-5611/3/4/016.

[106] G. Strang and G. Fix. A fourier analysis of the finite element variational method. *Constructive aspects of functional analysis*, page 796–830, 1971.

[107] C. De Boor, R. A. DeVore, and A. Ron. Approximation from shift-invariant subspaces of l 2 (R d). *Transactions of the American Mathematical Society*, 341(2): 787–806, 1994.

[108] S. G. Mallat. Multiresolution approximations and wavelet orthonormal bases of $l^2 (R)$. *Transactions of the American Mathematical Society*, 315(1):69–87, 1989.

[109] I. Daubechies. *Ten lectures on wavelets*. Society for Industrial Mathematics, 1992. ISBN 0898712742.

[110] D. L. Donoho. Nonlinear solution of linear inverse problems by wavelet-vaguelette decomposition. *Applied and Computational Harmonic Analysis*, 2(2):101–126, 1995.

[111] E. D. Kolaczyk. A wavelet shrinkage approach to tomographic image reconstruction. *Journal of the American Statistical Association*, 91(435), 1996.

[112] Eric D. Kolaczyk, David L. Donoho, and Richard A. Olshen. *Wavelet Methods For The Inversion Of Certain Homogeneous Linear Operators In The Presence Of Noisy Data.* PhD thesis, 1994. URL http://citeseerx.ist.psu.edu/viewdoc/summary?doi=10.1.1.50.6190.

[113] L. Cavalier and J. Y Koo. Poisson intensity estimation for tomographic data using a wavelet shrinkage approach. *Information Theory, IEEE Transactions on*, 48 (10):2794–2802, 2002.

[114] S. S Chen, D. L Donoho, and M. A Saunders. Atomic decomposition by basis pursuit. *SIAM journal on scientific computing*, 20(1):33–61, 1999.

[115] A. Beck and M. Teboulle. A fast iterative shrinkage-thresholding algorithm for linear inverse problems. *SIAM Journal on Imaging Sciences*, 2(1):183–202, 2009.

[116] J. Yang and Y. Zhang. Alternating direction algorithms for l1-problems in compressive sensing. *preprint*, pages 95616–8633, 2009.

[117] E. Hale, W. Yin, and Y. Zhang. *FPC: A fixed-point continuation method for l1-regularization.* 2007.

[118] J. Trzasko and A. Manduca. Highly undersampled magnetic resonance image reconstruction via homotopic 0-minimization. *IEEE Trans. Medical Imaging*, 28 (1):106–121, 2009.

[119] D. L Donoho and Y. Tsaig. Fast solution of $ ell _ 1 $-norm minimization problems when the solution may be sparse. *Information Theory, IEEE Transactions on*, 54 (11):4789–4812, 2008.

[120] S. Ma, W. Yin, Y. Zhang, and A. Chakraborty. An efficient algorithm for compressed MR imaging using total variation and wavelets. In *Computer Vision and Pattern Recognition, 2008. CVPR 2008. IEEE Conference on*, pages 1–8. IEEE, 2008. ISBN 1063-6919.

[121] W. Guo and W. Yin. Edgecs: Edge guided compressive sensing reconstruction. In *Proc. of SPIE Vol*, volume 7744, pages 77440L–1. Citeseer, 2010.

[122] E. J Candes, M. B Wakin, and S. P Boyd. Enhancing sparsity by reweighted 1 minimization. *Journal of Fourier Analysis and Applications*, 14(5):877–905, 2008.

[123] Y. Wang and W. Yin. Compressed sensing via iterative support detection. *Rice University CAAM Technical Report TR09-30, http://www. caam. rice. edu/~ wy1/paperfiles/Rice_ CAAM_ TR09-30. pdf*, 2009.

[124] D. Wipf and S. Nagarajan. Iterative reweighted $ ell_1 $ and $ ell_2 $ methods for finding sparse solutions. *Selected Topics in Signal Processing, IEEE Journal of*, 4(2):317–329, 2010.

[125] R. Chartrand and W. Yin. Iteratively reweighted algorithms for compressive sensing. In *Acoustics, Speech and Signal Processing, 2008. ICASSP 2008. IEEE International Conference on*, pages 3869–3872. IEEE, 2008. ISBN 1520-6149.

[126] E. Y Sidky, R. Chartrand, and X. Pan. Image reconstruction from few views by non-convex optimization. In *Nuclear Science Symposium Conference Record, 2007. NSS'07. IEEE*, volume 5, pages 3526–3530. IEEE, 2007. ISBN 1082-3654.

[127] J. Yang, Y. Zhang, and W. Yin. A fast TVL1-L2 minimization algorithm for signal reconstruction from partial fourier data. *IEEE Journal of Selected Topics in Signal Processing*, 4:288–297, 2009.

[128] P. Calmon, S. Mahaut, S. Chatillon, and R. Raillon. CIVA: an expertise platform for simulation and processing NDT data. *Ultrasonics*, 44:e975–e979, 2006. URL www-civa.cea.fr.

[129] R. Saab and Ö Y lmaz. Sparse recovery by non-convex optimization–instance optimality. *Applied and Computational Harmonic Analysis*, 2009.

[130] P. Binev, W. Dahmen, R. DeVore, P. Lamby, D. Savu, and R. Sharpley. Compressed sensing and electron microscopy. *Preprint*, 89, 2011.

[131] Michael A. Sheehy, Brian R. Tull, Cynthia M. Friend, and Eric Mazur. Chalcogen doping of silicon via intense femtosecond-laser irradiation. *Materials Science and Engineering: B*, 137(1-3):289–294, February 2007. ISSN 0921-5107. doi: 16/j.mseb.2006.10.002. URL http://www.sciencedirect.com/science/article/pii/S092151070600599X.

[132] J. Trampert and J. J Leveque. Simultaneous iterative reconstruction technique: Physical interpretation based on the generalized least squares solution. *J. geophys. Res*, 95(12):553–9, 1990.

[133] A. S Willsky. Constrained sinogram restoration for limited-angle tomography. *Optical Engineering*, 29(5/535), 1990.

[134] J. L Prince. An iterative approach to sinogram restoration. In *Engineering in Medicine and Biology Society, 1990., Proceedings of the Twelfth Annual International Conference of the IEEE*, pages 366–367. IEEE, 1987. ISBN 0879425598.

[135] H. Kudo and T. Saito. Sinogram recovery with the method of convex projections for limited-data reconstruction in computed tomography. *JOSA A*, 8(7):1148–1160, 1991.

[136] S. Helgason. *The radon transform*. Birkhauser, 1999.

[137] J. Barzilai and J. M. Borwein. Two-point step size gradient methods. *IMA Journal of Numerical Analysis*, 8(1):141, 1988.

[138] J. L Starck, F. Murtagh, and J. M Fadili. *Sparse image and signal processing: wavelets, curvelets, morphological diversity*. Cambridge Univ Pr, 2010. ISBN 0521119138.